A Study of Radio Astronomy Principles and SKA Pathfinder System Designs with Pulsar Science

by

Sunelle Otto

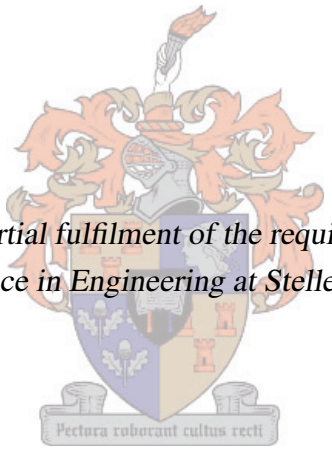

Thesis presented in partial fulfilment of the requirements for the degree of Master of Science in Engineering at Stellenbosch University

Supervisor: Prof. Petrie Meyer
Department of Electrical and Electronic Engineering

March 2011

Declaration

By submitting this thesis electronically, I declare that the entirety of the work contained therein is my own, original work, that I am the sole author thereof (save to the extent explicitly otherwise stated), that reproduction and publication thereof by Stellenbosch University will not infringe any third party rights and that I have not previously in its entirety or in part submitted it for obtaining any qualification.

March 2011

Abstract

Keywords – Radio Astronomy, Interferometry, Electromagnetic Radiation, Square Kilometre Array, Receiver System Design, Pulsar Observations

The Square Kilometre Array (SKA) is an international project to build the world's largest and most sensitive radio telescope interferometer. It will consist of thousands of antennas distributed over many kilometers, with the hosting country being either South Africa or Australia. Various pathfinders have been initiated to demonstrate the technologies needed to implement the SKA. The astronomy community has defined five Key Science Projects (KSP), which are the drivers for the SKA. The science goals determine the technical requirements needed to design SKA systems. Many years of planning and development are still needed in order to meet to the requirements of such a large and complex project.

This thesis aims to present the various SKA pathfinder systems in terms of their application to the SKA key science projects, with main focus that of pulsar observations. In order to achieve this, a thorough overview of basic radio astronomy principles and techniques is presented, followed by a detailed look at the various pathfinders. Throughout the work, aspects of pulsar observations are given particular attention with the goal of designing optimal systems for the SKA.

Opsomming

Sleutelwoorde – Radio Astronomie, Interferometrie, Elektromagnetiese Straling, Ontvanger Stelsel Ontwerp, Pulsar Waarnemings

Die Square Kilometre Array (SKA) is ’n internasionale projek om die wêreld se grootste en mees sensitiewe radio teleskoop interferometer te bou. Dit sal bestaan uit duisende antennas versprei oor etlike kilometers, met die gasheer land óf Suid-Afrika óf Australië. Verskeie koersbepalers is geïnisieer om die tegnologie te demonstreer wat benodig is om die SKA te implementeer. Die astronomie gemeenskap het vyf sleutel wetenskap projekte (KSP) gedefinieër wat dien as die drywers vir die SKA. Die wetenskap doelwitte bepaal die tegniese vereistes wat nodig is om SKA stelsels to ontwerp. Talle jare van beplanning en ontwikkeling word steeds benodig om te voldoen aan die vereistes van so ’n groot en komplekse projek.

Hierdie tesis het ten doel die aanbieding van verskeie SKA koersbepaler stelsels in terme van hulle aanwending tot die SKA sleutel wetenskap projekte, met hoof fokus op die van pulsar waarnemings. Om dit te behaal, word ’n deeglike oorsig van basiese radio astronomie beginsels en tegnieke aangebied, gevolg deur ’n gedetailleerde kyk na die verskeie koersbepalers. Regdeur die werk word spesifieke aandag gegee aan aspekte van pulsar waarnemings met die doel om optimale stelsels vir die SKA te ontwerp.

Acknowledgements

- Prof. Petrie Meyer, for guiding me throughout this project, always willing to help or give advice with a smile.
- Dr. Dirk de Villiers, for being such a good rolemodel and assisting with project details.
- Prof. David Davidson, for introducing me to the KAT project.
- Ludwig Schwardt, for giving us a tour at the KAT offices and passing on the Mac.
- Adriaan Peens-Hough, for helping with the XDM details.
- Marius van der Merwe, for helping with the KAT-7 details.
- Mattieu de Villiers, for answering my iAntConfig questions.

- David, Tinus, Dirk, Karla, Shamim, Werner and Phillip, for making office life interesting.
- Louis, for providing me with just the right amount of perspective.
- My family, for providing me with the support I needed.
- My friends, for being there in times of good and bad.

- Uncle Google, for being such a rich source of information and inspiration.
- NRF, for providing bursary support.

“Into this mysterious universe we are born,
with no apparent set of instructions, no maps or equations, no signs or guideposts,
nothing but our equally unfathomable instincts, intuitions, and reasoning abilities
to tell us where we came from, why we are here, and what we are supposed to do.
What we do possess - perhaps it is the key to our survival as a species -
is an almost unquenchable need to know.”
- Philip S. Berg -

Table of Contents

List of Figures

List of Tables

List of Acronyms

AA	Aperture Array
ADC	Analog-to-Digital Converter
ASKAP	Australian Square Kilometre Array Pathfinder
BPF	Bandpass Filter
BW	Bandwidth
EM	Electromagnetic
EMBRACE	Electronic Multi-Beam Radio Astronomy Concept
FoV	Field of View
FT	Fourier Transform
IF	Intermediate Frequency
ISM	Interstellar Medium
KAT	Karoo Array Telescope
KSP	Key Science Project
LNA	Low-Noise Amplifier
LO	Local Oscillator
LOFAR	Low Frequency Array
OMT	Orthogonal Mode Transducer
PAF	Phased Array Feed
PSF	Point Spread Function

RF	Radio Frequency
RFI	Radio Frequency Interference
SKA	Square Kilometre Array
VLBI	Very Long Baseline Interferometry
WBSPF	Wide-Band Single Pixel Feed
XDM	Experimental Development Model

Chapter 1

Introduction

Imagine an instrument that is capable of looking so far back in time, that is able to witness how the first galaxies formed. Making scientific discoveries that question the very fundamental laws that we build our world on. Perhaps even finding intelligent life. This instrument is the Square Kilometre Array (SKA).

1.1 Background

The idea behind the SKA is to design the largest radio telescope in the world, with a total collecting area of $1km^2$. The array design would consist of thousands of antenna dishes and ground aperture arrays distributed with baselines of up to at least 3000km. This instrument will be one of a kind, with 50 times more sensitivity and 10,000 times the survey speed of any other existing telescope in the world. The SKA has come a long way, starting as a concept in 1991, now almost 20 years in its design phase and estimated to be fully operational by 2024. A large project like the SKA stretches over many disciplines and involves professionals form all over, resulting in a global collaboration of 20 countries [1].

The decision was made in 2006 that South Africa and Australia would be the final candidates to host this telescope. The SKA specifications demand cutting-edge technology, which is being developed by many institutions and design groups for all parts of the system. This includes the antennas, Low-Noise Amplifiers (LNAs), feeds, Radio Frequency (RF) electronics, digital back-ends, beamformers, correlators, signal processing, Radio Frequency Interference (RFI), data transport, and the list goes on. Projects have been initiated as pathfinders for the SKA that contributes to testing the proposed technologies [2]. To name a few, South Africa is working on the MeerKAT project that demonstrates Wide-Band Single Pixel Feeds (WBSPFs). Australia is working on the Australian Square Kilometre Array Pathfinder (ASKAP) project, demonstrating Phased Array Feeds (PAFs). The Netherlands are developing sparse and dense Aperture Array (AA) technology with Low Frequency Array (LOFAR) and Electronic Multi-Beam Radio Astronomy Concept (EMBRACE).

The drivers for this instrument are the science observations, requested by the radio astronomers [3]. These are referred to as the Key Science Projects (KSPs) and include:

- The Cradle of Life
- Strong-Field Tests of Gravity using Pulsars and Black Holes
- The Origin and Evolution of Cosmic Magnetism

- Galaxy Evolution, Cosmology and Dark Matter
- Probing the Dark Ages

A set of top-level specifications for the SKA (see B.1) were initially defined as a guideline [1]. This project is an ongoing process to develop the technology and design the systems needed to satisfy these specifications.

1.2 Objectives

This thesis aims to present the various SKA pathfinder systems in terms of their application to the SKA KSP, with main focus that of pulsar observations. In order to achieve this, a thorough overview of basic radio astronomy principles and techniques is presented, followed by a detailed look at the various pathfinders. Throughout the work, aspects of pulsar observations are given particular attention with the goal of designing optimal systems for the SKA. The objectives of this document therefore include the following:

- A study of Radio Astronomy principles and techniques
- An analysis of various SKA pathfinder system designs
- A study of the Pulsar science case for optimal SKA system designs

1.3 Overview

This document in part presents a thorough overview of basic radio astronomy principles and techniques. Particularly relevant to an array such as the SKA, concepts such as interferometry are discussed in Chapter 2. The importance of the u,v-plane is given by examples of antenna configurations and the effect on the Point Spread Function (PSF). Much of the universe is revealed when studying objects at radio wavelengths and together with observational data from other parts of the Electromagnetic (EM) spectrum, can form complete images of the sky. In Chapter 3 the mechanisms of EM radiation, namely thermal and non-thermal radiation are described to form an understanding of how we receive information from radio objects. The effect of media on these waves are also considered. Chapter 4 presents practical examples of radio sources and emission found within our universe. This includes anything from spectral lines, molecular clouds, supernova remnants and pulsars to the more mysterious dark matter and black holes. Normal and active galaxies are considered and some radio phenomena described.

Focusing on the SKA project specifically, Chapter 5 gives a background description concerning the SKA technologies under development, pathfinders as well as the KSPs. A detailed study is then made of a number of these SKA pathfinder system designs. This starts with the Experimental Development Model (XDM) and Parkes telescopes as single dish designs and important SKA precursors [4]. Then antenna arrays systems including the KAT-7, MeerKAT [5], ASKAP [6] and EMBRACE [7] are considered. The discussion takes into account the system parameter specifications and investigates the top-level design of the signal path from the antenna and RF stages through to the digital and processing back-end. Layout simulations are made and evaluated for some of these pathfinders.

From the five KSPs, the pulsar science case is selected to evaluate the implications of the science on the system design with the goal of designing optimal systems for the SKA. This is given in Chapter 6, with a

detailed discussion for the pulsar science case including the science goals and technical specifications for pulsar survey, timing and astrometric observations [8] [9]. Antenna layouts were designed and simulated from these specifications for pulsar surveys and the results compared with existing systems.

1.4 Contributions

For an engineer, it is the responsibility or rather a privilege to be part of the design of such a respectable instrument. The SKA is a complex project and needs years of careful planning, designing and testing to build the best instrument possible. The driving factor is the science and is requested by the radio astronomers. They determine the science goals that must be translated into technical system specifications to be used in the design [1]. Often this transition lacks thoroughness as the one science field hands over to another with a very limited understanding of each others needs or capabilities. This is one of the aims of this thesis, to provide engineers with sufficient understanding of radio astronomy science to build and design better telescope systems. Being integrated over multidisciplinary fields, it helps to make decisions taking as many as possible aspects of the system into consideration.

The SKA pathfinder systems are included to consider the current state of technology achievable. The added value is a systems perspective that can be used to learn and build on these systems. The focus on one science case, pulsar observations, was chosen to demonstrate how the set of science requirements leads to the technical specifications used to design a system. The purpose was not to present one optimal design as this is an ongoing and complicated process, but more importantly for now, to go through the steps of thinking that is needed to develop such systems.

The layout simulations were made not only to demonstrate how an array can be evaluated, but also to emphasise the impact of the choice in configuration on the quality of, and complexity in making the radio images. The simulations made for the pulsar observations helps to determine the feasibility of implementing these configuration designs. It also demonstrates the effect that the layout has on the system performance.

Chapter 2

Basic Radio Astronomy Principles

2.1 Introduction

This chapter begins by laying out some fundamental concepts often used in radio astronomy. It goes on to explain a simple two-element interferometer and defines the *u*,*v*-plane. It concludes with a description of why the *u*,*v*-plane plays such a significant role in forming radio images.

2.2 Fundamentals

Some terms are used regularly in the field of radio astronomy and are therefore necessary to present as a first step in our discussion. We start with basic antenna theory that will build onto more extensive concepts.

2.2.1 Antenna Pattern

The antenna pattern describes the radiation properties of the antenna when transmitting or receiving a signal. It is represented graphically as in Fig.2.1 by using a coordinate system with θ and ϕ directions. The main lobe points in the direction of maximum radiation, while the side-lobes are usually any unwanted lobes in the beam [10]. The *near-field pattern* is a function of angle and distance. More often we use the *far-field pattern* which is at longer distances and a function of the mentioned coordinates.

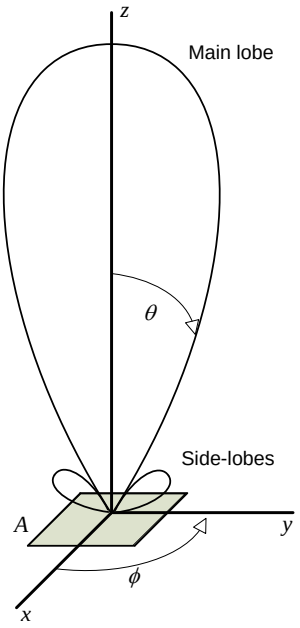

Figure 2.1: Antenna pattern with coordinates (θ, ϕ).

Fourier relation

The aperture distribution of an antenna is related the far-field pattern by the Fourier Transform (FT). Given a finite aperture with length a (in meters) so that a_λ (in wavelengths) is defined as $a_\lambda = a/\lambda$, the relation for the ϕ direction is given by (2.2.1) [11, ch.6].

$$E(\phi) = \int_{-a_\lambda/2}^{+a_\lambda/2} E(x_\lambda) e^{j2\pi x_\lambda sin(\phi)} \mathrm{d}x_\lambda \tag{2.2.1}$$

with $E(\phi)$ the far-field pattern

$E(x_\lambda)$ the aperture distribution

$x_\lambda = x/\lambda$ the distance in wavelengths

Fig.2.2 shows a uniform and inverse taper aperture distribution respectively with their corresponding field patterns.

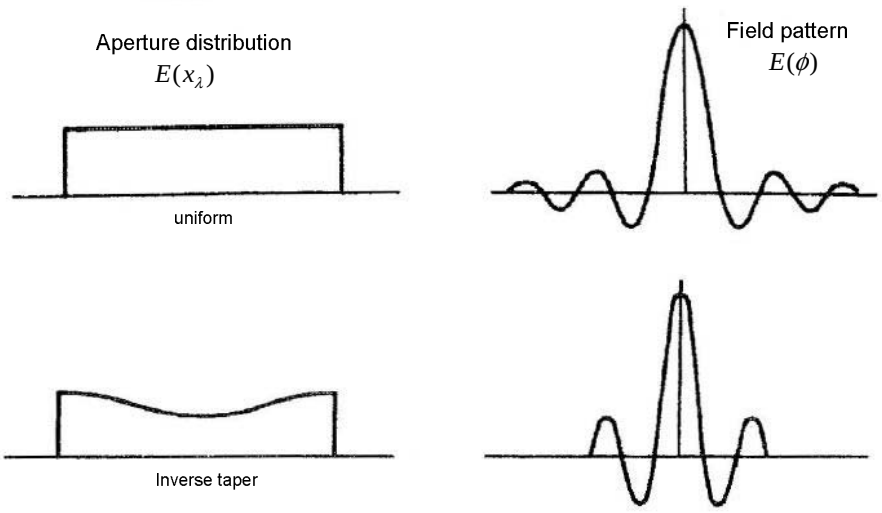

Figure 2.2: Aperture distributions with their far-field patterns.

Power pattern

The antenna power pattern is the square of the magnitude of the electric field. It is given by (2.2.2) as the far-field pattern multiplied with its conjugate [11, sec6-2].

$$P(\theta,\phi) = E(\theta,\phi)E^*(\theta,\phi) \tag{2.2.2}$$

with $E(\theta,\phi)$ the far-field pattern
$E^*(\theta,\phi)$ the complex conjugate of $E(\theta,\phi)$

The antenna power pattern can be represented by a solid angle as shown in Fig.2.3. This solid angle contains the total power of the power pattern, the radius being constant amplitude that is equal to the maximum value of the power pattern. This is referred to as the *beam solid angle* and is given by (2.2.3).

$$\Omega_A = \iint_{4\pi} P_n(\theta,\phi)\mathrm{d}\Omega \tag{2.2.3}$$

with $P_n(\theta,\phi)$ the normalised antenna power pattern
Ω_A the total beam solid angle

The power pattern is integrated over the solid angle (surface area) of a sphere, 4π.

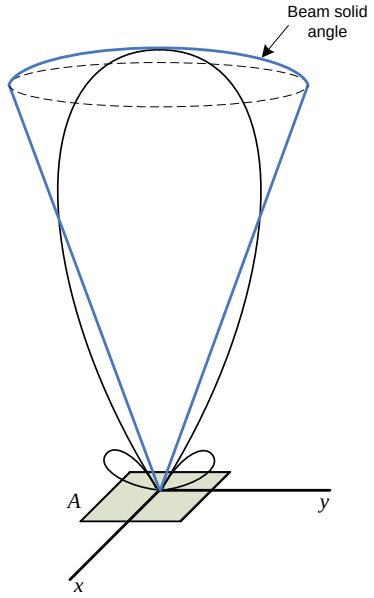

Figure 2.3: Antenna pattern with beam solid angle.

Array theory

From array theory [10, ch.6], [11, sec6-6] it is known that the array pattern can be described as follows:

array pattern = [element pattern] x [array factor]

With the element pattern the antenna far-field pattern of an individual element and the array factor (AF) the array pattern of point sources.

For an n-element array of similar sources with equal amplitude and spacing and the reference at the centre of the array, the array pattern is given by (2.2.4).

$$E = \underbrace{E_0}_{1^{st}} \underbrace{\frac{\sin(n\psi/2)}{\sin(\psi/2)}}_{2^{nd}} \tag{2.2.4}$$

With the first term being the element pattern, the second term the array factor and $\psi = \beta d \sin\phi + \delta$ (with $\beta = 2\pi/\lambda$, d the source spacing, δ the source phase difference).

2.2.2 Brightness Distribution

Brightness is the power received from an object in the sky and is often used when describing the intensity distribution of a source structure. It is also known as the sky or surface brightness and is defined as *power received per unit area per unit solid angle per unit bandwidth*. The following derivations are from [11, ch.3]. Consider Fig.2.4 that shows radiation from the sky with brightness, B that falls onto an area, A on the earth's surface.

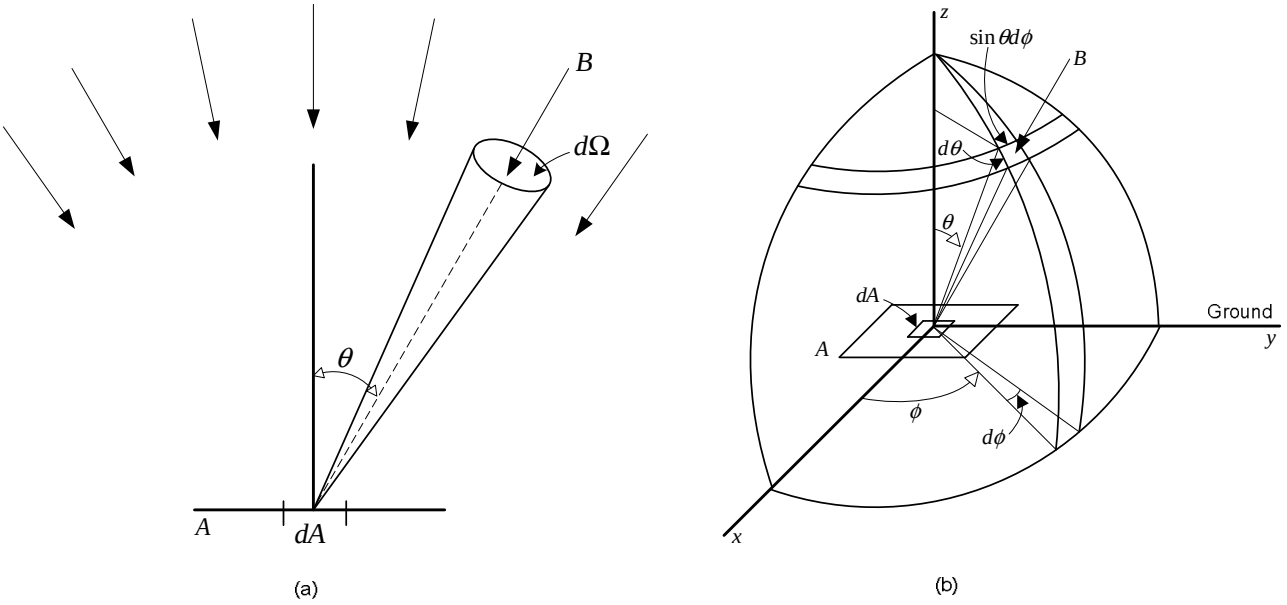

Figure 2.4: Brightness, B that is measured by (a) the solid angle dΩ and the area A. b) The (θ, ϕ) co-ordinate system which shows the element approximation as $sin\theta d\theta d\phi$.

The solid angle dΩ in Fig.2.4 a) is represented by a small element $\sin\theta d\theta d\phi$ in Fig.2.4 b) so that $d\Omega = sin\theta d\theta d\phi$. Here the (θ, ϕ) co-ordinate system is shown, with θ the zenith angle and ϕ the azimuth angle. The small element of power received from the source can be can therefore be described by (2.2.5).

$$dW = B\cos\theta d\Omega dA d\nu \tag{2.2.5}$$

with dΩ a small element of solid angle of the sky

B the brightness of the sky at the position of dΩ

dA a small element of the area

dν a small element of bandwidth

The *spectral power density*, w is the power per unit bandwidth so that if we assume that A is uniform over the area and integrate over a solid angle Ω of the sky, we get (2.2.6).

$$w = A\iint_{\Omega} B\cos\theta d\Omega \tag{2.2.6}$$

The spectral power is related to the power by $W = \int_{\nu}^{\nu+\Delta\nu} w d\nu$ so that the *power*, W is given by (2.2.7).

$$W = A\int_{\nu}^{\nu+\Delta\nu}\iint_{\Omega} B\cos\theta d\Omega d\nu \tag{2.2.7}$$

Brightness is a function of sky angle and can therefore be expressed as $B(\theta,\phi)$ so that (2.2.6) becomes (2.2.8).

$$w = A \iint B(\theta,\phi)\cos\theta \mathrm{d}\Omega \tag{2.2.8}$$

The power pattern (already mentioned in section 2.2.1) is the response of the antenna to radiation over the sky angles (θ,ϕ) and replaces the $\cos\theta$ term in (2.2.8) so that the spectral power becomes (2.2.9).

$$w = \frac{1}{2}A_e \iint_\Omega B(\theta,\phi)P_n(\theta,\phi)\mathrm{d}\Omega \tag{2.2.9}$$

with A_e the effective aperture of the antenna

When using a single polarised antenna that receives an unpolarised wave, only about half of the power available will be captured. The power is given by (2.2.10).

$$W = \frac{1}{2}A_e \int_\nu^{\nu+\Delta\nu} \iint_\Omega B(\theta,\phi)P_n(\theta,\phi)\mathrm{d}\Omega\mathrm{d}\nu \tag{2.2.10}$$

2.2.3 Discrete sources

A discrete source is a source that can be distinguished as separate from other sources or objects in the sky. It can take the form of a *point source*, *localised source* or an *extended source* as shown in Fig.2.5.

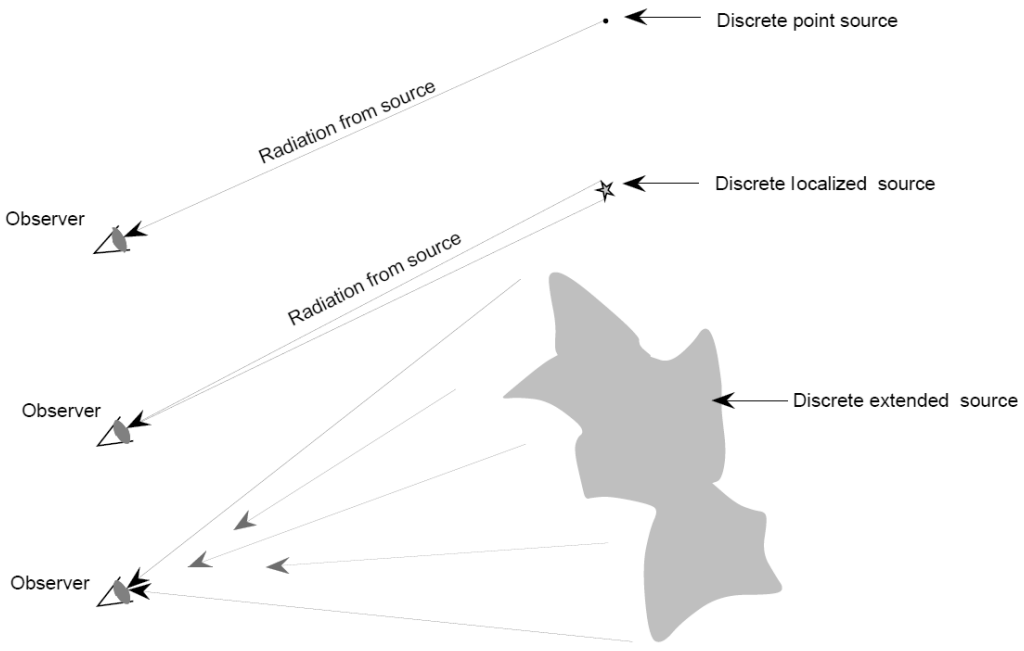

Figure 2.5: Illustration of the difference between different discrete sources, from [12].

A point source is just an idealisation and has a very small extent compared to the antenna beam size. A localised source has a small but finite extent, while an extended source has a still larger extent.

2.2.4 Flux density

Often in radio astronomy we use the term *flux density* which is the brightness measured over the whole source. Assume that the antenna beam is directed at a discrete source. The total flux density, S of the source in terms of the brightness function is then given by (2.2.11) [11, ch.3] [1].

$$S = \iint_{source} B(\theta,\phi)\mathrm{d}\Omega \tag{2.2.11}$$

This represents the *actual* or *true* value of the source flux. The *observed* flux density by an antenna however is given by (2.2.12).

$$S_o = \iint_{source} B(\theta,\phi)P_n(\theta,\phi)\mathrm{d}\Omega \tag{2.2.12}$$

The antenna pattern, $P_n(\theta,\phi)$ acts like a weighting function in that its value is one or less over the source angle. It therefore either matches the value of the brightness, $B(\theta,\phi)$ or decreases it so that the observed flux in (2.2.12) is less than the actual flux in (2.2.11).

When the antenna beam is not aligned with the source, the following applies. Let us assign the reference direction on ($\phi = 0$,$\theta = \pi/2$) as in Fig.2.6 a) and consider only one direction, ϕ as in Fig.2.6 b). The antenna pattern is displaced by an angle of ϕ_0 and the source is on the reference direction.

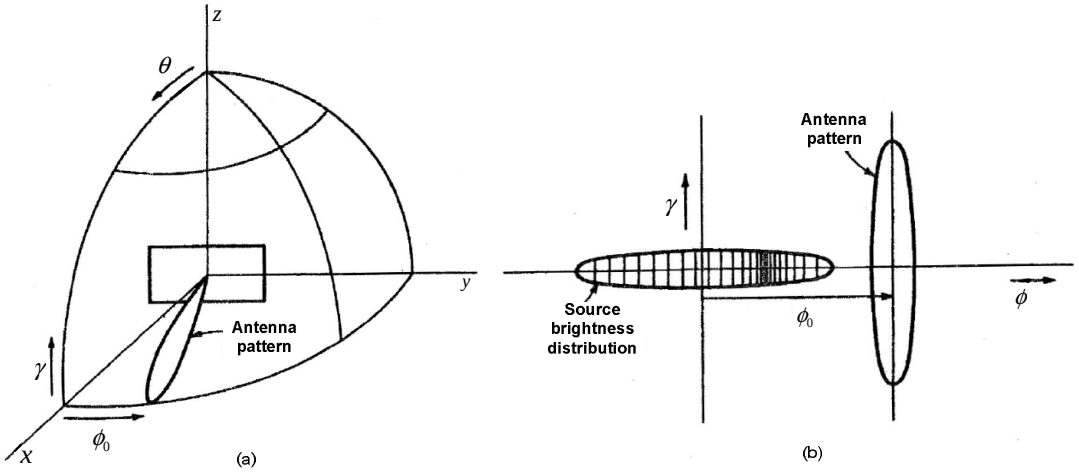

Figure 2.6: (a) The antenna pattern and (b) side view of a fan-beam antenna pattern displaced by ϕ_0.

The observed flux density is then given by (2.2.13). [11, eq(3-24)].

$$S(\phi_o) = \int B(\phi)\widetilde{P}_n(\phi_0 - \phi)\mathrm{d}\phi \tag{2.2.13}$$

This is the convolution of the brightness and antenna pattern, with $\widetilde{P}_n(\phi) = P_n(-\phi)$.

[1] Flux density is measured in *jansky* (*Jy*) which is equal to $10^{-26} watt\ m^{-2} Hz^{-1}$

Fig.2.7 shows the source as smaller than the antenna beam area. The source is now centered on $\theta = 0$ with the antenna directed at the source.

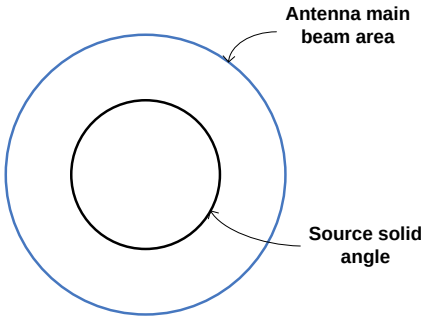

Figure 2.7: Source aligned with antenna pattern.

The *observed brightness* is then given by (2.2.14).

$$B_o = \frac{\iint B(\theta,\phi)P_n(\theta,\phi)\mathrm{d}\Omega}{\iint P_n(\theta,\phi)\mathrm{d}\Omega} = \frac{S_o}{\Omega_A} \tag{2.2.14}$$

With $B(\theta,\phi)$ the actual brightness distribution

B_o the observed brightness

S_o the observed flux density

Ω_A the antenna beam area

In the case where the source is very small compared to the antenna beam area, the observed flux density, S_o is equal to the actual flux density, S. The *actual average brightness* is then given by (2.2.15).

$$B_{avg} = \frac{S}{\Omega_s} = \frac{1}{\Omega_s}\iint B(\theta,\phi)\mathrm{d}\Omega \tag{2.2.15}$$

with Ω_s the source solid angle

2.2.5 Visibility

The visibility is measurements of the spatial frequencies of the brightness distribution of a source on the sky using an antenna interferometer. This concept will be explained further as the chapter progresses. For now, let us consider how the following derivations from [11, ch.6] resolve the visibility as a set of complex numbers.

Consider a two element array where we will only look at the one dimension, that is the co-ordinate direction, ϕ. The far-field array pattern for a two element array (see (2.2.4) with n=2) can be shown to result in (2.2.16).

$$E(\phi) = E_n(\phi)\cos\frac{\psi}{2} \tag{2.2.16}$$

with $E_n(\phi)$ the normalised far-field element pattern

$\psi = 2\pi s_\lambda \sin\phi$, with s_λ the baseline

The power pattern (see section 2.2.1) is then given by (2.2.17).

$$P(\phi) = |E(\phi)|^2 = |E_n(\phi)|^2 \cos^2 \frac{\psi}{2} = |E_n(\phi)|^2 (1 + \cos\psi)/2 \tag{2.2.17}$$

Assume the source is a point source with angular extent α and that it is small compared to the element pattern. This means that $|E_n(\phi)|$ is constant.

We get that the observed flux density is then that of (2.2.18).

$$\begin{aligned} S(\phi_0, s_\lambda) &= |E_n(\phi)|^2 \int_{-\alpha/2}^{+\alpha/2} B(\phi) \{1 + \cos[2\pi s_\lambda \sin(\phi_0 - \phi)]\} d\phi \\ &= |E_n(\phi)|^2 \left\{ S_o + \int_{-\alpha/2}^{+\alpha/2} B(\phi) \cos[2\pi s_\lambda \sin(\phi_0 - \phi)] d\phi \right\} \end{aligned} \tag{2.2.18}$$

With $S(\phi_0, s_\lambda)$ the observed flux density distribution

$B(\phi)$ the true source brightness distribution

S_o the flux density of the source

Note that here the observed flux density is equal to the actual flux density $S_o = S = \int_{-\alpha/2}^{+\alpha/2} B(\phi) d\phi$, because of the source being small compared to the beam area.

Further assumptions are that $|E_n(\phi)|^2 = 1$ and $\phi_0 - \phi << \pi$ so that (2.2.18) becomes (2.2.19).

$$S(\phi_0, s_\lambda) = S_o + \cos 2\pi s_\lambda \phi_0 \int_{-\alpha/2}^{+\alpha/2} B(\phi) \cos 2\pi s_\lambda \phi d\phi + \sin 2\pi s_\lambda \phi_0 \int_{-\alpha/2}^{+\alpha/2} B(\phi) \sin 2\pi s_\lambda \phi d\phi \tag{2.2.19}$$

A variable term, V is now defined by (2.2.20),

$$V(\phi_0, s_\lambda) = \frac{1}{S_o} \cos 2\pi s_\lambda \phi_0 \int_{-\alpha/2}^{+\alpha/2} B(\phi) \cos 2\pi s_\lambda \phi d\phi + \frac{1}{S_o} \sin 2\pi s_\lambda \phi_0 \int_{-\alpha/2}^{+\alpha/2} B(\phi) \cos 2\pi s_\lambda \phi d\phi \tag{2.2.20}$$

so that $S(\phi_0, s_\lambda) = S_o[1 + V(\phi_0, s_\lambda)]$.

The *fringe amplitude*, $V_o(s_\lambda)$ with displacement $\Delta\phi_0$ can be expressed by (2.2.21) and (2.2.22).

$$V_o(s_\lambda) \cos 2\pi s_\lambda \Delta\phi_0 = \frac{1}{S_o} \int_{-\alpha/2}^{+\alpha/2} B(\phi) \cos 2\pi s_\lambda \phi d\phi \tag{2.2.21}$$

$$V_o(s_\lambda) \sin 2\pi s_\lambda \Delta\phi_0 = \frac{1}{S_o} \int_{-\alpha/2}^{+\alpha/2} B(\phi) \sin 2\pi s_\lambda \phi d\phi \tag{2.2.22}$$

The combination of (2.2.21) and (2.2.22), results in (2.2.23) represents the *complex visibility function* which is an observable quantity.

$$V_o(s_\lambda) e^{j2\pi s_\lambda \Delta\phi_0} = \frac{1}{S_o} \int_{-\infty}^{+\infty} B(\phi) e^{j2\pi s_\lambda \phi} d\phi \tag{2.2.23}$$

It can then be shown that the true source brightness distribution given by (2.2.24) is the result of the inverse FT of (2.2.23).

$$B(\phi_0) = S_o \int_{-\infty}^{+\infty} V_o(s_\lambda) e^{-j2\pi s_\lambda (\phi_0 - \Delta\phi_0)} ds_\lambda \tag{2.2.24}$$

For the two dimensional case, the visibility function is given by (2.2.25) in terms of u,v- and x,y - coordinates.

$$V(u,v,w)e^{j2\pi w} = \int_{-1}^{+1}\int_{-1}^{+1} \frac{B(x,y)}{\sqrt{1-x^2-y^2}} e^{j2\pi(ux+vy+\sqrt{1-x^2-y^2}w)} \mathrm{d}x\mathrm{d}y \tag{2.2.25}$$

With $B(x,y)$ the brightness distribution of the object and $z = \sqrt{1-x^2-y^2}$.

When x and y is small, $\sqrt{1-x^2-y^2} \approx 1$ and the w-component can be ignored so that (2.2.25) becomes (2.2.26).

$$V(u,v) = \int_{-1}^{+1}\int_{-1}^{+1} \frac{B(x,y)}{\sqrt{1-x^2-y^2}} e^{j2\pi(ux+vy)} \mathrm{d}x\mathrm{d}y \tag{2.2.26}$$

The brightness distribution is then given by (2.2.27).

$$B(x,y) = \int_{-\infty}^{\infty}\int_{-\infty}^{\infty} V(u,v)e^{-j2\pi(ux+vy)} \mathrm{d}u\mathrm{d}v \tag{2.2.27}$$

Thus in theory, the true brightness distribution can be obtained by the inverse FT of the visibility function.

2.3 Interferometry

This section describes a method by which several antennas are used together to form images of the radio sky. This is the basic concept of the Square Kilometre Array (SKA) design and is therefore included here.

2.3.1 Two-element Interferometer

Two important parameters that describe a radio telescope are angular resolution and sensitivity. Angular resolution is the distance between two objects in the sky that can be resolved or distinguished by an antenna and is dependent on wavelength and the aperture diameter of the antenna by λ/D. Sensitivity is the ability to detect weak radio signals and depends on the aperture area of the antenna [13].

To increase the sensitivity and angular resolution of a radio telescope, a larger aperture is required. Instead of increasing the dish size, a more effective way would be to make use of interferometry. In interferometry, two or more antennas are used to form an antenna array. The spacing between any two antennas in the array is called a *baseline*. The array then operates as a single large antenna with an aperture diameter that is equal to the maximum baseline. The angular resolution, θ given by (2.3.1) depends on the maximum baseline of the array, while the sensitivity depends on the total collecting area of the array.

$$\theta = \frac{\lambda}{b_{max}} \tag{2.3.1}$$

Consider Fig.2.8 that gives an illustration of two antennas working together as an interferometer. Both are on the same height above ground, separated by the baseline distance and pointing in the direction of a source *s*.

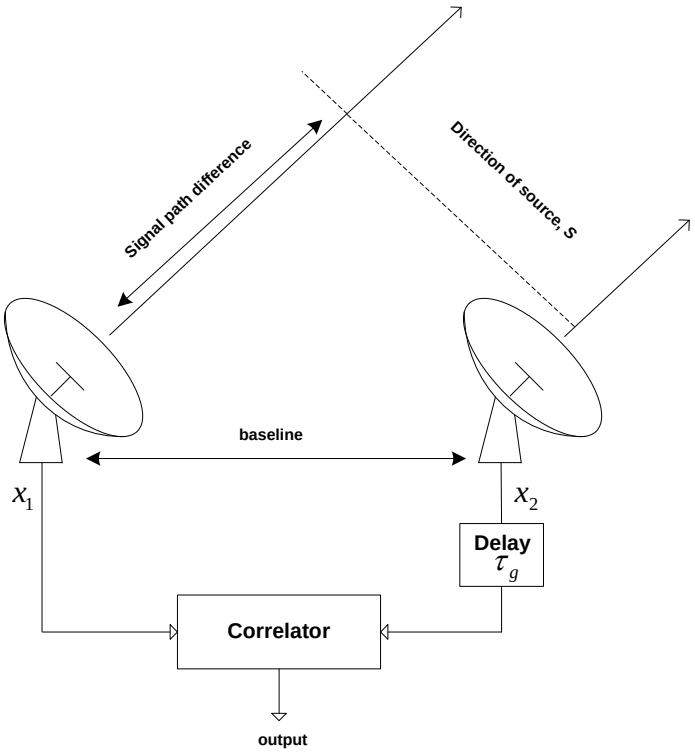

Figure 2.8: A simple two-element interferometer.

The voltage signals x_1 and x_2 are proportional to the electric field received at each antenna. When considering the radiation from the source that reaches the antennas, signal x_2 will arrive a moment earlier than x_1. This can be corrected for by adding a time delay τ_g to the one signal. The signals are here represented by (2.3.2) and (2.3.3) [13].

$$x_1(t) = v_1 \cos[2\pi\nu(t-\tau_g)] \tag{2.3.2}$$

$$x_2(t) = v_2 \cos[2\pi\nu t] \tag{2.3.3}$$

With v_1 and v_2 the voltage amplitudes of x_1 and x_2 respectively

ν the frequency

τ_g the geometrical time delay

These signals are then combined into the receiver called the correlator. The cross-correlation of the two signals is given by (2.3.4).

$$R_{x_1x_2}(\tau_g) = v_1 v_2 \cos[2\pi\nu\tau_g] \tag{2.3.4}$$

Note that this is the cosine component of the correlation. To get the sine component, a phase shift of 90° is added to the signal. The cos and sine components respectively, represents the real and imaginary part of the complex visibility (mentioned in 2.2.5). The correlator output is in a sinusoidal form referred to as the *fringe pattern* or *fringes*. It is the result of the change in source direction over time and therefore also τ_g given by (2.3.5)

$$\tau_g = \frac{b\sin\theta}{c} \tag{2.3.5}$$

With θ the direction of the source

b the baseline

c the speed of light

The amplitude, v_1v_2 from (2.3.4), is proportional to the effective collecting area, *A(s)* (with s a unit vector in the direction of the source) and flux density, S of the source. In the frequency domain the FT of the complex visibility can be represented by (2.3.6) [13].

$$S_{x_1x_2}(\nu) = A(s)Se^{i2\pi\nu\tau_g} \tag{2.3.6}$$

It is important to form as many different baselines as possible to increase the resolution of the image formed. Therefore, we can add more antennas and use *aperture synthesis*, *Earth-rotation synthesis* or a combination of these two techniques. In aperture synthesis many baselines of an interferometer are used to imitate a single large aperture at any given moment. It can also be done sequentially by varying the baselines. Fig.2.9 shows the Very Large Array (VLA) interferometer. It consists of 27 radio antennas that run on railway tracks so that the array configuration can be changed [13].

Figure 2.9: The VLA interferometer, courtesy of NRAO/AUI [14].

In Earth-rotation synthesis, the movement of the Earth is used to form arcs of baselines on the *u*,*v*-plane (see section 2.4.1). To a radio source in the sky, the baseline distance between A and B in Fig.2.10 will change with time as the Earth rotates. This corresponds to taking measurements with different antenna baselines.

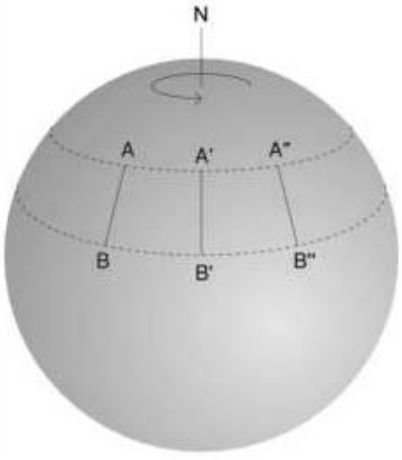

Figure 2.10: The rotation of the Earth results in various baselines, from [15].

2.4 The *u*,*v*-plane

The *u*,*v*-plane is a plane perpendicular to the direction of the source being observed and is used in interferometry (see section 2.3) to map points from projected baselines of antenna pairs. These points represent measurements of the complex visibility, used to obtain the true sky brightness distribution.

2.4.1 Coordinate system

Definition of *u*,*v*-plane

There is a convenient coordinate system (*u*, *v*, *w*) that is used to describe the response of an interferometer. Consider two antennas placed a certain distance apart on the ground plane, see Fig.2.11. If b is the baseline or distance between the two antennas in meters, then b_λ (dimensionless) is given by (2.4.1) [13].

$$b_\lambda = \frac{b}{\lambda} \tag{2.4.1}$$

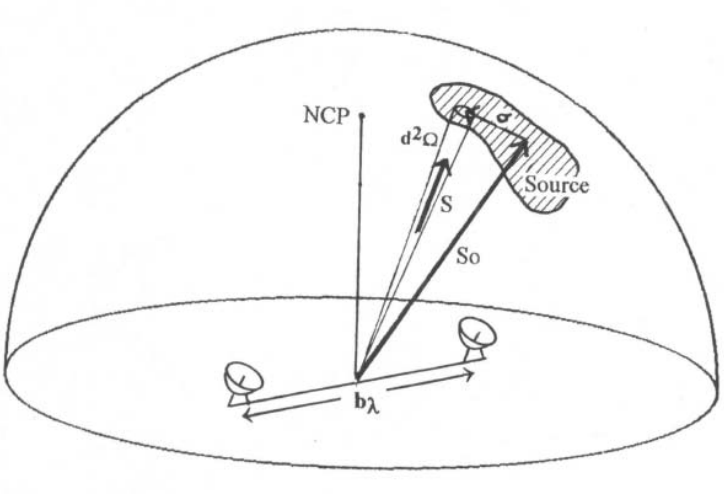

Figure 2.11: 2-element interferometer, from [13].

With $\vec{s_0}$ the phase tracking centre (direction of maximum antenna gain)
$\vec{s}$ is a vector pointing at a small element of an extended radio source
$\vec{\sigma}$ the vector so that $\vec{s} = \vec{s_0} + \sigma$
b_λ the baseline

Now consider the *u*,*v*-plane as shown in Fig.2.12, defined as the plane perpendicular to the source direction and parallel to the x-y plane (explained next).

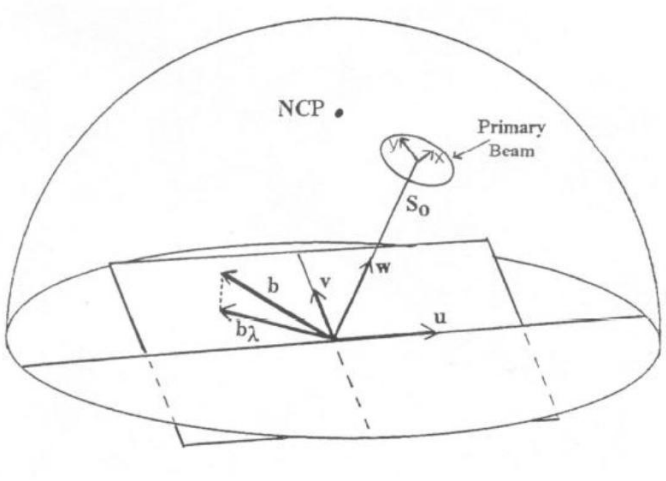

Figure 2.12: The *u*,*v*-plane, adapted from [13].

With $\vec{s_0}$ and *w* both pointing in the direction of the source
b_λ the actual baseline between two antennas on the ground plane
b indicates the projected baseline onto the *u*,*v*-plane.

Referring again to Fig.2.12, note that the vector $\vec{s_0}$ is perpendicular to the x-y plane so that $\vec{\sigma}$ is then only a function of *x* and *y*. This illustrates the slight tilt of the *u*,*v*-plane with respect to the ground plane and the orientation of the x-y plane. The significance of the *u*,*v*-plane will be discussed later on.

The x-y plane

The *w*-component (Fig.2.12) can be ignored when we are only looking at a small area of sky around $\vec{s_0}$. With this assumption, the x-y plane is seen as a result of projecting the celestial sphere onto a flat plane, see Fig.2.13.

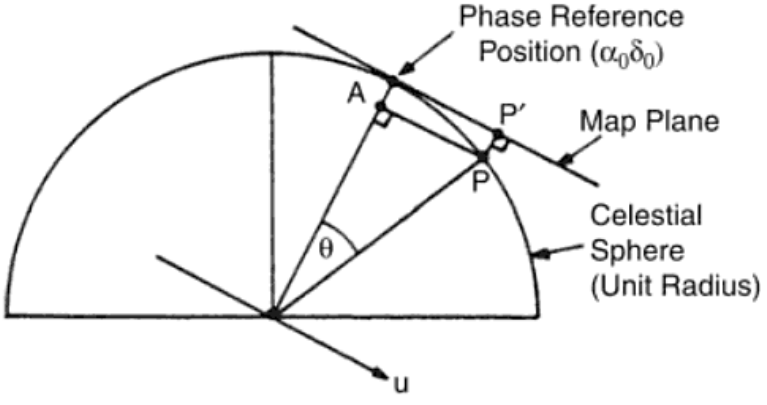

Figure 2.13: Points on the celestial sphere are mapped onto a flat plane, from [16].

While the *u*,*v* co-ordinates are spatial frequencies or projected baseline lengths in wavelengths, the (*x*,*y*,*z*) coordinates are the direction cosines of vector $\vec{s}$ taken with respect to the *u*,*v*-plane as shown in Fig.2.14 [16].

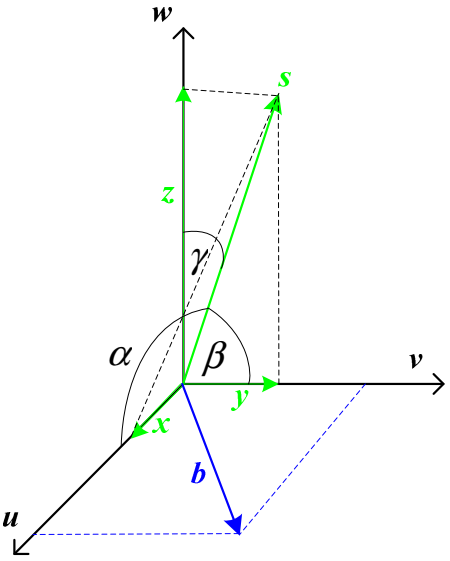

Figure 2.14: Direction cosines of vector $\vec{s}$, with b the projected baseline on the u,v-plane.

2.4.2 Examples of u,v-plots

Let us demonstrate the use of the u,v-plane with a few examples. Consider two antennas on the ground plane as given by Fig.2.15. The source direction is described by θ (blue plane) and ϕ the (red plane).

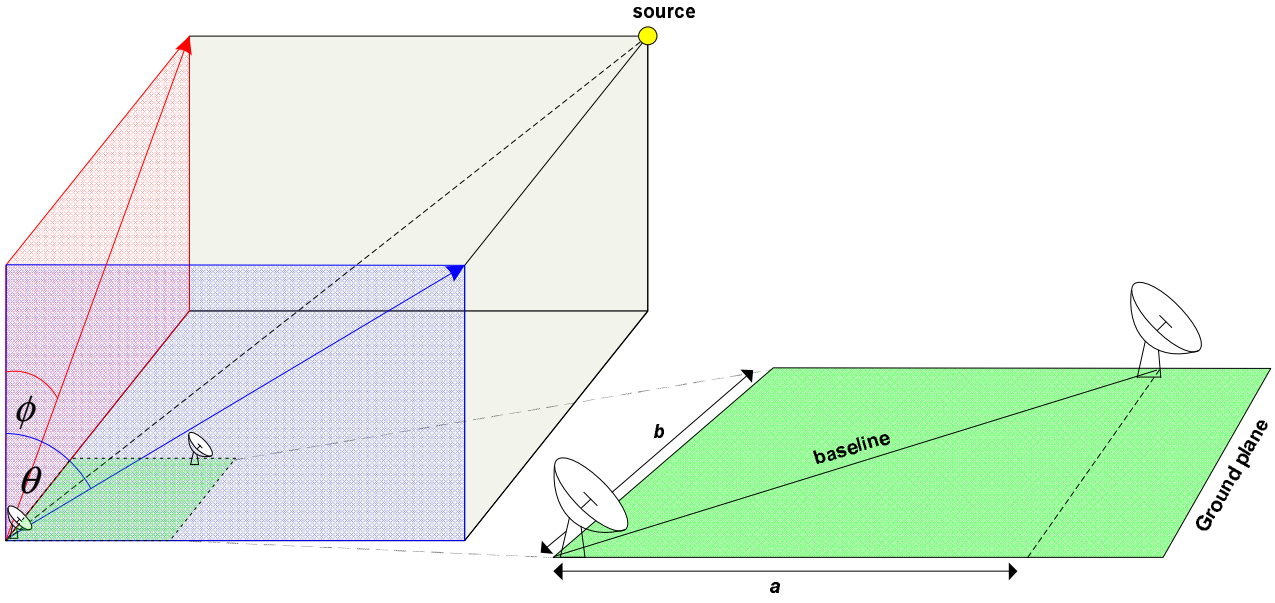

Figure 2.15: Two antennas on a ground plane with source direction described by θ and ϕ.

with (a,b) the coordinates of separation along the ground [in m]

θ in the plane of the a-axis

ϕ in the plane of the b-axis

The baseline is given by $\sqrt{a^2+b^2}$. The effective baseline, however, is the projected baseline onto a plane perpendicular to the direction of the source (see section 2.4.1). This can be described by coordinates (x,y) in (2.4.2).

$$(x,y) = (a\cos[\theta], b\cos[\phi]) \tag{2.4.2}$$

Fig.2.16 shows the same two antennas for the θ direction, with spacing a. When a is projected using (2.4.2), it gives the x-component on the x-y plane.

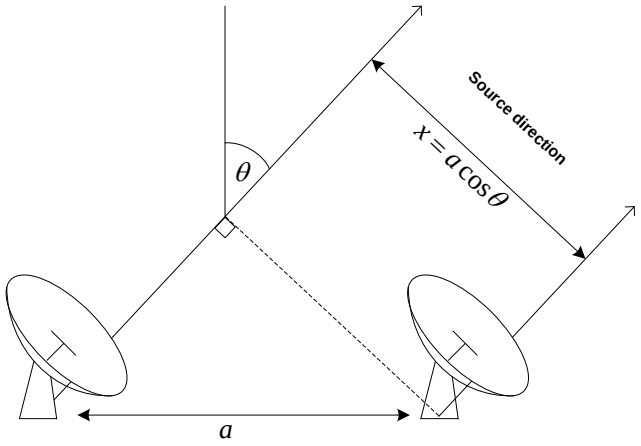

Figure 2.16: Two antennas with separation a and the projected x-component.

These baselines can be converted to points on the u,v-plane. If $u = kx$ and $v = ky$ with $k = 2\pi/\lambda$, then (2.4.3)–(2.4.4) follows:

$$(u,v) = (kx,ky) = (ak\cos[\theta], bk\cos[\phi]) \tag{2.4.3}$$

$$(u,v) = (-kx,-ky) = (-ak\cos[\theta], -bk\cos[\phi]) \tag{2.4.4}$$

Example 2.4*a*

Consider the two antennas with the following parameters as in Fig.2.17: $(a,b) = (3,5)$, $\phi = 0$ and $\theta = \pi/4$ at ν=1.4 GHz

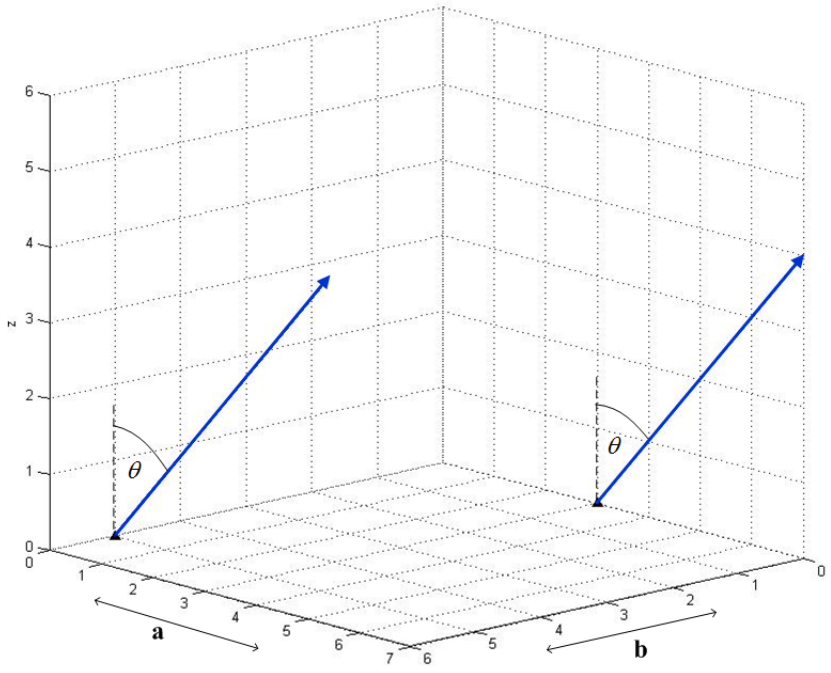

Figure 2.17: Two antennas on the ground plane pointing towards the source with angle θ.

By using (2.4.3)–(2.4.4), the (u,v) points can be calculated to produce two points (because of symmetry), as shown in Fig.2.18.

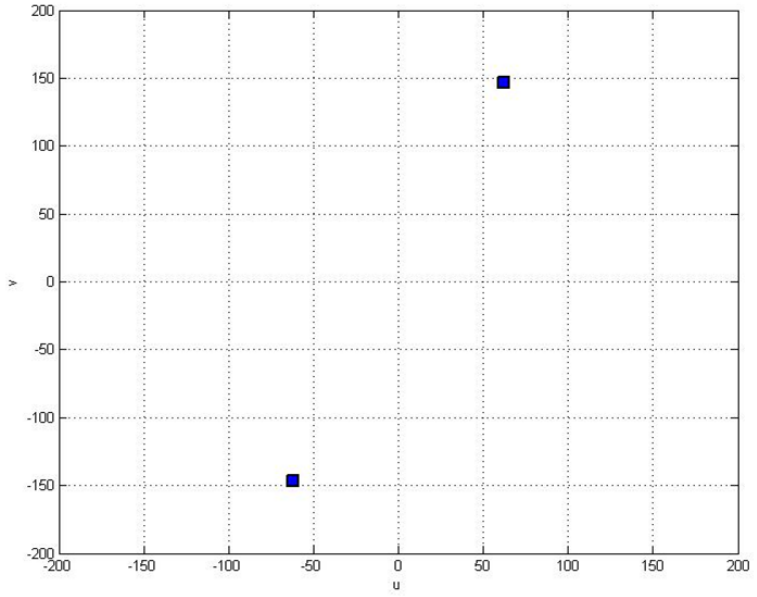

Figure 2.18: Points on the u,v-plane for antenna spacing as in Fig.2.17.

Example 2.4*b*

The two antennas are now pointing at a source directly upwards as in Fig.2.19, with the following parameters: $\phi = 0$, $\theta = 0$ at ν=1.4 GHz, b = 5 and a is varied from 0 to 3.

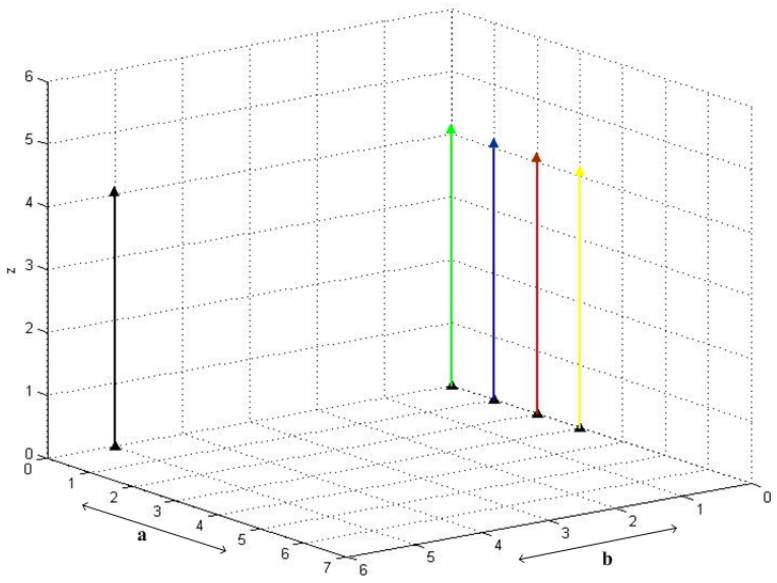

Figure 2.19: Two antennas on the ground plane pointing to a source directly upwards. The antenna on the left is fixed, the one on the right is moved sequentially so that a = 0 (green arrow) to a = 3 (yellow arrow).

The (u,v) points are again calculated using (2.4.3)–(2.4.4) and plotted on the u,v-plane for each spacing, totaling 4 different baselines and thus 8 points, see Fig.2.20.

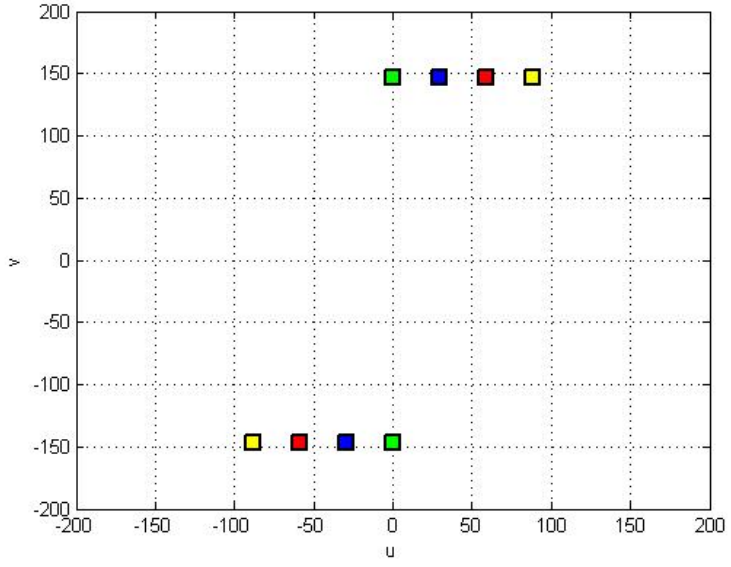

Figure 2.20: Points on the u,v-plane for antenna spacing as in Fig.2.19.

When this is repeated for b=5 through to b=1, the resultant u,v-coverage is given by Fig.2.21

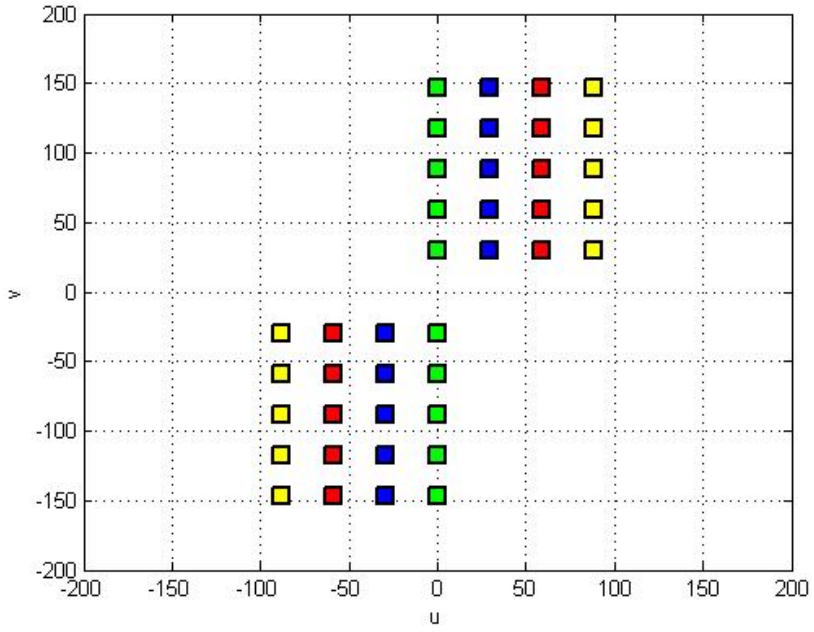

Figure 2.21: Points on the u,v-plane for a total of 20 different baselines.

This simulates aperture synthesis, where antennas can be moved around to form different baselines. The result is that instead of only two points as in Fig.2.18, the u,v-plane can be filled up by many points resulting in a better dirty map. To illustrate this further, consider an 8 antenna configuration as given by Fig.2.22 using [17].

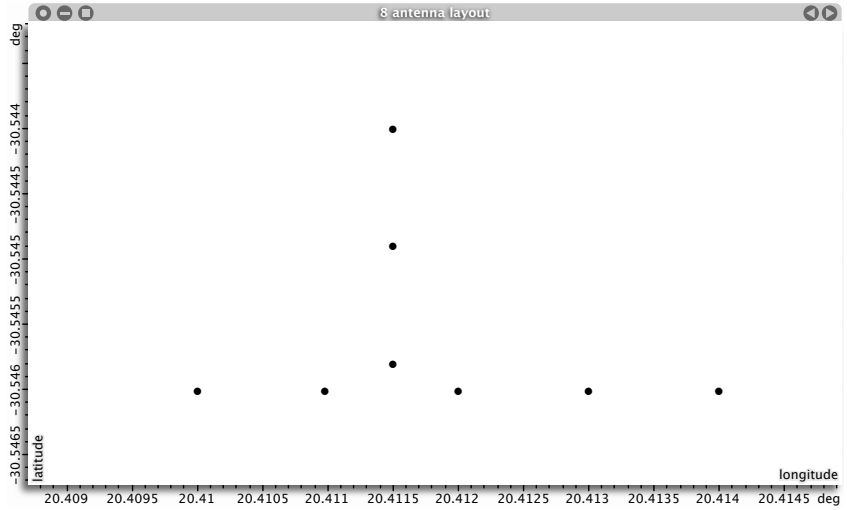

Figure 2.22: Top view of 8 antennas distributed on the ground plane.

The u,v-plane sampling for an 10 minute observation is then given by Fig.2.23. This demonstrates how a snapshot observation will form points on the u,v-plane.

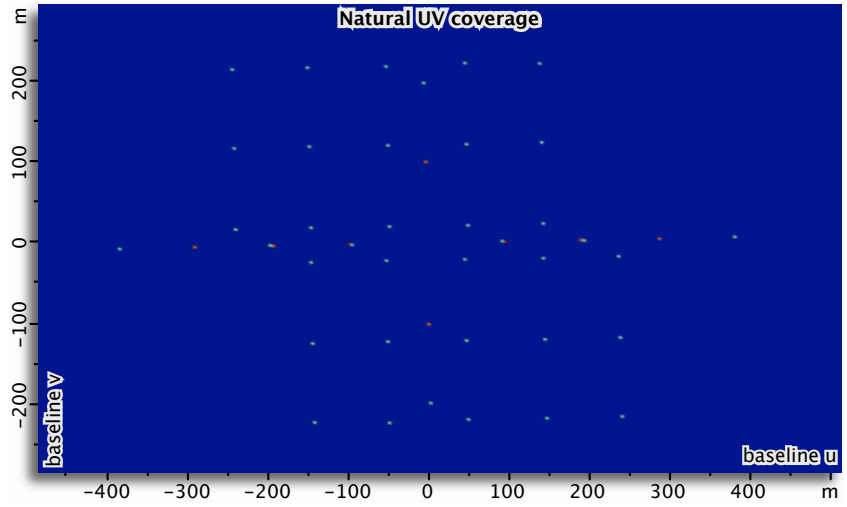

Figure 2.23: The corresponding u,v-points on the u,v-plane for an instant in time.

Fig.2.24 shows the u,v-coverage for a longer observation of 12 hours. This demonstrates how Earth-rotation synthesis results in arcs that covers the u,v-plane [18].

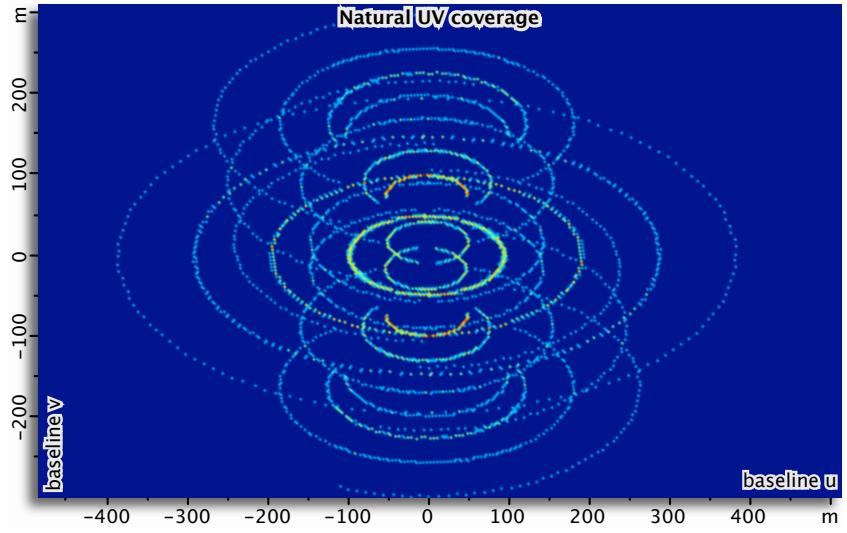

Figure 2.24: The corresponding u,v-points on the u,v-plane for an 12 hour observation.

2.4.3 Sampling Function

As demonstrated by the previous examples, each baseline represents a point on the u,v-plane. If there are N antennas, the number of baselines is given by $N(N-1)/2$. The collection of points gives a set of measurements (2.4.5) called the *sampling function*:

$$S(u,v) = \sum_k \delta(u-u_k, v-v_k) \tag{2.4.5}$$

It should be noted that this set is incomplete in that it only measures certain values on the u,v-plane. The measured *sampled visibility function* can then be found by multiplying the true visibility, $V(u,v)$ with the sampling function, $S(u,v)$ [18].

2.5 Significance of *u*,*v*-coverage

This section summarises the terms often used in imaging and explains how they fit together by means of their FT relations. The process of calibration and imaging is briefly touched and the Point Spread Function (PSF) is introduced. Throughout this section, the aim is to emphasise the importance of the *u*,*v*-plane.

2.5.1 Terminology and FT relations

Table 2.1 summarises the different terms used in image processing, followed by their mathematical representations [19].

Table 2.1: Terms used in image processing.

Function	Terms
$V(u,v)$	Fringe visibility or Complex visibility
$M(x,y)$	Map, Source image or Source brightness distribution
$M_d(x,y)$	Dirty map or Dirty image
$M_c(x,y)$	Ideal map or Ideal image
$B_d(x,y)$	Dirty beam or Dirty PSF
$B_c(x,y)$	Ideal beam or Ideal PSF

Note:

- The source brightness distribution, $B(x,y)$ (from section 2.2.2), is also referred to as the map, $M(x,y)$.
- $S(u,v)$ is defined in section 2.4.3.

Visibility: $$\boxed{V(u,v) = \iint M(x,y) e^{i2\pi(ux+vy)/\lambda} dxdy}$$

Map: $$\boxed{M(x,y) = \iint V(u,v) e^{-i2\pi(ux+vy)/\lambda} dudv}$$

dirty map: $$\boxed{M_d(x,y) = \iint V(u,v) S(u,v) e^{-i2\pi(ux+vy)/\lambda} dudv}$$

or $$\boxed{M_d(x,y) = M(x,y) \otimes B_d(x,y)}$$

ideal map: $$\boxed{M_c(x,y) = M(x,y) \otimes B_c(x,y)}$$

dirty beam (PSF): $$\boxed{B_d(x,y) = \iint S(u,v) e^{-i2\pi(ux+vy)/\lambda} dudv}$$

Consider Fig.2.25 that is now used to describe the FT relations of the various terms mentioned. [2]

[2]Note that *l*,*m* is similar to *x*,*y* which is the directional cosines of *u*,*v*

The antenna baselines produce a set of points, the sampling function $S(u,v)$ that is represented by e). The FT of these points gives the dirty beam or PSF as in b) here referred to as $B(l,m)$. (Note that this set of points is incomplete.) The measured visibility by the instrument from the correlated antenna signals is given by f). One can then take the FT of this visibility to produce the dirty map c). The brightness or true image, here referred to as $I(l,m)$ in a), is the image we are trying to reproduce during the imaging process. It forms a FT-pair with the perfect visibility function $V(u,v)$ as in d).

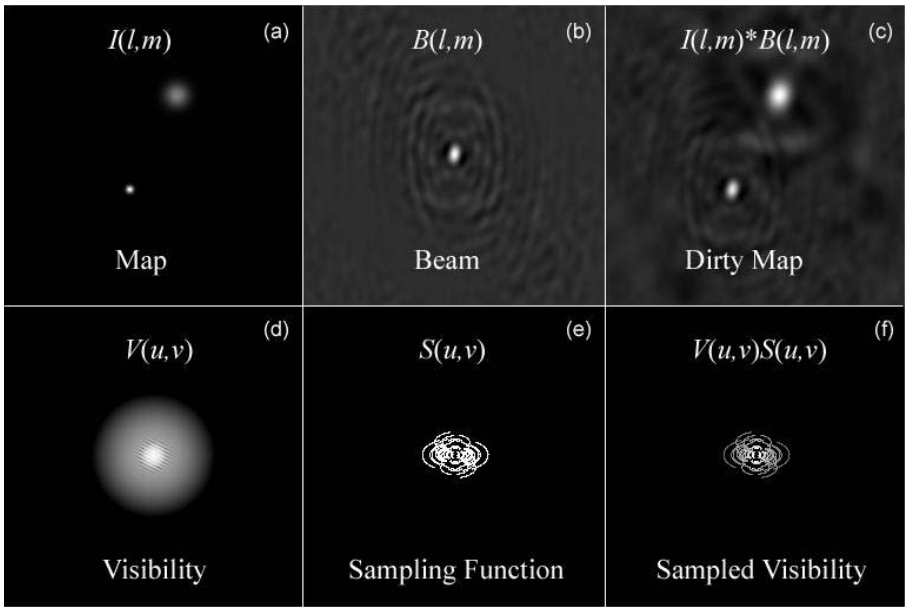

Figure 2.25: a) The model sky map, also the FT of (d);
b) The point spread function, also the FT of (e);
c) The dirty map, the convolution of (a) and (b), also the FT of (f);
d) The visibility model;
e) The sampling function;
f) The sampled visibility, also the multiplication of (d) and (e), from [18].

We do not have this visibility function (d) and therefore need to find another way to get to the true image. What we do have is the dirty beam and dirty map that is just the FT of the sampling function and sampled visibility respectively. We know in theory that the dirty map is the result of the convolution of the true image and the dirty beam. Thus the true image can be obtained by deconvolving the dirty beam from the dirty map to give the true image.

In practice, however there are problems. One always works with a limited array with an imperfect beam. Therefore the antennas can only sample parts of the sky that results in an incomplete set of points or sampling function. We also measure the visibility with system imperfections that result in bad or incomplete data. Radio interference is another problem that introduces noise in the image. The result is a very dirty map that is not easily cleaned, with the final image obtained being only an approximation of the true image observed.

2.5.2 Image Processing

Radio astronomers use the *u*,*v*-data measured from the correlator that is a set of complex numbers called the visibility data set to perform the image processing. Frequently the *u*,*v*-data contains bad or missing data that

needs to be flagged (edited). The reason for this could be problems that may occur within the correlator, but more likely the problem is the result of either an individual antenna or baseline measurements that are bad or incorrect. After the data is flagged, it needs to undergo amplitude (flux-density), phase and bandpass calibration by normally using a point source that has a constant visibility and a well known location.

The dirty map is obtained by the FT of the *u*,*v*-data. This map is noisy because of the non-ideal dirty beam and also Radio Frequency Interference (RFI) that can be any unwanted radio signals from the sky as well as from the telescope itself. The dirty map is then deconvolved with the dirty beam by using techniques such as *CLEAN* or *maximum entropy method*. This produces the cleaned radio image.

2.5.3 Point Spread Function

We have already given some examples of how the *u*,*v*-plane is filled using antenna baselines. To show the significance of the *u*,*v*-plane as a part of the imaging process, let us look at the PSF or dirty beam directly. We already know that each baseline of the antenna array represents one point on the *u*,*v*-plane. This point can be described by a vector s_p in (2.5.1).

$$s_p = \sqrt{u^2 + v^2} \tag{2.5.1}$$

Here, $u = x/\lambda$ and $v = y/\lambda$ (with x and y from (2.4.2)). When the FT of this point is taken, it results in a fringe pattern in the sky plane also known as the PSF. The angular separation or fringe spacing, is then $\theta = 1/s_p$, see Fig.2.26. This is the same concept as the angular resolution mentioned in section 2.3.1, given by $\theta = \lambda/b_{max}$.

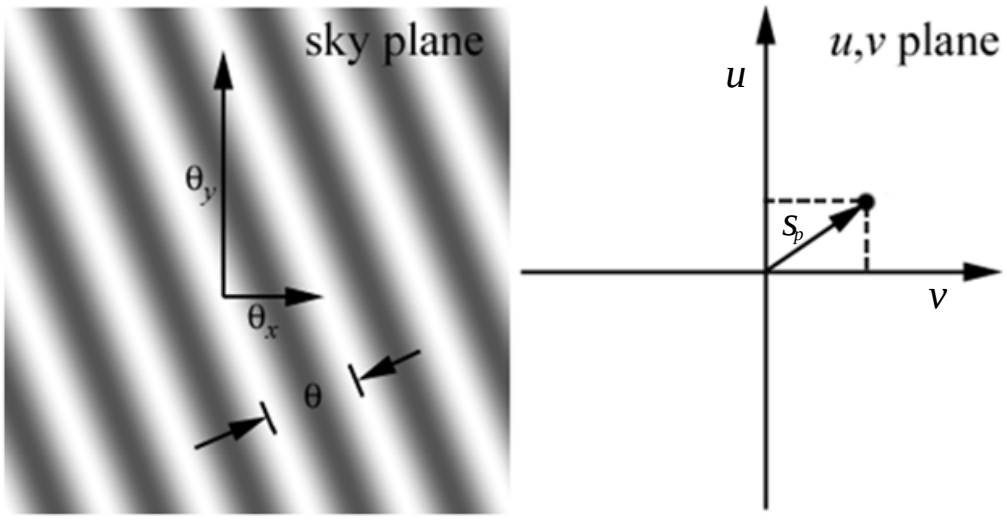

Figure 2.26: The FT of the point on the *u*,*v*-plane (right) results in the fringe pattern (left), adapted from [18].

Usually the angular resolution is measured by taking the *FWHM (full width half maximum)* measurement of the PSF. This is where the amplitude is half of its maximum.

When N antennas are used, it results in $\frac{N(N-1)}{2}$ baselines that each represents a fringe pattern or beam. When these outputs are averaged, it represents the total PSF as in Fig.2.27 (bottom). The more antennas that are used, the more the PSF will resemble a Gaussian type form [20].

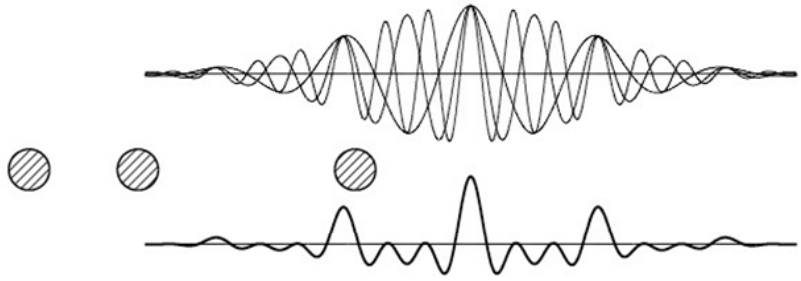

Figure 2.27: The baselines of 3 antennas (circles) form multiple beams (top) that when averaged results in a single synthesised beam or PSF (bottom), from [20].

Example 2.5*a*

Given two antennas with a baseline b, at frequency ν, the PSF may be given by Fig.2.28 (left). If the baseline is now doubled to $2b$, with the same frequency the PSF changes as in Fig.2.28 (right) using [17]. It can therefore be seen that an increase in antenna spacing will result in a decrease in the fringe spacing giving higher angular resolution. Notice the two stripped black lines that intersect in the centre of both images in Fig.2.28. These indicate the cross-section of the major and minor axis of the primary beam. Fig.2.29 shows the profile views of the PSFs from these cross-section cuts.

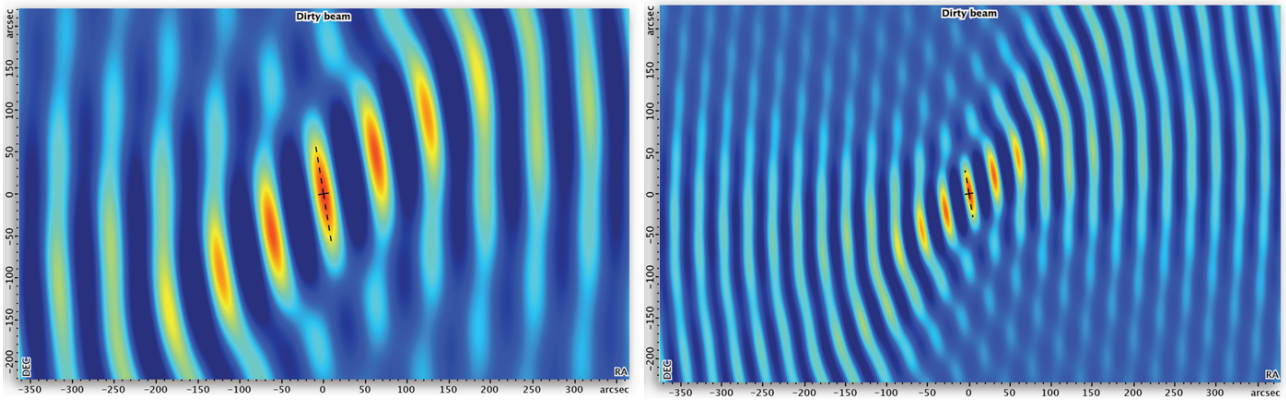

Figure 2.28: The simulated PSF given two antennas with spacing b (left) and $2b$ (right).

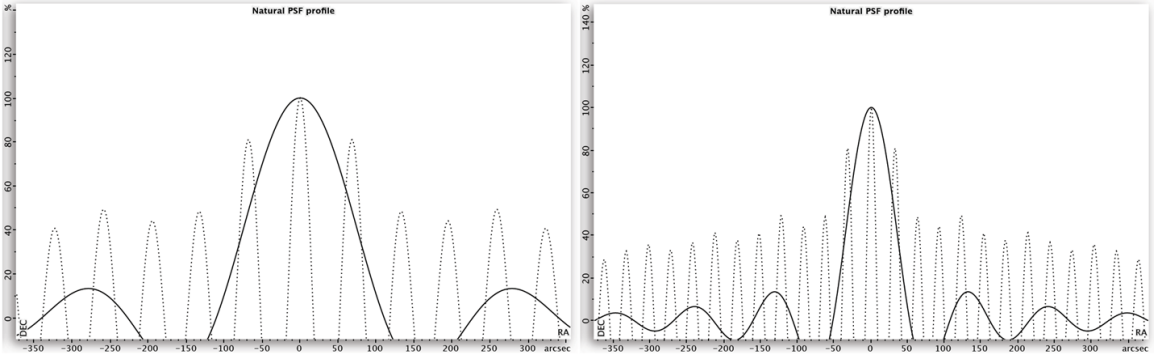

Figure 2.29: The PSF profiles given two antennas with spacing b (left) and $2b$ (right), with the dotted and solid curves indicating the minor and major PSF cuts respectively.

Consider the major axis curves (solid black line) - there is a main beam lobe in the centre and side-lobes can be seen on either side of this beam. As mentioned, the FWHM of the main beam represents the finest resolution with which you can observe. Ideally one would want the side-lobes to be as low as possible (in the dirty beam) as this increases the noise in the image (dirty map). These side-lobes result from gaps in the u,v-plane. It is therefore clear that the better your u,v-coverage, the better the PSF will be resulting in less noise in the dirty image.

2.6 Conclusion

This chapter covered some basic radio astronomy fundamentals. It introduced concepts like interferometry and the u,v-plane and described terms used in image processing including the complex visibility, dirty map and the PSF. The role of the u,v-plane was emphasised as this forms an integral part of antenna array design as will be discussed later on in this document.

Chapter 3

Electromagnetic Radiation from Astronomical Bodies

3.1 Introduction

The aim of this chapter is to introduce fundamental aspects of Electromagnetic (EM) radiation. First, some basic concepts and theory is covered. It goes on to describe the mechanisms of EM radiation and mentions the effects that different media can have on travelling EM waves. It concludes with a section on the flux density of radio sources.

3.2 Fundamentals

This section serves as an introduction to the rest of the chapter. Some mathematical and theoretical background concerning EM radiation is reviewed including radiation laws, optical depth and the equation of radiative transfer. This forms the basis of work discussed throughout the rest of the chapter.

3.2.1 Electromagnetic spectrum

To form a better understanding of our knowledge of EM radiation, the EM spectrum in Fig.3.1 indicates the classification of different types of waves according to their wavelength or frequency. The visible range is perhaps the most familiar in that it can be perceived with our eyes, while special equipment is needed to detect other parts of the spectrum. This includes gamma-ray, x-ray, ultraviolet, infrared and radio waves. For the most part of this document the focus will be on the radio spectrum.

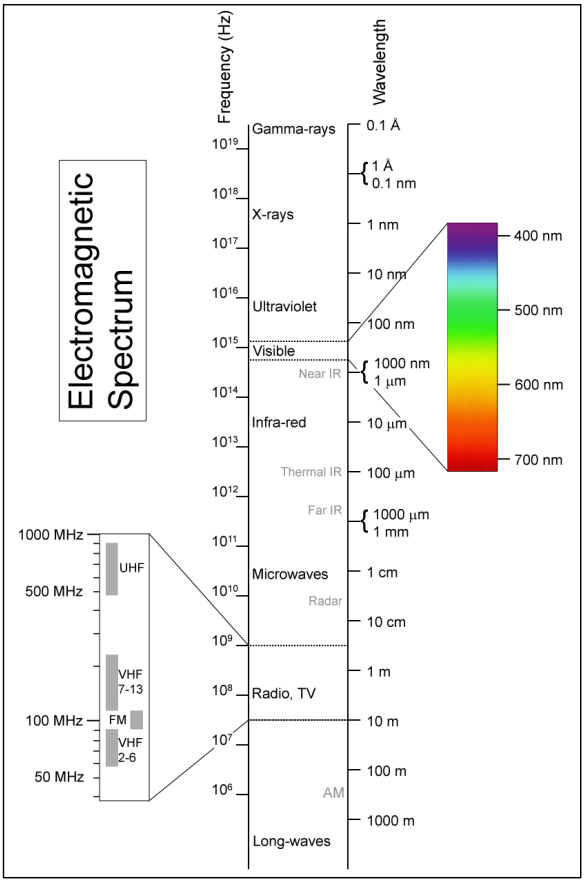

Figure 3.1: Electromagnetic spectrum, from [21].

The relationship between energy, frequency and wavelength is given by (3.2.1) [18].

$$E = h\nu = \frac{hc}{\lambda} \tag{3.2.1}$$

with h = Planck's constant, c = the speed of light, λ the wavelength and ν the frequency.

Fig.3.2 shows the optical, radio and partly infrared windows open for observations from telescopes on earth. The radiation from other parts of the spectrum is either absorbed by the earth's atmosphere or blocked by the ionosphere.

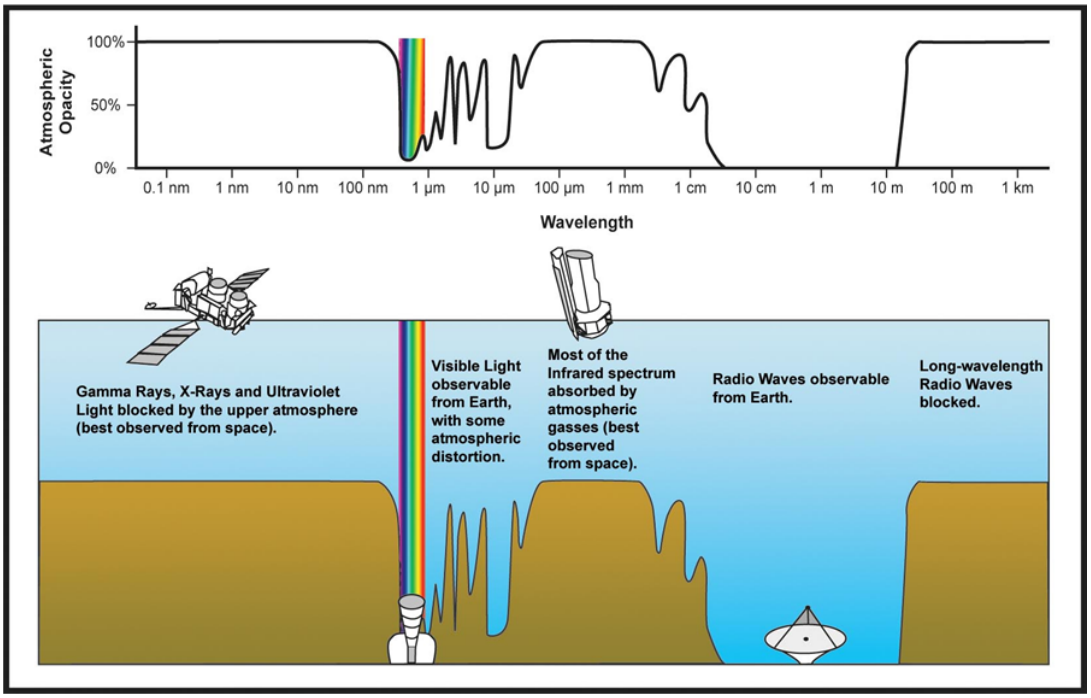

Figure 3.2: Atmospheric opacity over the electromagnetic spectrum, from [18].

The following sections will deal with the mechanisms of EM emission, namely thermal and non-thermal radiation. Thermal radiation is due to the fact that all objects above absolute zero radiate EM energy. The specific temperature determines the amount of energy radiated at each frequency over the EM spectrum. The higher the frequency, the more energy each particle carries. Table 3.1 shows the temperatures associated with different parts of the EM spectrum.

Table 3.1: Temperature of matter at different wavelengths, adapted from [12].

Type of Radiation	**Wavelength range** $(10^{-9}m)$	**Object Temperature**	**Typical Sources**
Gamma rays	< 0.01	$> 10^8 K$	A few astronomical sources, gamma rays produced in nuclear reactions
X-rays	$0.01 - 20$	$10^6 - 10^8 K$	Gas in clusters of galaxies, supernova remnants, solar corona
Ultraviolet	$20 - 400$	$10^5 - 10^6 K$	Supernova remnants, very hot stars
Visible	$400 - 700$	$10^3 - 10^5 K$	Exterior of stars
Infrared	$10^3 - 10^6$	$10 - 10^3 K$	Cool clouds of dust and gas, planets and satellites
Radio	$> 10^6$	$< 10K$	Dark dust clouds

On the other hand, non-thermal radiation is caused by mechanisms other than relating to the temperature of the object.

3.2.2 Radiation laws

Perfect absorbers are known as blackbodies. A blackbody absorbs all the energy that reaches it and then radiates the energy depending on the temperature and wavelength. It is however only an idealisation. According to *Planck's radiation law*, the brightness, B, of a blackbody radiator is given by (3.2.2) [11, sec3-6].

$$B = \frac{2h\nu^3}{c^2} \frac{1}{e^{h\nu/kT} - 1} \tag{3.2.2}$$

Fig.3.3 shows the Planck radiation-law curves for a blackbody radiator plotted to linear scales.

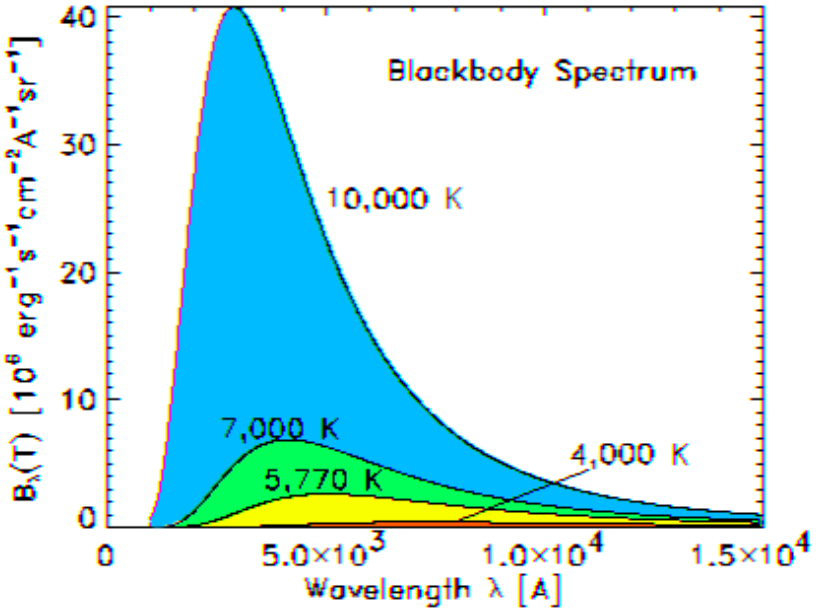

Figure 3.3: Brightness as a function of wavelength at different temperatures, from [18].

The area under a Planck-radiation-law curve can be taken as the total brightness for that specific temperature. It can be seen from these curves that with an increase in temperature, the maximum brightness is at shorter wavelengths. If we make λ_m the wavelength of the peak brightness, the product $\lambda_m T$ that is equal to a constant is known as the *Wien displacement law*.

Fig.3.4 shows Planck's radiation-law curves for a blackbody radiator plotted to logarithmic scales, also called the *brightness spectrum*. It should be noted that there is a specific temperature for each value of brightness at any given frequency [12].

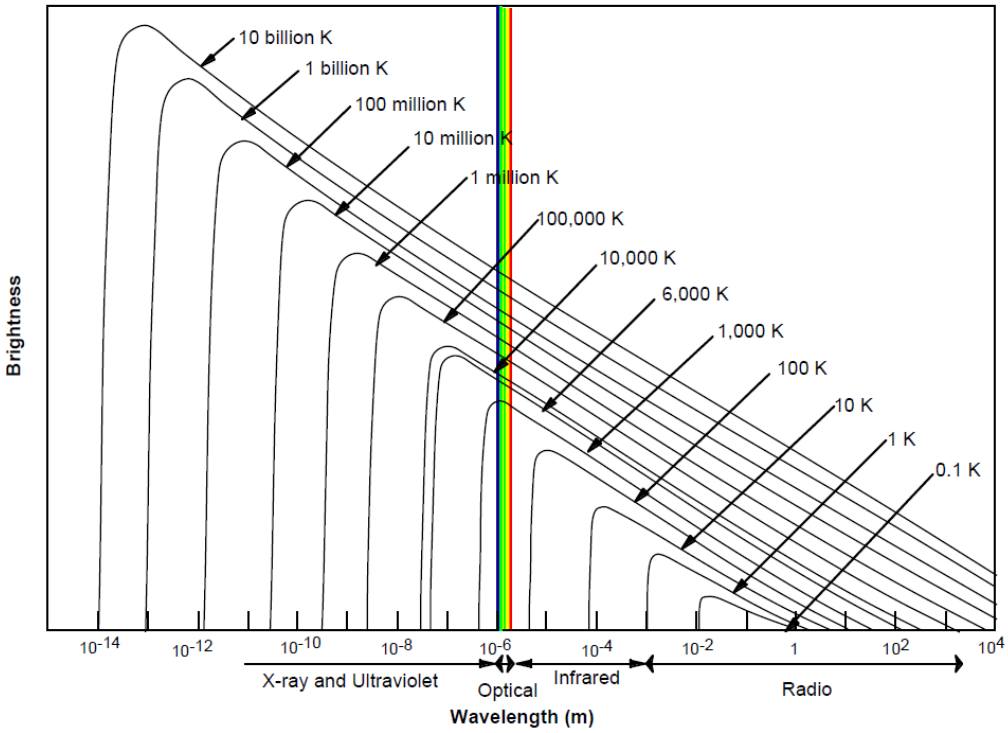

Figure 3.4: Brightness at different wavelengths for blackbody objects at various temperatures, from [12].

The total brightness, $B^{'}$, for a blackbody radiator is found by integrating the brightness over all frequencies, as in (3.2.3).

$$B^{'} = \frac{2h}{c^2}\int_0^{\infty} \frac{\nu^3}{e^{h\nu/kT}-1} d\nu \tag{3.2.3}$$

From this the *Stefan-Boltzmann* relation is obtained as in (3.2.4), with σ the Stefan-Boltzmann constant.

$$B^{'} = \frac{\sigma T^4}{\pi} \tag{3.2.4}$$

For the radio part of the spectrum, the condition $h\nu << kT$ holds, so that (3.2.2) changes into (3.2.5). This is a very useful equation known as the *Rayleigh-Jeans radiation Law*.

$$B = \frac{2kT}{\lambda^2} \tag{3.2.5}$$

For short wavelengths, the condition $h\nu >> kT$ holds, *Planck's Law* (3.2.2) now changes into (3.2.6). This equation is called *Wien's Radiation Law*.

$$B = \frac{2h\nu^3}{c^2} e^{-h\nu/kT} \tag{3.2.6}$$

From Fig.3.5 it can be seen that the *Planck-radiation-law* curve corresponds to the *Rayleigh-Jeans-law* curve at longer wavelengths and the *Wien-radiation-law* curve at short wavelengths.

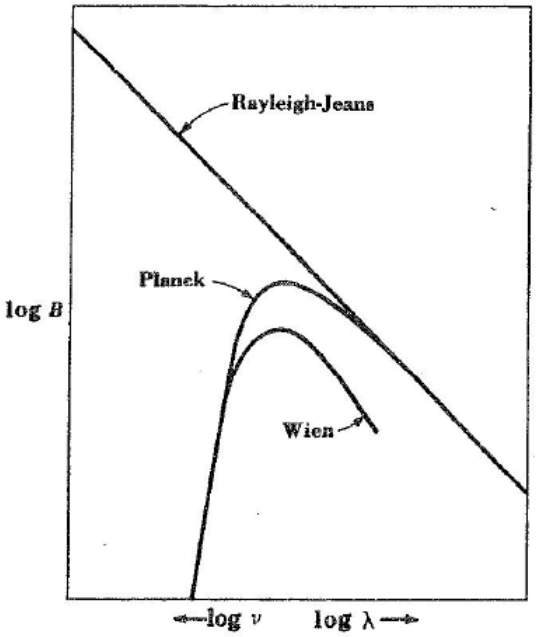

Figure 3.5: A comparison of the radiation-law curves, from [11].

3.2.3 Optical depth

When a wave passes through an absorbing medium such as a cloud, the flux density will decrease. Fig.3.6 shows a graph of the flux S, with the distance travelled, x [11].

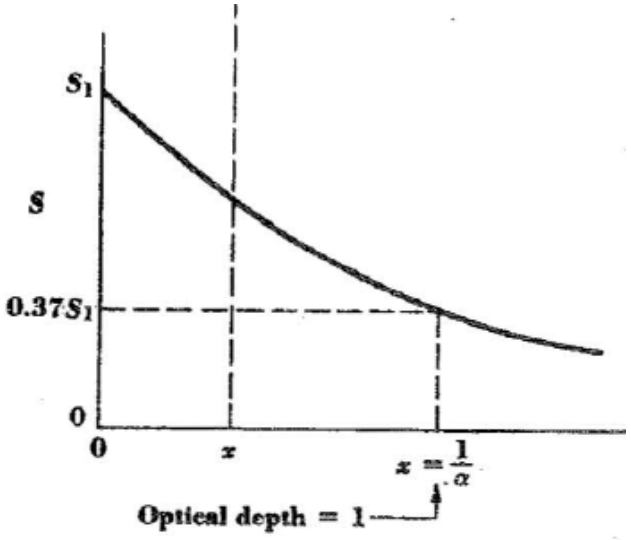

Figure 3.6: Flux density of a wave, as a function of distance travelled (x) through an absorbing cloud, from [11].

It can be shown that the flux density at any point is given by (3.2.7).

$$S = S_1 e^{-\alpha x} \tag{3.2.7}$$

with α the attenuation constant, S the observed flux density and S_1 the actual flux density

The optical depth τ, is defined by (3.2.8) with α the attenuation constant.

$$\tau = \alpha x \tag{3.2.8}$$

This is substituted into (3.2.7) to give (3.2.9).

$$S = S_1 e^{-\tau} \tag{3.2.9}$$

When the medium is a gas, the attenuation constant can be given by (3.2.10).

$$\alpha = K\rho \tag{3.2.10}$$

with K the absorption coefficient and ρ the density of the medium

The optical depth can then be defined by (3.2.11), when the cloud has a thickness of x_1.

$$\tau = \int_0^{x_1} K\rho \mathrm{d}x \tag{3.2.11}$$

The cloud is optically thick for $\tau >> 1$ and optically thin for $\tau << 1$ [18].

3.2.4 Equation of radiative transfer

Consider a source of brightness B_s, like that in Fig.3.7. Between the observer and the source, a cloud of matter absorbs and emits radiation to give a different observed brightness [11].

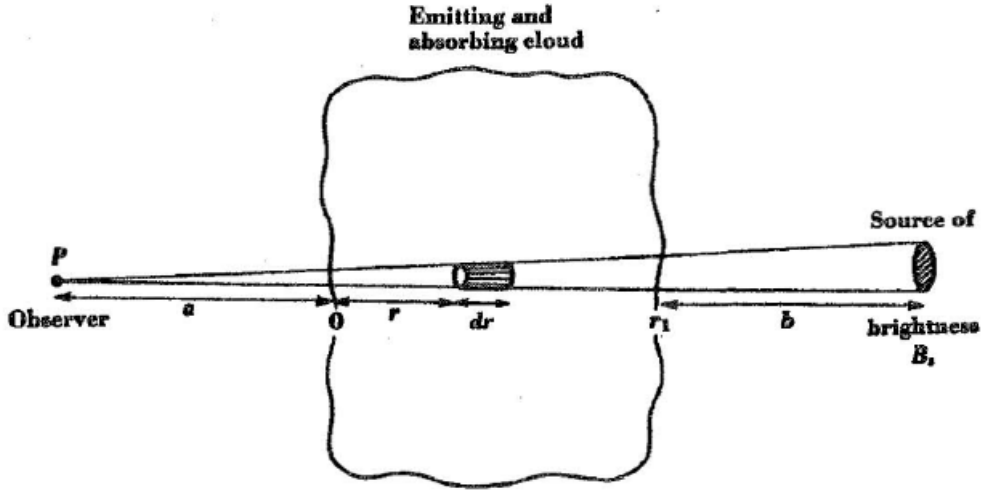

Figure 3.7: The brightness of a source observed from a point P, is independent of the distances a and b, but is affected by the emitting and absorbing cloud through which it passes, from [11].

This change in brightness is given by (3.2.12), also known as the *equation of radiative transfer*.

$$\mathrm{d}B = -BK\rho \mathrm{d}r + \frac{j}{4\pi}\rho \mathrm{d}r \tag{3.2.12}$$

with B the observed or apparent brightness, K the absorption coefficient, ρ the density and j the emission coefficient.

When solving for (3.2.12), a solution is given by (3.2.13).

$$B = B_s e^{-\tau_c} + \frac{j}{4\pi K}\left(1 - e^{-\tau_c}\right) \tag{3.2.13}$$

with B_s the actual brightness of the source

τ_c the optical depth

The optical depth τ_c (see sec.3.2.3) for a cloud of thickness r_1 is given by (3.2.14).

$$\tau_c = \int_0^{r_1} K\rho dr \tag{3.2.14}$$

The first part of (3.2.13) represents the loss in brightness due to absorption of the cloud. The second part is the contribution to the observed brightness, due to emission and absorption by the cloud. It can be replaced by $B_i = \frac{j}{4\pi K}$, the intrinsic brightness of the cloud, to give (3.2.15).

$$B = B_s e^{-\tau_c} + B_i(1 - e^{-\tau_c}) \tag{3.2.15}$$

The brightness is now replaced by temperature to give (3.2.16).

$$T_b = T_s e^{-\tau_c} + T_c(1 - e^{-\tau_c}) \tag{3.2.16}$$

with T_b the observed brightness temperature

T_s the source temperature

T_c the cloud temperature

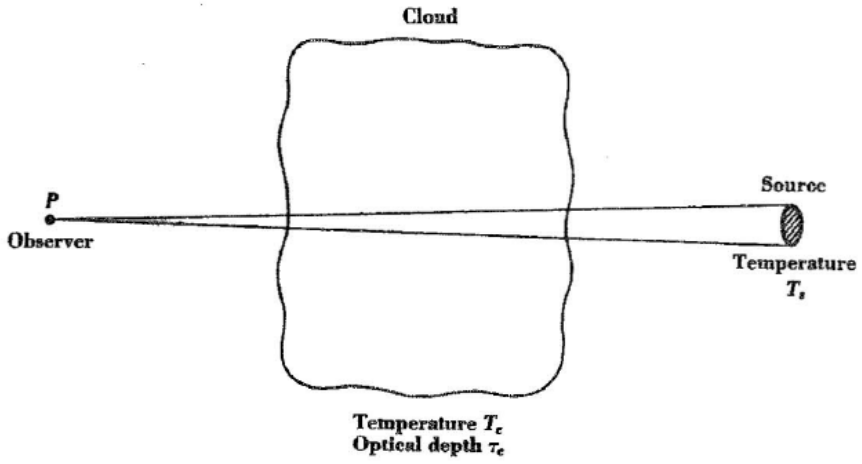

Figure 3.8: A source of temperature T_s, observed through a cloud with temperature T_c, from [11].

See Fig.3.8, for $\tau_c = 0$, the cloud is transparent, so that T_b is equal to the source temperature. For $\tau_c >> 1$, the cloud is opaque, so that T_b is equal to the cloud temperature. For $\tau_c = 1$, the cloud is partially transparent, so that T_b is equal to a reduced temperature of both the source and cloud.

3.3 Thermal Radiation

Two types of thermal emission are discussed. The first is called *free-free emission* where the electrons are free or unbound both before and after collisions. These electrons do not have a definite energy level and radiation occurs as a result of acceleration. The second type is that of *spectral line emission*. The electron radiates by releasing a photon when it drops to a lower energy state [11].

3.3.1 Free particle emission

Free particles or electrons radiate when they are accelerated. This is typically the radiation found from the sun and in the interplanetary medium. Fig.3.9 shows the radiation pattern where q is the charge, a is the acceleration and θ the angle from the direction of a (this is for the case of non-relativistic electrons [18]).

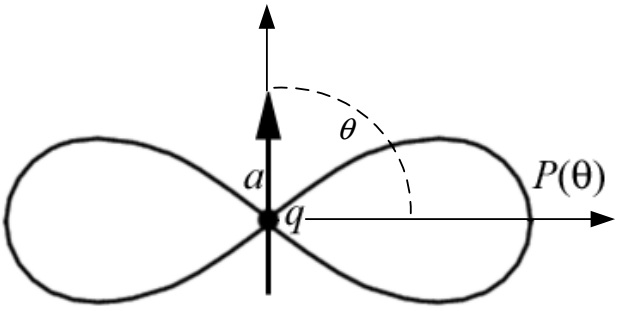

Figure 3.9: Radiation pattern from particle emission, from [18].

The electrons can act on their own to produce incoherent radiation like that of *Bremsstrahlung*, or act together to produce coherent emission. *Bremsstrahlung* is also known as free-free radiation and is the radiation resulting from electron and ion collisions. In a plasma (ionised gas), electrons are continuously moving through the relatively fixed ions. When an electron passes an ion, it is pulled towards it causing an acceleration and deviation in the path of the electron. This produces a radiation pattern in the direction of motion, see Fig.3.10.

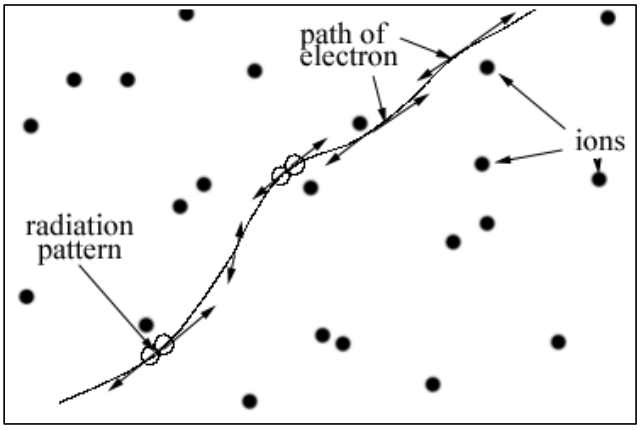

Figure 3.10: The path of an electron moving through ions with the resulting radiation pattern, from [18].

In stead of moving in a straight line, the electron curves off with an angle θ. This angle (see Fig.3.11) depends on the distance *b* called the impact parameter and also the speed at which the electron is moving.

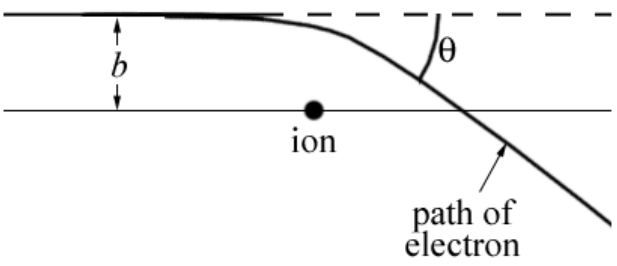

Figure 3.11: The deviation in path of the electron after the ion impact, from [18].

Particles in an ionised gas such as a plasma, act together to produce *coherent free particle emission*. For incoherent emission, the brightness temperature is determined by the actual temperature (thermal) or kinetic temperature (non-thermal) of the individual electrons, while for coherent emission, it can be much higher.

Consider two atoms in a gas approaching one another. Their impact is so great that the one atom is ionised. The resulting positive ion and a negative electron are attracted. The electron accelerates, causing it to emit energy. After they recombine, the process repeats itself continuously as the particles move around. At any given time there can exist concentrations of positive and negative charge that causes electric and magnetic fields. When enough atoms are ionised, the gas starts to behave in a collective manner and we refer to this as a plasma. Plasmas are a very common form of matter since it is found in stars and in the interstellar gas [12].

3.3.2 Spectral line emission

Line emissions from atoms and molecules occur when an electron changes its energy state, resulting in the emission of a photon at a specific wavelength depending on the atom. This wavelength represents a discrete line on the EM spectrum [12].

21-cm Line of Neutral Hydrogen

A specific case of line emission is that of neutral Hydrogen. In the ground energy state the hydrogen atom has proton and electron spins that are in different directions. If a collision occurs with another atom, the proton and electron spins may align. The atom is in an excited state and returns to the ground state once it loses this energy. This is accompanied by the emission of a photon at 21.11 cm wavelength, see Fig.3.12.

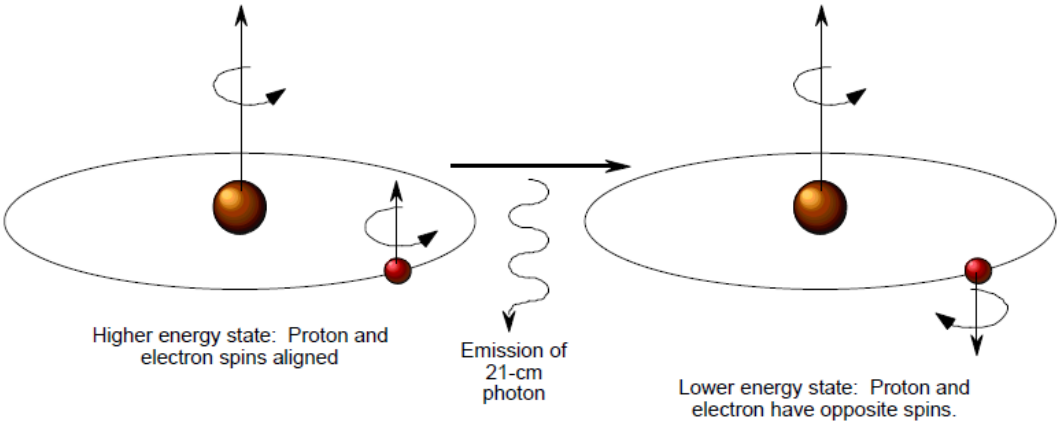

Figure 3.12: Formation of the 21-cm Line of Neutral Hydrogen, from [12].

The energy transition is called a *hyperfine transition*. Although it takes about 11 million years on average for an atom to fall back to the lower state, we can observe this emission frequently due to the large amount of hydrogen atoms in the universe [11].

Molecular lines

Molecular lines can be detected to provide information on molecular clouds. These clouds have low temperatures, usually around 100K or even down to 10K. The dust grains in the molecular cloud protect the molecules by absorbing the UV (Ultraviolet) radiation from stars and keeping temperatures low by emitting IR (Infra-Red). Chemical elements each have their own specific pattern of spectral lines. The study of these spectral lines is called spectroscopy. Molecular spectroscopy is used to detect molecules in our atmosphere or in the Interstellar Medium (ISM) [18] [22].

3.4 Non-thermal Radiation

Synchrotron radiation is a type of non-thermal emission that is found in high energy environments such as neutron stars, inside black holes, and other extragalactic sources. Another type of non-thermal radiation that will be discussed here is masers.

3.4.1 Synchrotron Radiation

Bremsstrahlung (section 3.3.1) is due to the acceleration by an electric field. When the electrons are accelerated by a magnetic field, it is called *magnetobremsstrahlung*. It is then further classified according to the electron speed as given by Table 3.2 [18] [23].

Table 3.2: Types of magnetobremsstrahlung.

Type of emission	**Electron speed**
Cyclotron emission	the electrons have a low velocity (non-relativistic)
Gyroresonance emission	the electrons have a higher electron velocity
Gyrosynchrotron emission	the electrons have mildly relativistic speeds
Synchrotron emission	the electrons have highly relativistic speeds

A charged particle moves in a circular or spiral motion when it enters a magnetic field. If the particle's speed is nearly the speed of light, the radiation emitted is called *synchrotron radiation*, see Fig.3.13.

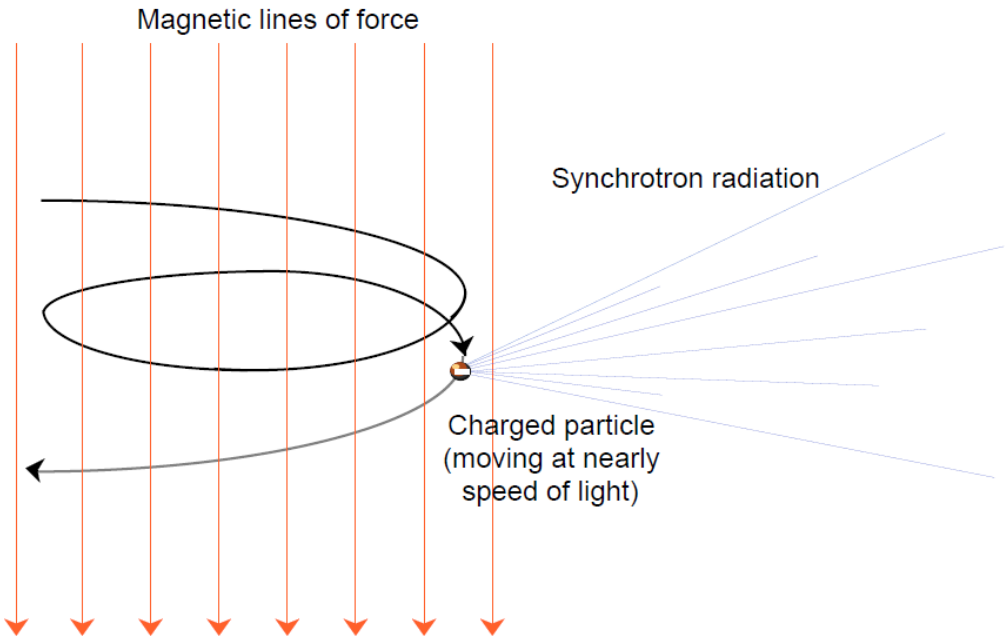

Figure 3.13: Synchrotron radiation, from [12].

The reason the particles move in a circular motion is explained by *Feynman* [24, p34-3 to p34-5] and a brief description now follows.

The force on a particle that enters a magnetic field is given by (3.4.1).

$$\vec{F} = q\vec{\upsilon} \times \vec{B} \tag{3.4.1}$$

with q the charge of the particle
υ the velocity of the particle
B the magnetic flux density

The force can also be described in terms of its momentum by (3.4.2).

$$\vec{F} = \frac{\Delta\vec{p}}{\Delta t} \tag{3.4.2}$$

This force is perpendicular to the magnetic field and also to the velocity. Fig.3.14 illustrates the momentum and force, given that the magnetic field direction is upwards (going out of the page).

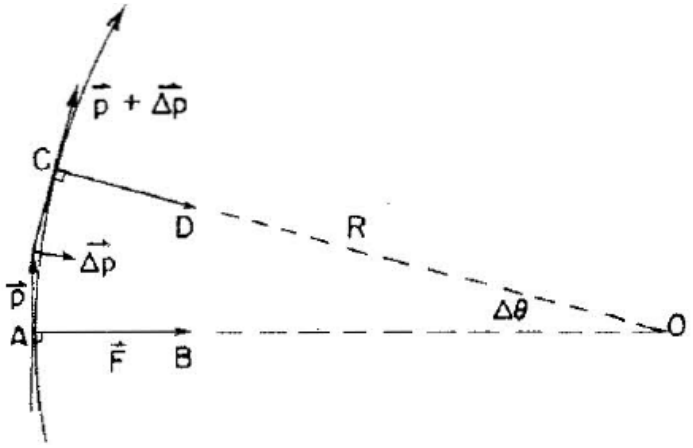

Figure 3.14: Circular path of electron in magenetic field, from [24].

For a duration of time Δt, the momentum changes with $\Delta\vec{p}$. The angle is given by (3.4.3) and (3.4.4).

$$\Delta\theta = \frac{\Delta p}{p} \tag{3.4.3}$$

$$\Delta\theta = \frac{q\upsilon B\Delta t}{p} \tag{3.4.4}$$

Within this time, the distance travelled by the particle is given by (3.4.5).

$$\Delta s = \upsilon\Delta t \tag{3.4.5}$$

The lines OA and OC are both equal to R (the radius) so that the distance can be described by (3.4.6).

$$\Delta s = R\Delta\theta \tag{3.4.6}$$

Combining (3.4.4), (3.4.5) and (3.4.6) gives

$$R\Delta\theta = \upsilon\Delta t$$

and

$$R\frac{\Delta\theta}{\Delta t} = \upsilon = R\vec{\omega} = R\frac{q\upsilon B}{p}$$

which results in (3.4.7) and (3.4.8).

$$p = qBR \tag{3.4.7}$$

$$\vec{\omega} = \frac{q\upsilon B}{p} \tag{3.4.8}$$

This is repeated for every instance of time, producing the circular movement of the particle with radius R and angular velocity $\vec{\omega}$.

For non-relativistic electrons it can be shown that the *gyro* or *cyclotron* frequency is given by (3.4.9) [25].

$$\omega = \frac{qB}{mc} \tag{3.4.9}$$

with c the velocity of light

m the mass of the particle

For relativistic electrons the Lorentz transformation is used to give (3.4.10), with m the relativistic mass and m_0 the rest mass. The reason for this is that the mass of a body will increase as the velocity increases [24, p15-1] [11].

$$m = \frac{m_0}{\sqrt{1-\left(\frac{\upsilon}{c}\right)^2}} \tag{3.4.10}$$

The energy of the particle, E is then given by (3.4.11).

$$E = mc^2 = \frac{m_0 c^2}{\sqrt{1-\left(\frac{\upsilon}{c}\right)^2}} \tag{3.4.11}$$

If (3.4.11) is modified so that the energy is expressed in eV, we get (3.4.12).

$$E_v = 6\times 10^{18}\frac{m_0 c^2}{\sqrt{1-\left(\frac{\upsilon}{c}\right)^2}} \tag{3.4.12}$$

When viewing Fig.3.14 from the top as in Fig.3.15, the radiation is in the direction of instantaneous velocity in the form of a cone.

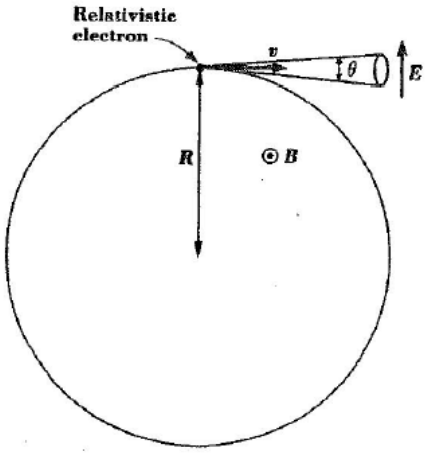

Figure 3.15: The plane of orbit of an electron with radiation in the form of a cone, from [11].

This cone has an angle of θ (in rad) given by (3.4.13).

$$\theta = 2\sqrt{1-(\upsilon/c)^2} = 1.2\times 10^{19}\,\frac{m_0\,c^2}{E_v} \tag{3.4.13}$$

It can be shown that for the relativistic case, the angular frequency is then given by (3.4.14) [25].

$$\omega = \frac{qB}{mc}\sqrt{1-\left(\frac{\upsilon}{c}\right)^2} \tag{3.4.14}$$

3.4.2 Masers

Maser is short for *microwave amplified stimulated emission of radiation*. When masing occurs, molecular line emissions can be amplified so that certain molecules are detected that are otherwise very hard to find. A source such as a star can give off an intense radiation field. When a molecular cloud comes into contact with such a field, masing occurs. The molecules are 'pumped up' so that more are in a higher state than the normal ground state. The effect is that the original ray, while still having the same frequency and phase, is greatly amplified [12].

3.5 Effects of Media

When EM radiation travels through space, it might pass though different media before reaching the earth. One such medium, a gas cloud can cause emission and absorption lines to occur. The ISM can result in scintillation of the radiation, while magnetic fields can cause faraday rotation.

3.5.1 Absorption and Emission Lines

A blackbody radiates at all wavelengths. When the radiation moves through a gas cloud, some of the energy is absorbed by the electrons of the cloud. The radiation that leaves the cloud produces a spectrum that contains dark absorption lines. These dark lines are at wavelengths unique to the atoms of the gas [12].

When the spectrum of the gas cloud is viewed against a dark background, the result is bright emission lines. The cloud thus emits energy at the specific wavelengths absorbed from the radiation. This is known as Kirchhoff's laws of spectral analysis. At a quantum level, the spectral lines correspond to the electrons moving between different energy states. Fig.3.16. shows radiation passing through a gas cloud and the resulting spectral lines.

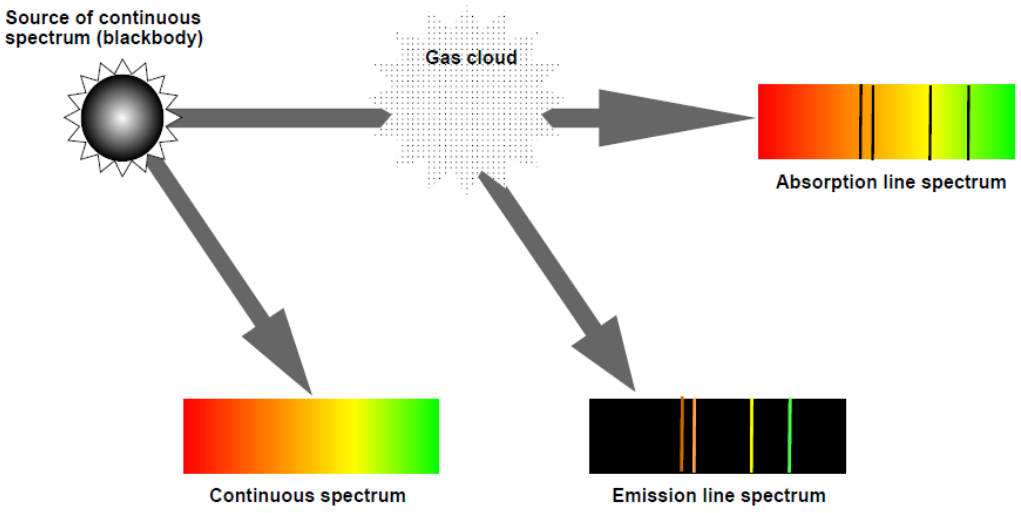

Figure 3.16: Resulting spectral lines from cloud absorption and emission, from [12].

3.5.2 Scintillation

Random fluctuations in the ISM can cause amplitude fluctuations referred to as scintillation, see Fig.3.17. This is the equivalent of stars twinkling in the visual spectrum.

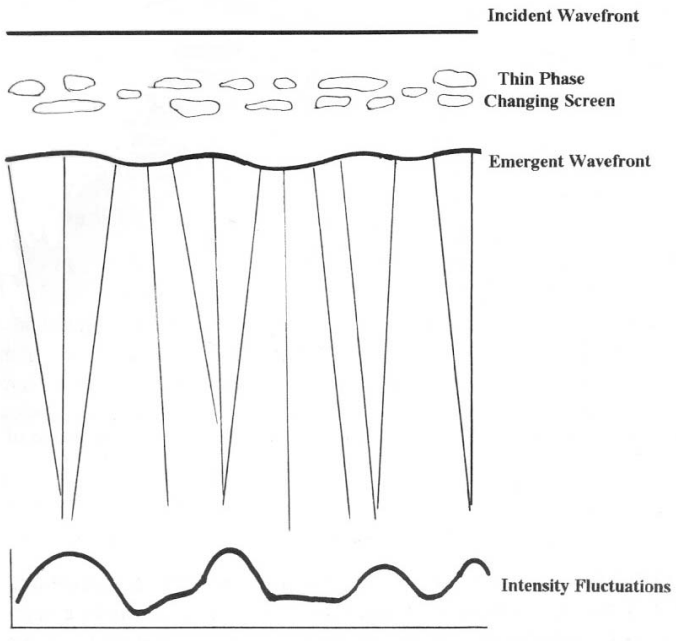

Figure 3.17: A wavefront encounters fluctuations in the ISM causing scintillation, from [13].

3.5.3 Faraday rotation

When a linearly polarised EM wave passes through a magnetic field in a plasma, the plane of polarisation is rotated (see Fig.3.18). The linearly polarised wave can be seen as two circularly polarised waves that move in opposite directions. One component moves faster than the other to result in a rotation of the plane over time. The density of the plasma is known by looking at the amount of rotation [12].

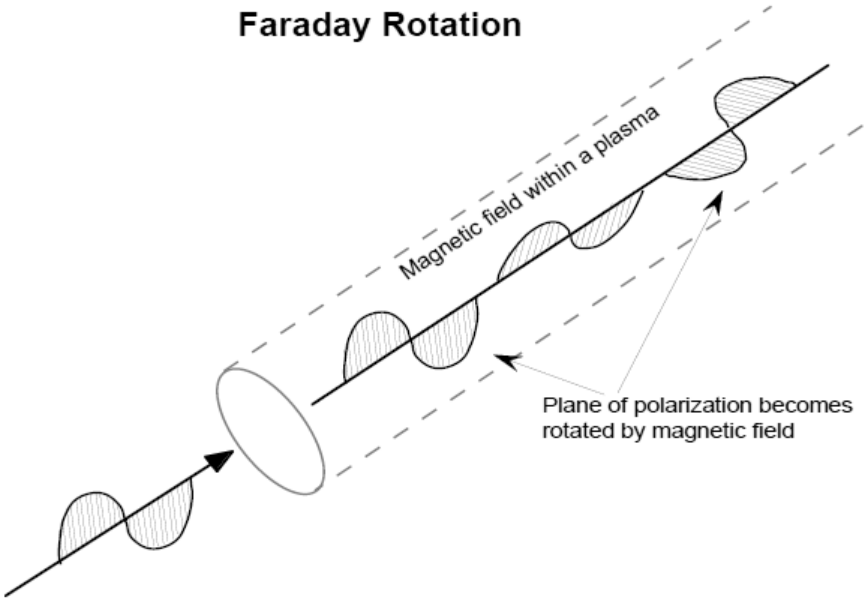

Figure 3.18: Faraday rotation, from [12].

The *rotation measure (RM)* is given by (3.5.1) [in $rad\,m^{-2}$] [13] [26] [27].

$$RM = 0.81 \int B \cos\theta n_e \mathrm{d}l \tag{3.5.1}$$

With B the magnetic field strength

θ the angle of the magnetic field from the line of sight

n_e the density of free electrons

and the integral along the line of sight from the observer to the source

The position angle observed, ϕ_1 is rotated with frequency and related to the RM as given by (3.5.2) [27].

$$\phi_1 = \phi_0 + RM\lambda^2 \tag{3.5.2}$$

with ϕ_0 the intrinsic position angle

λ the observed wavelength

Finding the intrinsic angle

When these measurements are made, the intrinsic angle may not be apparent. It can be determined by taking measurements of the observed position angles at different frequencies and applying some mathematical manipulation.

Let us define $\Delta\psi$ as the total rotation of position angle

ϕ_0 the intrinsic position angle

λ_N (with *N=1-3*) the observed wavelength at three different frequencies

ϕ_N the observed position angle at the specific frequency

RM_N the rotation measure at the specific frequency

The total rotation angle is given by (3.5.3) from (3.5.2).

$$\Delta\psi = \phi_1 - \phi_0 = RM\lambda^2 \tag{3.5.3}$$

For the first frequency *N=1*,the total rotation angle is given by (3.5.4).

$$\Delta\psi_1 = \phi_1 - \phi_0 = RM_1(\lambda_1)^2 \tag{3.5.4}$$

So that:

$$RM_1 = \frac{\phi_1 - \phi_0}{(\lambda_1)^2} \tag{3.5.5}$$

The only known variables for (3.5.5) are ϕ_1 and λ_1. Similar observations are made for *N=2* and *N=3* to give (3.5.6) and (3.5.7).

$$RM_2 = \frac{\phi_2 - \phi_0}{(\lambda_2)^2} \tag{3.5.6}$$

$$RM_3 = \frac{\phi_3 - \phi_0}{(\lambda_3)^2} \tag{3.5.7}$$

The 3^{rd} frequency is chosen so that the RM can be redefined as in (3.5.8), also refer to Fig.3.19.

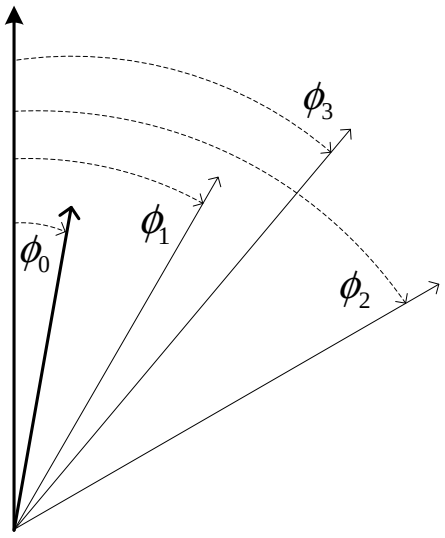

Figure 3.19: The intrinsic angle ϕ_0, can be determined using measurements of position angles at different frequencies.

$$RM_3 = \frac{\Delta\psi_2 - \Delta\psi_1}{(\lambda_2)^2 - (\lambda_1)^2} = \frac{\phi_2 - \phi_1}{(\lambda_2)^2 - (\lambda_1)^2} \tag{3.5.8}$$

The intrinsic angle cancels and RM_3 is known. By using (3.5.7), the intrinsic angle can now be determined.

3.6 Flux density of radio sources

This section describes flux density as a means of differentiating between different types of radio sources. It goes on to demonstrate a particular case of flux spectra - that of ionised hydrogen clouds.

3.6.1 Flux density and the spectral index

Consider again the flux density of a source (section 2.2.4) and the *Rayleigh-Jeans Law* (3.2.5) for the radio spectrum. The flux density, S, of a radio object is then given by (3.6.1) [11].

$$S = \frac{2k}{\lambda^2} \iint T(\theta,\phi)\mathrm{d}\Omega \tag{3.6.1}$$

Here, T is the temperature as a function of angle. If T is uniform over the solid angle (3.6.1) becomes (3.6.2).

$$S = \frac{2k}{\lambda^2} T\Omega_s \tag{3.6.2}$$

with Ω_s the source solid angle
The flux can also be described by (3.6.3).

$$S \propto \lambda^{\alpha} \tag{3.6.3}$$

With α the spectral index which can be used to describe the properties of a source. Thermal sources have a negative spectral index while non-thermal sources have a positive index (between 0.3 and 1.3).

Fig.3.20 shows that the brightness of thermal radiation increases with frequency, while it decreases with frequency for non-thermal radiation.

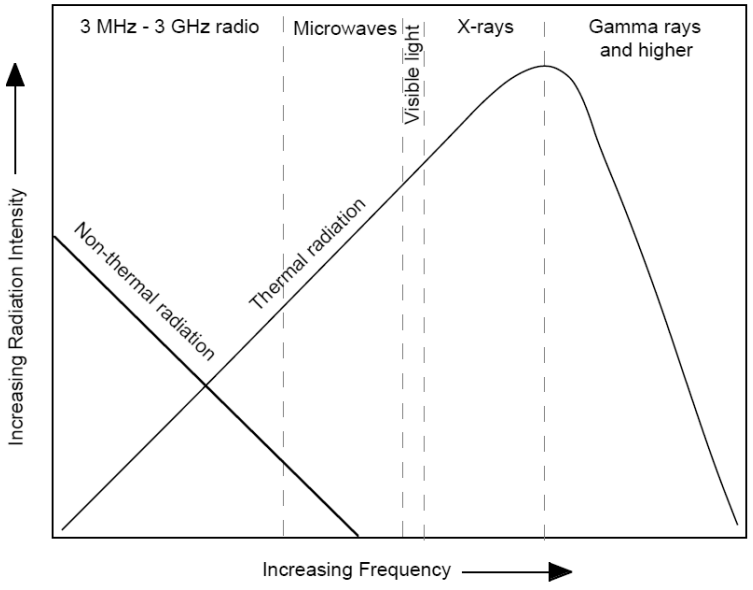

Figure 3.20: Relative intensity of thermal and non-thermal radiation across frequency spectrum, from [12].

Fig.3.21 shows (a) the flux density over a frequency range for various radio sources and (b) also for different values of spectral index.

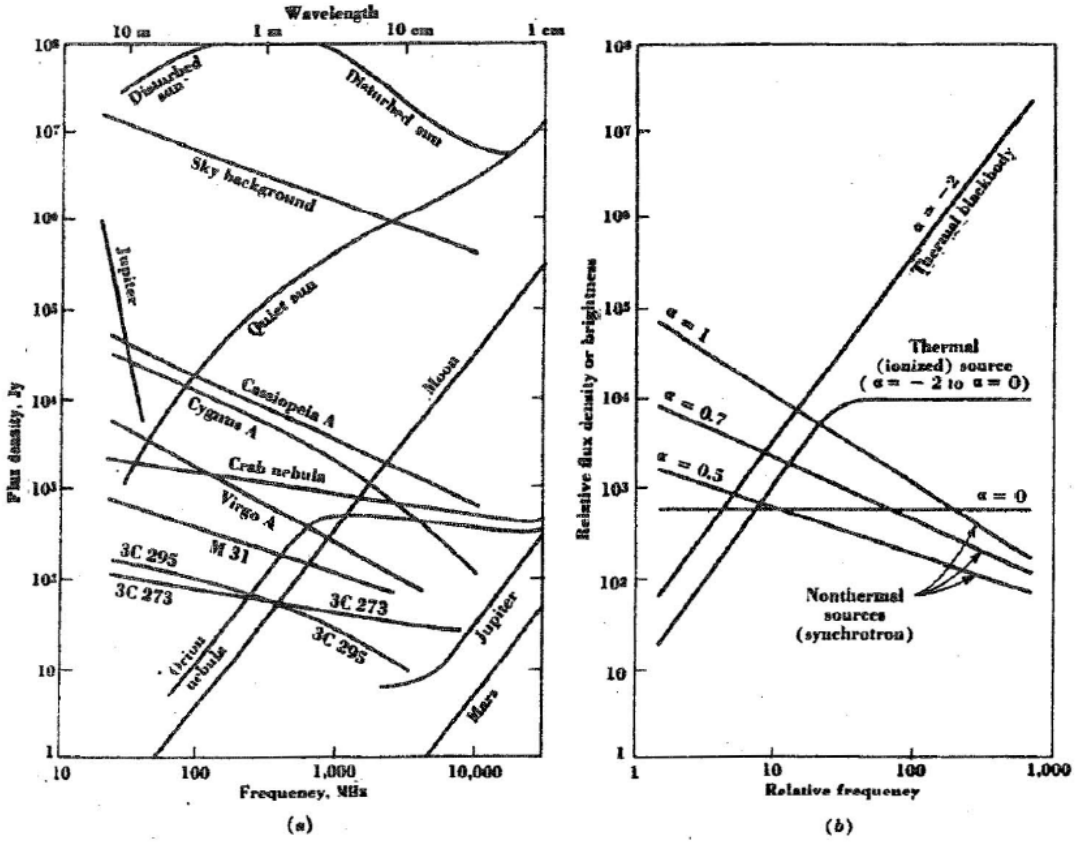

Figure 3.21: Spectra for a) different radio sources and b) for values of spectral index, from [11].

3.6.2 Ionised Hydrogen cloud

The Orion nebula is an example of an ionised hydrogen (H II) cloud. The slope of its spectrum in Fig.3.21a) is that of a thermal source for low frequencies and remains constant for higher frequencies. The reason is because there is a difference in optical thickness in the cloud depending on the frequency. To explain further, consider diffuse ionised hydrogen at radio wavelengths ($h\nu << kT$). The absorption coefficient is given by (3.6.4) [11].

$$K' = 9.8 \times 10^{-13} N^2 T_e^{-3/2} \nu^{-2} [19.8 + ln(T_e^{3/2} \nu^{-1})] \tag{3.6.4}$$

with N the free-electron density number per m^{-3}

T_e the electron temperature

Assume that T_e=10,000K and that the frequency is about 1000MHz, then (3.6.4) becomes (3.6.5).

$$K' = 1.3 \times 10^{-11} N^2 T_e^{-3/2} \nu^{-2} \tag{3.6.5}$$

The optical depth (3.6.6) is then the integral of the absorption coefficient over the path length, l.

$$\tau = \int_0^l K' \mathrm{d}s = 1.3 \times 10^{-11} T_e^{-3/2} \nu^{-2} \int_0^l N^2 \mathrm{d}s \tag{3.6.6}$$

When T_e=10,000K and ν is in MHz, (3.6.7) results.

$$\tau = 0.4 \nu^{-2} \int_0^l N^2 \mathrm{d}s = 0.4 \nu^{-2} EM \tag{3.6.7}$$

with EM the emission measure

N the free-electron density number per cm^{-3}

Assume N is constant over the integral, then we get (3.6.8).

$$\tau = 0.4\nu^{-2}N^2 l \tag{3.6.8}$$

The brightness temperature of the cloud is given by (3.6.9).

$$T_b = T_e(1 - e^{-\tau}) \tag{3.6.9}$$

From (3.6.2), we have the flux density as (3.6.10).

$$S = \frac{2k}{\lambda^2} T_b \Omega_s \tag{3.6.10}$$

Optical thickness of cloud

At short wavelengths the cloud is optically thin, with the optical depth τ , smaller than unity so that (3.6.9) reduces to (3.6.11).

$$T_b = T_e\tau \tag{3.6.11}$$

Now, it can be noted from (3.6.10) and (3.6.11) that:

$$S \propto \frac{T_b}{\lambda^2} \propto \frac{\tau}{\lambda^2} \propto \frac{1}{\nu^2\lambda^2} \tag{3.6.12}$$

For the short wavelength range, the flux will thus remain constant (see Fig.3.21) with a spectral index of $\alpha = 0$. At longer wavelengths the cloud is optically thick, with the optical depth τ , greater than unity to give (3.6.13) and (3.6.14).

$$T_b = T_e \tag{3.6.13}$$

$$S \propto \lambda^{-2} \tag{3.6.14}$$

The difference in (3.6.14) is that the flux now changes with the square of the wavelength with a spectral index of $\alpha = -2$. Fig.3.22 shows the spectrum of the Orion nebula. Note the change in slope that occurs at about 30cm wavelength.

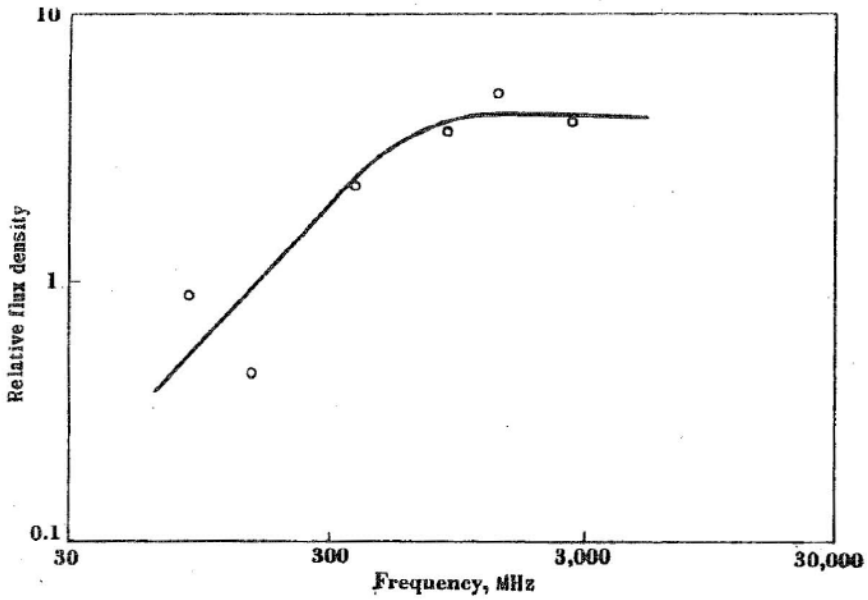

Figure 3.22: The spectrum of the Orion nebula with circles indicating observed points, from [11].

Another example of an H II cloud is the Rosette nebula. Fig.3.23 shows the flux density of both nebulae, with the arrows pointing at the break frequencies.

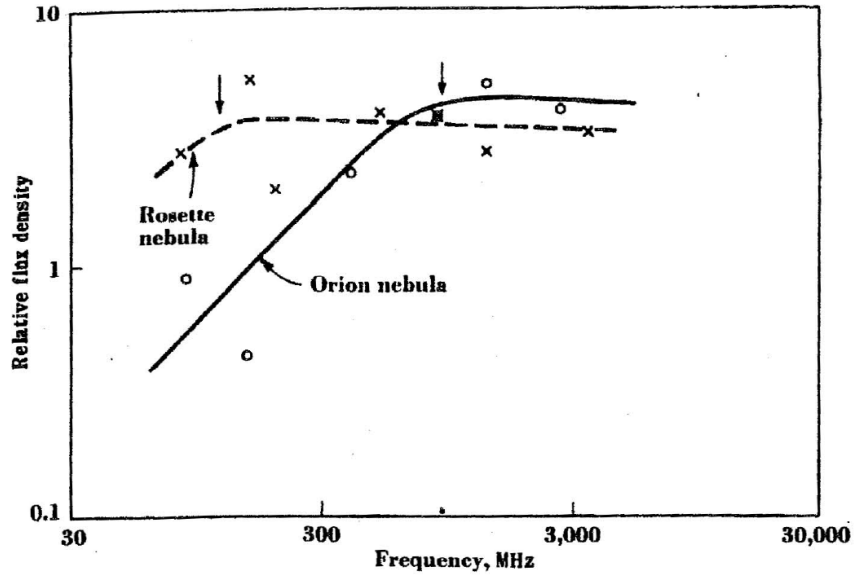

Figure 3.23: The spectra for both the Orion and Rosette nebula, from [11].

The break of spectrum occurs at 30 cm for the Orion nebula, while the Rosette nebula has a flat spectrum ($\alpha = 0$) up to 3 m.

3.7 Conclusion

This chapter covered fundamental EM theory including radiation laws, optical depth and the equation of radiative transfer. It described the thermal and non-thermal radiation mechanisms and mentioned some effects of media on EM waves. It concluded with a description on the flux density of different radio sources with an example of an ionised Hydrogen cloud.

Chapter 4

Radio Sources

4.1 Introduction

This chapter will focus on practical examples of different radio sources that is found throughout our galaxy and beyond. It starts with a section on our solar system, describing radio emission from the Sun, Moon and planets. It then goes further out into our galaxy, describing emission from the interstellar medium, radio stars and our galaxy's core. This is followed by looking at different types of normal and active galaxies found in the universe. It ends with a section on some radio phenomena and concepts.

4.2 Our Solar System

This section describes emission from objects in our solar system which includes the Sun, Moon and planets.

4.2.1 The Sun

The sun is not only a thermal source, it can also be observed through radio emission. At wavelengths below 1 cm, the flux density curve of the sun (Fig.4.1) follows Planck's radiation law (see section 3.2.2). At larger wavelengths it follows one of two curves, representing the *disturbed sun* or the *quiet sun*. It reaches a maximum flux density of around 100 MJy at 1m wavelength [11].

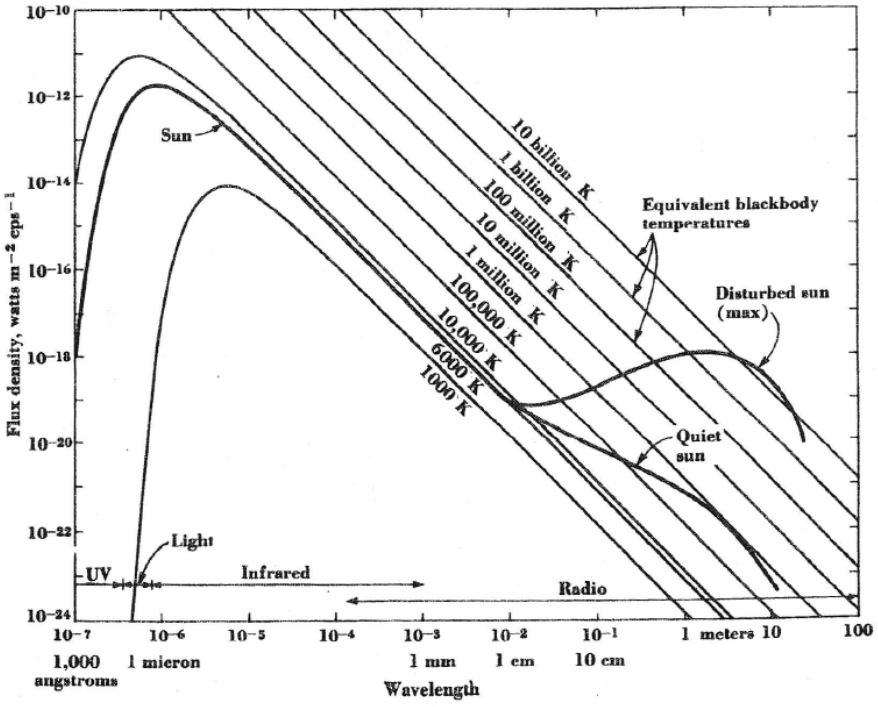

Figure 4.1: Solar flux density from UV to radio wavelengths, from [11].

Emission from quiet sun

This represents the minimum background radiation from the sun during no or little sunspot activity. Three types of emission occur: bremsstrahlung (section 3.3.1), gyroresonance (section 3.4.1) and plasma emission. Fig.4.2 shows the type of emission in the solar atmosphere for a range of radio frequencies, depending on the height above the surface.

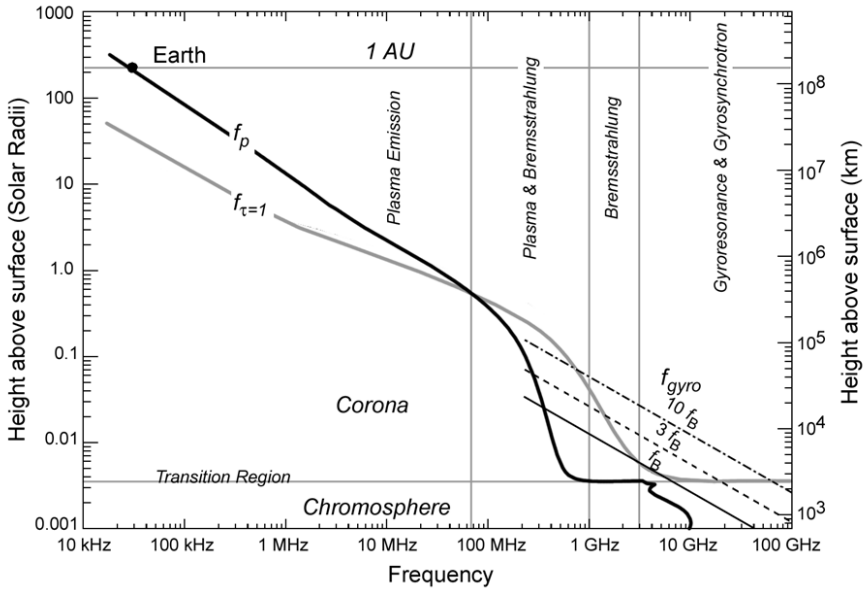

Figure 4.2: Types of emission in the solar atmosphere for different radio frequencies, from [18].

Emission from disturbed sun

This represents the radiation from the sun during sunspot activity. It can be further divided into the *slowly varying component* which is observed in the 3–60 cm range for periods of days to months, and the *rapidly varying component* which is bursts of radiation for intervals of seconds to hours. The emission is classified into five types according to Table 4.1.

Table 4.1: Types of solar radio emission, adapted from [11].

Type	**Duration**	**Bandwidth**	**Mechanism**
Quiet sun	Constant (or 11-year period)	Continuum	Thermal
Slowly varying component	Days or months	Continuum	Thermal
Rapidly varying component Phase 1			
Type III Type V	Seconds Minutes	100 MHz Continuum	Plasma Synchrotron
Phase 2			
Type II Type IV Type I Type I noise storm	Minutes Hours Seconds Hours	50 MHz Continuum 5 MHz 50 MHz	Plasma Synchrotron

Fig.4.3 shows a flux density graph of the Sun together with the galactic background. It starts at 1 cm, with a gap from 10 m to 1 km (due to the ionosphere) and then continues with measurements from space to about 10 km.

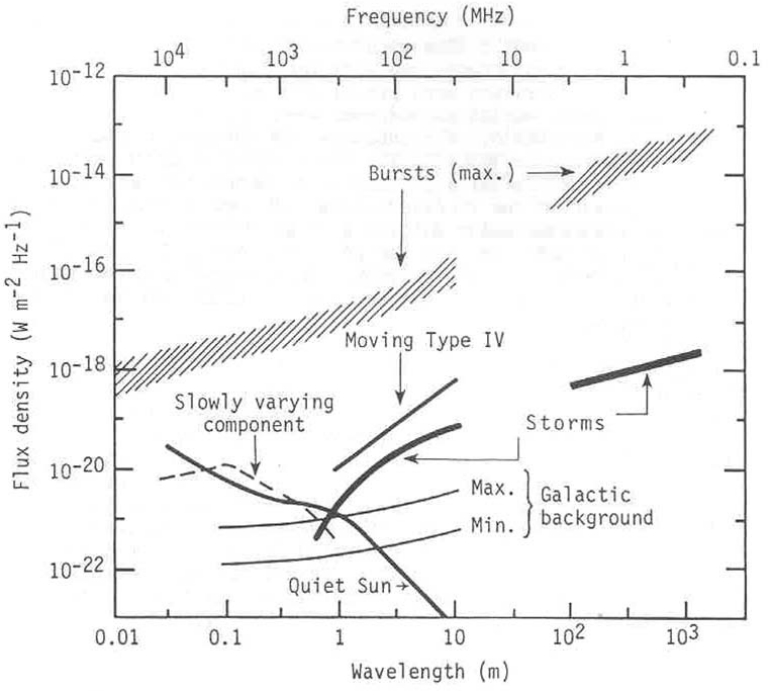

Figure 4.3: Flux density of the Sun and galactic background, from [18].

4.2.2 The Moon and planets

The moon and planets are seen at optical wavelengths due to the reflection of the sun's light. At radio wavelengths, they radiate like blackbodies at temperatures in the order of 100 K. When looking at Planck's radiation curves like that in Fig.3.4, it can be seen that for this temperature the main radiation is at infrared and short wavelengths. The temperature of the moon varies with the lunar phase. Fig.4.4 shows the lunar temperature during the lunar phase at different wavelengths.

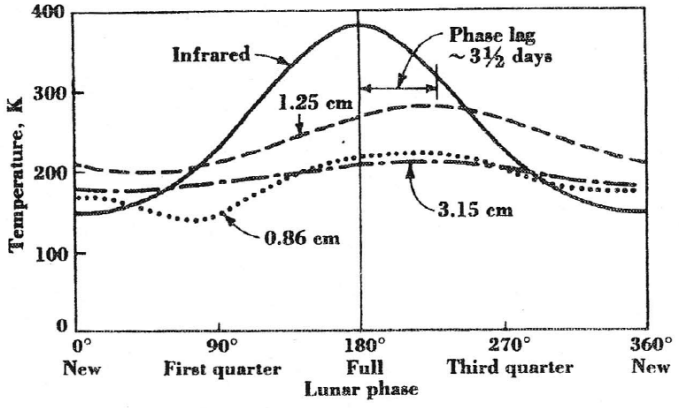

Figure 4.4: Lunar temperature as a function of lunar phase, from [11].

At infrared, the radiation shows symmetry around the full moon phase. At microwave temperatures, there is a phase lag with no symmetry at the maximum temperature. At still longer wavelengths the temperature variation decreases to only 10% at 75 cm. This lower temperature may indicate that the microwave radiation

originates somewhere below the moon's surface, while the higher infrared temperature comes from a thin layer on the surface.

Mercury is not easy to observe, as it is very close to the direction of the sun. Radio emission has been detected at 3 cm with a blackbody temperature of 400 K. Measurements show that the dark side of Venus has a blackbody temperature of about 600 K at 2–20 cm wavelength, which then decreases to about 350 K at 5 mm. The side facing the sun has higher temperatures that may increase up to about 730 K. The radio emission for Mars is similar to that of Venus, but with lower temperatures due to its larger distance from the sun. At km wavelengths, the temperature of the Earth is determined by the opaque ionosphere. At cm wavelengths, the radiation is similar to a thermal blackbody.

Measurements from Jupiter show temperatures much higher than expected for just thermal radiation. Also, unlike thermal radiation, it is usually circularly or elliptically polarised [12]. At centimeter wavelengths, thermal radiation occurs at about 3 cm and non-thermal radiation around 30 cm. The non-thermal radiation is synchrotron emission from electrons trapped in a magnetic field outside the planet's atmosphere. Fig.4.5 shows the radiation from these electrons [11].

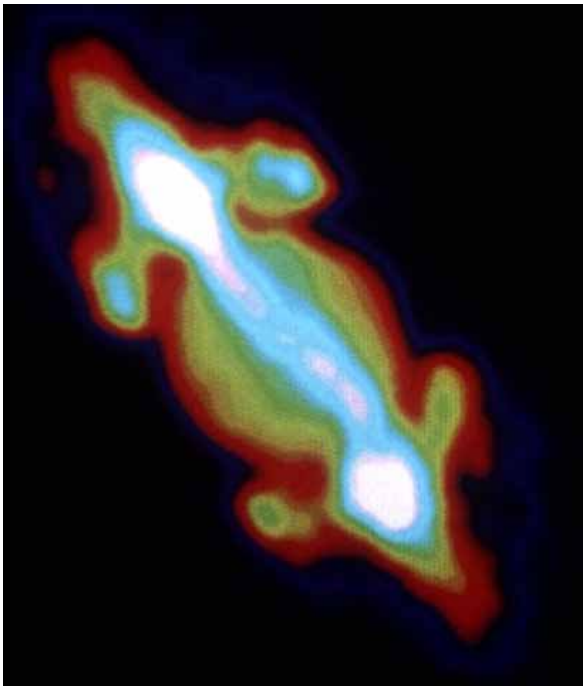

Figure 4.5: Jupiter at 20cm wavelength, image courtesy of NRAO/AUI [28].

In the kilometre range there is broadband radiation from 10–1000 kHz and narrow band radiation centered on 100 kHz. Fig.4.6 shows the flux density spectrum of Jupiter for a part of the radio spectrum.

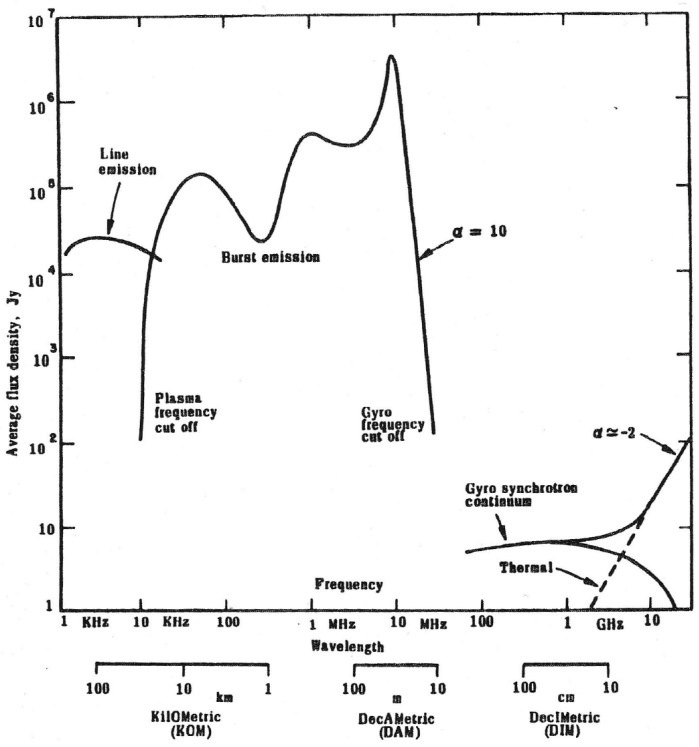

Figure 4.6: Flux density spectrum of Jupiter, from [11].

In the decameter range, some of the radiation is related to Jupiter's satellite Io. When Io moves through Jupiter's magnetic field, it generates an electric field. This field allows for a current to flow from Io to Jupiter's atmosphere that reaches up to 5 million Amps [12]. This current causes noise storms made up of radio bursts called *L-bursts* and *S-bursts*. The *L-burst* (long burst) lasts about 1–6 seconds and is caused by scintillation (see section 3.5.2). The *S-burst* (short burst) each lasts about 5–50 milliseconds. The *Io plasma torus* is a magnetospheric region in the form of a doughnut, surrounding Io's orbit. It contains trapped ions and electrons that originally came from Io's volcanoes [11]. Fig.4.7 shows an illustration of Jupiter's magnetosphere that contains its magnetic field and Io's plasma torus.

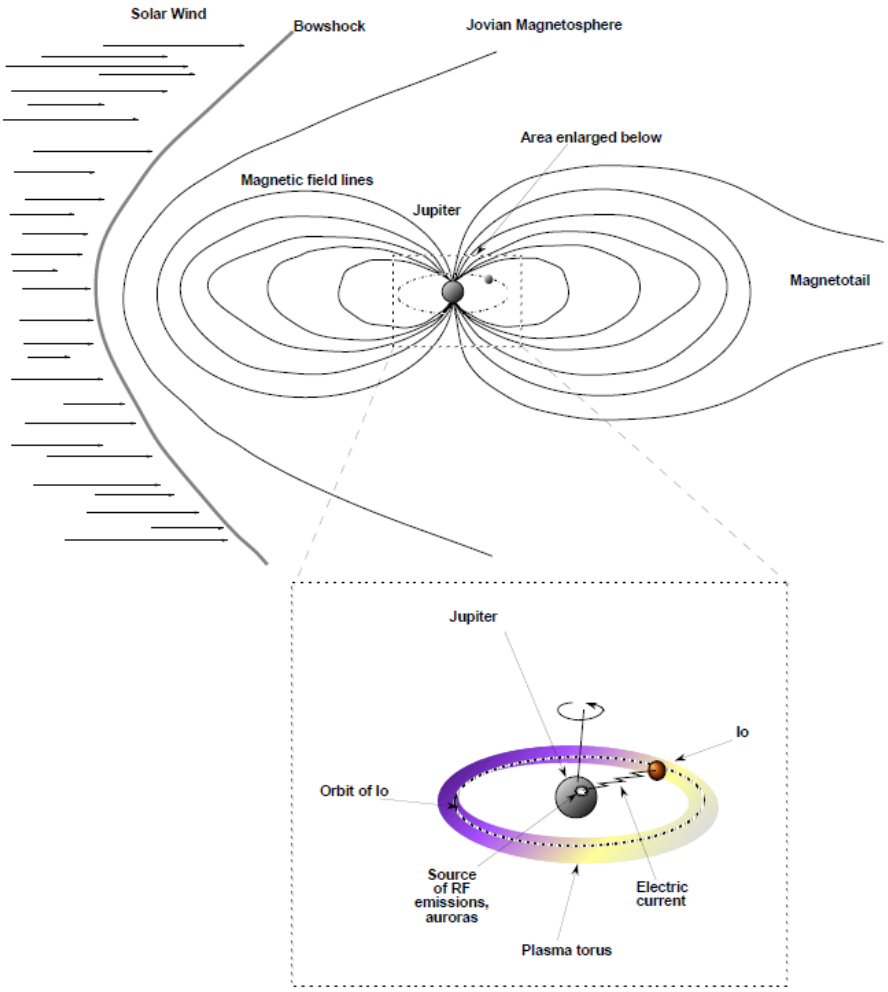

Figure 4.7: Jupiter's magnetosphere and (enlarged) Io's plasma torus, from [12].

Saturn has thermal and non-thermal radiation. The latter is synchrotron emission similar to the burst emission from Jupiter. This occurs in the range of 20–500 kHz. Fig.4.8 shows the thermal emission from Saturn.

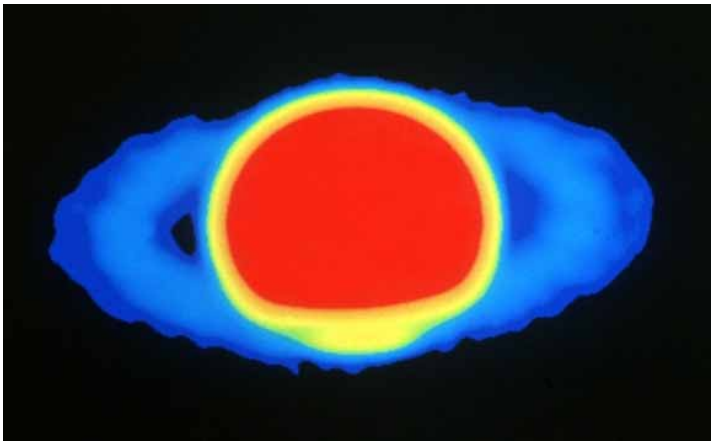

Figure 4.8: Saturn at 2cm wavelength, image courtesy of NRAO/AUI [29].

4.2.3 Solar system spectra

Fig.4.9 shows the radiation spectrum of sources found in our solar system.

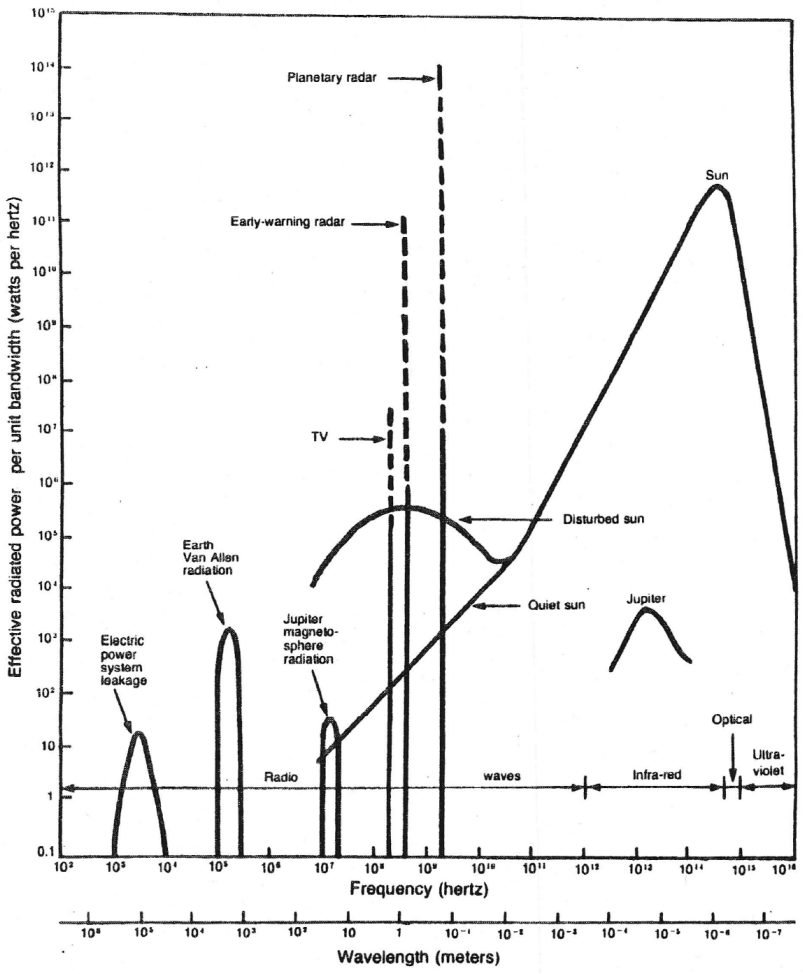

Figure 4.9: The spectral power for sources of radiation in our solar system, from [11].

Table 4.2 gives the radio and infrared temperatures of the moon and planets [11].

Table 4.2: Radio and infrared temperatures of the moon and planets, from [11].

Object	**Blackbody Temperature,** *K*		**Wavelength (*mm*)**
	Infrared	**Radio**	
Moon	150–375	145–280	10
Mercury	610 (sunlit side)	400	30
Venus	370 (sunlit side)	550–700	30–100
	250 (dark side)	500	20
Earth	287 (avg)		
Mars	250 (sunlit side)	211	30
	217 (avg)	190	3
Jupiter	140	145	30
		220	61
		320	210
Saturn	125	106	30
		140–213	90
Uranus	90	125	10
		169	31
Neptune	70	134	10
		115	31

4.3 Our Galaxy: The Milky Way

There are several types of sources within our galaxy that can be observed within the radio spectrum. We discuss the interstellar medium, radio stars and the galactic nucleus.

4.3.1 Interstellar Medium

The Interstellar Medium (ISM) is the material found between the stars, made up of 99% gas and 1% dust. The gas itself consists of 90% atomic and molecular hydrogen and 10% helium and other elements. Table 4.3 summarises what can be observed from the ISM at different wavelengths [13].

Table 4.3: Observations of the ISM at different parts of the EM spectrum.

Part of EM spectrum	**Observation**
Optical	Dust absorbs starlight
Infrared	Thermal radiation emitted by dust
Sub-mm and mm	Spectral lines from gas molecules
21-cm	Hyperfine line of hydrogen
cm and m	Thermal bremsstrahlung from H II regions
Radio spectrum	Recombination lines from hydrogen atoms

The ISM is under the influence of radiation from stars and supernova explosions so that different parts of the ISM are either in a neutral or ionised state. The temperatures associated with these regions is summarised in Table 4.4 [13].

Table 4.4: Different states and temperatures of the ISM.

Ionised state		**Neutral state**		
Hot ISM	Warm ionised medium	Warm neutral medium	Cool neutral ISM	Cold neutral medium
>500,000K	10,000K	100K–1000K	100K	10K
	H II regions		21-cm line of H	Molecular line emission

Hydrogen regions

It is known that hydrogen is the most abundant element found in the universe and is distributed throughout the galaxy in the form of clouds. When a region in space is comprised of neutral hydrogen it is referred to as an *H I region*. If the hydrogen is ionised, it is known as an *H II region* [12]. When studying the 21cm line of neutral hydrogen (described in section 3.3.2), information on the following is obtained [18]:

- The velocity of neutral hydrogen clouds
- The rotation of galaxies
- The distribution of neutral hydrogen in galaxies

- Tidal interactions between galaxies
- The amount of gas in the interstellar medium

Fig.4.10 shows an example of tidal interactions in the M81 group of galaxies, seen by observing the 21cm spectral line of hydrogen.

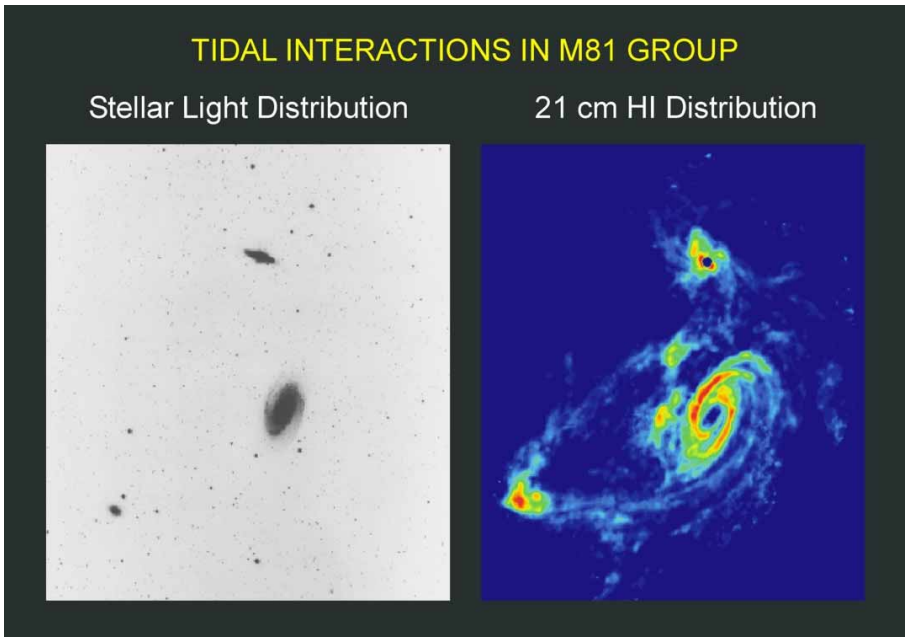

Figure 4.10: Observation of the M81 group with an optical image (left) and observation of the 21cm line of hydrogen (right), image courtesy of NRAO/AUI [30].

When a hot stellar source (such as O and B stars) is in or near a neutral hydrogen cloud, the UV light from the source ionises the hydrogen. Ionised Hydrogen (H II) clouds emit continuum radiation and can have temperatures of 10,000 K. The Orion Nebula, which is a good example of an ionised hydrogen cloud, is shown in Fig.4.11. The distribution of ionised hydrogen is also shown (right).

Figure 4.11: The Orion Nebula images shows stars, dust and gas (left) and ionised gas (right), image courtesy of NASA and NRAO/AUI [31] [32].

Line emission

Continuum radiation is observed with receivers of wide bandwidth where the exact frequency is not important. The emission occurs at nearly all frequencies with varying intensity. When observing spectral lines (see section 3.3.2) however, the exact frequency is important and therefore narrowband receivers are used. The observation of the 21-cm line (at 1420 MHz) of neutral hydrogen makes it possible to from a picture of the structure of our galaxy. When a neutral hydrogen cloud is scanned with a narrowband receiver, the intensity-frequency plot profile is given by Fig.4.12(a). Here, the centre frequency is 1420 MHz and the cloud is stationary.

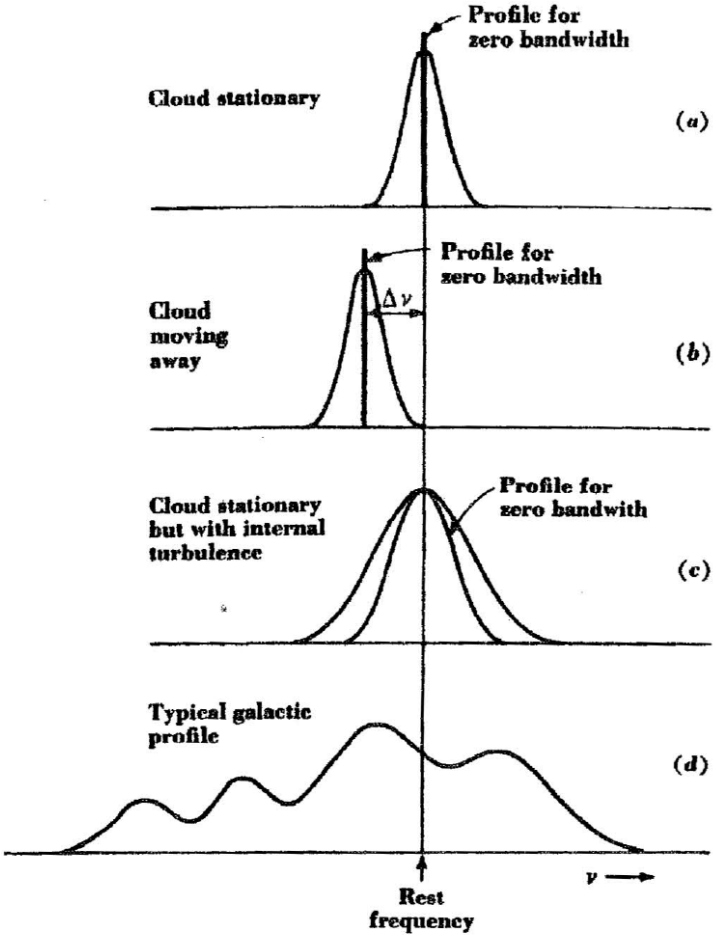

Figure 4.12: Hydrogen-line profiles, from [11].

When the cloud is moving with respect to the observer, there is a frequency shift (see section 4.5) of illustrated by Fig.4.12(b). The velocity of the moving cloud is given by (4.3.1).

$$\mp \upsilon = c\frac{\pm\Delta\nu}{\nu} \tag{4.3.1}$$

With υ the velocity of approach (-) or recession (+) and ν the rest frequency for $\upsilon << c$.

The profile for a receiver of zero bandwidth is also indicated for each case (delta function). If the cloud has thermal broadening or turbulence while stationary, the profile is wider, see Fig.4.12(c). The true profile is represented by the zero bandwidth profile. The observed profile is then the convolution of the true profile and the receiver profile. A typical profile is that of Fig.4.12(d), where multiple clouds with internal motion are moving at different velocities. Such profiles are used to map the movement and distribution of neutral hydrogen in our galaxy [11].

Line absorption

Consider a line cloud (any atomic or molecular line) in the antenna beam between the observer and a discrete source given by Fig.4.13.

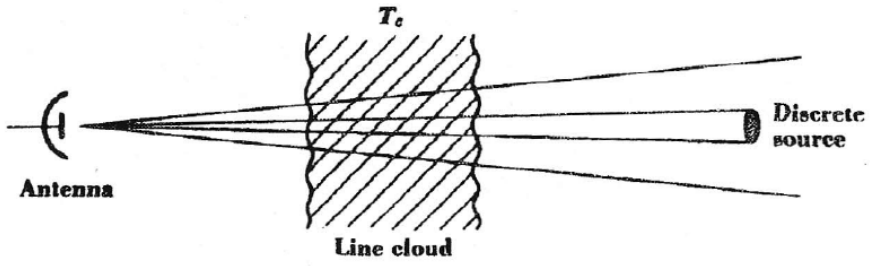

Figure 4.13: Line cloud between the observer and discrete source, from [11].

The line temperature, T_l within the cloud's line frequency range (signal band) is measured. The observed antenna temperature T_s' is measured next to this line and is given by (4.3.2).

$$T_s' = T_s \frac{\Omega_s}{\Omega_A} \tag{4.3.2}$$

with T_s the true source temperature
Ω_s the source solid angle
Ω_A the antenna beam solid angle

The same method applies when defining T_c', using Ω_M as the main beam solid angle instead of Ω_s. Cloud absorption is discussed in section 3.2.4 where (3.2.16) is now used to express T_l in (4.3.3).

$$T_l = T_s' e^{-\tau} - T_c'(1 - e^{-\tau}) \tag{4.3.3}$$

with T_s' the apparent source temperature due to the source
T_c' the apparent cloud temperature due to cloud in the line
T_c the true cloud temperature in the line

When evaluating (4.3.3), the first part involves the line absorption from the cloud, while the second part is due to the cloud's internal line emission and absorption. For the comparison band (frequencies off of line), it holds that $\tau = 0$ and the temperature is given by (4.3.4).

$$T = T_s' \tag{4.3.4}$$

The difference of the signal and comparison bands is then given by (4.3.5).

$$T_l - T = \Delta T = (T_c' - T_s')(1 - e^{-\tau}) \tag{4.3.5}$$

This is the output when observing on-source. If $T_c' > T_s'$, then the line is seen as emission, while $T_c' < T_s'$ shows absorption. If the cloud is measured off-source, the difference in temperature is given by (4.3.6).

$$\Delta T' = T_c'(1 - e^{-\tau}) \tag{4.3.6}$$

The first, (4.3.5) is an absorption measurement, while (4.3.6) is an emission measurement. The difference between these two equations is given by (4.3.7).

$$\Delta T - \Delta T' = -T_s'(1 - e^{-\tau}) \tag{4.3.7}$$

By using (4.3.6) and (4.3.7), τ and T_c can be determined.

The case for more than one line cloud within the antenna beam is described as follows. Fig.4.14 shows two line clouds, i and j with i in line with the source.

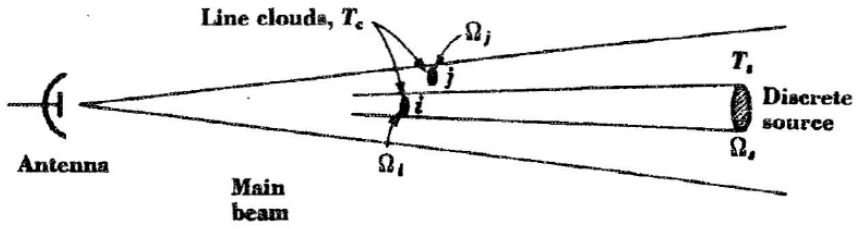

Figure 4.14: Multiple line clouds within the antenna beam, from [11].

The line temperature is given by (4.3.8).

$$T_l = T_s \frac{\Omega_s - \Omega_i}{\Omega_A} + T_s \frac{\Omega_i}{\Omega_A} e^{-\tau_i} + T_c(1 - e^{-\tau_i}) \frac{\Omega_i}{\Omega_A} + T_c(1 - e^{-\tau_j}) \frac{\Omega_j}{\Omega_A} P_{nj} \tag{4.3.8}$$

with Ω_i the solid angle of cloud i

Ω_j the solid angle of cloud j

τ_i the optical depth of cloud i

τ_j the optical depth of cloud j

P_{nj} the normalised antenna power pattern value in the direction of cloud j

The first term of (4.3.8), describes the temperature due to the source that is not covered by cloud i. The second term is from the part of the source covered by cloud i. The last two terms concern the internal absorption and emission from both clouds i and j separately.

The comparison band results in (4.3.9).

$$T = T_s \frac{\Omega_s}{\Omega_A} \tag{4.3.9}$$

The on-source difference output is given by (4.3.10).

$$\Delta T = \left(T_c \frac{\Omega_i}{\Omega_A} - T_s' \frac{\Omega_i}{\Omega_s} \right) (1 - e^{-\tau_i}) + T_c (1 - e^{-\tau_j}) \frac{\Omega_j}{\Omega_A} P_{nj} \tag{4.3.10}$$

For the case of more than two clouds, the on-source output is given by (4.3.11).

$$\Delta T = -\sum_i T_s' (1 - e^{-\tau_i}) \frac{\Omega_i}{\Omega_s} + \sum_{i,j} T_c (1 - e^{-\tau_{i,j}}) \frac{\Omega_{i,j}}{\Omega_A} P_{ni,j} \tag{4.3.11}$$

The first summation is over the i clouds (within the solid angle of the source) and the second part is over all the clouds (i and j) within the antenna beam (not inside the angle of the source). This second part can be described by $\overline{\Delta T'}$, which is the mean temperature of the nearby off-source line clouds. This can be reduced to (4.3.12) with the condition that $\Omega_i \approx \Omega_s$.

$$\Delta T = -T_s' (1 - e^{-\tau_t}) + \overline{\Delta T'} \tag{4.3.12}$$

With τ_t the total optical depth of all the line clouds within Ω_s.

Molecular clouds

A large part of gas in the universe is in the form of molecular clouds, also known as the birthplace of stars. These clouds are usually dark in the optical spectrum due to dust, but can be observed through the molecular lines (see section 3.3.2) they emit. Fig.4.15 shows that the L483 molecular cloud in infrared is seen as a dark cloud, where as in the radio spectrum it can be seen through the emission of carbon monoxide molecules.

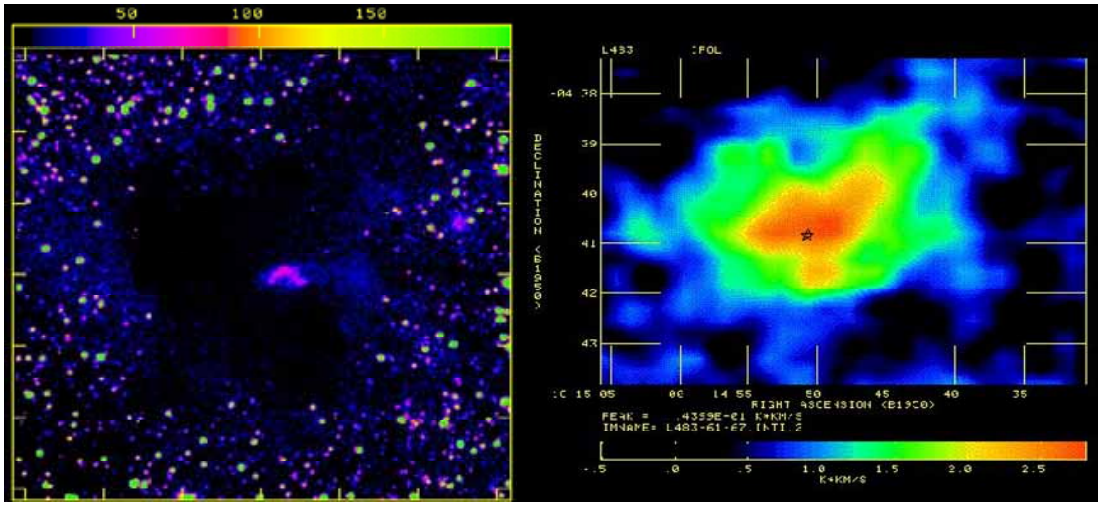

Figure 4.15: Infrared (left) and radio (right) images of the L483 molecular cloud, image courtesy of NRAO/AUI [33] [34].

Fig.4.16 shows the spectacular Eagle Nebula molecular cloud lit up by ultraviolet stars.

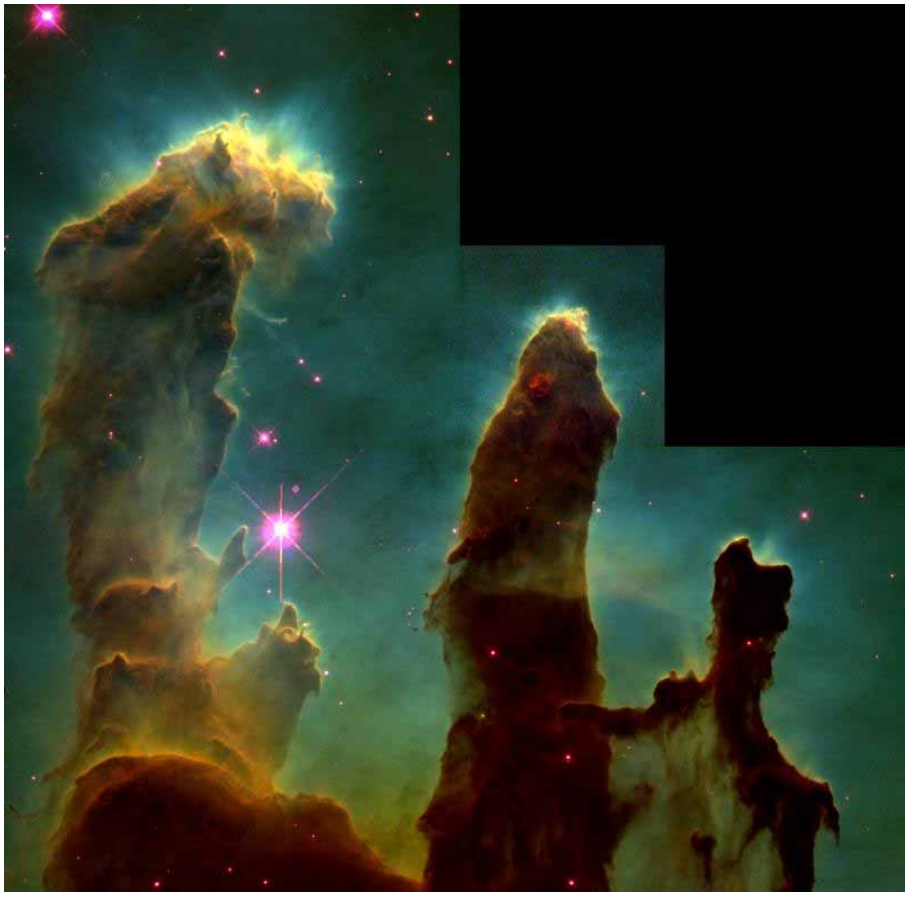

Figure 4.16: The Eagle Nebula (M16) molecular cloud, image courtesy of NASA [35].

Recombination lines

When two oppositely charged ions recombine to a neutral state, the electrons move between energy states. The result is absorption and emission lines, called recombination lines. When studying recombination lines, information about the temperature, density, composition, velocities and motions of the region can be obtained [12] [18].

An electron falls from the initial level $(n+\Delta n)$ to a lower level n (with n being any natural number) and releases a photon with energy ΔE, see Fig.4.17.

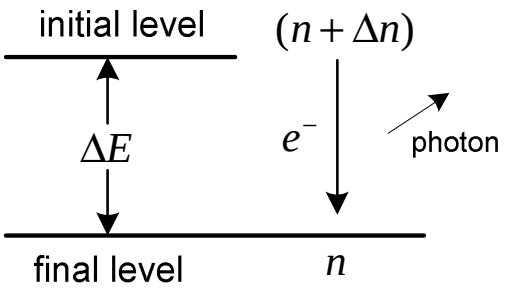

Figure 4.17: Electron falling to lower energy state.

Recombination line names are then given by [name of element][final level number n][Δn] with Δn described by Greek symbols ($\alpha = 1$, $\beta = 2$, etc.). A hydrogen atom for example, that moves from $n = 92$ to $n = 91$ would then produce what we would call a $H91\alpha$ line. A place for these lines to occur is in H II regions, where the hydrogen gas is ionised. The hydrogen ion and electron recombine to form a highly excited atom that emits and absorbs radiation. This atom is different from the neutral hydrogen atom that emits at 21cm wavelength. Fig.4.18 shows an image of the nebula NGC 2080 made up of three colours:

- red - ionised hydrogen from the H-α recombination line
- green - ionised oxygen
- blue - ionised hydrogen from the H-β recombination line

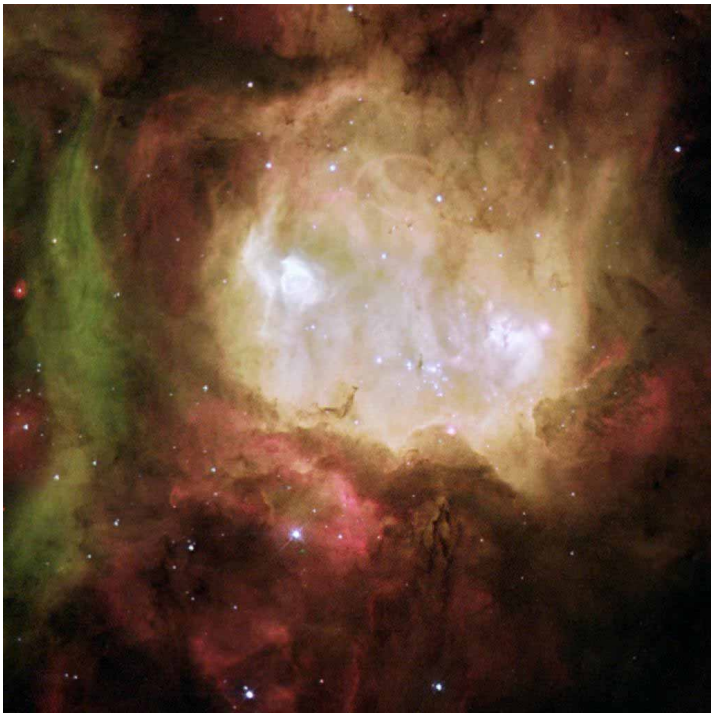

Figure 4.18: NGC 2080 or the Ghost Head Nebula shows H II regions traced by recombination lines, from [36].

Supernova Remnants

When a large star dies, it may result in a supernova explosion. The ejected material in the surrounding medium forms a supernova remnant, which is a type of non-thermal source (see section 3.4). Supernovas can be divided into two groups, called a *type I supernova* and *type II supernova*. *Type I* releases no hydrogen and ejects only a small fraction of solar mass, while *type II* releases hydrogen and ejects several solar masses [11].

The brightest radio source in the sky, apart from the sun, is the supernova remnant Cassiopeia A. It is classified as a *type II supernova*. The radiation mechanism is synchrotron radiation and the source has a spectral index of $\alpha = +0.8$. Fig.4.19 shows a false-colour image of Cassiopeia A with infrared radiation in red, visible light in yellow and x-ray in green and blue.

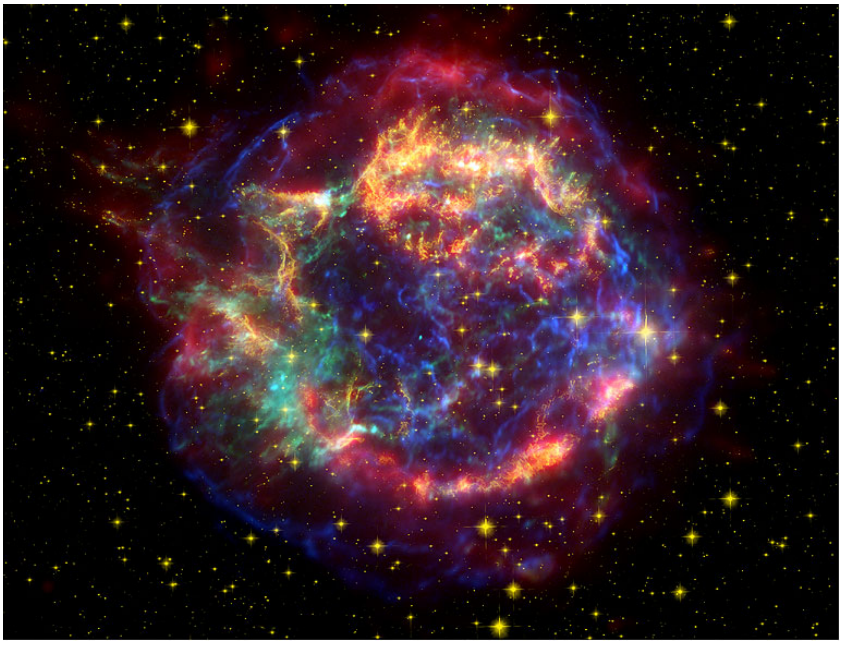

Figure 4.19: Composite false-colour image of Cassiopeia A, image courtesy of NASA/JPL [37].

Another well-known supernova remnant witnessed by Chinese astronomers in 1054 is *The Crab nebula*, which is a *type I supernova*. The radiation mechanism is also synchrotron radiation and the source has a spectral index of $\alpha = 0.27$. Fig.4.20 shows an image of the Crab Nebula with the colours representing different elements present. The blue glow is from electrons moving very fast around the central neutron star which is a rapid pulsar.

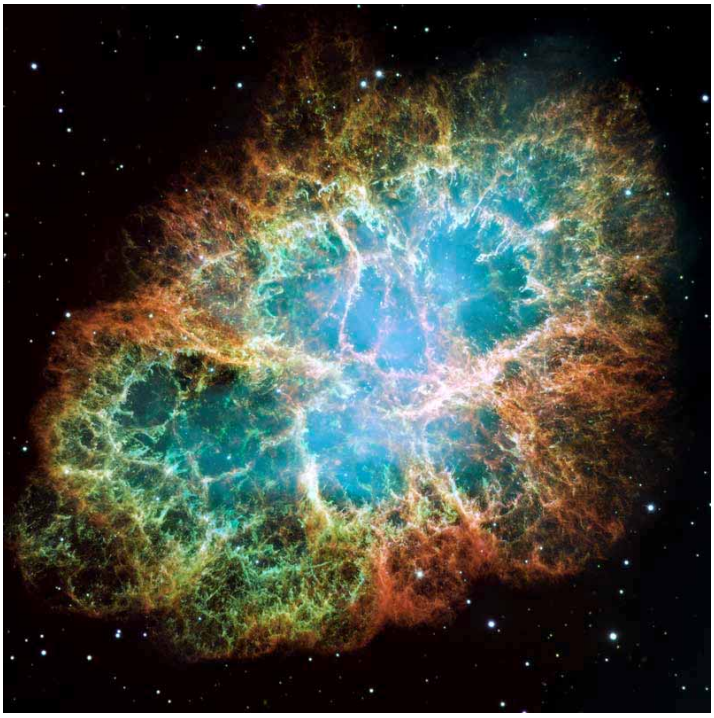

Figure 4.20: The Crab Nebula, image courtesy of NASA [38].

Dark Matter

It is believed that as much as 90% of matter in the universe is *dark matter*, a non-luminous matter that can't be detected from Electromagnetic (EM) radiation. It is based on the fact that there is more mass than can be explained by the known matter [13]. For example we can measure the rotational velocity of galaxies and from this the total mass of the galaxy can also be determined mathematically. The result is that the theoretical rotation curve does not correspond with the measured curve. The theory is that there must be another component - dark mater - that contributes to the total mass. Fig.4.21 shows such a graph of rotational velocity against the distance from the centre of the spiral galaxy M33. It is argued whether the dark matter is large objects like black holes or rather made up of small subatomic particles.

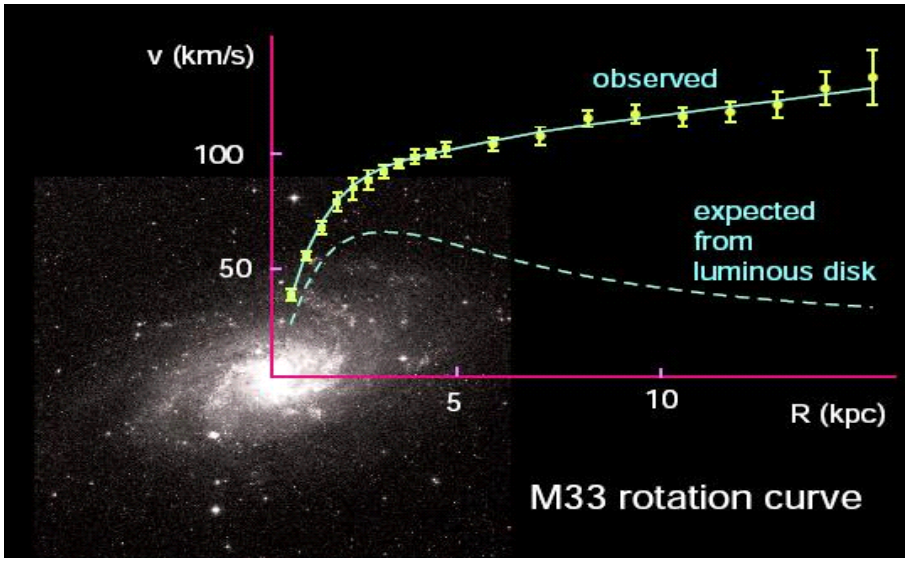

Figure 4.21: The observed and expected rotational velocity curves for the spiral galaxy M33 are compared. The difference in the curves is thought to be the contribution of dark matter, from [39].

4.3.2 Radio Stars

A radio star is any visible stellar object that also emits at radio wavelengths. Most stars are thermal sources and can be detected at radio wavelengths, although the signals may be weak. Strong radio emission is usually found in very young or old stars. Examples of radio stars include *flare stars*, *binary star systems* and *pulsars*. Flare stars are faint red dwarf stars. They emit radio flares, much larger than solar flares that usually last for a few minutes. Binary stars are so-called double stars that orbit each other around their centre of mass. The emission is non-thermal radiation due to the interaction of their magnetic fields [12].

X-ray binary star system

In this system the one star is in the form of a black hole that pulls matter in to produce x-ray emission, see Fig.4.22.

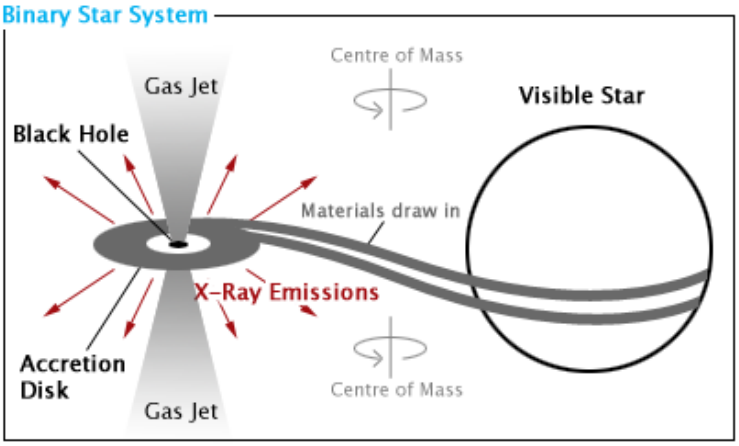

Figure 4.22: X-ray binary star system, from [40].

Cygnus X-3 is an example of an x-ray binary system. It emits radio waves, x-rays and γ-rays, see Fig.4.23.

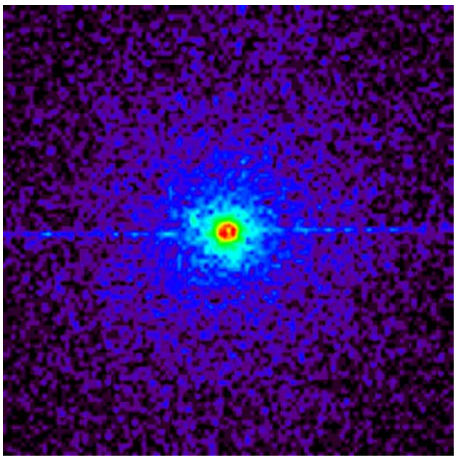

Figure 4.23: Cygnus X-3 binary system in x-ray, taken by the Chandra satellite, image courtesy of NASA [41].

Pulsars

A pulsar is a neutron star that spins very fast and emits radio signals in the form of pulses. The type of emission from these pulses is believed to be synchrotron emission (section 3.4.1). In a neutron star the electrons and protons are pressured together to form neutrons. It is therefore an extremely dense material that takes up a relatively small area. The spin axis of the pulsar is not aligned with its magnetic axis, thus producing pulses to the observer. Each spin produces a pulse and has a period of about 4 s to 1.6 ms. Pulsars can be observed at optical, x-ray as well as radio frequencies [18] [12]. Fig.4.24 shows the rotation- and magnetic axis of a pulsar.

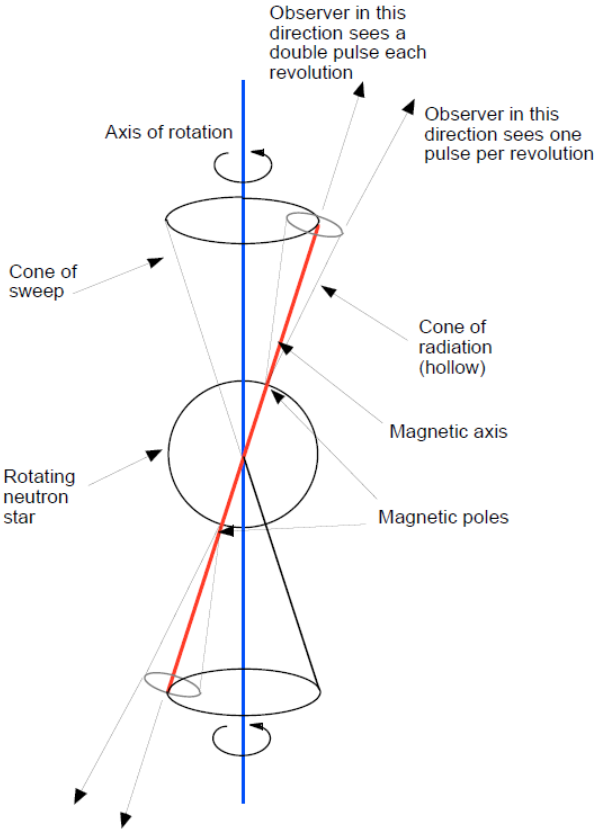

Figure 4.24: The rotation- and magnetic axis of a pulsar, from [12].

4.3.3 Galactic Nucleus

Taking a step back it should be noted that the first radio object ever observed was the centre of our galaxy when it was found by Karl Jansky in 1931. It is believed that our galactic nucleus is in the form of a black hole, because of the large amount of energy produced in a relatively small volume of space. Fig.4.25 shows the distribution of neutral hydrogen through 21cm observations, looking towards the centre of our galaxy.

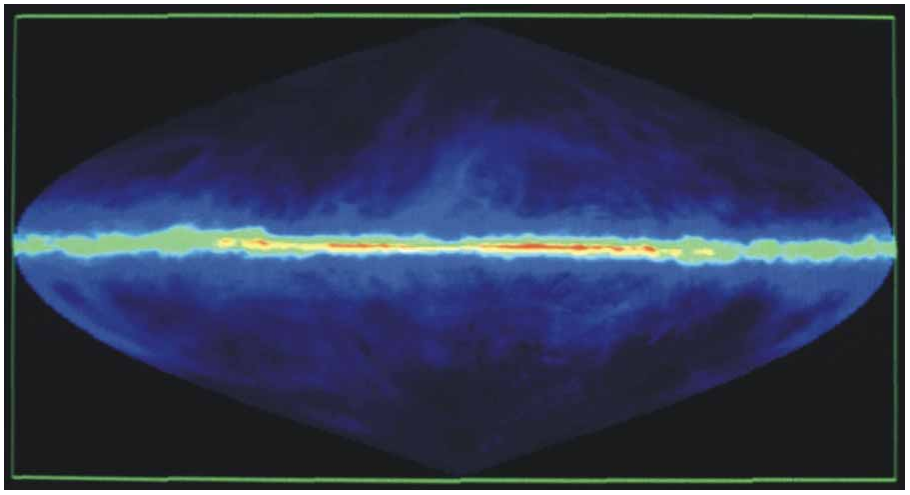

Figure 4.25: H I distribution of our galaxy, image courtesy of NRAO [42].

Black holes

When a massive star collapses, the gravity increases as the matter is compressed to extreme densities. There exists a single point of infinite density at the centre of the black hole, called the singularity. The strong gravity causes the surrounding space to curve, while further away it remains flat. The event horizon is the location in space where the escape velocity equals the speed of light. This means that nothing crossing this horizon can escape the gravitational pull of the black hole. The *Schwarzschild* radius is the distance from the singularity to the event horizon. Fig.4.26 shows the geometry of a black hole.

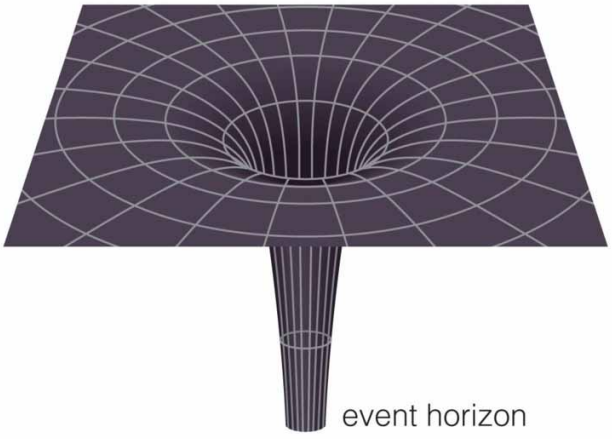

Figure 4.26: The geometry of a black hole, from [43].

The structure of a black hole is given by three properties: it's mass, electrical charge and angular momentum. Observing a black hole is not done directly, but indirectly by looking at the effect of its gravity on other matter. One way would be to look for a black hole that acts as a gravitational lens (see section 4.5). A good chance of finding a black hole is to look at binary systems that produce x-rays (see section 4.3.2) [22].

4.4 Galaxies beyond our own

Further away galaxies can be distinguished by the radio power they emit as either normal galaxies or active galaxies. It is believed that all galaxies contain a black hole at their centre.

4.4.1 Normal Galaxies

A galaxy like ours, the Milky Way, is a normal galaxy that is classified with a power output in the range of $10^{30} - 10^{32}$ W. The types of radiation mechanisms present include thermal, synchrotron and bremsstrahlung radiation [44]. The *Andromeda Galaxy (M31)* is the nearest external system similar in form to our own galaxy and has a power output of 10^{32} W. Fig.4.27 shows the galaxy, which is about 2 million light years away. Some of the more distinct stars in the image are stars from our own galaxy in the direction of Andromeda [11].

Figure 4.27: Optical image of the Andromeda Galaxy, image courtesy of NASA [45].

The *Magellanic clouds* (see Fig.4.28) are the nearest external systems outside of our galaxy and have a power output of 10^{30} W.

Figure 4.28: The Large Magellanic Cloud (left) and Small Magellanic Cloud (right), image courtesy of NASA [46] [47].

4.4.2 Active Galaxies

An active galaxy is named after its Active Galactic Nucleus (AGN) that shows above normal radiation over most of the EM spectrum. It is believed that the cause of the intense radiation is a black hole at the centre of the galaxy that accelerates the material to very high speeds to produce synchrotron radiation. The power output ranges from $10^{35} - 10^{38}$ W. Active galaxies can be classified into *radio galaxies*, *quasars*, *blasars* and *Seyfert galaxies* as discussed below.

When observing radio galaxies, the radiation occurs mainly at radio wavelengths due to synchrotron radiation. *Virgo A (M 87)* is an elliptical radio galaxy with a power output of 10^{35} W. This galaxy is famous for a blue jet that extends from the core in the form of ejected matter. It produces synchrotron radiation from electrons that spiral in the jet's magnetic field [11]. Fig.4.29 shows the jet of M87 at optical, radio and x-ray wavelengths, with the bright nucleus (bottom left).

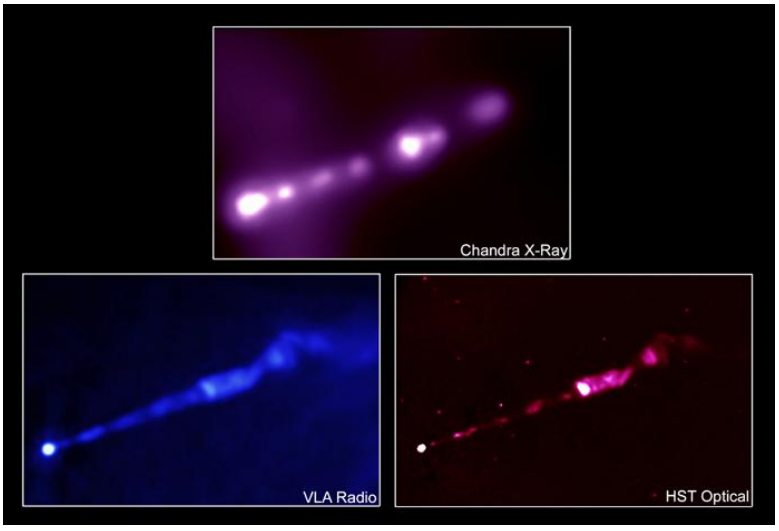

Figure 4.29: X-ray (top), radio (bottom left) and optical (bottom right) images of M87, from [48].

A 'quasi-stellar radio source' (*QSO* or *quasar*) is seen as a point source similar to a star, but is in fact a distant galaxy. They are the most powerful, energetic objects known in the universe that radiate across the spectrum, with bright gamma-rays. These galaxies are very far away, seen from their very high redshifts (see section 4.5) and many fluctuate in brightness. An example is quasar *3C273* shown in Fig.4.30 at gamma-rays.

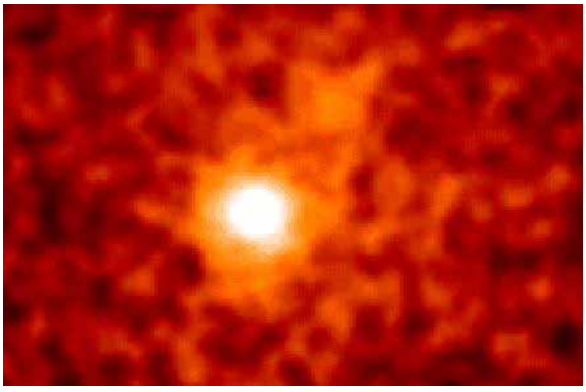

Figure 4.30: λ-ray image of Quasar 3C273, image courtesy of NASA [49].

A blazar is similar to a quasar, but is less luminous with a jet pointing towards us. One type of blazar is a BL Lac object which has radio and optical variability. Seyfert galaxies are like quasars, but with lower power outputs. They radiate strongly in the radio, IR, x-ray and γ-ray part of the spectrum. A possible explanation is that a Seyfert galaxy is a quasar seen from a different jet angle. They are classifies into two types:

- Type 1: with broad emission lines
- Type 2: with narrow emission lines and bright infrared emission

An example of a Seyfert galaxy is *Perseus A (NGC 1275)* (see Fig.4.31) which has a power output of 10^{35} W.

Figure 4.31: NGC 1275 galaxy in x-ray, radio and optical composite, image courtesy of NASA [50].

A double radio source is a radio galaxy with a central source (black hole) that ejects electrons in jets to produce synchrotron radiation. *Centaurus A (NGC 5128)* is a double radio source that has a power output of 10^{35} W. It emits at radio, x-ray and γ-ray wavelengths. Fig.4.32 shows Centaurus A for the x-ray, radio and optical part of the spectrum. The radio and x-ray images show jets produced from the centre of the galaxy, while the optical image shows stars, dust and gas. *Cygnus A* is a double radio source with a power output of more than 10^{38} W, the second strongest radio source in the sky (apart from the sun). Fig.4.33 shows the compact core, a black hole that speed electrons to nearly the speed of light through thin jets. The electrons get trapped in the magnetic field of the galaxy to form two radio lobes.

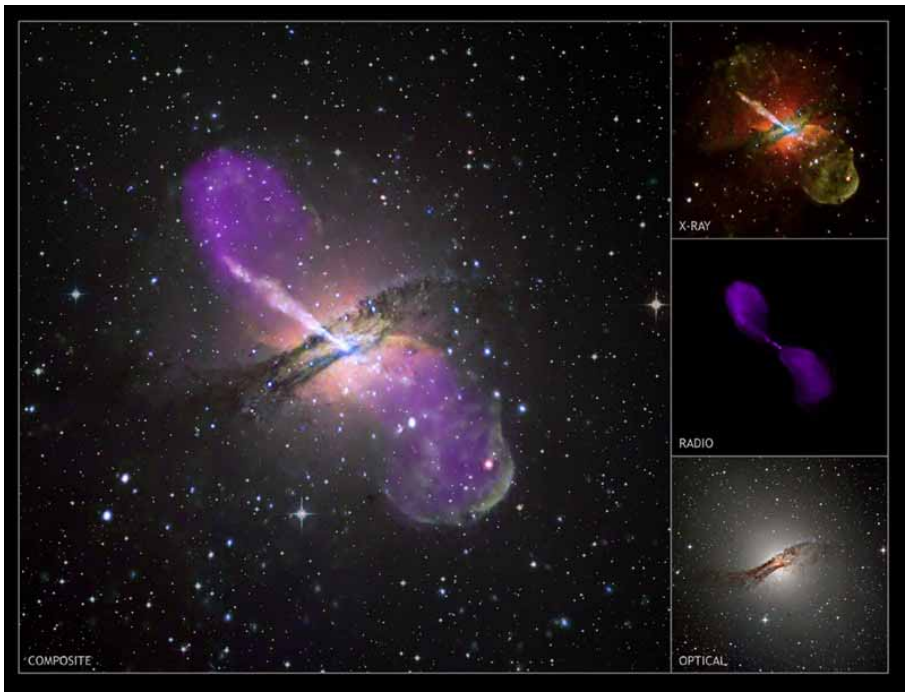

Figure 4.32: Centaurus A for the x-ray, radio and optical range together with a composite image, courtesy of NASA [51].

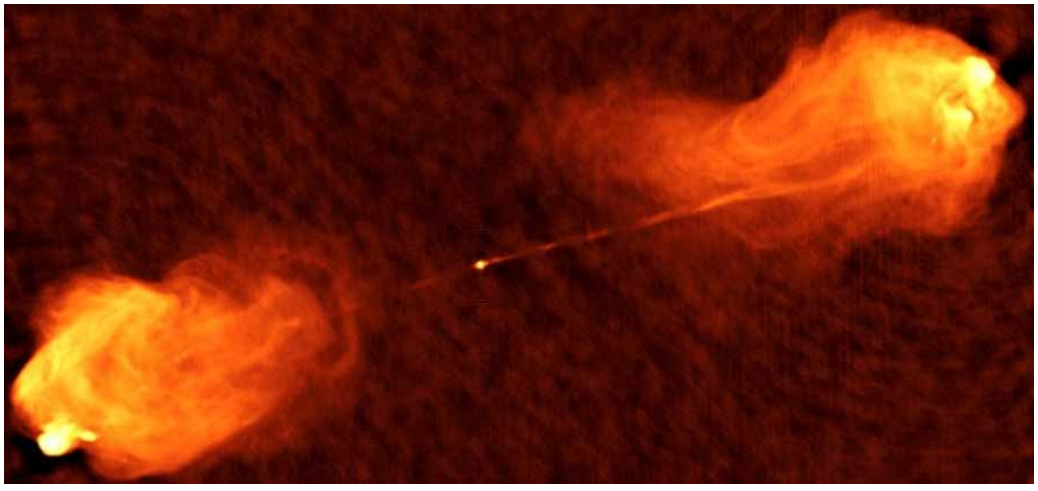

Figure 4.33: Radio image of Cygnus A, image courtesy of NRAO/AUI [52].

4.5 Radio Phenomena

Some concepts should be considered in understanding how objects in the universe behave and interact with one another. The phenomena described in this section include the doppler effect, gravitational lensing and waves, superluminal velocities, synchrotron self-absorption and inverse compton scattering.

Doppler Effect

The frequencies of EM waves are affected by relative motion between a source and an observer, called the *Doppler effect*. The observed spectrum of a source that is approaching will be *blueshifted* (moved to a higer frequency), while a receding source will be *redshifted* (lower frequency). The shift in wavelength is given by (4.5.1) [22].

$$\Delta\lambda = \lambda - \lambda_0 \tag{4.5.1}$$

with λ_0 the intrinsic wavelength

λ the observed shifted wavelength

The speed at which the source is moving parallel to the observer, called the radial velocity, can then be determined by using (4.5.2) (for $\upsilon << c$).

$$\upsilon = c\frac{\Delta\lambda}{\lambda_0} \tag{4.5.2}$$

Redshift is denoted by z, as given by (4.5.3) and (4.5.4) [11].
for $\upsilon << c$:

$$z = \frac{\Delta\lambda}{\lambda_0} = \frac{\upsilon}{c} \tag{4.5.3}$$

for relativistic speeds:

$$z = \frac{\Delta\lambda}{\lambda_0} = \frac{1+\upsilon/c}{\sqrt{1-(\upsilon/c)^2}} - 1 \tag{4.5.4}$$

Gravitational Lensing

A massive object can act as a gravitational lens, warping light from a distant source. Consider a galaxy (the lens) located between the observer and a quasar (the source), see Fig.4.34.

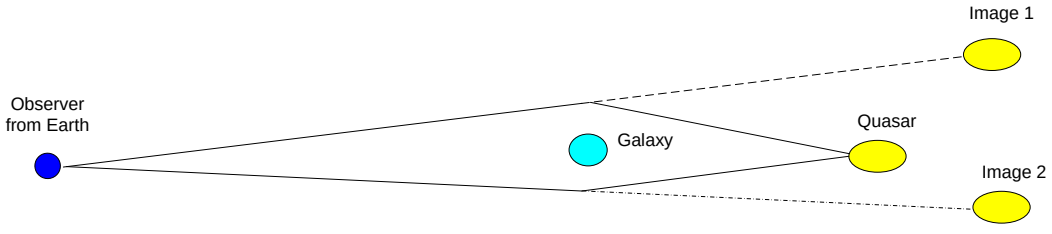

Figure 4.34: The effect of gravitational lensing, from [12].

The observer will see two or more images (sometimes brighter), caused by the bending of light when it moves through the space surrounding the galaxy [12].

Gravitational waves

A gravitational wave is caused by a mass that changes its gravitational field (by moving) and therefore curves space and time. These waves result in gravitational radiation, but are difficult to detect [22].

Superluminal Velocities

When material is ejected from a radio source at relativistic speeds, the apparent velocity to an observer may be more than the speed of light [12]. Fig.4.35 shows the apparent superluminal motion of quasar 3C279. Different radio images over time are compared. The jet on the right seemed to have moved 25 light years in the period of 7 years, thus faster than the speed of light.

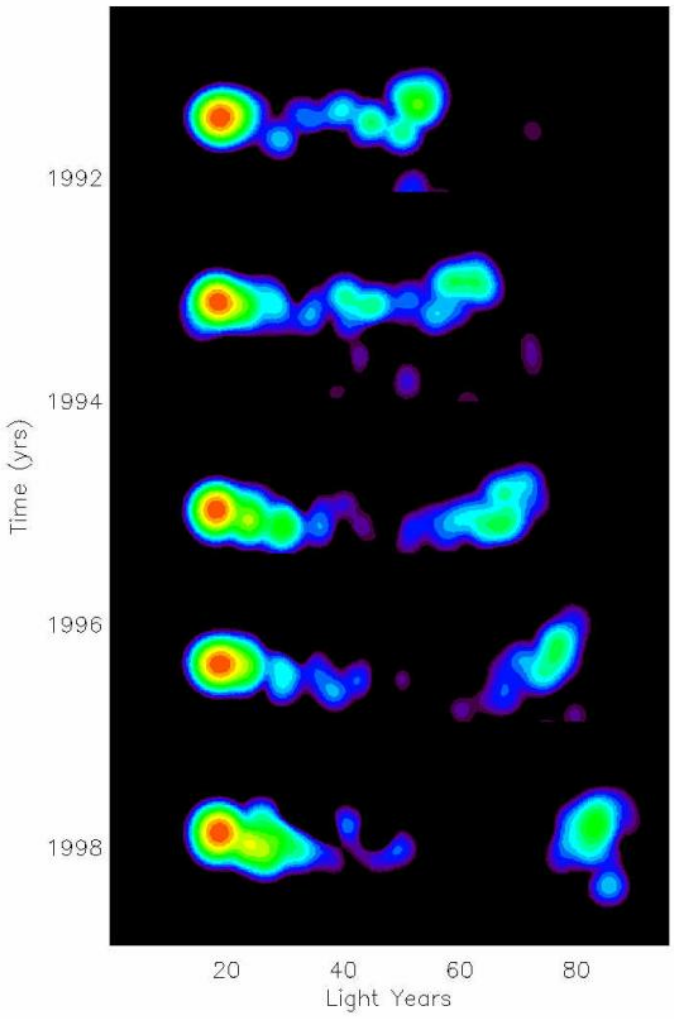

Figure 4.35: Radio images of quasar 3C279 shows apparent superluminal motion, image courtesy of NRAO/AUI [53].

Synchrotron Self-absorption

Non-thermal sources usually have spectra with $\alpha > 0.5$ (see section 3.4). Some QSOs like PKS 1934-63 have spectra with $\alpha < 0.5$ at high frequencies and α around -2 for lower frequencies, see Fig.4.36 [11].

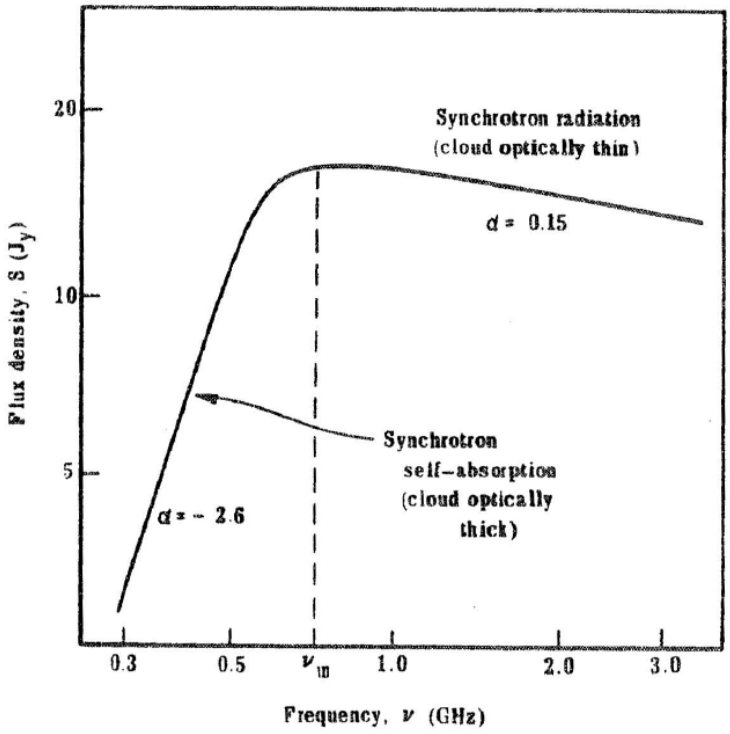

Figure 4.36: Flux density spectrum of PKS 1934-63, from [11].

The reason for this is that *synchrotron self-absorption* occurs at the lower frequencies. This is when the synchrotron radiation becomes very high so that the synchrotron electron re-absorbs the radiation.

Inverse Compton Scattering

This is when energy from a moving electron is given to a photon, so that the radio photon frequency is up-converted to optical, x-ray or γ-ray wavelengths, see Fig.4.37 [11].

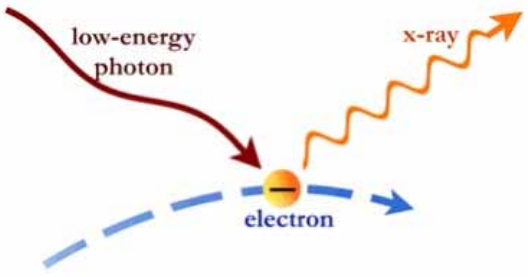

Figure 4.37: Inverse Compton scattering, from [54].

4.6 Conclusion

This chapter looked at various radio sources and emission from our galaxy and beyond. It described emission from our solar system and ventured further onto radio stars and the ISM. This included anything from spectral lines, molecular clouds and supernova remnants to pulsars, dark matter and black holes. It went on to describe normal and active galaxies and concluded with some radio phenomena.

Chapter 5

Radio Telescope Receiver System Design

5.1 Introduction

This chapter aims to describe the design of a basic radio telescope receiver system. It does so by investigating the system design for a number of radio telescopes and arrays, most of them being part of the Square Kilometre Array (SKA) project. It is therefore seemed fit to start this chapter with a section on the SKA background, giving an overview of SKA technologies, pathfinders and key science projects.

5.2 SKA Background

This section starts with an introduction of two important SKA pathfinders, namely the Karoo Array Telescope (KAT) and Australian Square Kilometre Array Pathfinder (ASKAP) projects. It then gives an overview of the technology being designed for and used in SKA pathfinders, including the antenna, feed, Low-Noise Amplifier (LNA), beamformer, correlator and pulsar back-end technologies. It ends with a listing of the SKA key science projects.

5.2.1 SKA Pathfinders

The *Karoo Array Telescope (KAT)* is a South African project that demonstrates the use of wide-band single pixel feeds on reflector antennas. The project is realised through a number of phases. The first phase of the KAT project was the *eXperimental Development Model (XDM)*, a 15m diameter parabolic reflector installed at the *Hartebeesthoek Radio Astronomy Observatory (HartRAO)*, fitted with a 7 horn cluster feed. This was the prototype for the KAT-7 array.

Figure 5.1: The KAT-7 radio telescope, from [55].

The *KAT-7* is an array of 7 reflector antennas (each 12m diameter) fitted with a single horn at prime focus, as shown in Fig.5.1. It demonstrates the working of an interferometer and is the predecessor of the MeerKAT. The *MeerKAT* is the final phase of the KAT project with one design option being an array of 80 prime focus parabolic reflector dishes, each 12m in diameter fitted with Wide-Band Single Pixel Feeds (WBSPFs). A recent design considered is to use 64 offset Gregorian dishes, each 13.5m in diameter that includes multiple receiver systems.

Australian SKA Pathfinder (ASKAP) is an Australian project that demonstrates the use of Phased Array Feeds (PAFs) and their multiple beam formation capability. It is located in the Midwest region of Western Australia at the Murchison Radio Observatory [56]. The *Parkes Testbed Facility* is a 12m antenna that was installed at *Parkes Observatory* as prototype for ASKAP, demonstrating the use of PAFs. When ASKAP is finished it will be an array of 36 parabolic reflectors (each 12m diameter) fitted with PAFs, as shown in Fig.5.2. These two countries, South-Africa and Australia, are currently competing to host the SKA. The final decision is estimated to be made by 2012.

Figure 5.2: Illustration of ASKAP radio telescopes, from [57].

5.2.2 SKA Technologies

To cover the frequency range specified for the SKA, more than one antenna concept will be required. Two types of antennas were chosen by the *Square Kilometre Array Design Studies (SKADS)* to be used for the SKA, namely Aperture Arrays (AAs) and Parabolic Reflector Dishes.

At the lowest SKA frequencies (<1 GHz) large collecting areas are needed to compensate for the sky noise. The most practical technology for this is AAs. As the number of elements of these arrays and therefore also the cost increases as $(frequency)^2$, they are not feasible to be used for higher frequencies [1]. AAs can be divided into dense and sparsely spaced tiles. The separations of the elements found to be most optimal are given by (5.2.1). This is normally chosen keeping in mind factors such as minimising the number of elements and reducing grating lobes for a required scan [58].

$$d = \frac{\lambda}{1+\sin\theta} \tag{5.2.1}$$

With d the element separation

λ the wavelength at the operating frequency

θ the maximum scan angle

The dense array element spacing is $d \leq \lambda/2$ and is optimal for the frequency range of 300–700 MHz. The frequency range is chosen by taking into consideration the element performance for the array layout, the signal transportation, digitisation and processing. The type of antennas used will be Vivaldi antennas. Examples of SKA pathfinders that demonstrate this technology are *EMBRACE (Electronic Multi Beam Radio Astronomy Concept)* and *THEA (Thousand Element Array)*, see Fig.5.3.

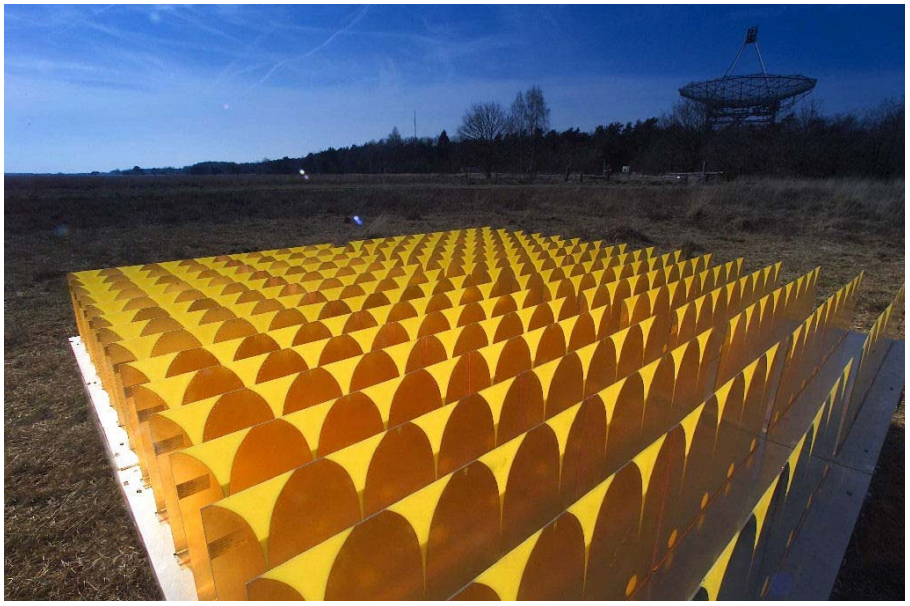

Figure 5.3: Dense Aperture Array tiles developed for THEA, from [59].

The sparse array element spacing is $d > \lambda/2$ and is optimal for the frequency range of 70–300 MHz. For these arrays dipole antennas are used. SKA pathfinders include *LOFAR (Low Frequency Array)*, *LWA (Long Wavelength Array)* and *MWA (Murchison Widefield Array)*. Fig.5.4 shows the sparse array at Low Frequency Array (LOFAR) [60].
The reflectors antennas are more suited for the higher frequency range (>1GHz). The type of dish technology that will most likely be used in the SKA is the prime focus parabolic reflector. The KAT and ASKAP projects (see section 5.2.1) both use these reflectors as demonstrators for the SKA. The Offset Gregorian dish is also considered as a possible reflector design for the SKA, see Fig.5.5. Multiple receivers can be used as the feed structure is stronger than for the focus fed dish design. The Allen Telescope Array (ATA) is a demonstrator of this type of dish [61] [62].

The two types of receptor technologies being developed, most likely to be used for the SKA are the *Wide-Band Single Pixel Feed (WBSPF)* and *Phased Array Feed (PAF)*. The WBSPFs will typically be used in the frequency range 2–10 GHz or even higher. The advantages of these feeds are that they can provide high sensitivity. The KAT project is a demonstrator of this feed technology. The PAFs will typically be used in the frequency range 0.5–2 GHz, while the optimal frequency is in the range 0.7–2 GHz. The advantages of these feeds are their large Field of View (FoV) and beamforming capability. The ASKAP project is a demonstrator

Figure 5.4: Sparse Aperture array developed at LOFAR, from [59].

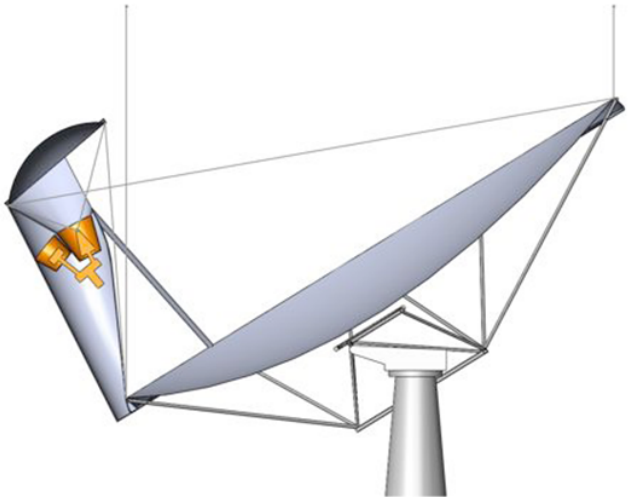

Figure 5.5: An offset Gregorian dish design, from [55].

of this feed technology. Fig.5.6 shows the different receptor technologies as part of a central SKA core.

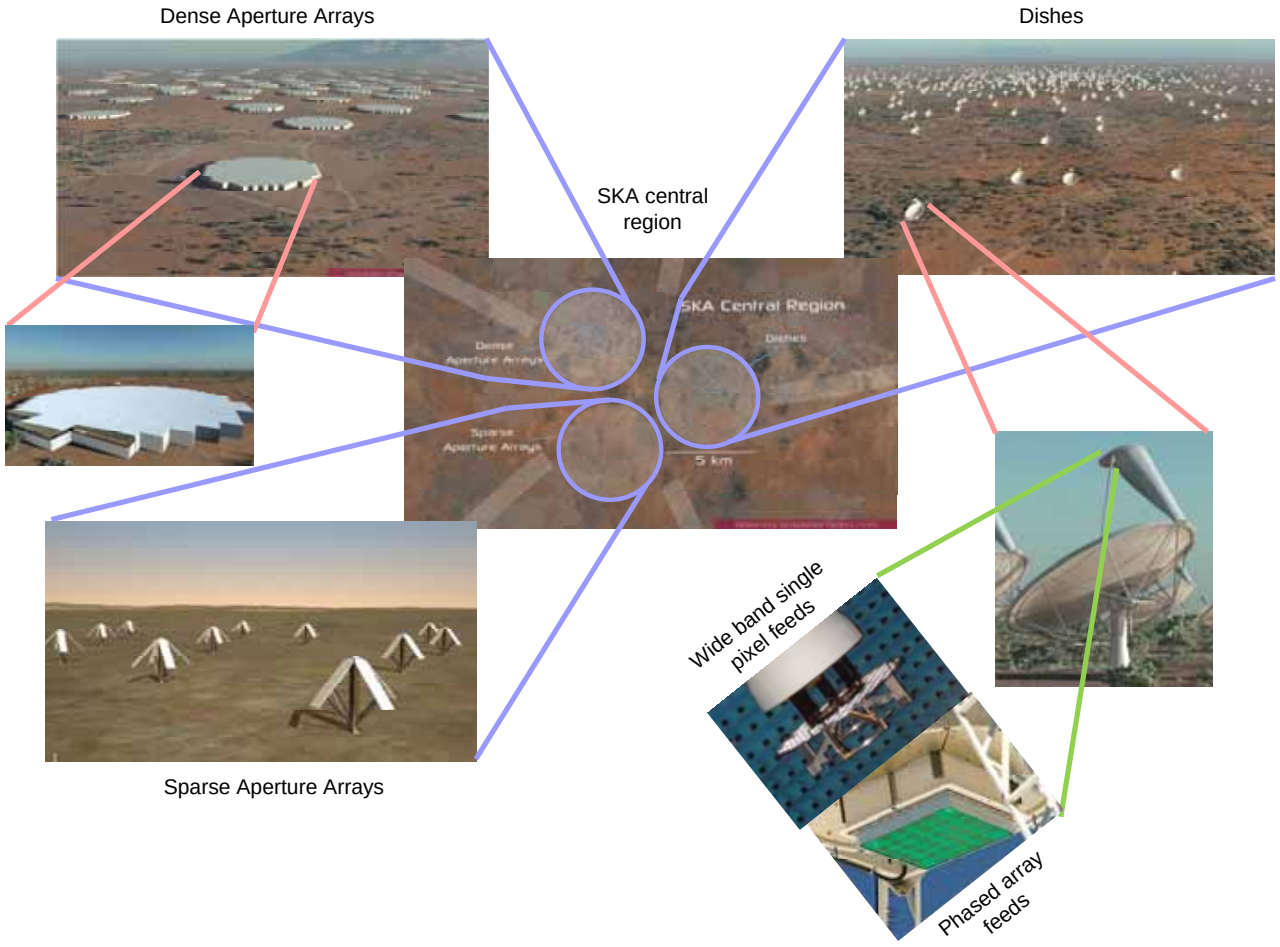

Figure 5.6: Different SKA antenna and receiver technologies, from [55].

A type of LNA, the RF-CMOS[1] 'receiver on a chip' is being developed for ASKAP. The receiver includes the LNA, filters and mixer all on one integrated circuit. It has an input frequency range of 500–1700 MHz and Intermediate Frequency (IF) Bandwidth (BW) = 500MHz [6]. *HEMT (high electron mobility transistor)* LNAs were developed at Jodrell Bank for the Parkes 21cm Multibeam Receiver [4].

Beamformers are used to form multiple beams from antenna elements (also see Appendix A.2). Most beamformers are implemented as either digital or analog, while some arrays like EMBRACE use both techniques, see Table 5.1 [64].

Table 5.1: Types of beamformers used in various radio telescope arrays, from [65].

Telescope array	**Type of beamformer**
ASKAP, LOFAR, LWA	Digital beamformer
MWA	Analog beamformer
EMBRACE	Both digital and analog beamformer

[1] '..it is anticipated that CMOS could be the technology of choice for building large numbers of high performance, inexpensive receivers covering the frequency range of 1 to 10 GHz.' [63]

Two types of correlator architectures are often used and mentioned here, they are the *FX* and *XF correlators*. Their design difference is the order in which the tasks are to be performed, namely the Fourier Transform (FT) and multiplication operations (see AppendixA.1.1). Both FX and XF correlators were build in the past using *ASICs (Application Specific Integrated Circuits)*. Nowadays they are being built using *FPGA (Field Programmable Gate Array)* hardware, see Table 5.2. These FPGAs are reconfigurable and therefore more flexible than ASICs. The traditional correlator has an XF architecture like those used by eVLA and ALMA. When dealing with larger antenna arrays, with a higher computational load like the SKA, the FX architecture is more efficient. The *SKA array molonglo prototype (SKAMP)* correlator is an SKA demonstrator of FX correlator technology [66] [65] [67].

Table 5.2: The type of correlator used in various radio telescope arrays, from [65].

Telescope array	**Correlator hardware**
KAT	FPGA hardware developed by CASPER
ATA, ASKAP, SKAMP, MWA, CABB	building own hardware (FPGA)
eVLA, ALMA	both FPGAs and ASICs
LOFAR	high performance computer, *BlueGene*

Another example of an FX correlator architecture is the *Reconfigurable Open Architecture Computing Hardware (ROACH)* that is being developed by *CASPER (Centre for Astronomy Signal Processing and Electronics Research)*. It is platform independent, open source hardware so that it can be used for a variety of applications. It has an FPGA processor and a 10 Gigabit Ethernet interface [68]. This correlator technology will be used in the KAT-7 project. The initial correlator design, already implemented for the first two antennas of the KAT-7 array, is called *Fringe-Finder*. It is a pocket-correlator, a single ROACH board with four inputs (see Fig.5.7).

Figure 5.7: The ROACH board designed by CASPER for the KAT-7, from [69].

The full KAT-7 array correlator design will also be based on these ROACH boards, extending it to allow for 8 dual polarisation inputs. Fig.5.8 shows the digital back-end architecture for the KAT-7 using multiple ROACH boards.

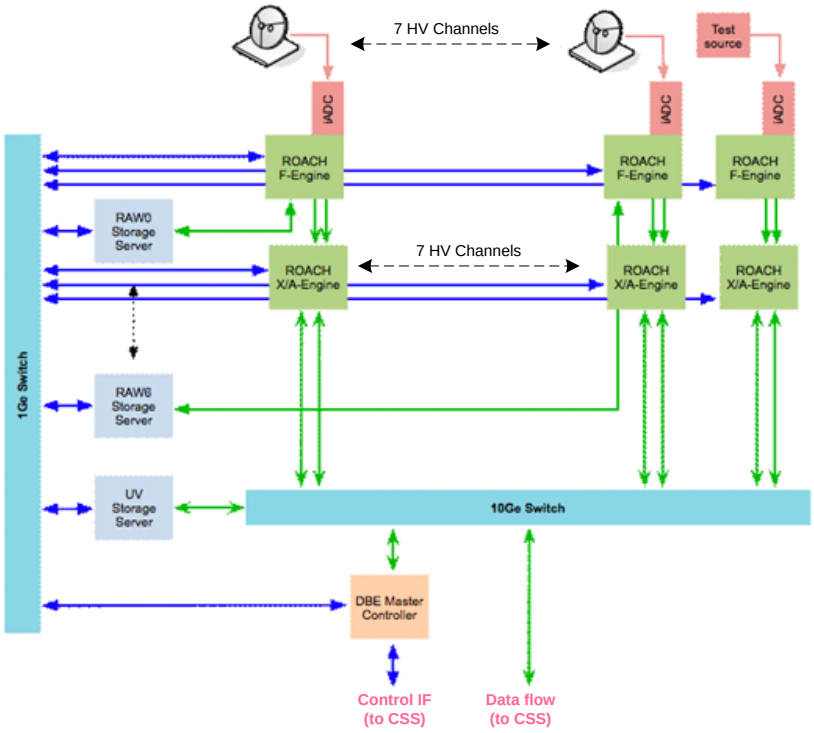

Figure 5.8: The DBE architecture for the KAT-7, from [70].

The pulsar back-end's purpose is to detect and process pulsar signals. It can be implemented by either hardware or software techniques. Processing can include coherent or incoherent de-dispersion and folding. The Experimental Development Model (XDM) telescope uses SIGPROC as part of the pulsar back-end, which is pulsar signal processing software that performs de-dispersion, folding and glitch detection. Other pulsar processing software includes DSPSR and GPU. Specially designed hardware used on existing radio telescopes includes the Pulsar Spigot, GUPPI, WAPP, COBRA and PuMa-II for pulsar search and timing observations.

5.2.3 SKA Key Science Projects

The astronomy community has defined five key science areas as driver for the specifications of the SKA. Each Key Science Projects (KSPs) is specific in that it (i) addresses unanswered questions in fundamental physics or astrophysics, (ii) is science that is unique to the SKA or for which the SKA plays a key role, and (iii) can excite the broader community. The Five KSPs are given here to form an overall picture of the science goals the SKA is aspiring to.

I) The Cradle of Life

This science case will study terrestrial planet formation by imaging proto-planetary disks and looking at

their molecular chemistry. Another aspect will be to search for intelligent life, which includes looking for leakage radiation [71].

II) Strong-Field Tests of Gravity using Pulsars and Black Holes
This science case aims to do surveys during which thousands of pulsars will be detected and then to time these pulsars with high precision. Another goal is to test relativistic gravity with pulsar-black hole binaries. The millisecond pulsars discovered will allow the use of pulsar clock arrays to detect gravitational waves [8].

III) The Origin and Evolution of Cosmic Magnetism
It is of interest to measure and map the origin and evolution of magnetic fields found in our universe. This can be done through studies of Faraday rotation, polarised synchrotron emission and the Zeeman effect [72].

IV) Galaxy Evolution, Cosmology and Dark Matter
With this science case, studies of the cosmic evolution of HI (neutral hydrogen) can be made. Measurements of galaxy power spectrums can be done in detail, allowing the study of dark energy and dark matter [73].

V) Probing the Dark Ages
This science case aims to study the epoch of reionisation (EoR), which was when the first luminous objects were formed in the universe that ionised the neutral intergalactic medium (IGM). The SKA will be able to image the neutral IGM by 21cm emission and study HI 21cm absorption. It will also be able to the study molecular gas, dust and star formation in the first galaxies and detect radio continuum emission from the first massive black holes [74].

Key science project II), concerning pulsar observations, will become the focus of this chapter as we proceed and will therefore also be discussed in detail in a later section.

5.3 Receiver System Designs for SKA Pathfinders

In this section various receiver systems designed[2] and implemented as SKA pathfinders will be discussed. The designs include an example of a dense AA as well as parabolic reflector antennas, while different types of feed systems are also demonstrated. It starts with single antenna system designs followed by antenna array system designs. Throughout the discussion an emphasis will be on pulsar observations, as this will form the focus of the next chapter.

5.3.1 Single dish system design

From all the examples discussed here, the single dish receiver has the most basic design on a system level. It can then be further extended by the feed design. This is demonstrated by first discussing the XDM dish with a single horn feed, followed by the Parkes telescope with a multiple horn feed.

5.3.1.1 XDM

As mentioned in section 5.2.1, the XDM was designed as a prototype for the KAT-7 project and demonstrates the use of *wide-band single pixel feeds*. The system parameters are given by Table 5.3 below and Fig.5.9 shows the block diagram of the XDM receiver system followed by a signal path description [75].

Table 5.3: XDM telescope system design and operating parameters.

System Parameters	**Reference design**
Dish diameter (D_{dish})	15m
F/D	0.5
Feed	WBSPF
Aperture efficiency (e_{ap})	65% (at 1.4GHz)
Frequency range	1.414–1.67 GHz
System noise Temperature (T_{sys})	∼70 K
Polarisation	dual linear
Number of channels	1024
Channel bandwidth	167kHz
Total instantaneous bandwidth	172MHz
Dynamic Range	8 bits
Sampling rate	680MHz
Integration time	∼0.5 msec
DBE output rate	∼2000 samples/sec

[2]Reference to the 'receiver system design' as used here refers to the design of the whole antenna system which includes the Radio Frequency (RF) frond end, digital back-end as well as further processing

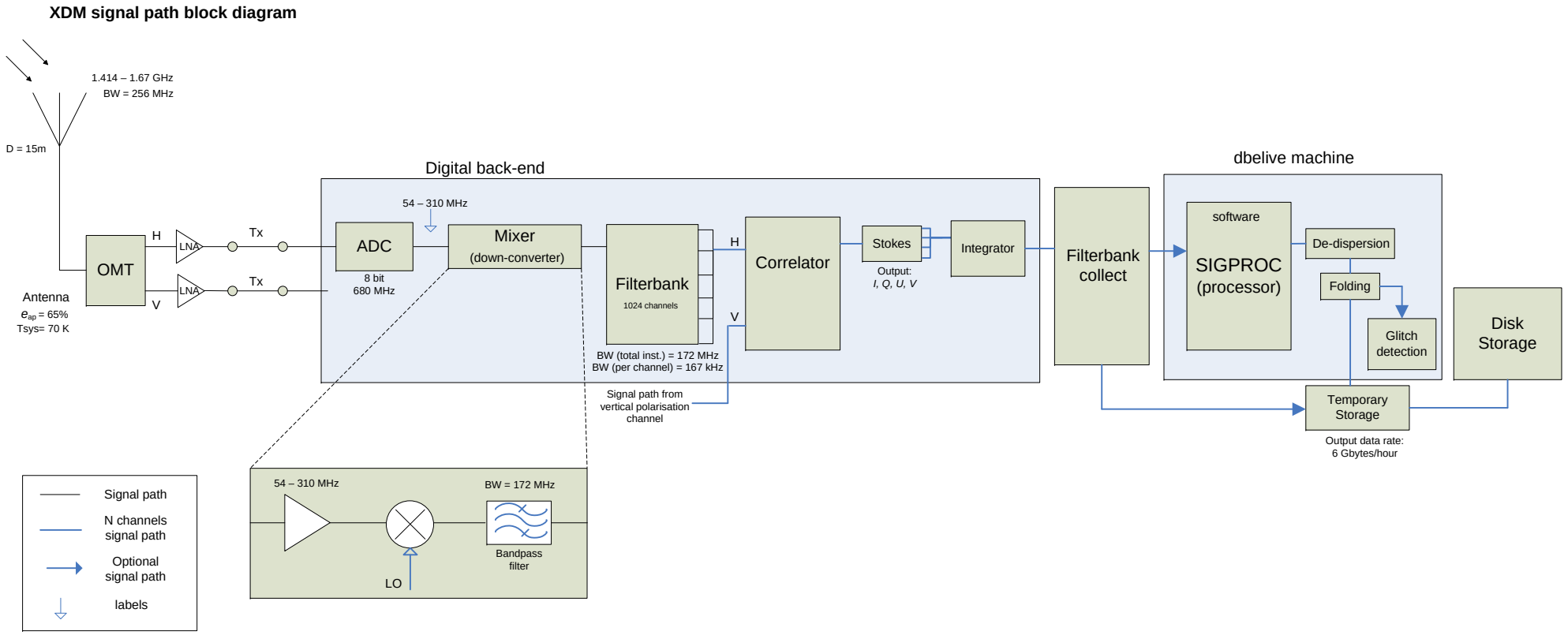

Figure 5.9: XDM signal path block diagram.

The signal path of the system passes through the RF-front end, digital back-end (DBE), filterbank collect (FBcollect) and signal processing software (SIGPROC) components.
The RF-front end starts right where the antenna receives the signal through the 15m dish and horn feed. The Orthogonal Mode Transducer (OMT) then splits the signal into the horizontal (H) and vertical (V) polarisation components as two separate channels. Each channel signal first goes through the RF receiver electronics, which includes the LNA to amplify the signal (down-conversion is done digitally at a later stage). It is then sent via fibre-optic transmission to the DBE control room.

Here the Analog-to-Digital Converter (ADC) samples the signal with 8 bits at 680MHz. The next component is the mixer that down-converts and filters the signal to a total instantaneous bandwidth of 172MHz. The signal is now ready to be received as input by the filterbank that splits the signal into 1024 channels with 167kHz per channel. This is repeated for both the horizontal and vertical channels. Next, the two channels are combined in the correlator[3] to calculate the Stokes parameters (see Appendix A.1) and the output is averaged.

The averaging time (τ_s) is about 0.5msec. This is given by (5.3.1) where N is chosen to produce the desired output rate (f_{out}) here $\sim$2000 samples/sec. The averaging time is sufficient to sample the Vela pulsar, which is $\sim$180 samples over the pulse period, as the XDM is now mainly used for observations of the Vela pulsar.

$$\tau_s = \frac{1}{f_{out}} = \frac{1024}{680 \times 10^6 \times N} \tag{5.3.1}$$

The FBcollect does basic processing like data conversion and reduction, and produces filterbank files that are sent to temporary storage. SIGPROC receives these filterbank files from FBcollect and performs more signal processing like de-dispersion, folding and glitch detection. These files are also sent to temporary storage. This processing is done 'live' and therefore reduces the data rate. The storage manager assures that data from temporary storage are moved to the external hard disk from time to time. The filterbank collect and SIGPROC can be referred to as the pulsar back-end, as it is specifically designed to include pulsar observations [75].

5.3.1.2 Parkes 21cm Multibeam Receiver

The Parkes 64m single dish telescope is located at NSW, Australia. This 21cm multibeam receiver was originally designed to detect neutral hydrogen emission but is now also known for its excellent observations of pulsar searching and timing. As such this hybrid receiver system was found useful to include in this discussion. The Parkes signal path block diagram is given by Fig.5.10, a description now follows.

[3]Note that although the filterbank usually forms part of the correlator, it is here separated into two components to describe their functionality. The correlator therefore (as in Fig.5.9) represents the multiplication/correlation, while the filterbank represents the FT/channelisation.

Parkes 21cm multibeam receiver signal path block diagram

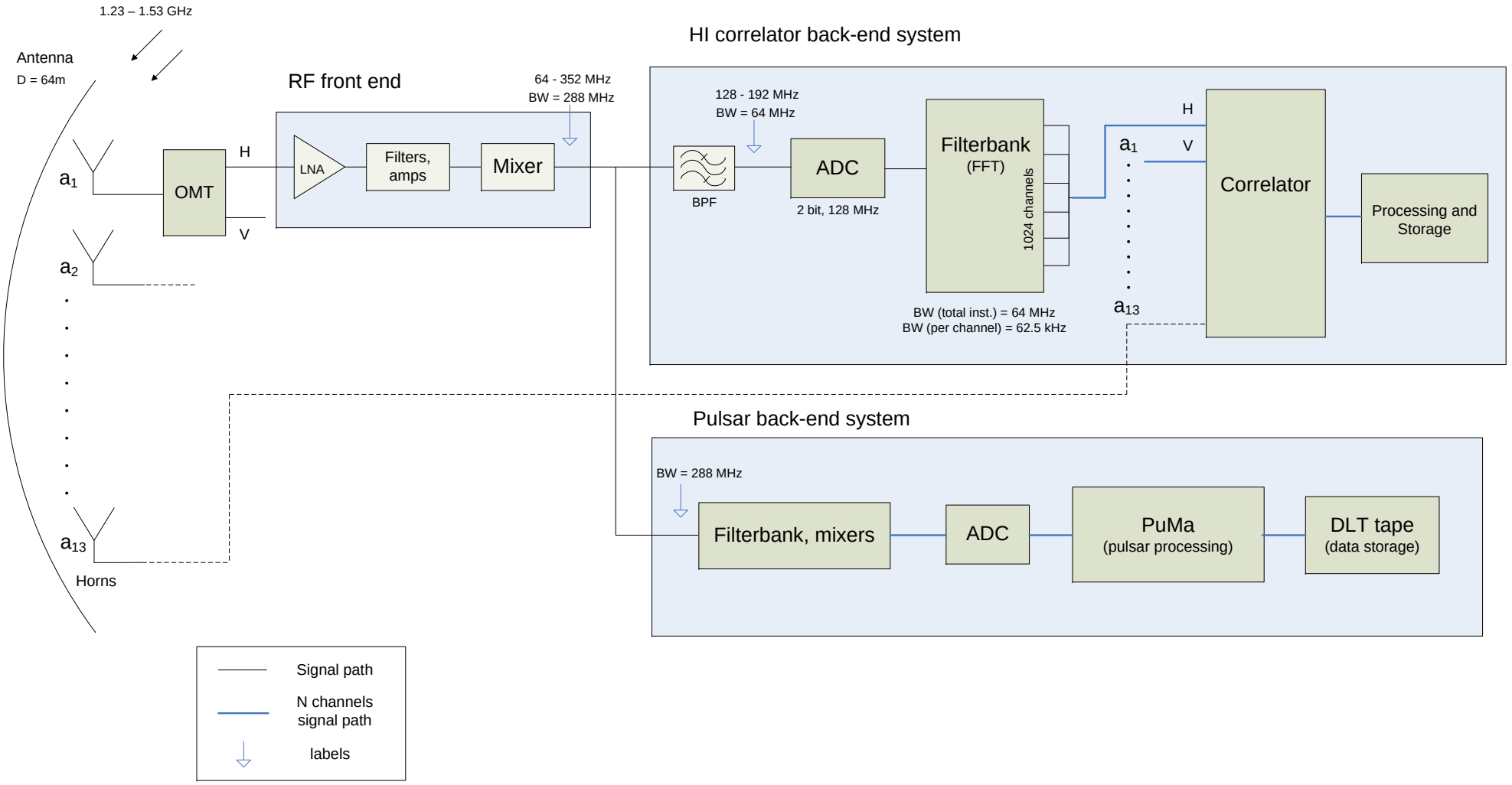

Figure 5.10: Parkes 21cm receiver signal path block diagram.

The feed consists of 13 circular horns at prime focus distributed in a hexagonal pattern. Each horn diameter is $\sim \lambda$ with horn spacings of 1.2λ. The feed can be rotated to map areas of the sky, see Fig.5.11.

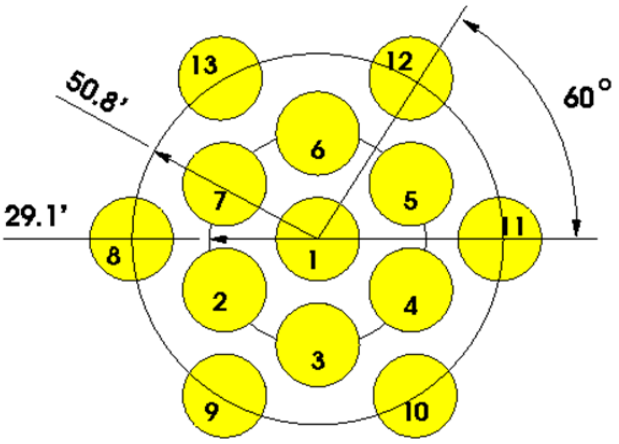

Figure 5.11: The 13-horn feed layout with rotation angle, from [76].

The Parkes multibeam receiver specifications are given by Table 5.4 below [76].

Table 5.4: System parameters for the Parkes 21cm multibeam receiver.

Parameter	**Beam 1**	**Beams 2 - 7**	**Beams 8 - 13**
Frequency range	1.23–1.53 GHz	1.22–1.52 GHz	1.22–1.52 GHz
Polarisation	Duel linear	Duel linear	Duel linear
Average System Temperature	21 K	21 K	21 K
FWHP angular resolution	14.0 arcmin	14.1 arcmin	14.5 arcmin
Frequency Range	1230–1530 MHz		
Dish diameter (D_{dish})	64m		
Feed	Circular horn array		
Spectral line correlator BW	64 MHz		
Number of beams	13		
Number of channels	1024		
Dynamic Range	2 bit		
Sampling rate	128 MHz		
Channel bandwidth	62.5 kHz		

The signals are dual polarised, thus producing 26 channels in total. The front-end includes the OMTs and HEMT LNAs that are cryogenically-cooled. At the output of the OMT, a calibration signal can be added. The receiver performance given by [4] is summarised in Table 5.5.

Each channel is further amplified and filtered, sent to the control room via coaxial cables and filtered again. The signal is then mixed down to an IF of 64–352 MHz. It is here that the system incorporates a multi back-end: the signal path is divided into both a correlator and pulsar back-end.

Table 5.5: The Parkes 21cm multibeam receiver performance.

Overall front end RF gain	60dB (40 dB cryogenic, 20 dB ambient)
Receiver noise temperature	6 K
HEMT amplifier operating temperature	16 K
Overall system noise temperature	24 K (average of 26 receivers)

The correlator back-end is used to detect the 21cm line of neutral Hydgrogen (HI) and therefore a smaller signal bandwidth at this frequency is needed. Bandpass Filters (BPFs) are implemented to separate a 64MHz signal band from 128 - 192 MHz. The signal is then sampled with 2 bits at 128MHz by the digitiser and sent to the correlator. The correlator accepts 2 bit data streams with rates up to 140MHz and produces either cross-correlation or autocorrelation data. Also performed is the FT, so that each signal is divided into 1024 channels, with a bandwidth of 62.5 kHz. As a measure, the velocity of neutral hydrogen can now be observed up to a resolution of 13km/sec.

The pulsar back-end first consists of a filterbank system, as illustrated by Fig.5.12 [77]. From the 1230–1518 MHz (or 288MHz band) input, each of the 26 channels is split into three bands. The signals are further mixed using Local Oscillators (LOs) that results in a frequency band in the range 64–160 MHz. This forms the input of the filterbank, dividing the signal into 96 channels, each with a BW = 3MHz for both polarisations, from all 13 beams. After the signal is digtised, processing is done by *PuMa*, a digital pulsar machine. The data can then be stored on a *DLT (digital linear tape)* tape for later off-line processing. In terms of pulsar science, the telescope can perform observations including large area surveys, timing of regular pulsars and high precision timing of millisecond pulsars [78].

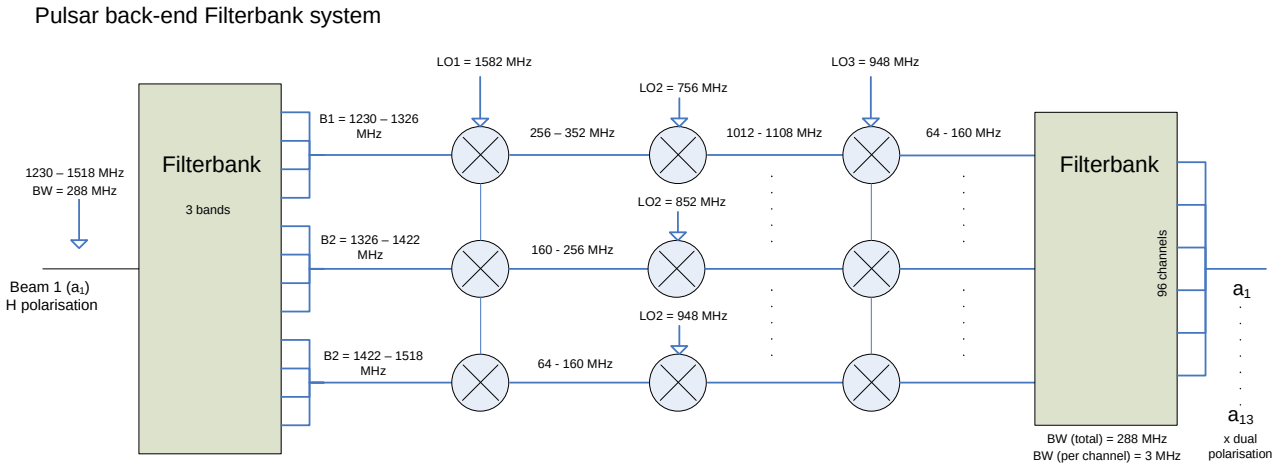

Figure 5.12: The Parkes 21cm pulsar back-end filterbank system.

In conclusion it can be mentioned that the horn array is more flexible than a single horn feed with its multiple beamforming capability. When comparing a different type of feed technology, PAFs (in the next section) with horn clusters however it is found that this type of feed has more advantages, like providing a more complete sampling of the sky [79].

5.3.2 Array system design

In this section, different array system designs will be discussed. We will look at the KAT-7, MeerKAT, ASKAP and Electronic Multi-Beam Radio Astronomy Concept (EMBRACE) projects that each contributes to the development of the technology required for the SKA and evaluate their array configurations.

5.3.2.1 KAT-7

The KAT-7 (see section 5.2.1) is the predecessor of the MeerKAT and is designed to demonstrate the working of an interferometer using WBSPF reflector antennas. The KAT-7 project is still in progress, with all 7 antennas only recently installed. Two of these antennas demonstrated the working of *fringe-finder*, which is a correlator hardware design also mentioned in section 5.2.2. The KAT-7 specification and operation parameters are given by Table 5.6 below [80] [81].

Table 5.6: System design parameters for the initial and final KAT-7 design.

System Parameters	**Reference design**
Number of antennas	7
Dish diameter (D_{dish})	12m
F/D	0.38
Feed	WBSPF
Aperture efficiency (e_{ap})	62.6%
Frequency range	1.2–1.95GHz
System noise Temperature (T_{sys})	25K+spillover (50–70K cryogenic)
Polarisation	dual linear
Minimum baseline	20m
Maximum baseline	200m
Number of channels	512 (final: 4096)
Channel bandwidth	1MHz
Total instantaneous bandwidth	256MHz (final: 500MHz)
Maximum processed bandwidth	256MHz
Dynamic Range	8 bits
Sampling rate	800MHz

Fig.5.13 shows the block diagram of the KAT-7 receiver system, followed by a description of the signal path flow.

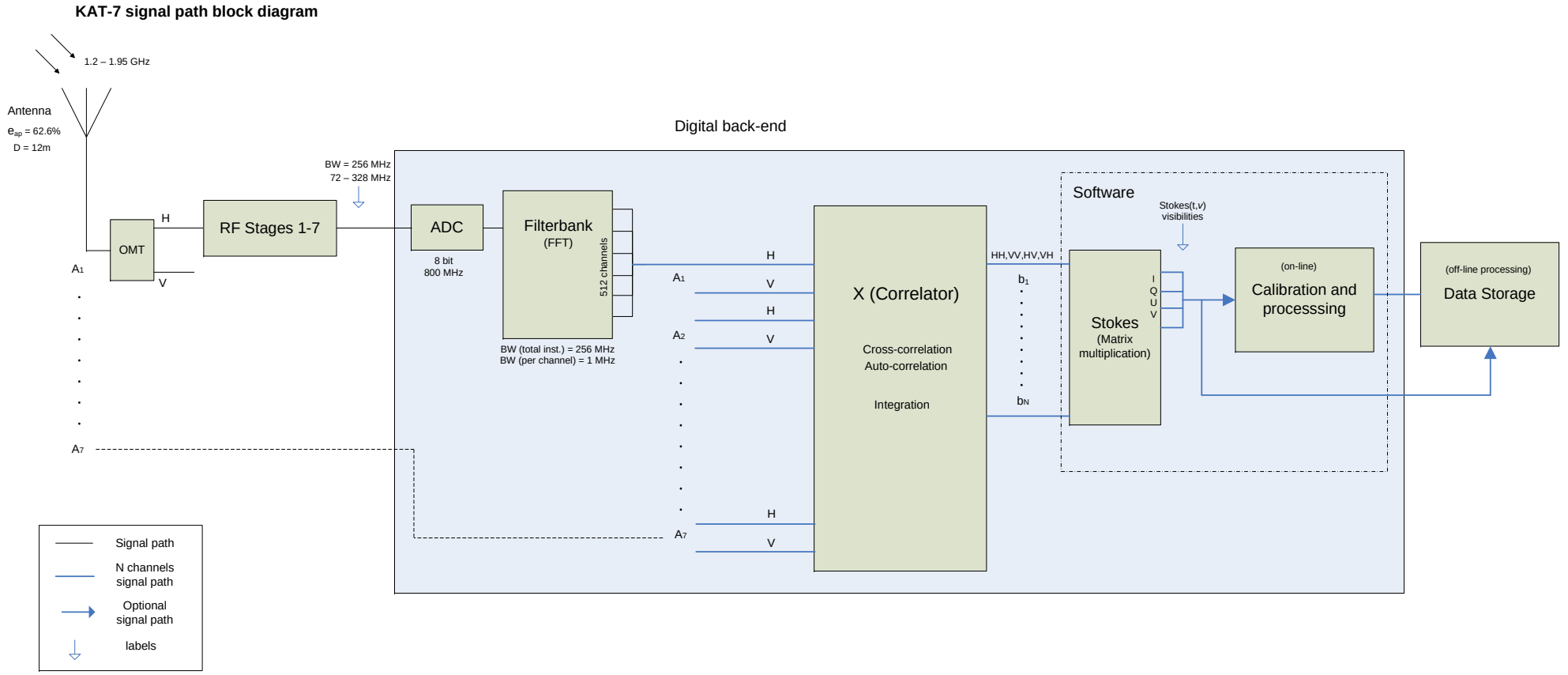

Figure 5.13: KAT-7 signal path block diagram.

The KAT-7 system design block diagram can be divided into the RF-front end and Digital back-end. Starting with the RF-front end, the signal is received through an antenna array of 7 parabolic reflectors each 12m in diameter fitted with single-pixel feeds at prime focus. The OMT divides the signal into two separate channels for the horizontal (H) and vertical (V) polarised signal components. Each signal goes through seven RF stages (a description will follow) where the signal is amplified, calibrated, down-converted and carried from the pedestal to the container.

The digital back-end contains an ADC which samples the signal with 8 bits at 800MHz. The next component used is an FX correlator (see Appendix A.1.1). For the first phase of the KAT-7, this correlator was designed using a ROACH board (see section 5.2.2). The 256MHz bandwidth signal is split up into 1MHz channels by the filterbank, which in total can produce 512 channels. The dual polarisation channels for all 7 antennas are combined as input into the correlator to perform correlation and integration. The Stokes parameters are then calculated from the output data, using software. The resulting visibilities are further calibrated and processed either on-line (to reduce data rates) or off-line (where it is stored to process at a later stage).

To describe the RF Stages 1-7 in more detail, Fig.5.14 is included as illustration, with each stage's function laid out as follows [82]:

stage 1: An LNA is necessary to amplify the weak signal while maintaining low noise.

stage 1.5: A calibration source is included here to calibrate the signal.

stage 3: A BPF is used, set to the same frequency range of the incoming signal, to filter out any unwanted signals. Stages 1-3 are located at the back of the antenna focus where it is also cryogenically cooled to keep the temperature low.

stage 4: Co-axial cables transmit the signal from the focus of the antenna to the pedestal.

stage 5: This stage is located at the antenna pedestal and contains attenuators, amplifiers and a BPF.

stage 6: Optical fiber transmission lines (about 4km) connects the pedestal to the *antenna services container (ASC)*.

stage 7: The down-converter is located in the ASC. In this stage, a BPF is first included to remove any unwanted signals picked up from the transmission cable, with the input frequency still being 1.2–1.95 GHz. Then a LPF is used to perform image rejection, so that higher harmonics of the input frequency do not interfere with the pass band at a later stage. After the filtering, a mixer with a variable local oscillator (VLO) is used to perform 'high side injection' to first up-covert the signal and then a LPF is used to remove any LO leakage. Another BPF is included to produce a signal of 4.128–4.384 GHz. Next, a fixed local oscillator (FLO) at 4GHz is used to down-covert the signal to 128–384 MHz. Finally a BPF is used for anti-aliasing before sent to ADC.

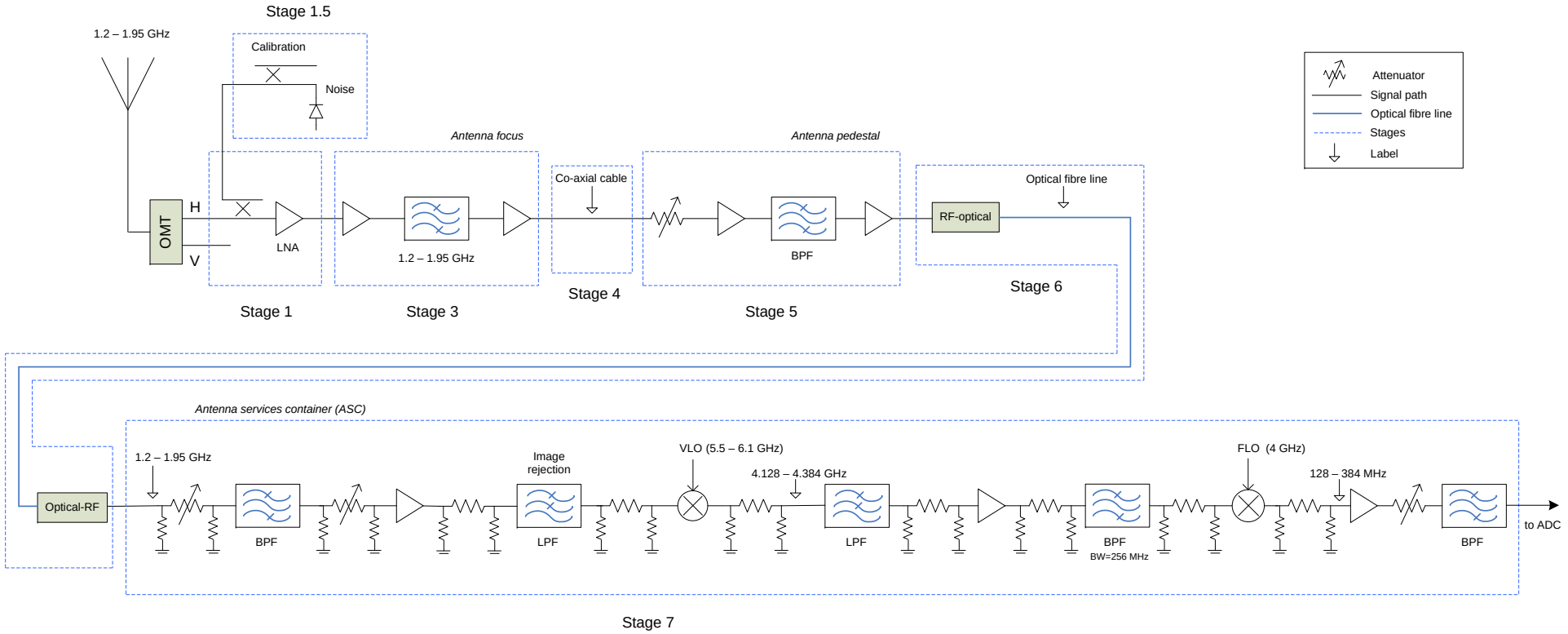

Figure 5.14: RF stages 1-7 for the KAT-7 receiver system.

When designing an interferometer system, the configuration also plays an important role and is included in this section for each design. The KAT-7 layout consists of 7 antennas distributed in an area with a diameter of 200m, see Fig.5.15 using [17].

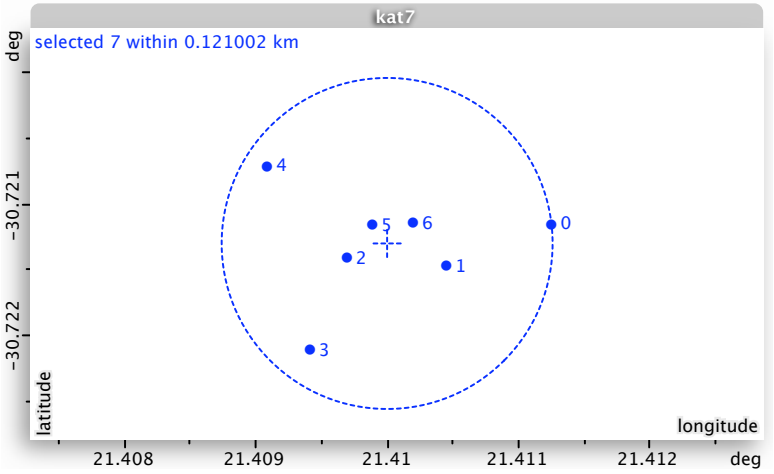

Figure 5.15: The 7 antenna configuration of KAT-7.

To cover the u,v-plane effectively with such a small number of antennas, the baselines should be kept short, while forming as many different baseline distances as possible. This is to decrease the number of gaps in the u,v-plane and therefore also the side-lobe level in the Point Spread Function (PSF). Let us demonstrate this with the KAT-7 where the antennas within 200m diameter are distributed in a random order. Fig.5.16 and Fig.5.17 shows the u,v-distributions for both a snapshot and 8hour observation respectively.

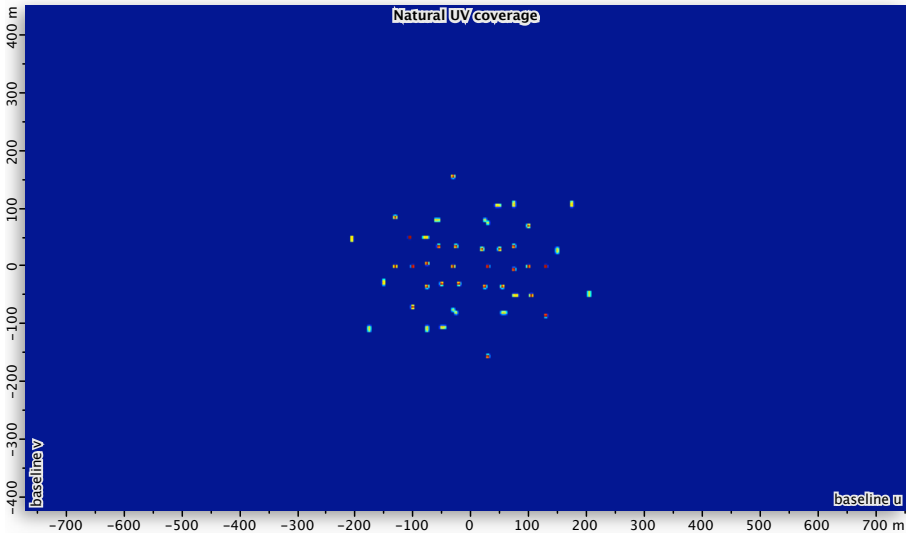

Figure 5.16: The u,v-coverage for a 10 min observation with the KAT-7 layout.

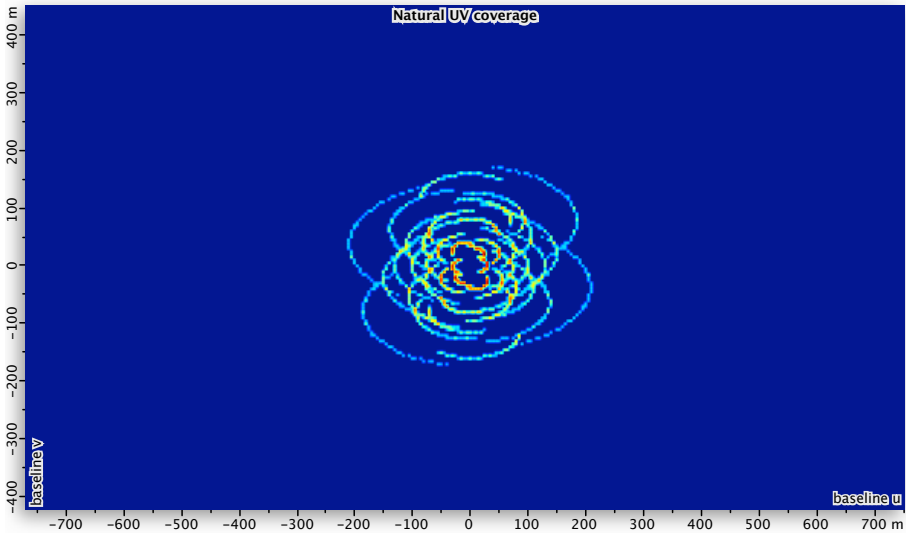

Figure 5.17: The *u*,*v*-coverage for a 8 hour observation with the KAT-7 layout.

It is clear that the 8hour observation covers the *u*,*v*-plane more than the snapshot observation. Fig.5.18 gives the horizontal profile of the *u*,*v*-distribution for the snapshot (black) and 8hour (green) observation.

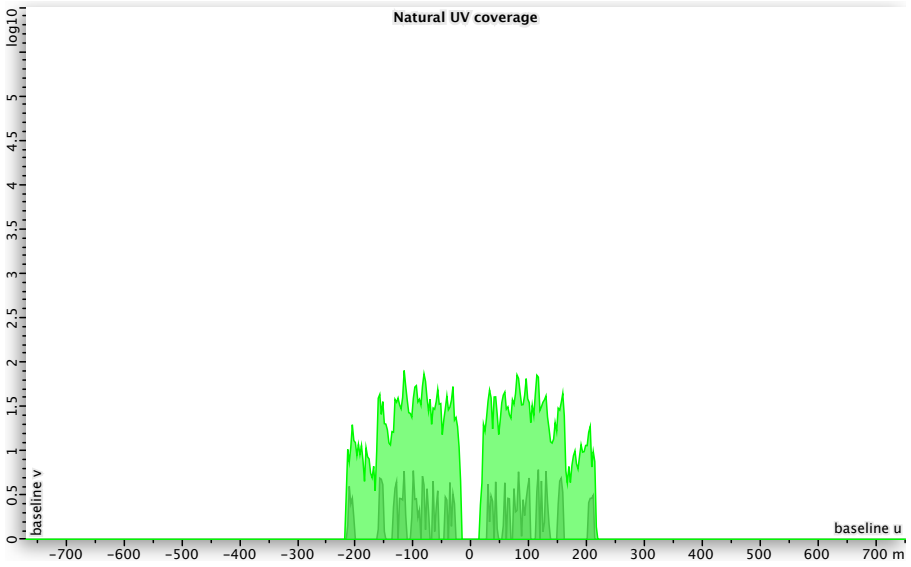

Figure 5.18: The KAT-7 layout *u*,*v*-coverage profile distribution for a 10 min (dark green) and 8 hour (green) observation.

The *u*,*v*-coverage for the snapshot observation is not very good. There is a lot of gaps in the *u*,*v*-plane as seen by the profile view. The 8hour observations covers the *u*,*v*-plane more and therefore gives a better PSF as can be seen by Fig.5.19 and Fig.5.20 that shows the PSFs for both a snapshot and 8hour observation respectively.

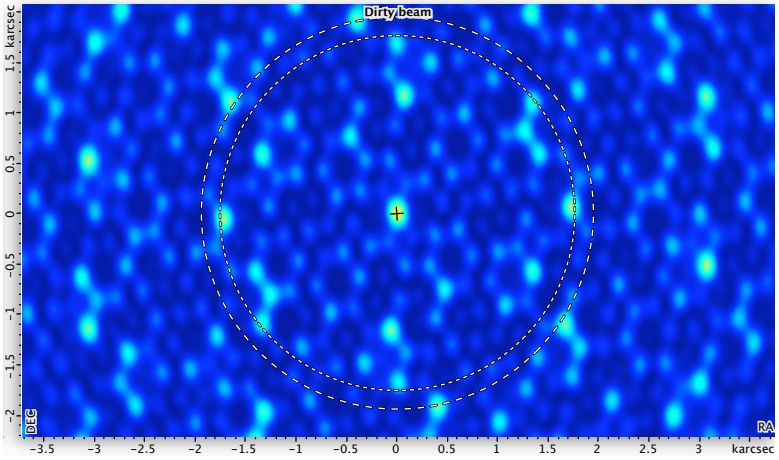

Figure 5.19: The corresponding PSF top view for a 10 min observation with the KAT-7 layout.

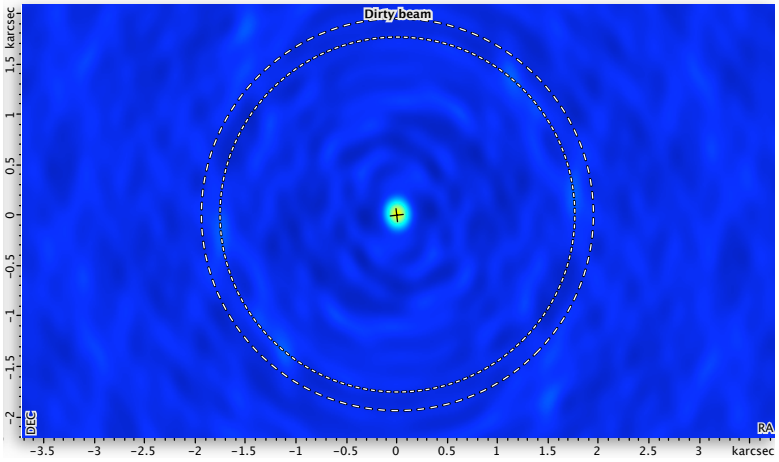

Figure 5.20: The corresponding PSF top view for an 8 hour observation with the KAT-7 layout.

It can clearly be seen that the PSF for the 8hour observation is a lot smoother. Consider Fig.5.21 that gives the horizontal profile of the PSF major and minor axis cross-sections for snapshot (black) and 8hour (green) observations.

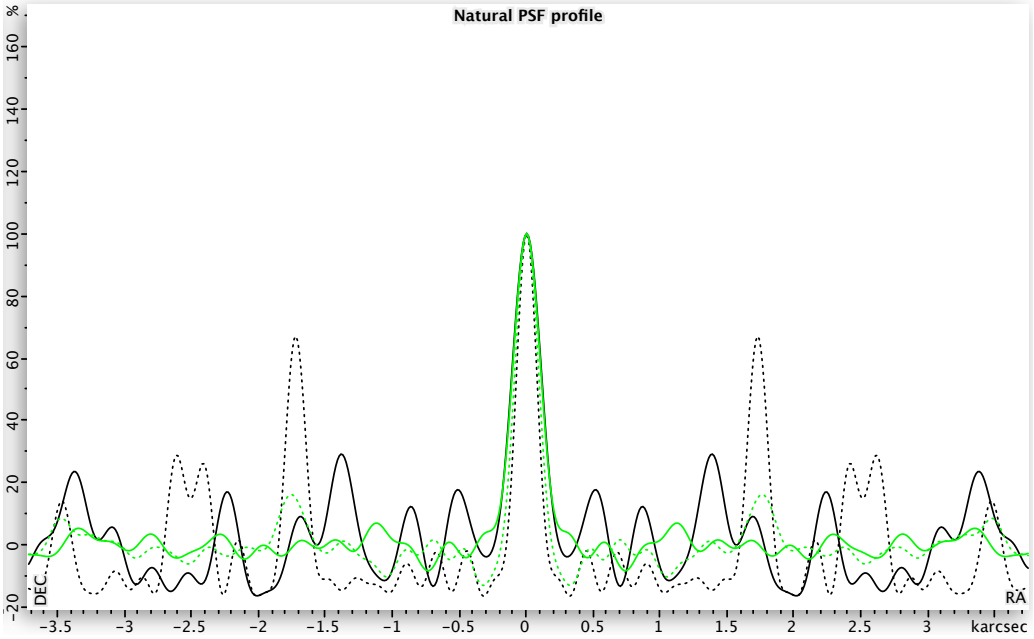

Figure 5.21: The horizontal profile of the PSF for snapshot (black) and 8hour (green) observations for the KAT-7 layout. The major and minor axis cross-sections are indicated by the solid and dotted lines respectively.

Note how to side-lobes are higher for the snapshot than for the 8hour observations, refer to Table 5.7. The side-lobe level for the snapshot case ($\sim$50–70 %) is very high and will produce a lot of noise in the dirty image. Compare this with the side-lobes for the 8-hour case ($\sim$7–16 %) which is much lower so that the improvement of the noise in the dirty map can easily be seen by the PSF top-view.

Table 5.7: The KAT-7 layout PSF minor and major side-lobe levels as a % of the PSF main beam for both the snapshot and 8-hour observations.

Side-lobe level	**snapshot**	**8-hour**
PSF major	$\sim$50%	$\sim$7%
PSF minor	$\sim$70%	$\sim$16%

For this specific layout, the highest theoretical angular resolution is $\sim$210 arcseconds using (2.3.1) which is the limit to the finest detail that can be seen, restricted by the maximum baseline of $\sim$210m. The largest structures that can be resolved are limited by the minimum baseline of $\sim$30m which corresponds to a resolution of 1.471 karcsec.

5.3.2.2 MeerKAT

The MeerKAT (see section 5.2.1) is the final phase of the KAT project. It will extend the KAT-7 array to a total of 80 antennas with WBSPFs. When it is finished, it will be the most sensitive radio telescope interferometer in the Southern hemisphere. The MeerKAT specifications is given by Table 5.8 below [5].

Table 5.8: Reference system design parameters for the MeerKAT.

System Parameters	**Reference design**
Number of antennas	80 (+7 antennas for spur)
Dish diameter (D_{dish})	12m
Feed	WBSPF
Aperture efficiency (e_{ap})	70%
Frequency range	f_{low} = 0.58–2.5 GHz f_{high} = 8–14.5 GHz
System noise Temperature (T_{sys})	30K (cryogenic) (Goal: 25K)
Sensitivity (A_{eff}/T_{sys})	200 m^2/K
Field-of-view (FoV)	1 deg^2 @ 1.4GHz
Polarisation	dual linear
Polarisation purity	-25dB across field
Minimum baseline	20m
Maximum baseline	8km (up to 60km with spur)
Angular Resolution	1 arcs -1 arcmin (at 1.420GHz)
Number of channels	16384 (Goal: 64k)
Total instantaneous bandwidth	512MHz (Goal: 1024MHz)
Minimum and maximum processed bandwidth	0.85–4 GHz
Dynamic range (spectral and continuum)	1:10^5
Minimum sampling time	0.1 ms

The block diagram of the MeerKAT receiver system would be similar in principle to the KAT-7 design (see Fig.5.13). The main difference being more antennas included in the system, which means an increase in computation and data rates, requiring a more advanced correlator. For the purpose of this discussion we will focus only on the array configuration and frequency range of the MeerKAT.

The MeerKAT configuration consists mainly of two parts, here referred to as the inner and outer regions. They are specified as follows: inner region: $\sim$70% of the antennas within 1km diameter, outer region: $\sim$30% out to a maximum baseline of 8km. At a later stage, the KAT-7 antennas will form an added spur to provide further E-W baselines of up to 60km. These will be positioned to optimise angular resolution [81]. Fig.5.22 shows the MeerKAT layout using [17].

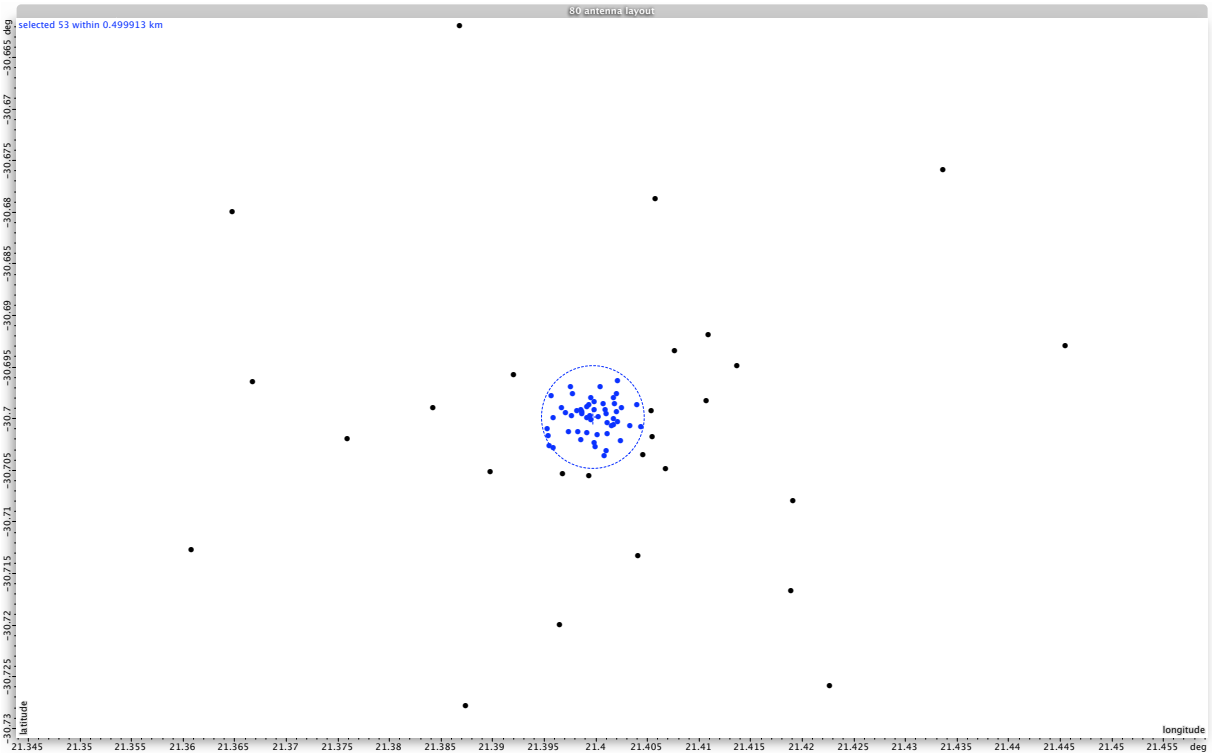

Figure 5.22: The MeerKAT antenna layout, with 53 antennas within a 1km diameter (inner region) and 27 antennas distributed further out (outer region).

The inner region is a relatively tight core and is needed for a good coverage of the u,v-plane. The short baselines provide good survey capability as these antennas can be correlated with data rates that are still manageable. The outer region contains randomly distributed antennas. This is to provide different baselines so that when the Earth rotates, arcs form on the u,v-plane to cover it more. Fig.5.23 and Fig.5.24 shows the u,v-distributions for both a snapshot and 8hour observation respectively.

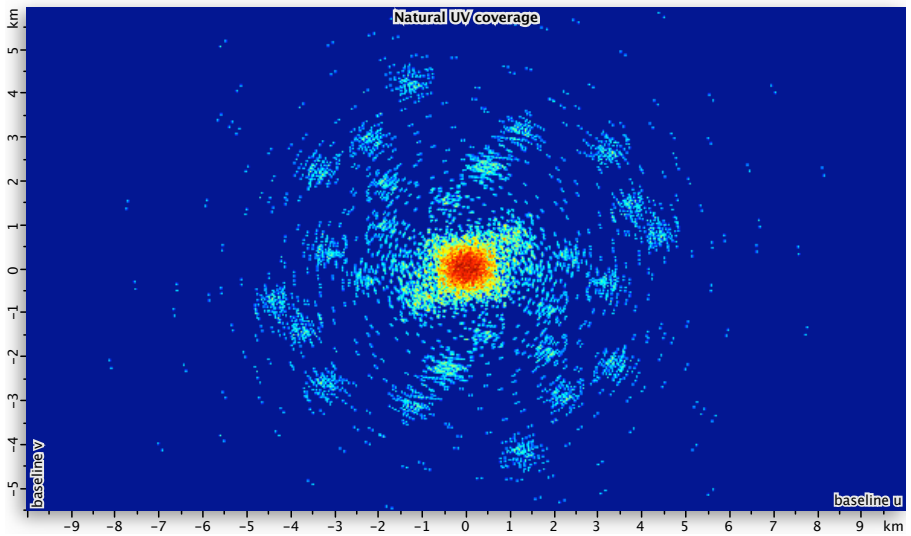

Figure 5.23: The u,v-coverage for a 10 min observation with the MeerKAT layout.

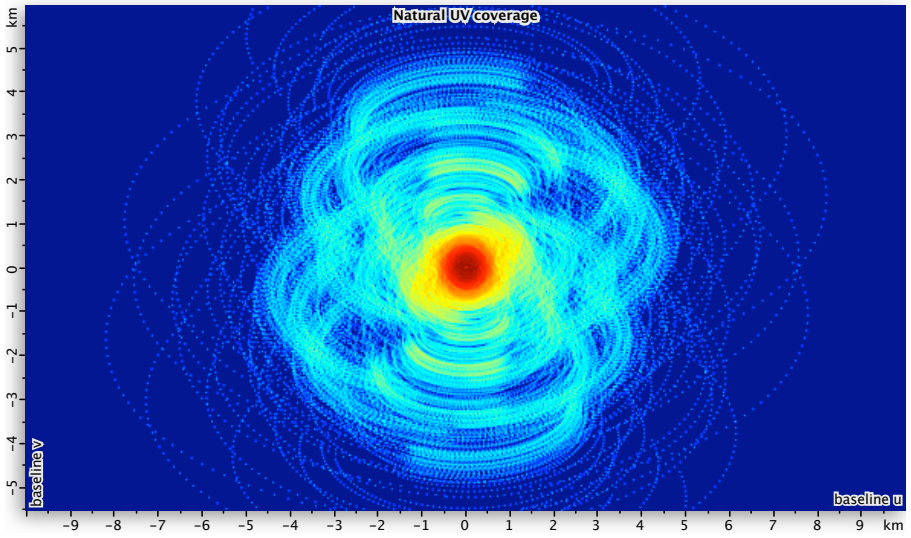

Figure 5.24: The *u*,*v*-coverage for a 10 min observation with the MeerKAT layout.

The snapshot case is not ideal, when the observation is extended to 8hours it gives good *u*,*v*-coverage. Fig.5.25 gives the horizontal profile of the *u*,*v*-distribution for snapshot (black) and 8hour (green) observations.

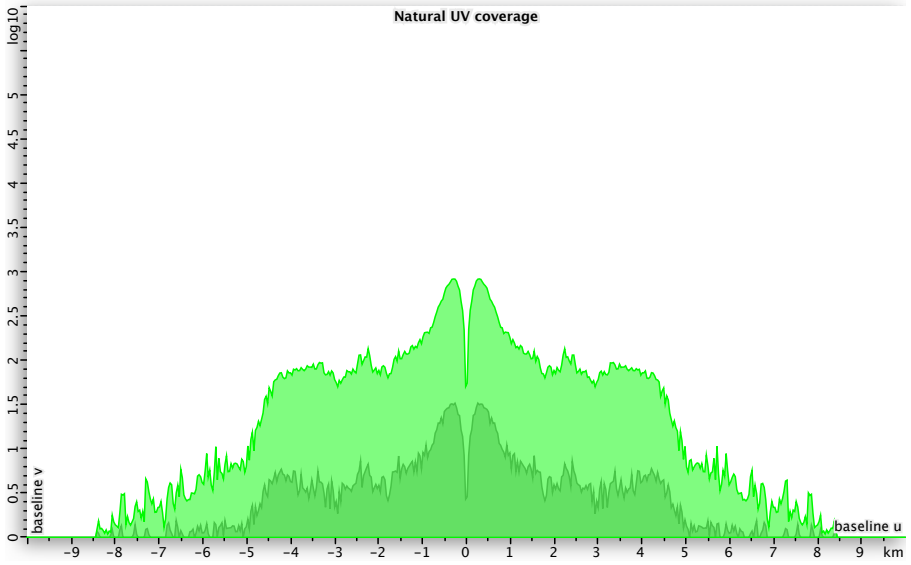

Figure 5.25: The MeerKAT layout *u*,*v*-coverage profile distribution for a 10 min (dark green) and 8 hour (green) observation.

No large *u*,*v*-gaps can be seen by these distributions, which means that the PSF will not have very large sidelobes. Fig.5.26 and Fig.5.27 shows the PSFs for both a snapshot and 8hour observation respectively.

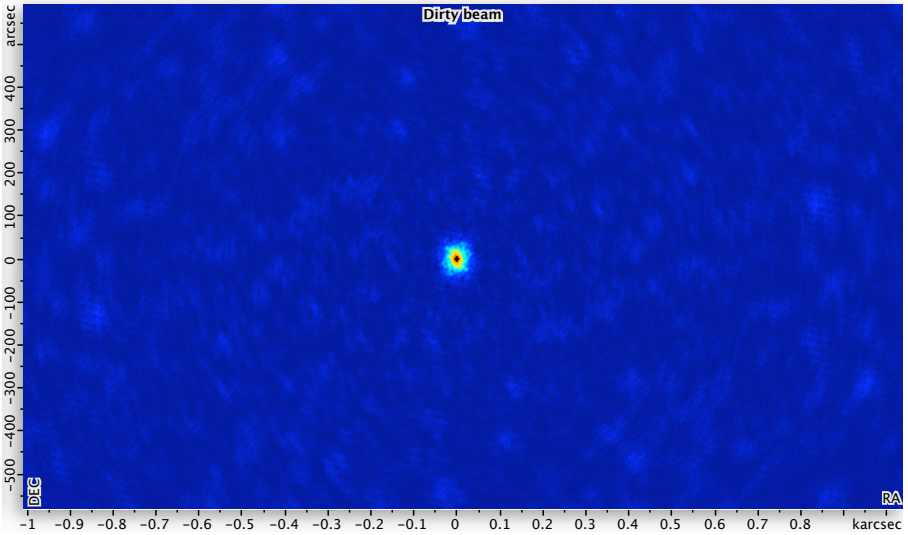

Figure 5.26: The corresponding PSF top view for a 10 min observation with the MeerKAT layout.

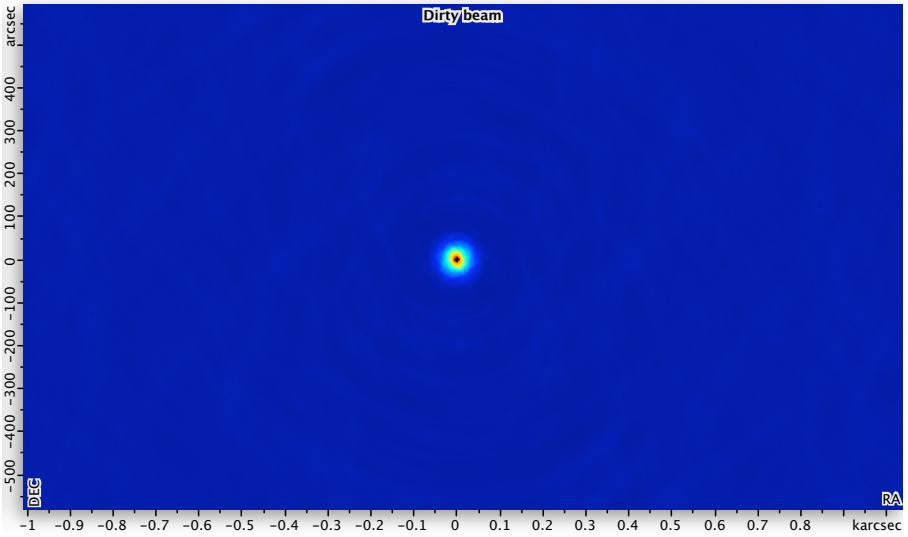

Figure 5.27: The corresponding PSF top view for an 8 hour observation with the MeerKAT layout.

It is clear that both give a fairly good PSF, with the snapshot observation containing some unwanted noise in the beam. Fig.5.28 gives the horizontal profile of the PSF major and minor axis cross-sections for snapshot (black) and 8hour (green) observations.

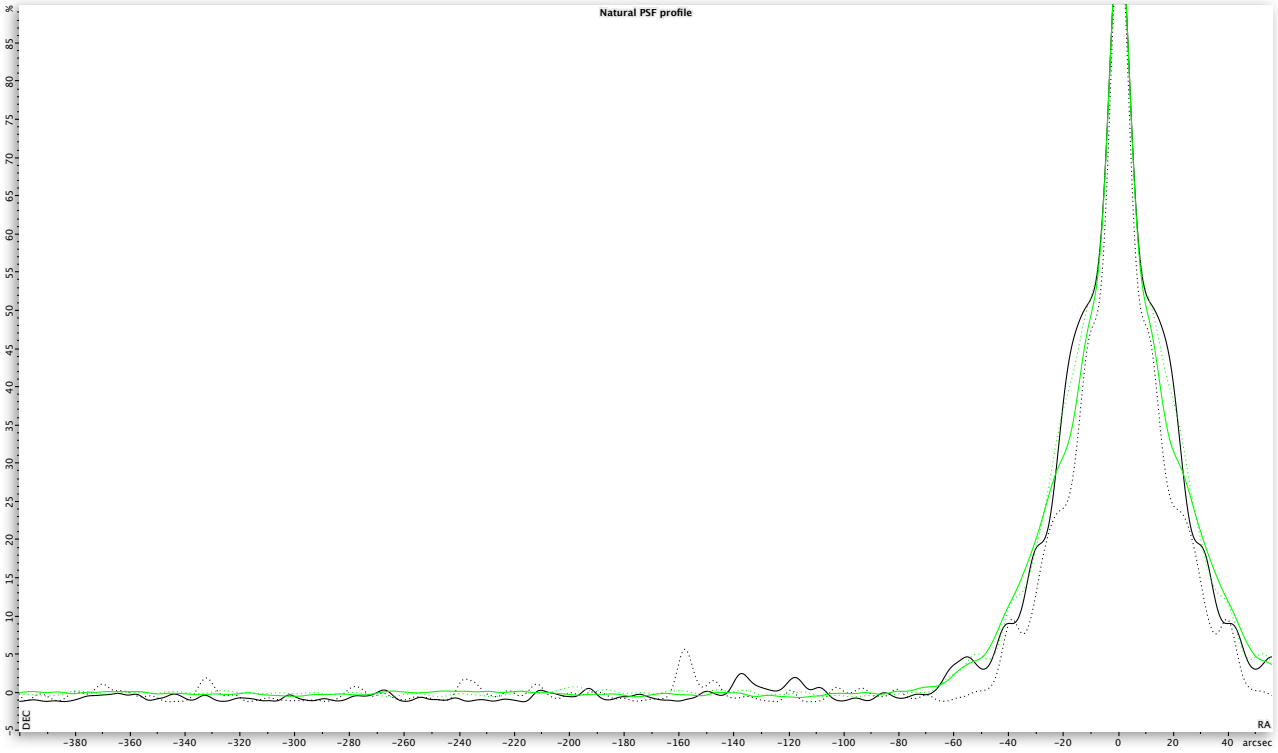

Figure 5.28: The horizontal profile of the PSF for snapshot (black) and 8hour (green) observations for the MeerKAT layout. The major and minor axis cross-sections are indicated by the solid and dotted lines respectively.

Here can be seen how the 8hour case is a much better improvement from the snapshot case, giving a more Gaussian like PSF profile. Let us consider the side-lobe levels for these two observations summarised in Table 5.9. Both the snapshot and 8-hour observations side-lobe levels are relatively low, but not ideal.

Table 5.9: The MeerKAT layout PSF minor and major side-lobe levels as a % of the PSF main beam for both the snapshot and 8-hour observations.

Side-lobe level	**snapshot**	**8-hour**
PSF major	∼4.5%	∼0.65%
PSF minor	∼5.5%	∼1.3%

The MeerKAT layout was designed for a wide range of angular resolutions, giving it high dynamic range to resolve both faint and strong sources [83]. For this configuration, the maximum and minimum baseline is ∼8400m and ∼20m respectively, setting the resolution range from ∼5.3 arcsec to ∼2.3 karcsec. The long baselines provide the highest angular resolution for observing point like sources, while the short baselines give lower resolution to see extended sources. This means that a large scope of science can be done with this array layout. Among others, this science could include VBLI observations made by using the central core. With the higher frequency component f_{high}, (∼10 GHz or higher) pulsar searches can be made and Galactic Centre pulsars can be monitored [81].

5.3.2.3 ASKAP

The ASKAP (see section 5.2.1) is a project in development equivalent to the MeerKAT project, but instead demonstrates the use of PAFs as part of an interferometer. The ASKAP array will have a wider FoV, but less sensitivity and a smaller frequency range than the MeerKAT. Because there is a trade-off between wide FoV and high sensitivity, these two projects complement each other in each demonstrating one of these parameters [81]. The ASKAP specifications is given by Table 5.10 below [84].

Table 5.10: System design parameters for ASKAP.

System Parameters	**Reference design**
Number of antennas	36
Dish diameter (D_{dish})	12m
F/D	0.5
Feed	PAF
Array elements per feed	100
Aperture efficiency (e_{ap})	60–75%
Frequency range	0.7–1.8 GHz
System noise Temperature (T_{sys})	35K < 50K (after beamforming)
Sensitivity (A_{eff}/T_{sys})	$\sim$70 m^2/K
Field-of-view (FoV)	30 deg^2 @ 1.4GHz
Number of beams	30
Polarisation	dual linear
Minimum baseline	22 m
Maximum baseline	6 km
Maximum resolution	8 arcseconds
Number of channels	16384
Channel bandwidth	19kHz
Instantaneous bandwidth	300MHz
Dynamic range	8 bits
Sampling rate	768MHz

What follows is a possible design of the ASKAP receiver system from [56]. Fig.5.29 shows the basic block diagram of the ASKAP receiver system.

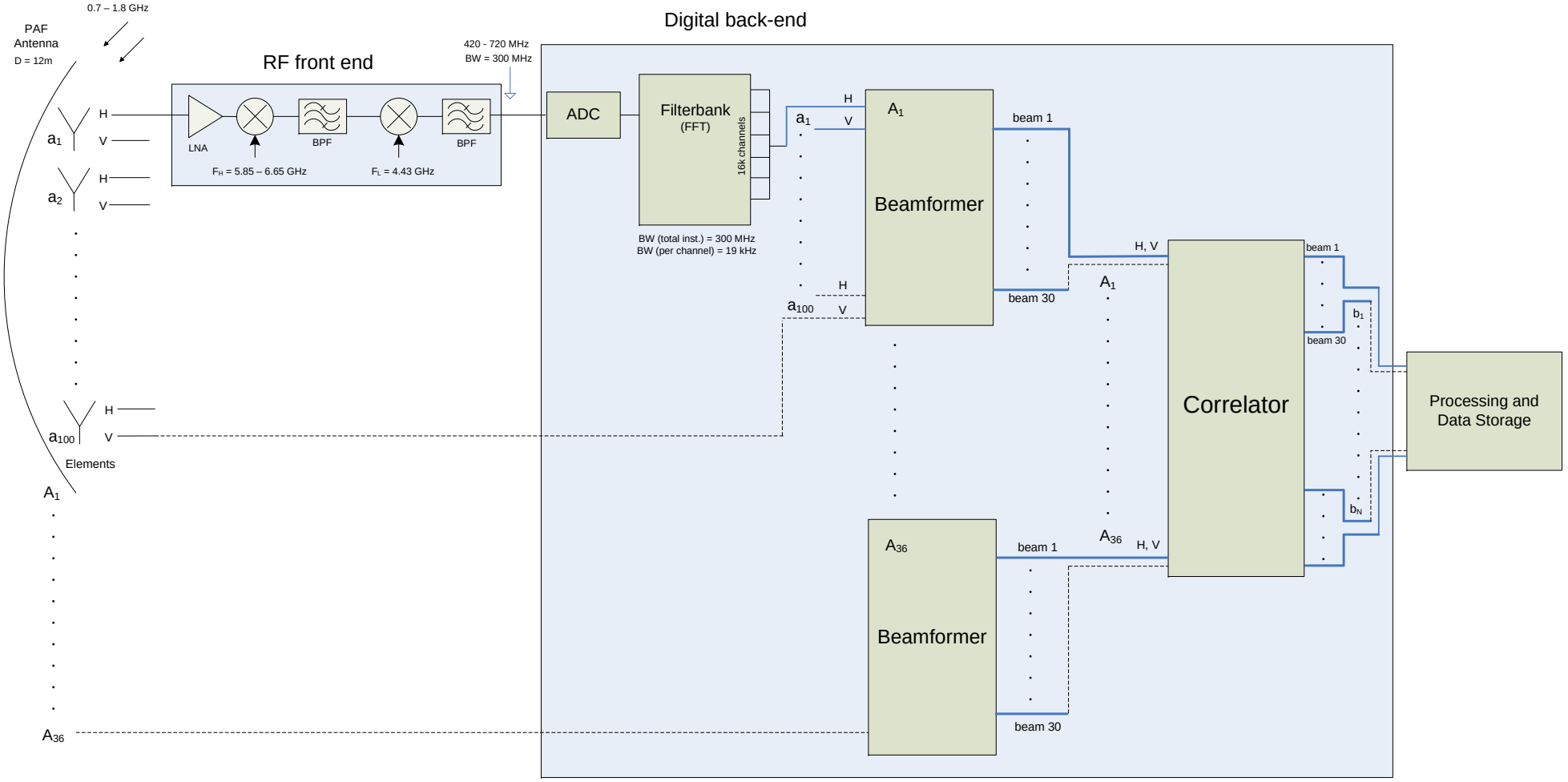

Figure 5.29: ASKAP signal path block diagram.

ASKAP will be an array of 36 parabolic reflector antennas. Each antenna is fitted with a phased array feed containing 100 receiver elements. The signals are dual polarised, thus each antenna contributes 200 signal paths. The receiver system can once again be divided into the RF-front end and Digital back-end.

The front end allows each element (with output impedance of 300Ω) to connect to a differential amplifier (LNA) designed to have an input impedance of 300Ω and noise of 25–35K. The LNA is cooled to keep T_{sys} minimal, located as near as possible to the antenna feed. A design option considered for converting the signal frequency is that of a super-heterodyne form. A mixer with a VLO first up-converts the signal to ∼5GHz using 'high side injection' and is then sent through a BPF with IF = 5GHz. A second mixer follows with a FLO of 4.43GHz that down-convert the signal ('low side injection') to base band and goes through a anti-aliasing BPF with IF = 570MHz to pass the 300MHz BW signal.

The signal is then sent via a transmission cable from the antenna feed to the base, using either RF over fibre (RFoF) or Coaxial cables, where the ADC samples the signal. The signal goes through a coarse filterbank in the pedestal to allow PAF calibration. It is then sent to the MRO control building where the beamformers and corrrelators are located [6].

At the digital back-end, the fine filterbank (as part of beamformer) takes the 300MHz signal and divides it into 16384 channels each 19 kHz wide. This process is repeated for all 200 signal paths. For each antenna there is a beamformer that takes these channelised signals as input and produces 30 separate beams by means of weight and sum calculations. Each of these beams has a 1 deg^2 FoV that combines to make a total FoV of 30 deg^2 at 1.4GHz. The correlator receives the output from the beamformer as input to do calculations on each antenna pair or baseline, for all 30 beams (see Appendix A.2). The correlator output can then be further processed and stored [85].

Some data rates for the ASKAP system from [86] include:

- Output data rate per antenna ∼2Tbps
- Total input data rate for beamformer - continuous 72Tbps
- Output rate for correlator - 40 Gbps

The antenna layout for the ASKAP is 26 antennas distributed within about a 2km diameter circle, 4 antennas just outside of this circle and the furthest 6 antennas in a reuleaux pattern as shown by Fig.5.30 using [17] [87].

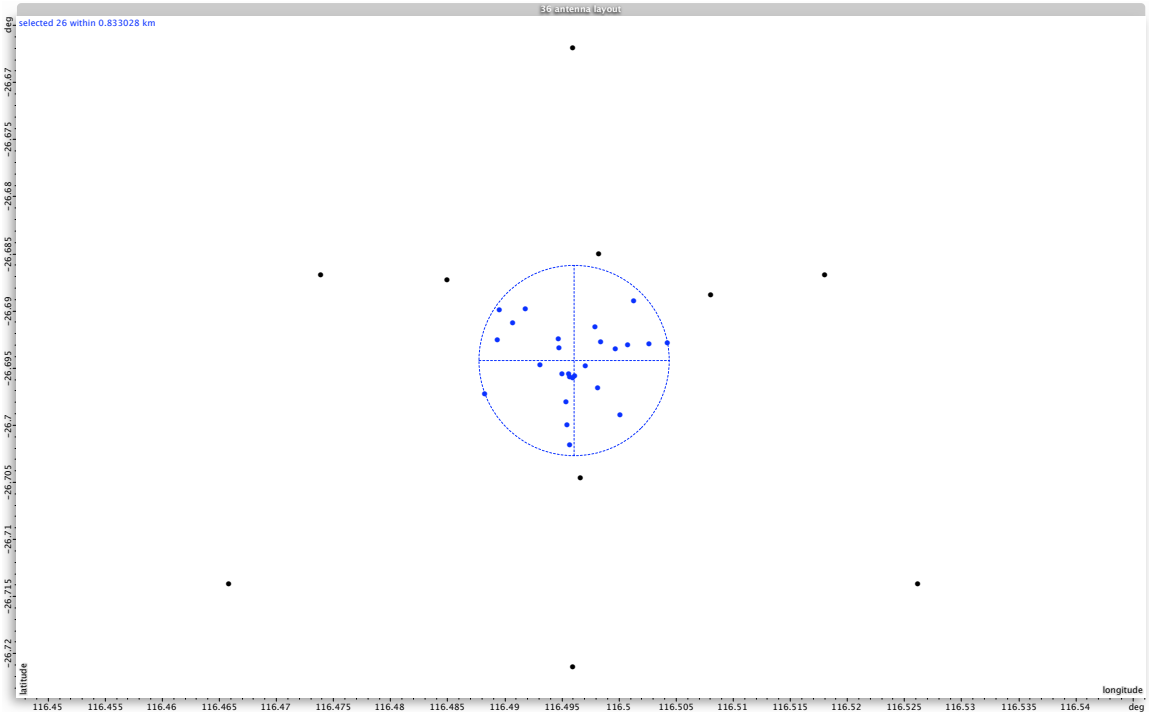

Figure 5.30: Antenna layout for the ASKAP array, with 26 antennas inside a 2km diameter core, 4 just outside this circle and 6 antennas in a reuleaux pattern up to 6km separation.

This type of antenna layout follows a similar reasoning to the MeerKAT layout, with a concentrated core and longer baselines further out. Fig.5.31 and Fig.5.32 shows the *u*,*v*-distributions for both a snapshot and 8hour observation respectively.

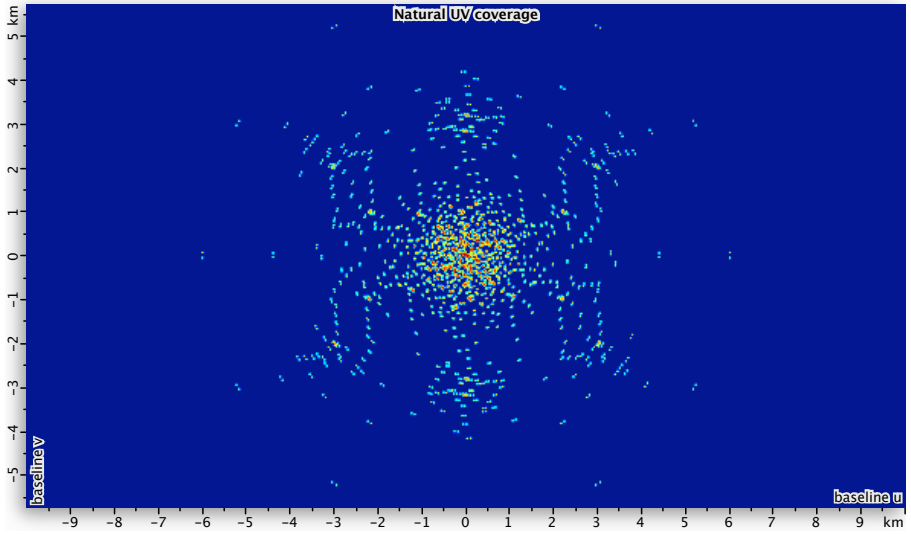

Figure 5.31: The *u*,*v*-coverage for a 10 min observation with the ASKAP layout.

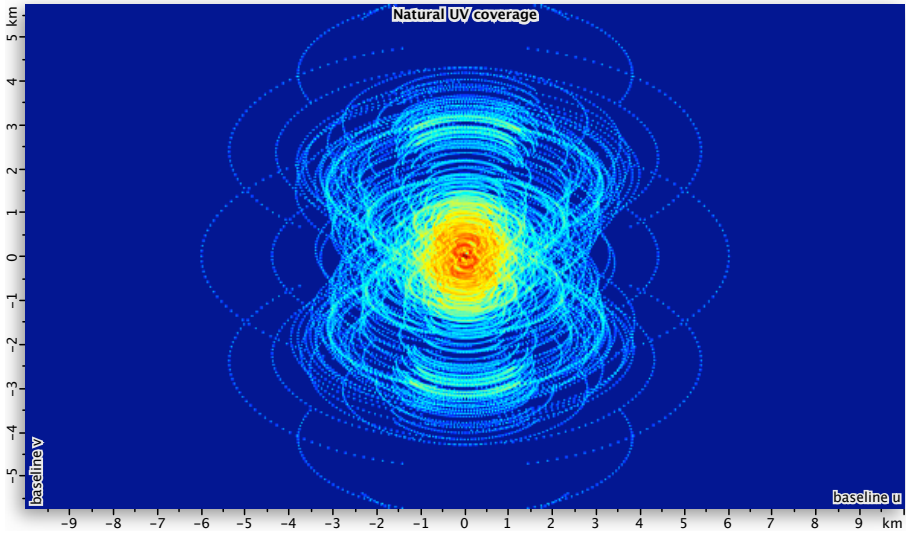

Figure 5.32: The *u*,*v*-coverage for an 8 hour observation with the ASKAP layout.

The snapshot observation *u*,*v*-coverage is not ideal, while the 8hour observation is an improvement. Fig.5.33 gives the horizontal profile of the *u*,*v*-distribution for snapshot (black) and 8hour (green) observations.

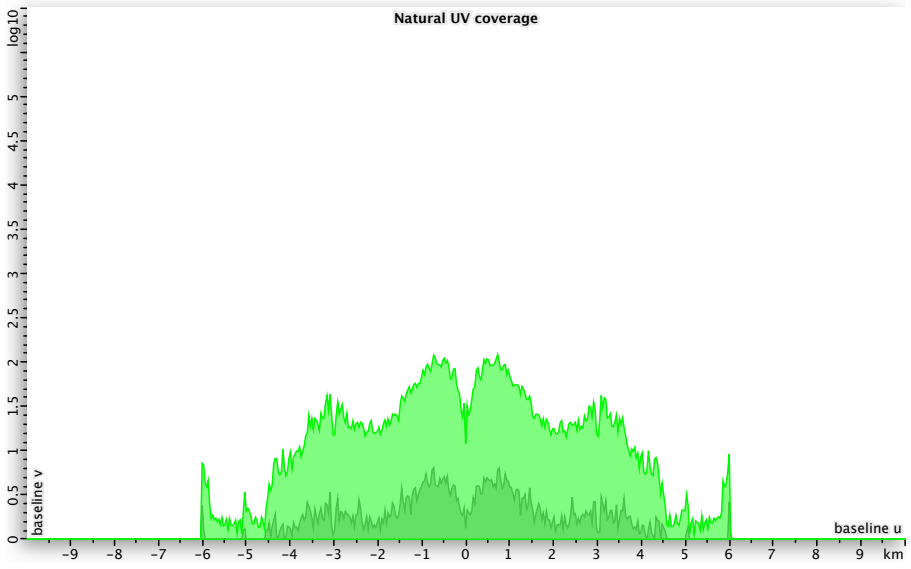

Figure 5.33: The ASKAP layout *u*,*v*-coverage profile distribution for a 10 min (dark green) and 8 hour (green) observation.

The snapshot distributions shows that there are some gaps in the *u*,*v*-plane, but can be improved by increasing the observation time. Fig.5.34 and Fig.5.35 shows the PSFs for both a snapshot and 8hour observation respectively.

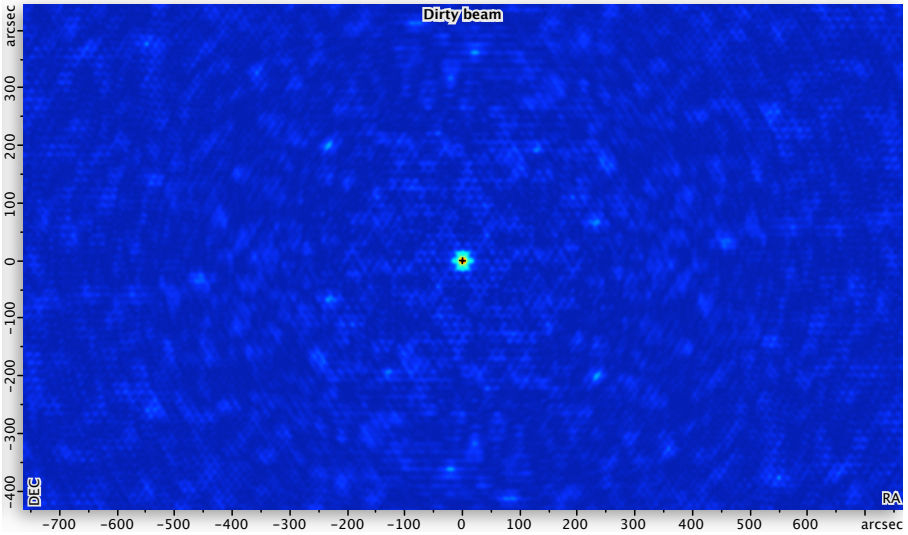

Figure 5.34: The corresponding PSF top view for a 10 min observation with the ASKAP layout.

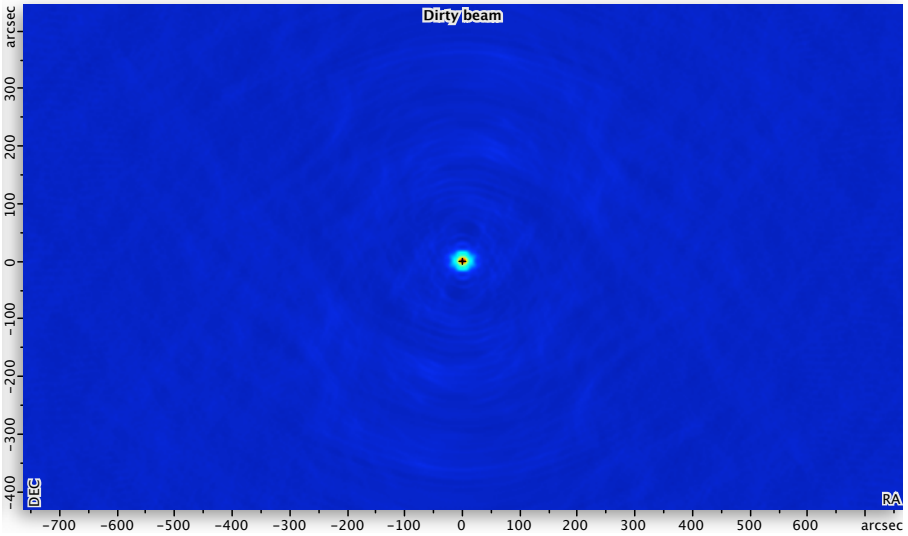

Figure 5.35: The corresponding PSF top view for an 8 hour observation with the ASKAP layout.

The 8 hour observation gives a good PSF, while for the snapshot case, there is unwanted noise. The side-lobe levels of the snapshot (black) and 8hour (green) observations can be seen by the horizontal profile of the PSF in Fig.5.36 and is summarised by Table 5.11.

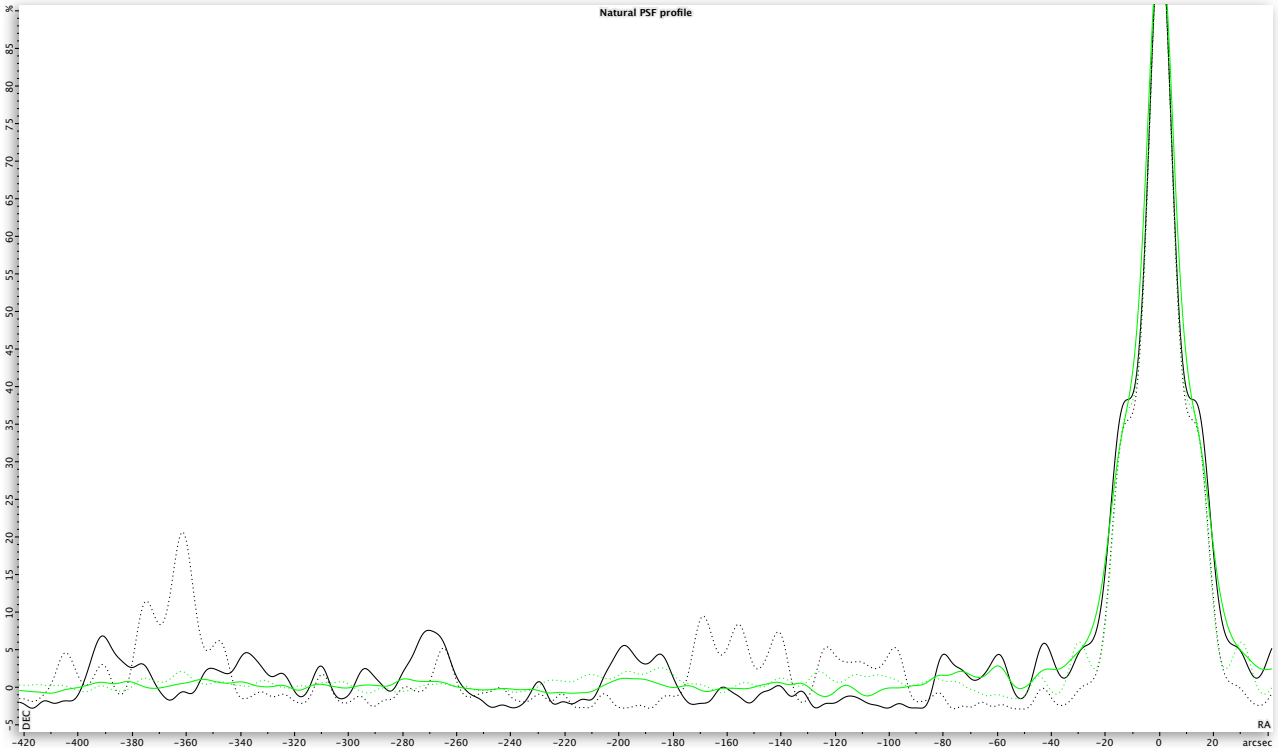

Figure 5.36: The horizontal profile of the PSF for snapshot (black) and 8hour (green) observations for the ASKAP layout. The major and minor axis cross-sections are indicated by the solid and dotted lines respectively.

Table 5.11: The ASKAP layout PSF minor and major side-lobe levels as a % of the PSF main beam for both the snapshot and 8-hour observations.

Side-lobe level	snapshot	8-hour
PSF major	∼8%	∼4%
PSF minor	∼20%	∼4%

The side-lobe level for the snapshot case is fairly high and for the 8hour observation there is an improvement, but still not the ideal case. Refer again to Fig.5.34 and Fig.5.35 to compare the noise difference for both cases on the dirty map. The highest angular resolution of ∼7.35 arcsec is given by the maximum baseline of 6000m, while the minimum baseline of ∼22m gives ∼2 karcsec. These values cannot be read off the PSF, as the beam is not in an ideal Gaussian form.

Although the ASKAP array will not be significantly better at pulsar search and timing observations compared to some existing large telescopes like the Parkes 21cm Multibeam receiver (section 5.3.1), it will initiate the transition from using single dish to using interferometers for pulsar observations. Pulsars were not usually detected in the past by interferometers, because of storage and computing requirements [88]. The ASKAP array will have a large FoV and thus very fast survey speed. It will therefore be able to perform large surveys including that of pulsar searches. The data storage requirements will however not allow for detecting millisecond pulsars. The high instantaneous sensitivity will make it possible to do precision timing on pulsars, while the beamforming capability will allow for multiple pulsar timing [78].

5.3.2.4 EMBRACE

The *Electronic Multi-Beam Radio Astronomy ConcEpt (EMBRACE)* is an example of the dense AA technology developed as part of the SKADS together with ASTRON. It follows from the same principles used to develop the THEA project. It is included in this section to demonstrate the use of both a digital and analog beamformer in a single system. The EMBRACE specification and operation parameters are given by Table 5.12 below [89].

Table 5.12: System design parameters for the EMBRACE design.

System Parameters	**Reference design**
Frequency range	0.5–1.5 GHz (maximum: 0.4–1.6 GHz)
Physical collecting area	625 m^2
Aperture efficiency (e_{ap})	>80%
Number of independent beams (FoVs)	At least 2
Antenna tile size	1 m^2
Polarisation	single linear
System Temperature (T_{sys})	<100K@1.4 GHz
Instantaneous bandwidth	>40 MHz
Electronic scan range	Full hemispherical
Dynamic Range	60dB

For these dense AAs, the type of antenna used is the Vivaldi antenna, as shown here by Fig.5.37.

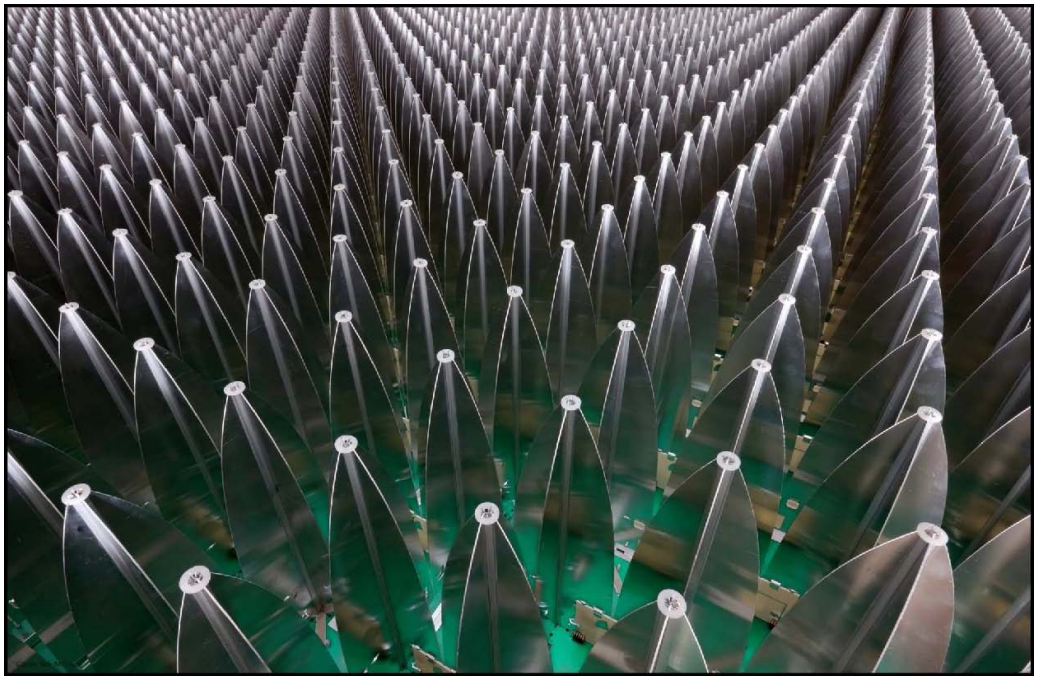

Figure 5.37: The EMBRACE aperture array Vivaldi antennas, from [90].

The element spacing is $d = \lambda/2$ (from eq. 5.2.1). To fill the collecting area of 625 m^2 about the same amount of tiles are needed, resulting in nearly 50000 elements in total. The front-end architecture of a tile is given by Fig.5.38.

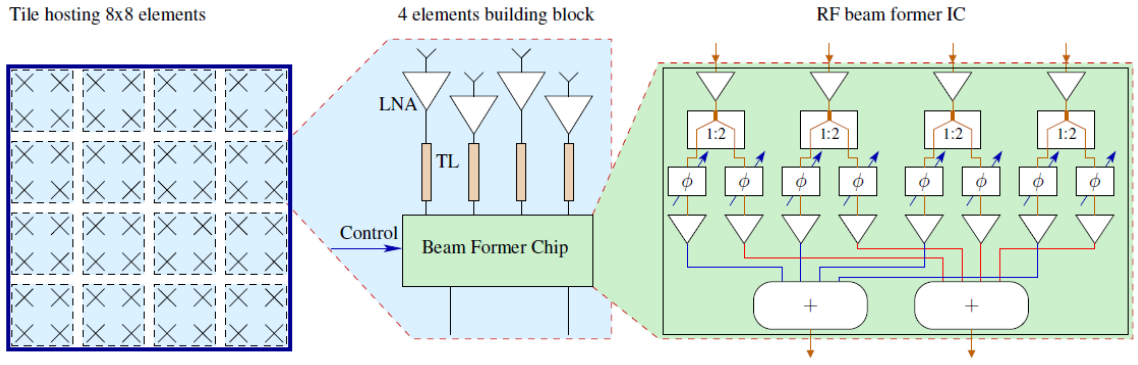

Figure 5.38: The EMBRACE tile design, divided into blocks each containing the receiver elements and RF beamformer, from [7].

The design for the tiles is 1m x 1m wide each, containing 16 building blocks. These blocks are further divided into 4 elements. The signals from each element is amplified and sent to the analog (RF) beamformer. The beamformer receives these 4 elements as input and produces 2 beams as output. The block output beams are combined to produce two independent FoVs at tile level.

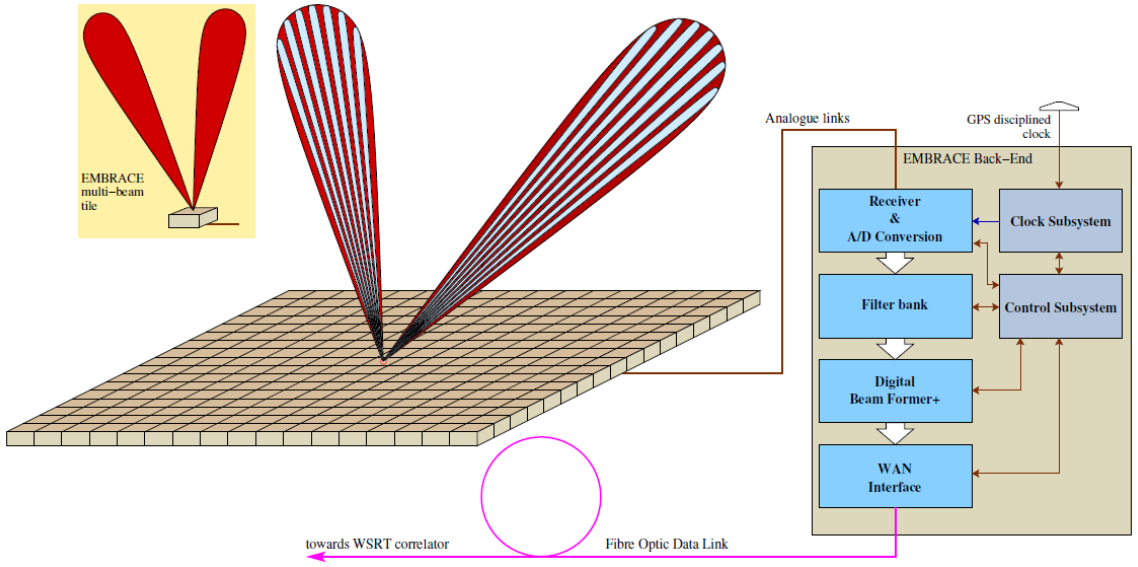

Figure 5.39: Beam-formation at tile and station level and the station back-end, from [7].

The tile signals are sent via RF-on-fibre cables to the central station back-end, see Fig.5.39. The receiver has two LOs to convert the incoming signal of 400–1600 MHz. The first is a VLO from 1400–2600 MHz that up converts the band to an IF1 of 3000MHz. The second is a FLO at 2850MHz and down converts the band to an IF2 of 150 MHz with a BW = 100MHz [91]. The IF signals are digitised and sent to the filterbank. Here

the signals are divided into narrow band channels so that it can be received as input by the digital beamformer. Two beams are formed again at station level and sent via fibre optic links to the correlator.

To summarise, we have seen that the XDM telescope demonstrates the use of WBSPFs, while the Parkes telescope demonstrates multiple beam formation. It should be mentioned that basic pulsar observations can be made using a single telescope. When using a telescope with a multiple horn feed however, the observations are more flexible providing multiple beams to perform surveys and timing measurements much faster. It was further shown that the KAT-7 array demonstrates the working of an interferometer with WBSPFs, while the MeerKAT extends this technology. The ASKAP array on the other hand demonstrates PAF technology, while EMBRACE shows how dense AAs can be implemented. The MeerKAT and ASKAP projects can also contribute to the SKA pulsar system design by evaluating their pulsar observations capabilities - this will be discussed in the next chapter.

5.4 Conclusion

This chapter started with a discussion on SKA background that included the SKA pathfinders, technologies and key science projects. It then evaluated various SKA pathfinder receiver systems, with focus on the technology they demonstrate. Some of the antenna configurations were simulated to evaluate the layouts performance in terms of the u,v-coverage and PSFs.

Chapter 6

Pulsar Receiver System Design

6.1 Introduction

This chapter aims to investigate pulsar receiver system designs, particularly for the Square Kilometre Array (SKA). A description is first given regarding some pulsar properties and the basic pulsar receiver system design. This follows with the SKA pulsar science case goals and technical specifications. It continues with a discussion on designing receiver systems for pulsar search, timing and astrometric observations. It concludes with simulations of antenna layouts designed for the SKA pulsar science case.

6.2 Observing pulsars

Pulsars have already been introduced in a previous chapter (see section 4.3.2) as a type of radio star. Some pulsar properties will now be discussed that is of concern when doing pulsar observations. These pulsar properties sets the technical requirements for the receiver system design and therefore these implications are also briefly given.

6.2.1 Pulsar properties

Pulsars have an average spectral index of $\alpha = 2 \pm 1$, which indicates a type of non-thermal radiation (see 3.6.3). The pulse emission mechanism is not entirely understood, but can most probably be attributed to synchrotron radiation. The solid lines in Fig.6.1 (left) show typical pulsar compared to non-thermal source spectra. Some pulsar spectra like that of PSR B0329+54 shown in Fig.6.1 (right), have a low-frequency turn-over around 200MHz. This is indicated by the dashed line in Fig.6.1 (left), which also shows a cut-off in the spectrum around 100MHz that often occurs. The spectral slopes indicate an increase in flux density with a decrease in frequency [92] [13].

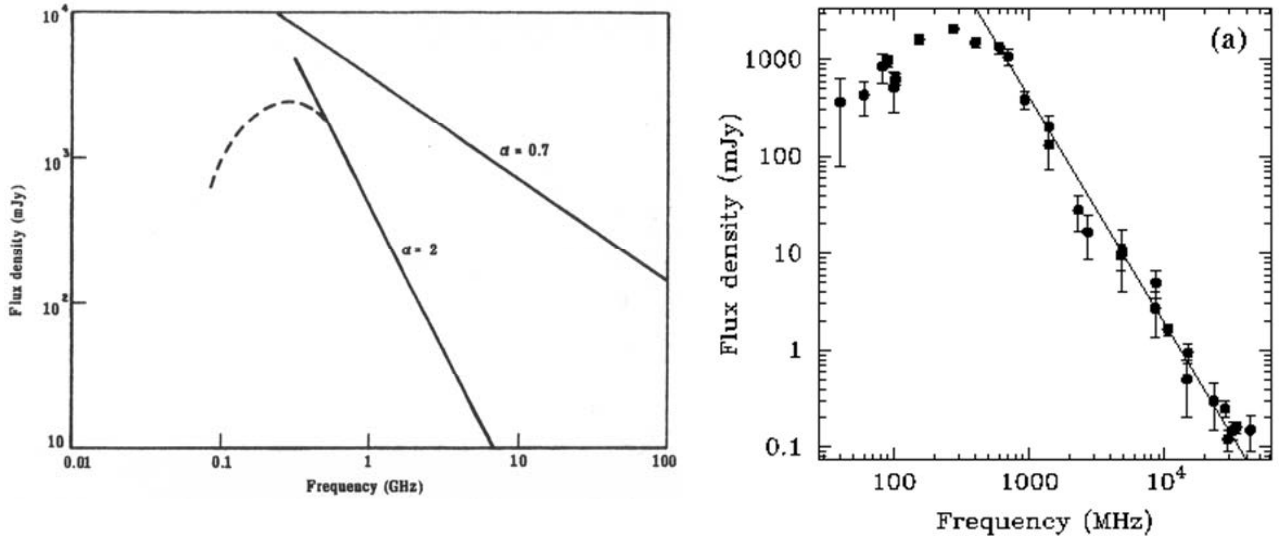

Figure 6.1: The pulsar spectrum for (left) a typical pulsar (with $\alpha = 2$), a non-thermal radio source (with $\alpha = 0.7$) and (right) the pulsar PSR B0329+54, from [11] [93].

Pulsar radiation is seen as a short burst in time and as a result is spread over a wide frequency range with the maximum radiation depending on the specific pulsar. Pulsars are generally weak radio sources with a mean flux density[1] of about 0.8 mJy at 1.4 GHz. Table 6.1 summarises some properties of pulsars [94] [26].

Pulsar signals are periodic and can therefore be very accurately predicted. Using this attribute, gating can be performed - where only data near the actual pulse of the pulsar period is considered. The pulsar pulses vary from one pulse to the next in shape and intensity due to interstellar scintillation. Fig.6.2 shows an example of the signal received from the pulsar PSR B0329+54. It may therefore be necessary to fold the data when searching for pulsars so that each pulsar has a unique profile. Folding is the method by which the pulses are

[1] This value was obtained with a set of near a thousand pulsars, measured at 1.4 GHz with flux densities in the range 20 μJy to 5 Jy [93].

Table 6.1: Pulsar properties.

Average spectral index	$\alpha = 2 \pm 1$
Mean flux density	0.8 mJy (at 1.4 GHz)
Pulsar period	seconds to milliseconds
Pulse width	5- 10% of the pulsar period
Polarisation	Mainly linear, circular also found

added together to produce an average pulse profile that peaks above the noise level [95].

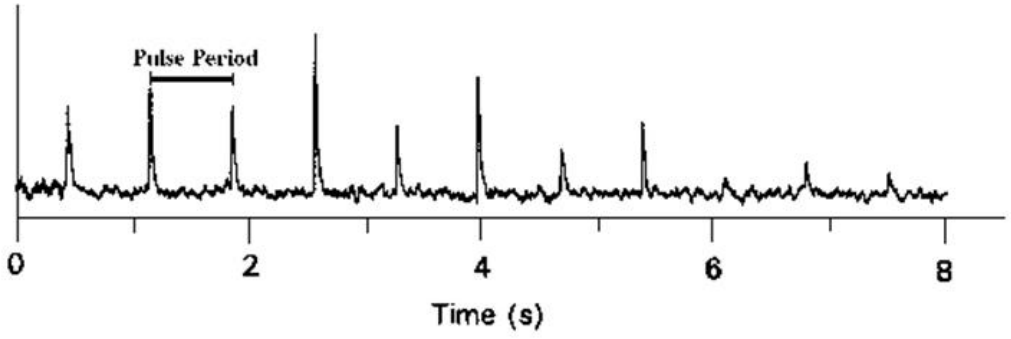

Figure 6.2: The pulse period for the pulsar PSR B0329+54 - note the varying intensity, from [96].

A pulsar signal undergoes *dispersion* as it moves through the Interstellar Medium (ISM) (see section 4.3.1) so that the speed of the signal varies with frequency. This results in the higher frequencies components arriving earlier than the lower frequency components as shown in Fig.6.3. This difference in arrival time of the pulsar signal observed at two different frequencies ν_1 and ν_2 (with $\nu_2 < \nu_1$) is given by (6.2.1) [26].

$$t_2 - t_1 = K\left[\frac{1}{(\nu_2)^2} - \frac{1}{(\nu_1)^2}\right] DM \tag{6.2.1}$$

The *dispersion measure (DM)* is defined as the total column density of free electrons along the line of sight and given by (6.2.2) (in $cm^{-3}pc$).

$$DM = \int_0^d n_e \mathrm{d}l \tag{6.2.2}$$

with n_e the density of free electrons

d the distance to the pulsar

The constant K, is given by (6.2.3) [in $cm\,pc^{-1}$].

$$K = (2\pi^2 e^2/\varepsilon_0 mc)(3.0856 \times 10^{18}) \tag{6.2.3}$$

To correct for this effect, de-dispersion is implemented by using one of methods: *coherent* or *incoherent de-dispersion*, through either hardware or software techniques.

For incoherent de-dispersion, the observed frequency band is divided into separate channels so that each channel is then delayed by the appropriate dispersion measure. The signals are added together to produce

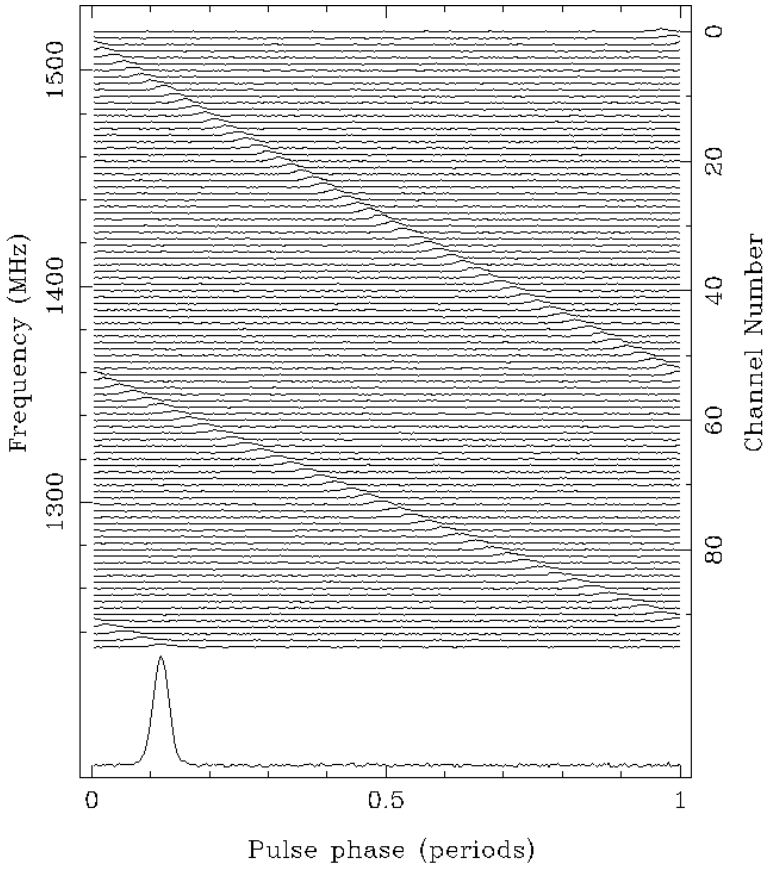

Figure 6.3: Pulsar dispersion from the pulsar B1356-60, from [93].

the net signal. De-dispersion is therefore done after detection, and only corrects for this effect partially. An advantage is that the de-dispersion can be done in real time, making it effective for pulsar search observations.

For lower frequencies or high *DM*, coherent de-dispersion is preferred. This method is based on the idea that the dispersion in the ISM can be represented by a transfer function. To de-disperse the signal, the appropriate inverse transfer function is applied to the raw complex voltage signal in the frequency domain. When this result is transformed back into the time domain it represents the intrinsic voltage from the pulsar, which is now the corrected signal. De-dispersion is therefore done before detection and corrects for this effect completely. The advantage is the high time resolution it can achieve, making it effective for pulsar timing observations [16].

6.2.2 Implications on receiver

The pulsar properties mentioned in the previous section sets the technical requirements for the system design. These implications on the receiver are briefly given here [94].

Spectral resolution - The pulsar signals are dispersed by the ISM, therefore a filterbank is needed when doing incoherent de-dispersion. The filterbank as part of correlator must be able to divide the frequency band into the number of channels required. The dispersion delay per frequency channels is given by (6.2.4) [9].

$$\Delta t_{DM} = 8.3\mu s \times DM \times \Delta\nu_{ch} \times \nu^{-3} \tag{6.2.4}$$

with $\Delta\nu_{ch}$ the channel bandwidth in MHz
ν the centre frequency in GHz

The number of channels needed is roughly given by (6.2.5).

$$N_{ch} \approx \frac{1600}{\nu^2}\left(\frac{DM_{max}}{10^3 pc.cm^{-3}}\right) \tag{6.2.5}$$

The bandwidth and number of channels therefore needs to be chosen accordingly.

Time-resolution - The pulse widths are very small and the time-resolution should be even a thousand times smaller than the period, thus in the range of milliseconds to microseconds. These fast sampling times adds to the complexity of the back-end, data acquisition system and off-line computing.

Polarimetry - Generally it is required that all four Stokes parameters (see A.1) are determined for use in polarisation studies. This increases the data flow and complexity by a factor of four.

Calibration - The pulse flux intensity varies from one pulse to the next. The signal needs to be calibrated, which can be done by:

- placing a calibrated noise source into signal path or
- using a calibrated sky source

Processing - Further processing can be done on the received pulsar signal. Pulsar signals are periodic, therefore gating can be applied. The pulse shapes also vary, therefore folding is necessary. A special pulsar back-end can be used for this. The pulsar signals are dispersed and to correct for this by using the method of coherent de-dispersion, will require a type of hardware or software processor. This can be implemented as part of the back-end [93].

Table 6.2 summarises the above mentioned requirements for doing pulsar observations. From this table can be seen that a number of components are involved in satisfying the requirements of pulsar observations.

Table 6.2: System requirements for pulsar observations.

System parameter	**Requirement**	**System component**
Spectral resolution	need narrow band channels	filterbank
Time-resolution	need very fast sampling times	correlator
Polarimetry	need full Stokes computation	correlator/polarimeter
Calibration	need to calibrate	Calibration source
Processing	need to do further processing	pulsar back-end

6.3 Basic pulsar receiver system design

Fig.6.4 shows the basic block diagram of a pulsar receiver system. The signal path of this receiver is now described with an emphasis on the changes in the system to do pulsar observations [94].

The voltage signal from the antenna is split into two polarisation channels, say horizontal (H) and vertical (V). It then goes through an Radio Frequency (RF)-stage, designed for the particular system. This may include at the very least an Low-Noise Amplifier (LNA), mixer and filters. The resulting signal (at or near base-band) is then digitised using an Analog-to-Digital Converter (ADC).

The digital back-end contains a filterbank or a type of spectrometer that divides the broad-band signal into a number of narrow-band frequency channels. This process is repeated for each polarisation channel. The polarimeter is included for the calculation of the Stokes parameters using both polarisation channels as inputs. Alternatively the total power detector can be used to do calculations instead of the polarimeter when only the total intensity is required. The output data is integrated with a time constant, τ_s.

The integrated data is then sent to a data recorder to store the data for (off-line) processing at a later stage. If the data rate is too high and difficult to handle, some of the processing like de-dispersion, folding or gating can be done on-line by using special hardware designed for this (section 5.2.2). This part of the receiver is usually referred to as the pulsar back-end.

When considering a receiver system layout, it should be noted that the front-end generally follows the same basic design for all types of observations. The back-end on the other hand is designed specifically for continuum, spectroscopic or pulsar observations. Each of these requires different signal processing. A pulsar is seen as a point source (section 2.2.3) and therefore a single dish is sufficient to do pulsars observations. However, because of the weak nature of the pulsar signal, it is more efficient to observe with larger collecting area like using an interferometer. As discussed in the next section, this is the manner in which pulsar observations will be made using the SKA.

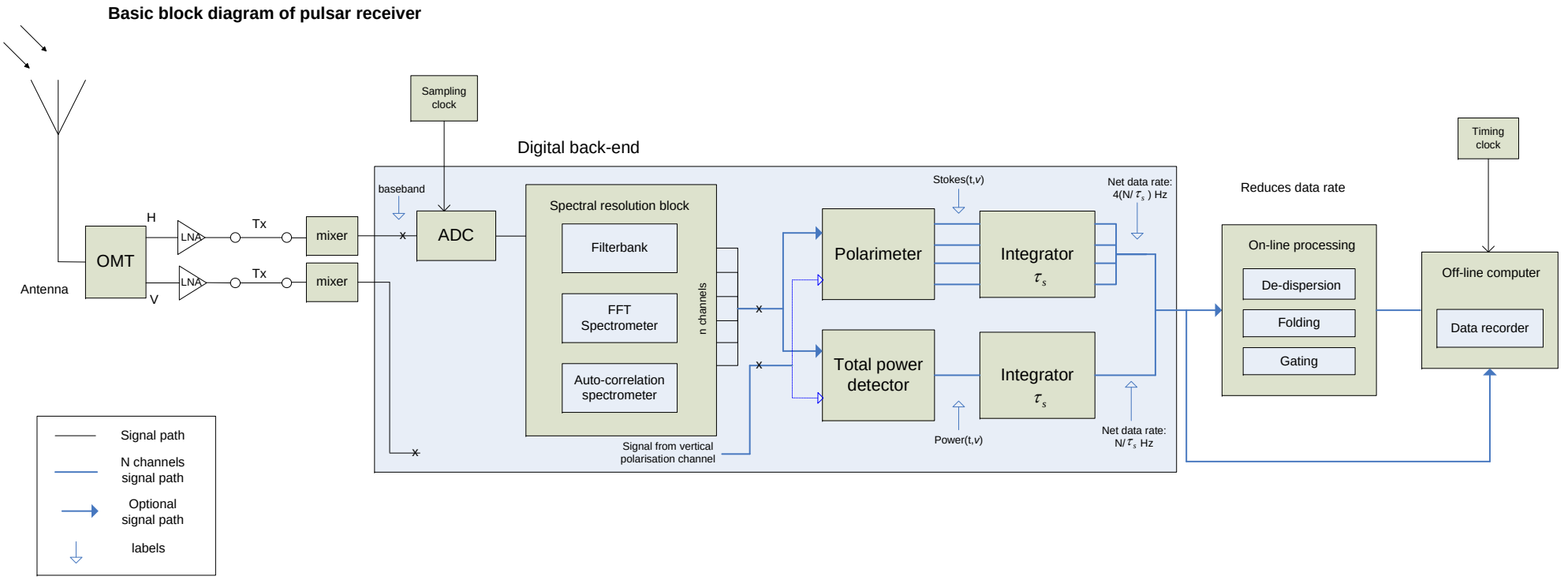

Figure 6.4: Basic block diagram of pulsar receiver.

6.4 Pulsar science case

The Astronomy community has defined five Key Science Projects (KSPs) for the SKA (see section 5.2.3). The project that will be discussed throughout this chapter is *KSP II) Strong-Field Tests of Gravity using Pulsars and Black Holes*. This section contains a brief summary of the main science goals and technical specifications regarding the specific science case. For a detailed discussion, refer to [8] and [9].

6.4.1 Scientific goals

- *Galactic pulsar census* - Pulsar searches over the whole sky will be performed and recorded. It is estimated that about 20 000 pulsars may be found with the SKA.
- *Strong-field tests of gravitational theories* - From the pulsar survey mentioned, many binary pulsars and also pulsars with black hole companions (PSR-BH systems) will be found. These pulsars systems have large enough velocities and gravitational potentials to test the strong-filed limit of relativistic gravity.
- *Gravitational wave detector* - While performing the pulsar survey, many millisecond pulsars (MSPs) will also be found. These MSPs can then form a pulsar timing array that, when timed with high precision, can function as a cosmic gravitational wave detector.
- *Astrometric measurements* - The SKA will be able to perform Very Long Baseline Interferometry (VLBI) observations that will provide accurate measurements of pulsar distances and motions, as well as pulsar parallaxes and velocities.

6.4.2 Technical Specifications

The given technical specifications for the pulsar science case are now discussed, while also providing some insight into the reasoning behind the choice in parameter values. Note that when a critical requirement is given, it refers to the requirement that is crucial in achieving the science goal - this becomes important when compromising between science goals [9] [95]. To achieve these science goals, three types of observations are frequently mentioned and will be used in a later section as part of the pulsar system design for the SKA.

- Search observations - includes searching for pulsars, generally in the form of doing a pulsar survey. These observations have different technical requirements depending on which part of the sky is observed.
- Timing observations - measuring the time-of-arrival and pulse properties of the pulsars, can be done with high precision.
- Astrometric observations (or VLBI observations) - accurate measurements of pulsar distances and motions, pulsar parallaxes and velocities.

Frequency
Science goal: Observe pulsars near the Galactic centre
Requirement: 9–15 GHz
Critical: > 8 GHz
When observing pulsars towards the Galactic centre, interstellar scattering of radio waves occur that causes

temporal broadening of the pulsar emission. This scattering occurs around 1 GHz and is reduced at $\geq$10 GHz, with this effect being the result of fluctuations in the free-electron density [97] [8].

Science goal: Search for pulsars at Galactic and extragalactic lines of sight
Requirement: 0.5–5 GHz
Critical: 0.4 - > 1.5 GHz
Simulations done by [98] show that when searching in line of the Galactic plane, defined as $|l| < 45^\circ$ and $|b| < 5^\circ$ a centre frequency of just above 1 GHz is optimal. For the rest of the sky (excluding the Galactic centre) a frequency of around 600 MHz is optimal. According to [9], the standard search frequency for pulsars is at 1.4 GHz, while the optimal frequency depends on the particular pulsar being observed.

Science goal: Timing observations
Requirement: 0.5–3 GHz
Critical: 0.4–3 GHz
Pulsars have steep spectra (see section 6.2.1) so that they are hard to observe at higher frequencies. On the other hand, observations at low frequencies (<1 GHz) are affected by the ISM and often pulse broadening occurs. Thus for the majority of pulsars, timing at a frequency of around 1.4 GHz is more ideal in terms of these effects. Due to factors that limit the time-of-arrival (TOA) precision of the pulsars, a wide frequency range is specified [78].

Science goal: Timing observations
Requirement: multi-frequency observations
The reason for multi-frequency observations is that it is of interest to study the emission of pulsars over a broad frequency band. It is also necessary to correct the pulsar signal for propagation effects in the ISM. The requirement is 3 pairs of observing bands (for both polarisations) over 2 octaves.

Science goal: VLBI observations
Requirement: 2–8 GHz
Within this frequency range, high astrometric accuracy can be obtained, while unwanted ionospheric and tropospheric phase fluctuations are also reduced. It does however give a steeper pulsar spectrum, which is best observed at lower frequencies $\leq$1 GHz.

Data Rates
Science goal: Pulsar surveys
Requirement: continuous data streams
Need to handle continuous data streams up to many hours or days. This is due to the sampling of a large Field of View (FoV) during surveys [99].

Angular resolution
Science goal: Astrometric observations
Requirement: high angular resolution (1 mas at 5 GHz)

To have sufficient resolution so that accurate distances of pulsars can be obtained.

Time-resolution
Science goal: Search observations
Requirement: $\sim$50 μs
The time-resolution needs to be high enough to sample even the smallest pulse widths.

Science goal: Timing observations
Requirement: $\leq$1 μs
To produce the highest accuracy required for timing observations, very fast sampling is necessary (especially when observing MSPs).

Number of channels
Science goal: Search observations
Requirement: 1024 channels (across 400MHz)
To perform (incoherent) de-dispersion on the pulsar signal, it needs to be channelised sufficiently.

Field-of-View
Science goal: Pulsar surveys
Requirement: 1 deg^2 at 1.4 GHz
A fully sampled, wide FoV is required during search observation to cover large parts of the sky and thus reduce searching time.

Science goal: VLBI observations
Requirement: 1 deg^2 at 1.4 GHz

Multiple beams
Science goal: Timing observations
Requirement: 50–100 $beams/deg^2$
To observe more than one pulsar at the same time, the use of multiple beams is required.

Polarisation
Science goal: Timing observations
Requirement: high polarisation purity (- 40dB)
These observations require high polarisation purity, but only at the centre of the FoV and only after calibration.

6.5 Pulsar Receiver System Design for the SKA

From the technical specifications given by the previous section, a discussion about how these requirements will be met in the design now follows. Please refer back to this section when needed. First some general assumptions are set as basis for the discussion. The three types of pulsar observations search, timing and astrometric are then considered each as a separate system.

–> Antenna
The antennas and feeds that will be considered in this discussion are those that fall into the frequency range needed to do the pulsar observations. The lowest requirement is 400MHz and therefore sparse Aperture Arrays (AAs), optimal in the range 70–300 MHz, will not form a part of the design. Dense AAs can be considered, from 300MHz up to a maximum of 1GHz. Also for the parabolic reflectors, the Wide-Band Single Pixel Feeds (WBSPFs) and Phased Array Feeds (PAFs) can be included.

–> Antenna dimensions
The dish diameter that is used for the majority of the pathfinders described and most likely to be used for the SKA is 12m. This value results from various studies that includes cost, speed survey and sensitivity trade-offs. For the purposes of this discussion, this value will also be assumed [5] [1].

6.5.1 Search Observations

The first consideration is what type of antenna should form part of the design. One option would be to use dense AAs (up to 1 GHz) to do all-sky surveys, while dishes (with WBSPF or PAF) can be used for the Galactic plane (and centre) surveys. This reasoning follows from the frequency requirements [98]. The search for pulsars can be divided into two frequency ranges corresponding to the position in the sky where we will be observing. Let us refer to this as f_{high} and f_{low}.

- pulsars near the Galactic centre will be at f_{high} = 9–15 GHz
- pulsars at Galactic and extragalactic lines of sight will be at f_{low} = 0.5–5 GHz

For f_{low} either PAFs, dense AAs or WBSPFs (or a combination or these) can be used. For f_{high} the only option is to use WBSPFs, as these observations are at much higher frequencies. A factor that would further influence the choice in feed type is the FoV required. AAs as well as PAFs give wide FoV, while in general the FoV is limited by the computational resources [98]. In this case, the FoV requirement is 1 deg^2 at 1.4GHz and therefore AAs, PAFs and WBSPFs all can provide this.

To perform a survey, the signals from each element must be coherently added to form beams. The computational load from combining these signals increases with the square of the maximum baseline. It is therefore preferred to have a large number of short baselines. This can be achieved by using a dense core array with 1km diameter. Possible configuration designs will be discussed in the next section [95] [99] [100].

As mentioned in section 6.2.2, when incoherent de-dispersion is performed the bandwidth and number of channels needs to be chosen accordingly. The specification is that at least 1024 channels are needed across

400MHz and can be implemented in the filterbank. The correlator should be able to provide a time-resolution of $\sim 50\mu s$ as well as handle the high data rates needed. Tasks of the correlator should include sampling the FoV, doing a search analysis on pixels and enabling real-time post processing. Further studies are however needed to perfect these requirements.

When coherent de-dispersion is performed, special processors are needed. This may be implemented as part of the pulsar back-end. Where real-time post processing is necessary, the back-end must be able to provide this at the data rates required. Table 6.3 gives a summary of the system components discussed with the concluding design elements.

Table 6.3: Summary of system component design parameters for pulsar search observations.

System component	Design choice
Feeds	–> use WBSPF for f_{high} (f_{low} can also be considered) –> use PAF for f_{low} –> use dense AA for f_{low}
Configuration	–> Tight core, 1km diameter (see section 6.6.2)
Filterbank	–> number of channels: >1024 channels –> bandwidth: 400MHz
Correlator	–> Time resolution: $\sim 50\mu s$ –> handle high data rates
Back-end	–> real-time post processing –> coherent de-dispersion processor

6.5.2 Timing Observations

For pulsar timing, multi-frequency observations are required. It should therefore be able to observe over a broad band (2 octaves) simultaneously. This can be realised by using different types of feeds designed to work at different frequencies for each band required. An alternative would be to make use of sub-arrays, where each array is assigned a different part of the frequency band. The critical frequency range is 0.4–3 GHz. Therefore WBSPF, PAF, dense AA or a combination of these can be used to get 3 bands over 2 octaves. The requirement for multiple beams favors the use of PAFs and AAs however. A possible implementation could be to use the PAF over 0.4–1 GHz and the dense AA for 0.4–3 GHz.

When doing incoherent de-dispersion, the filterbank must provide a large and sufficient number of channels over the bandwidth (refer to section 6.2.2) [9]. The correlator should be able to provide the specified time-resolution of $\leq 1\mu s$ and also perform full Stokes calculations.

Multiple beams are required, specified as 50–100 $beams/deg^2$. This can be implemented by using a single FoV containing a number of beams, while an alternative would be to make use of multiple simultaneous FoV (see Appendix A.2). The FoV are then required to be separated by $10^\circ - 45^\circ$. The beamformer should therefore be capable of producing the required number of beams.

For coherent de-dispersion a hardware or software processor is required. This can be done using the beamformer (in frequency domain) or a pulsar-specific processor [95]. Table 6.4 gives a summary of the system components discussed with the concluding design elements.

Table 6.4: Summary of system component design parameters for pulsar timing observations.

System component	Design choice
Feeds	–> use PAF for 0.4–1 GHz –> use dense AA for 0.4–3 GHz
Configuration	–> non-critical
Correlator	–> Time resolution: $\leq 1\mu s$ –> Full Stokes parameters
Beamformer	–> 50–100 $beams/deg^2$ –> FoV separated by $10^\circ - 45^\circ$
Back-end	–> coherent de-dispersion processor

6.5.3 Astrometric Observations

For the frequency range of 2–8 GHz required, WBSPFs will be the most suitable feed type. For this type of observations, high angular resolution is needed. The resolution depends on the baseline distances, and therefore the antenna configuration. It is given that the antenna layout should be designed to include baselines of up to 8000km [95]. To get precise distances for pulsars 1 mas at 5GHz is needed [8]. VLBI observations with intercontinental baselines must also be considered as this will form part of these observations, providing the highest resolution. One design could include arranging a number of antennas into small stations far from the central core to form large baselines. These stations can then also be correlated with the central core [101].

The filterbank must be able to divide the band into the number of channels required, which is specified as 1024 channels across 400MHz. Table 6.5 gives a summary of the system components discussed with the concluding design elements.

Table 6.5: Summary of system component design parameters for pulsar astrometric observations.

System component	Design choice
Feeds	–> use WBSPF for 2–8 GHz
Configuration	–> baselines of up to 8000km (1 mas at 5 GHz) Small stations, distributed far from central core
Filterbank	–> number of channels: >1024 channels –> bandwidth: 400 MHz

This section considered the design parameters for the 3 types of pulsar observations. The purpose of this discussion was not to give a complete system design, but to envision the elements that need to be taken into account when designing such systems. This chapter now concludes with simulations of antenna layout designs for pulsar studies.

6.6 Antenna Layout Simulations for Pulsar Studies

One way of advancing the pulsar receiver system designs are to look at current SKA pathfinders. Two such pathfinders, the Australian Square Kilometre Array Pathfinder (ASKAP) and MeerKAT projects, already discussed in section 5.3.2 will in this section be evaluated for their pulsar observation capabilities. The layouts will then be extended to optimal layout designs for SKA pulsar observations that follow from the previous section's design specifications.

6.6.1 General assumptions

The total SKA configuration is specified to have the following collecting area distribution:

- 20% of the total collecting area within 1km diameter
- 50% of the total collecting area within 5km diameter
- 75% of the total collecting area within 150km diameter

with minimum baselines of 20m and maximum baselines of at least 3000km from the core. The core (within 5km diameter) will most likely contain sparse and dense AAs, as well as WBSPF and PAF dishes distributed in compact form. From the core outwards, dish antennas will be distributed in stations, most likely in the form of spiral arms. The furthest inter-continental baselines may also be included. The total collecting area specified is 1,000,000 m^2, with a total sensitivity of 20000 m^2/K at 1.4GHz. For this discussion however, we will design antenna layouts with only the pulsar science case in mind, while using the overall SKA configuration specifications as a guideline (see Appendix B).

The simulations for this section were made using *iAntConfig*, which is software that was developed to assist in designing antenna array layouts for the Karoo Array Telescope (KAT) and ASKAP projects [17]. The following general assumptions were made, while Table 6.6 summarises the parameters used that were similar for all simulations:

– the layouts do not take into consideration elevation and ground restrictions

– all simulations are done at 1.4GHz (to compare results)

– a snapshot observation is taken as 10 min

Table 6.6: Input parameters used for all simulations.

Dish diameter	12m
Frequency	1.4 GHz
Declination, hour angle	(-30.7, 1.4267)
Onsource time	10 min
Offsource time	0 min
Observation time	Snapshot and 4hour or 8 hour
Source position	Zenith

The layouts were evaluated and compared by using system performance metrics including the gain, sensitivity, survey speed, system equivalent flux density and rms noise. See Appendix B for the relevant equations, with general parameters used given by Table 6.7.

Table 6.7: Parameters used for calculation of system performance metrics.

T_{sys} (WBSPF)	30K
(PAF, dense AA)	35K
e_{ap} (dishes)	0.7
(dense AA)	0.8
FoV (WBSPF)	1 deg^2
(PAF)	>= 1 deg^2
(dense AA)	$\sim$ 200 deg^2

6.6.2 Pulsar survey layout simulations

To do pulsar surveys, or any survey for that matter, we want high survey speed. The survey speed increases with the FoV and (sensitivity)^2. Therefore we ideally want a large FoV to see more of the sky at any given time or have high sensitivity. However because of the large amount of computations involved with a survey, the reality for now is that we restrict the configuration to have only short baselines within about 1km diameter (as mentioned in section 6.5). This means that there is a limit to the amount of antennas that can be used (to correlate) and thus also the sensitivity.

For a Galactic centre survey, the area of interest in the sky is relatively small and the WBSPF FoV capability of 1deg^2 at 1.4GHz will be sufficient [102]. For PAF and dense AA, these antenna types can provide wider FoVs compared to the WBSPF. Especially for the all sky survey, the AA is capable to observe with very wide FoV which will be beneficial, reducing the survey time by a large factor. In all cases however, the FoV is limited by the system's computational capability. For now, these observations are requirement to have a FoV of 1deg^2 at 1.4GHz. The sensitivity required is estimated as $2000m^2/K$, which is 10% of the total SKA sensitivity. As the SKA technology develops and allow for handling higher data rates, the FoV, sensitivity and therefore also the survey speed will increase.

Based on the 3 core design as shown in Fig.5.6, the design of the larger core is chosen here to include WBSPF and PAF dishes together with the dense AA distributed over about 1km diameter smaller cores. Each of these cores can do observations independently with high sensitivity or be combined for example to do multi-frequency observations. This core design will be discussed more later, for now let us start with simulations of the ASKAP and MeerKAT cores.

ASKAP core

The ASKAP array layout was already discussed in section 5.3.2. For the purposes of this discussion, we will only consider the 2km diameter core of the array. The layout of the 26 dish antennas with PAF for this simulation is given by Fig.6.5.

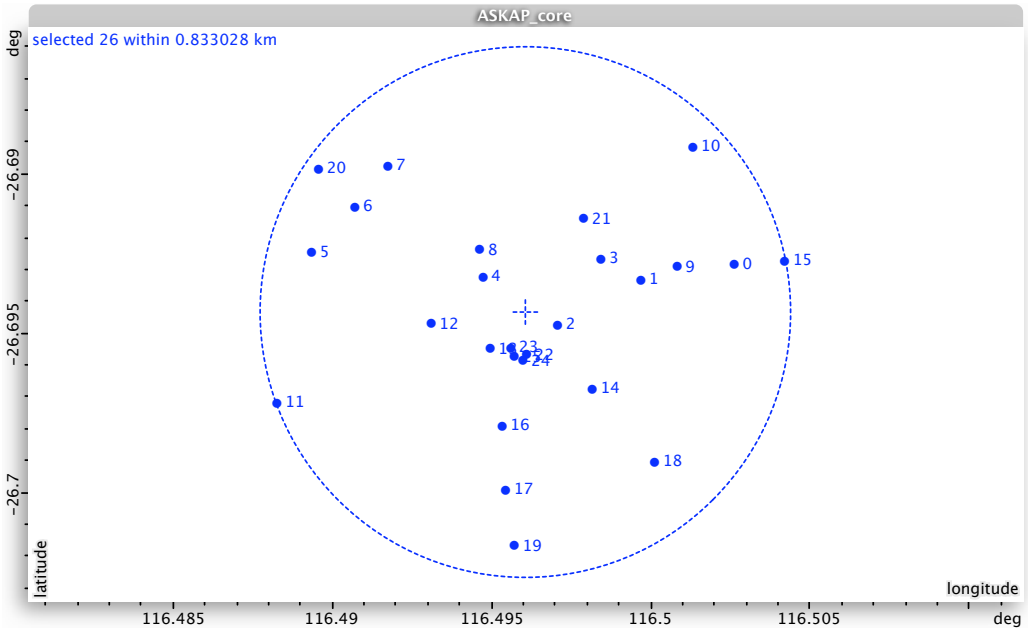

Figure 6.5: Antenna layout for the ASKAP core.

The u,v-distributions for this layout for a snapshot and 4hour observation are given by Fig.6.6 and Fig.6.7 respectively.

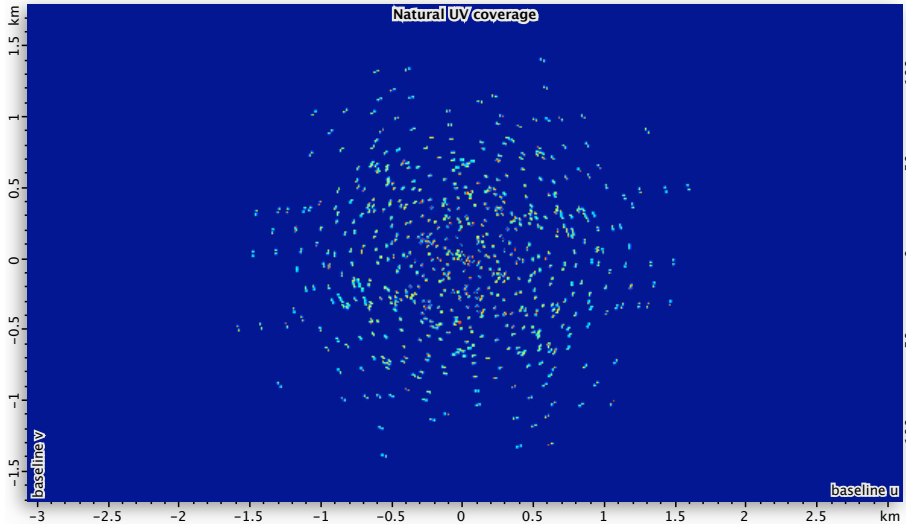

Figure 6.6: The u,v-coverage for a 10 min observation with the ASKAP core layout.

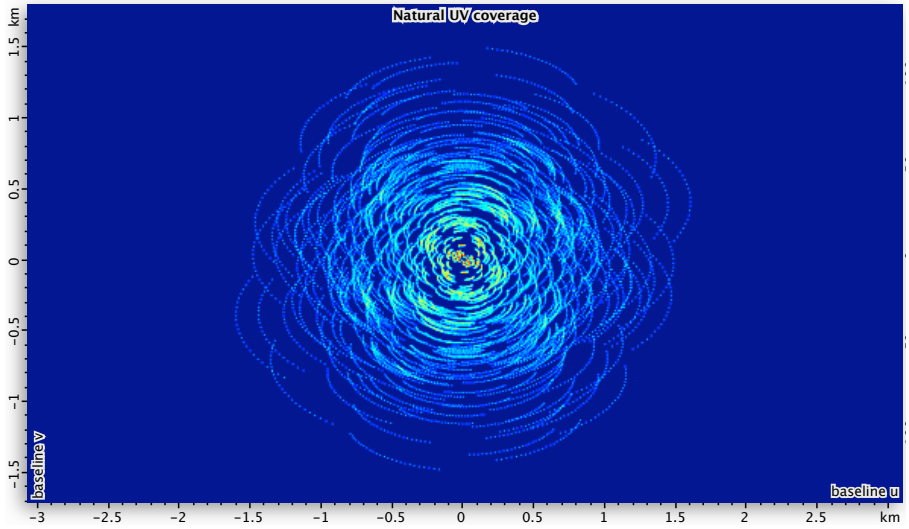

Figure 6.7: The *u*,*v*-coverage for a 4hour observation with the ASKAP core layout.

The *u*,*v*-distribution profile is given by Fig.6.8 with the snapshot (black) and 4hour (green) observations overlain. The *u*,*v*-coverage is not ideal. While the 4hour observation is an improvement from the snapshot case, the *u*,*v*-profile still shows a lot of spikes.

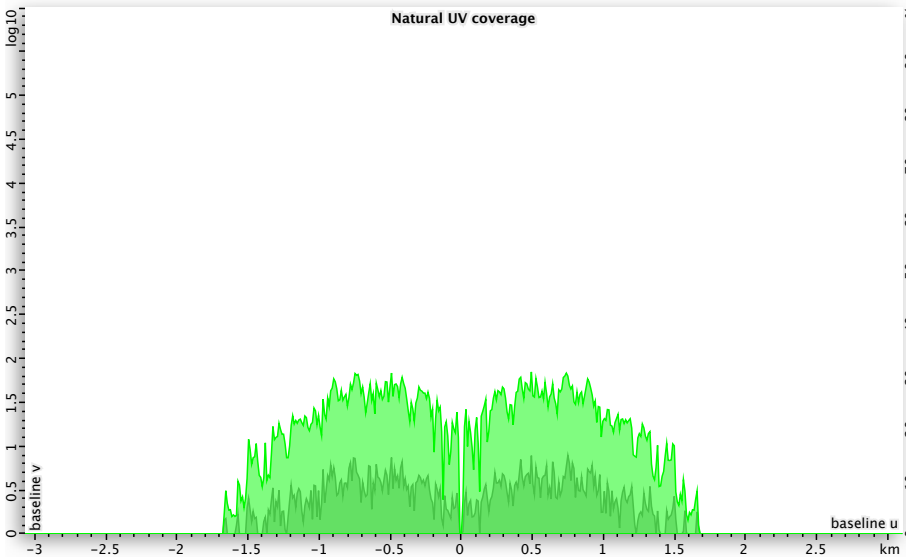

Figure 6.8: The ASKAP core layout *u*,*v*-coverage profile distribution for a 10 min (dark green) and 4 hour (green) observation.

The PSFs for the snapshot and 4hour observations are given by Fig.6.9 and Fig.6.10 respectively.

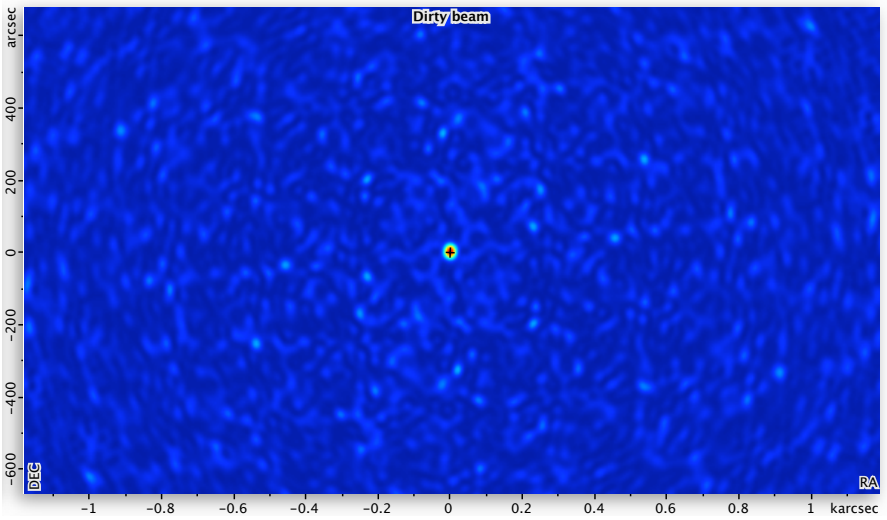

Figure 6.9: The corresponding PSF top view for a 10 min observation with the ASKAP core layout.

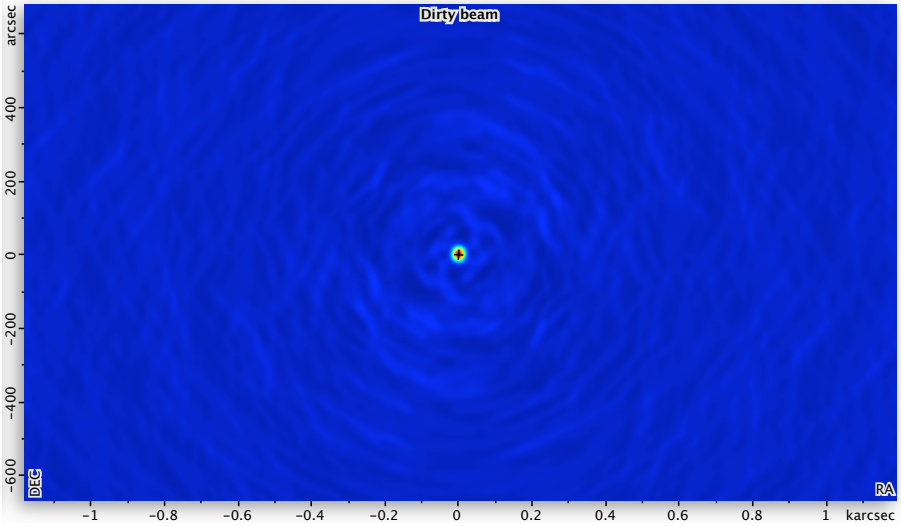

Figure 6.10: The corresponding PSF top view for a 4hour observation with the ASKAP core layout.

The PSFs are not ideal as can be seen by the noise in these maps. Fig.6.11 gives the horizontal profile of the PSF for the snapshot (black) and 4hour (green) observations, while a summary of the layout performance and system parameters are given by Table 6.8.

The theoretical highest resolution with b_{max} = 1660 m at 1.4GHz gives ∼26.6 arcsec. The simulated resolution is higher, but is not an accurate measurement as the PSF does not have a perfect Gaussian form. When the observation time is increased to about 8 hours, the PSF resolution value is a more accurate representation of the theoretical value. The side-lobe levels for the PSFs are too high; it should be significantly lower when doing surveys. Other parameters will be discussed later.

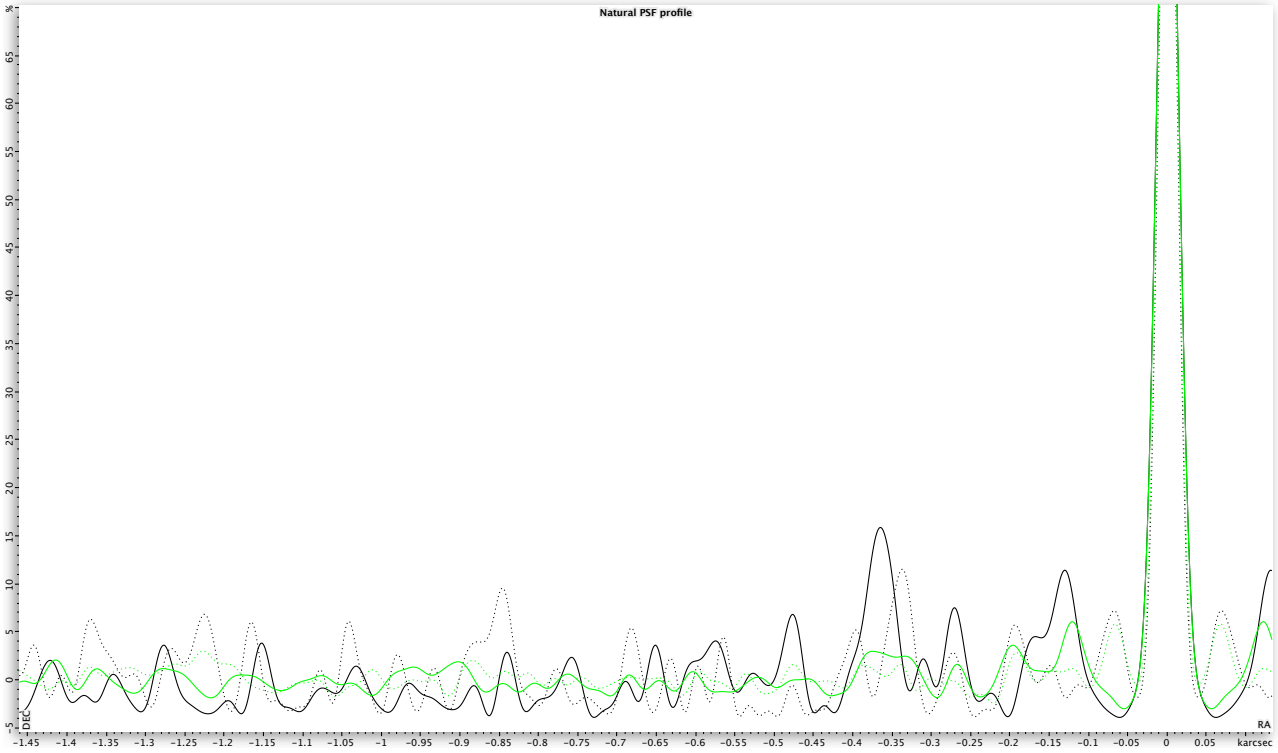

Figure 6.11: The horizontal profile of the PSF for snapshot (black) and 4hour (green) observations for the ASKAP core layout. The major and minor axis cross-sections are indicated by the solid and dotted lines respectively.

Table 6.8: Layout performance and parameters for the ASKAP core layout.

	snapshot	**4 hour**
side-lobe level (major)	(16%, -3.8%)	(6%, -1.8%)
side-lobe level (minor)	(11.5%, -3.9%)	(5.8%, -2%)
FWHM resolution (at 1.4GHz)	23.4 arcsec	
Number of antennas	26	
Number of baselines	325	
Configuration	random	
Maximum baseline	1660.52 m	
Minimum baseline	22.28 m	
Frequency Range	0.7–1.8 GHz	
Instantaneous Bandwidth	300MHz	
Number of polarisations	2	
A_{eff}	$2058.37m^2$	
$sensitivity$	$58.81m^2/K$	
FoV	30 $\deg^2$ (at 1.4GHz)	

MeerKAT core

For this layout, the MeerKAT 1km diameter core is considered (refer to section 5.3.2). The layout of the 53 dish antennas with WBSPF for this simulation is given by Fig.6.12.

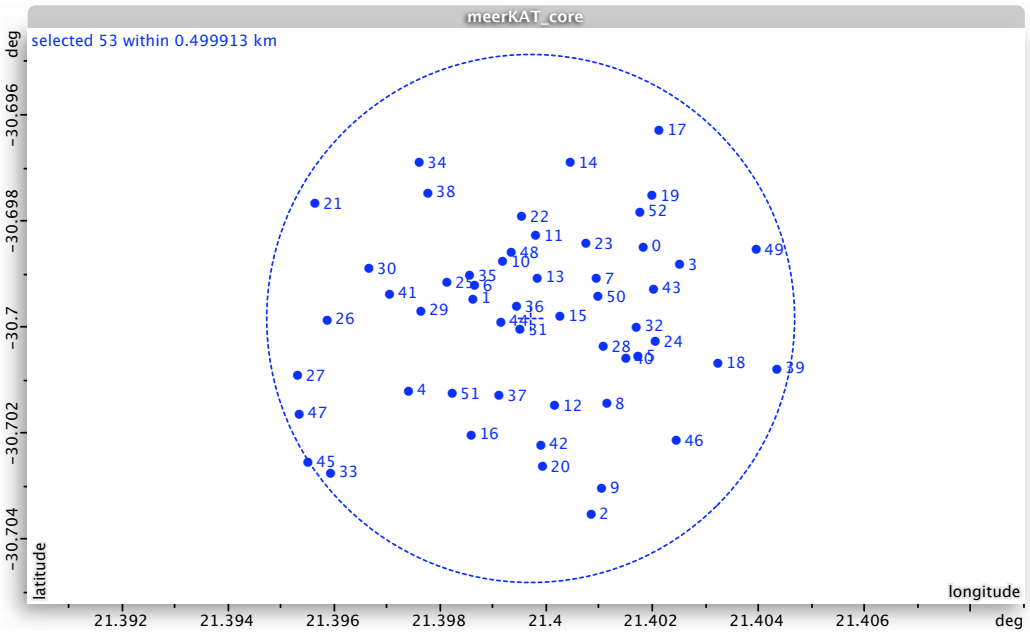

Figure 6.12: Antenna layout for the MeerKAT core.

The *u*,*v*-distributions for this layout for a snapshot and 4hour observation are given by Fig.6.13 and Fig.6.14 respectively.

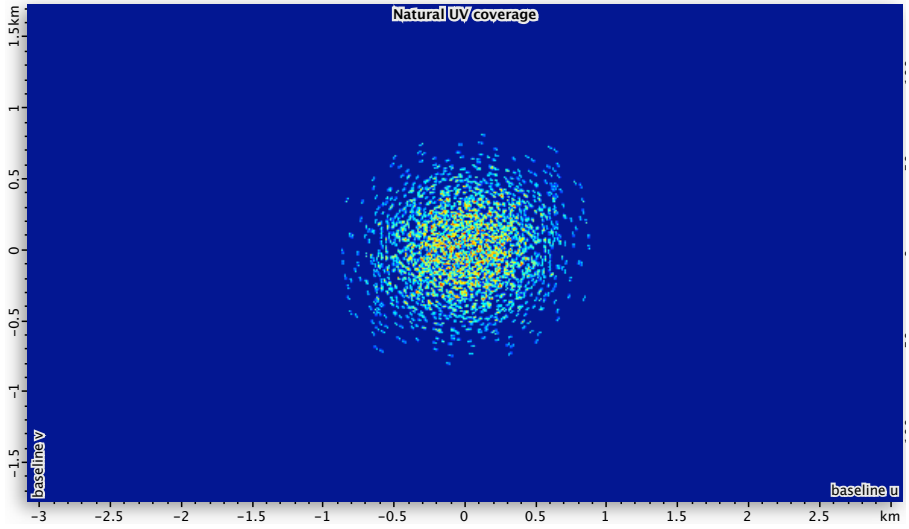

Figure 6.13: The *u*,*v*-coverage for a 10 min observation with the MeerKAT core layout.

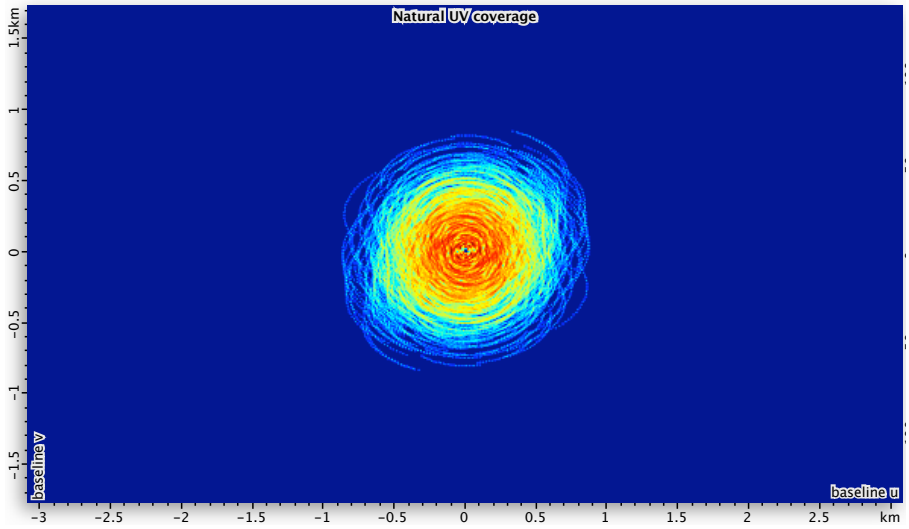

Figure 6.14: The *u*,*v*-coverage for a 4hour observation with the MeerKAT core layout.

The *u*,*v*-distribution profile is given by Fig.6.15 with the snapshot (black) and 4hour (green) observations overlain. The *u*,*v*-coverage is much better compared with the ASKAP core layout. This is due to the increase of antennas and smaller configuration. The *u*,*v*-profile is a lot smoother, but still not ideal.

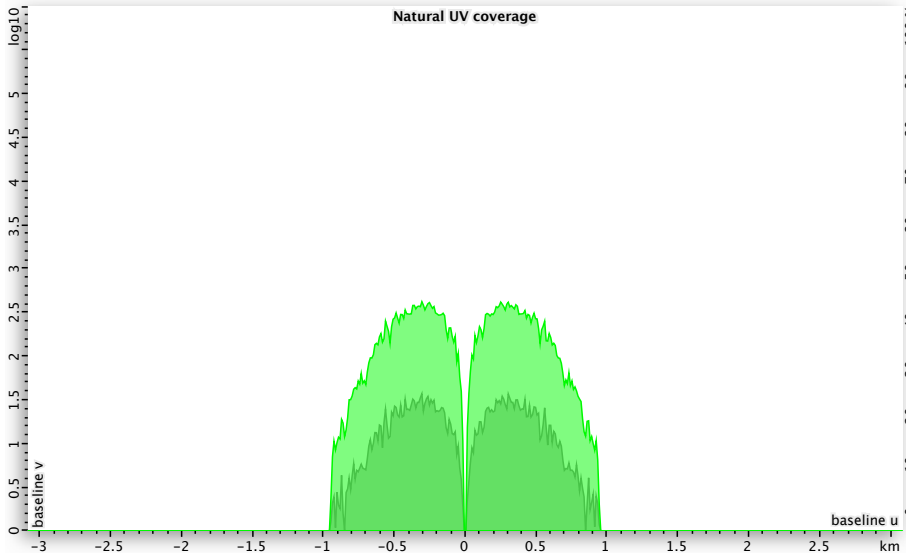

Figure 6.15: The MeerKAT core layout *u*,*v*-coverage profile distribution for a 10 min (dark green) and 4 hour (green) observation.

The PSFs for the snapshot and 4hour observations are given by Fig.6.16 and Fig.6.17 respectively.

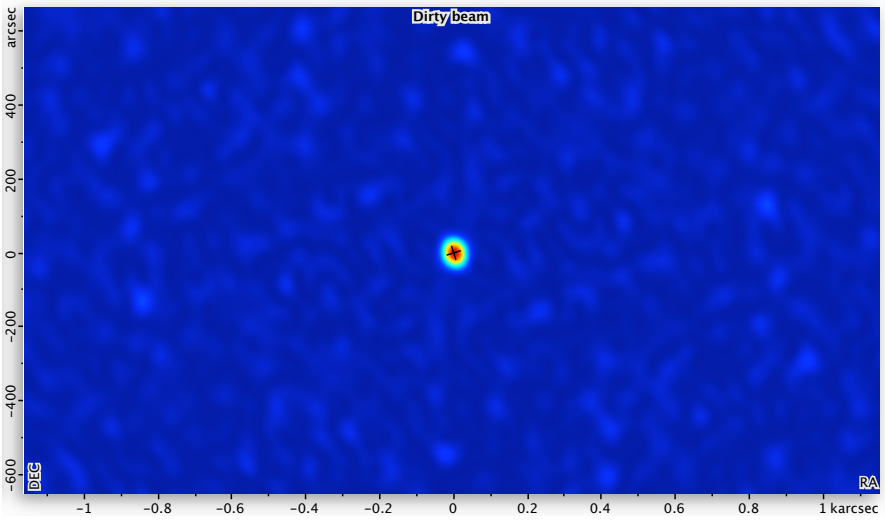

Figure 6.16: The corresponding PSF top view for a 10 min observation with the MeerKAT core layout.

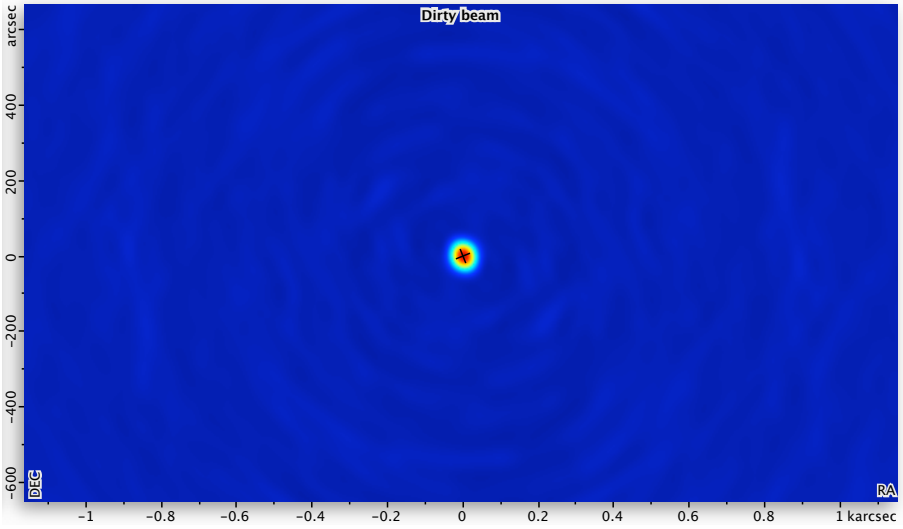

Figure 6.17: The corresponding PSF top view for a 4hour observation with the MeerKAT core layout.

Fig.6.18 gives the horizontal profile of the PSF for the snapshot (black) and 4hour (green) observations, while a summary of the layout performance and system parameters are given by Table 6.9.
The theoretical highest resolution with b_{max} = 940 m at 1.4GHz gives $\sim$47 arcsec. The simulated value will give a more accurate reading if the observation time is increased. The side-lobe levels are a bit high for the snapshot case, but relatively good for the 4hour case, being just over 1%. This is a good example where it can be seen how the uneven spikes in the u,v-coverage profile results in the side-lobes seen by the PSF profile.

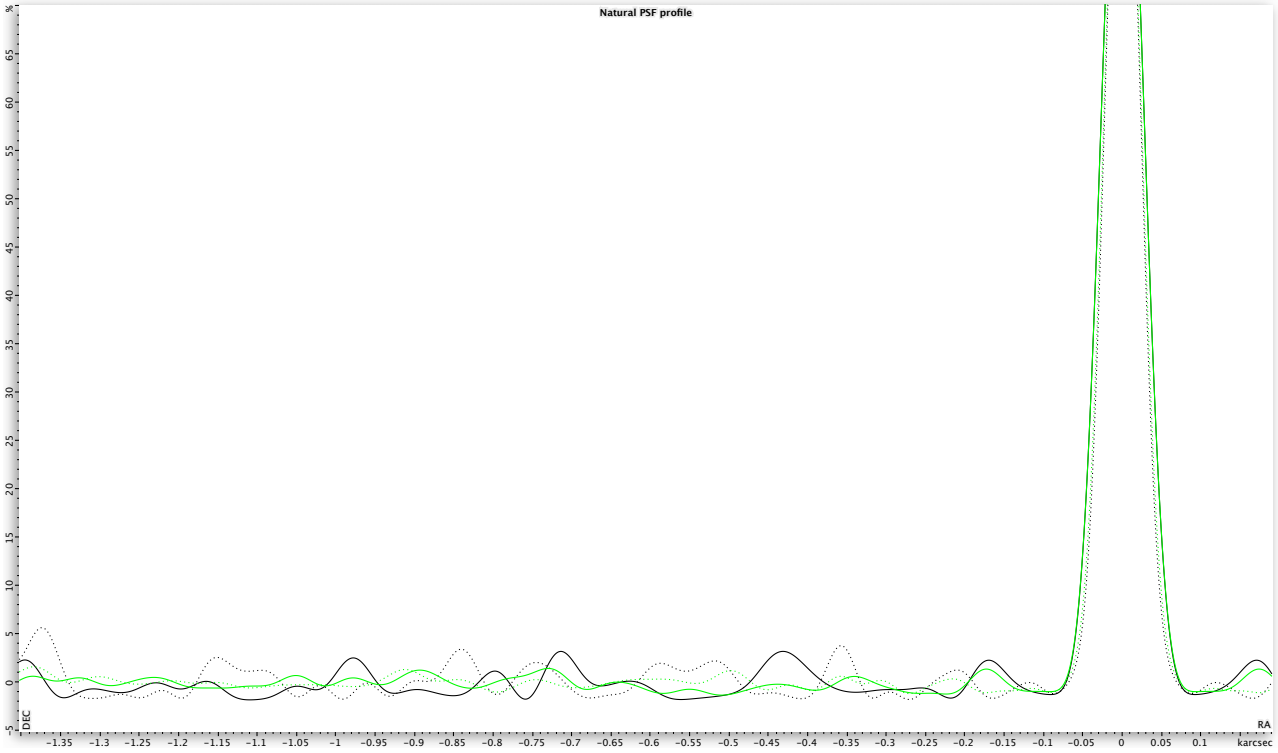

Figure 6.18: The horizontal profile of the PSF for snapshot (black) and 4hour (green) observations for the MeerKAT core layout. The major and minor axis cross-sections are indicated by the solid and dotted lines respectively.

Table 6.9: Layout performance and parameters for the MeerKAT core layout.

	snapshot	**4 hour**
side-lobe level (major)	(2.2%, -1.7%)	(1.3%, -1.3%)
side-lobe level (minor)	(5.6%, -1.7%)	(1.5%, -1.1%)
FWHM resolution (at 1.4GHz)	44.4 arcsec	
Number of antennas	53	
Number of baselines	1378	
Configuration	random	
Maximum baseline	939.69 m	
Minimum baseline	22.03 m	
Frequency Range	f_{high}= 8–14.5 GHz	
Instantaneous Bandwidth	512MHz	
Number of polarisations	2	
A_{eff}	$4195.91m^2$	
$sensitivity$	$139.86m^2/K$	
FoV	1 deg^2 (at 1.4GHz)	

With the high frequency range of MeerKAT, (∼10GHz or higher) pulsar searches near the Galactic Centre can be made. The frequency range of ASKAP, allows for pulsar surveys at Galactic and extragalactic planes of sight. When comparing the two pathfinder core simulations, the MeerKAT core has higher sensitivity, while ASKAP core has a higher FoV. The ASKAP array use PAF technology to form beams, thus allowing it to have a large FoV of 30 deg^2. The survey speed of ASKAP is therefore much higher than for MeerKAT even with less collecting area, making it a very good survey instrument.

Layout 1.1: Galactic Centre

This survey searches for pulsars at the Galactic centre with the frequency range f_{high}= 9–15 GHz. The specifications for this survey as discussed in section 6.5 will now be used to extend the MeerKAT core layout to an optimal pulsar layout design. The following changes in design should be considered:

- The frequency range is about the same, slightly shifted to 9–15 GHz. Therefore the same feed technology will be used (WBSPF).
- The correlator needs to have a higher time-resolution from 0.1 ms to $\sim 50\mu s$. The number of channels and instantaneous bandwidth required is sufficient, so that 1024 over 400MHz can be met.
- The configuration should be a 1km diameter core, while the number of antennas must increase. A 14.3% increase in sensitivity is required from 139.86m^2/K to 2000m^2/K, therefore an increase in antennas from 53 to 760.

–> The resulting layout design consists of 760 WBSPF antennas distributed uniformly within a 1km diameter core, as given by Fig.6.19 and will from here on be referred to as *Layout 1.1*.

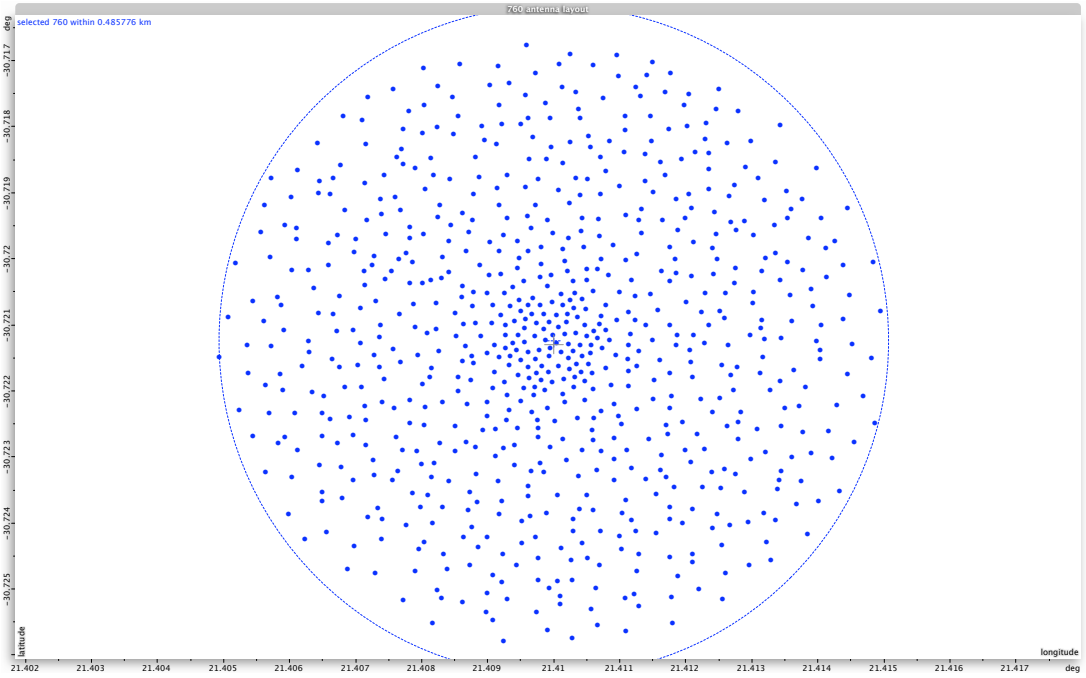

Figure 6.19: *Layout 1.1*: 760 antennas within 1km diameter.

The *u*,*v*-distributions for the snapshot and 4hour observation are given by Fig.6.20 and Fig.6.21 respectively.

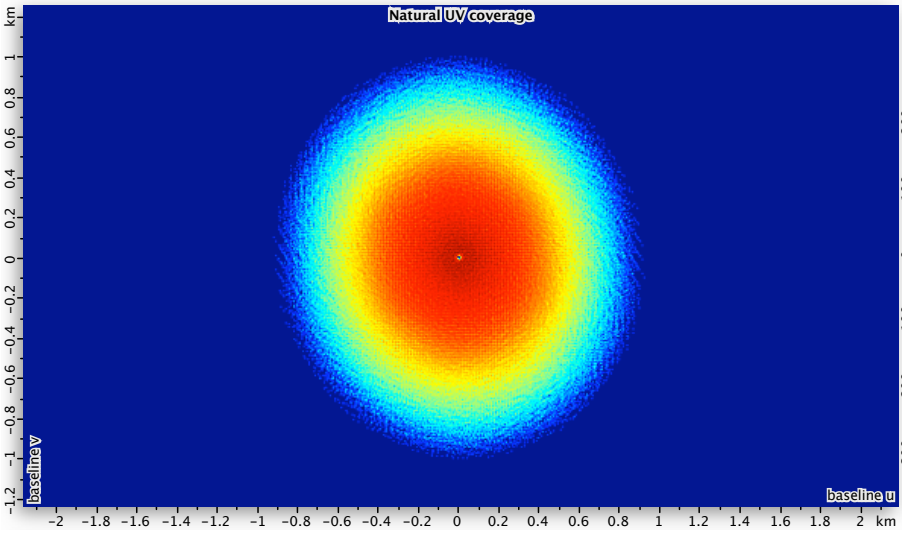

Figure 6.20: The *u*,*v*-coverage for a 10 min observation with *Layout 1.1*.

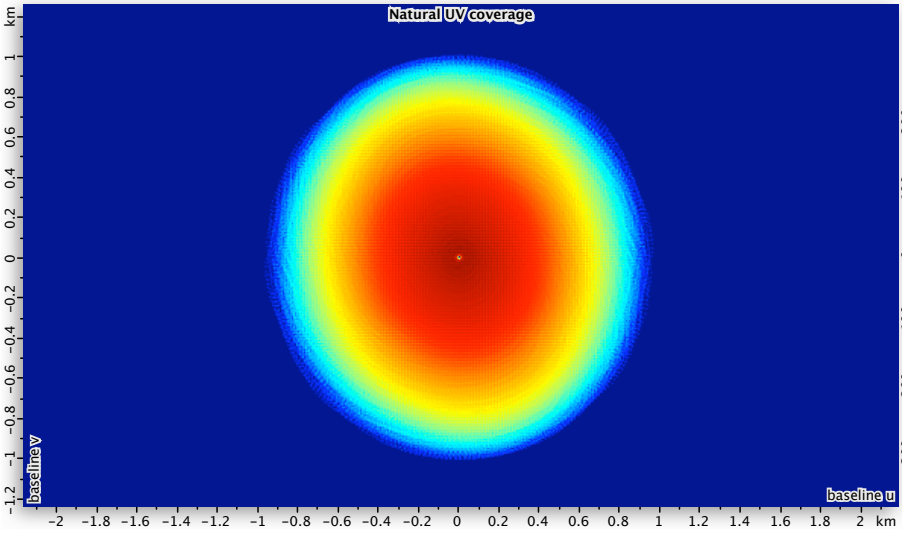

Figure 6.21: The *u*,*v*-coverage for a 4hour observation with *Layout 1.1*.

The *u*,*v*-coverage for the snapshot case is very good. The 4hour is even better, with almost a perfect covered uniform disk. The *u*,*v*-distribution profile is given by Fig.6.22 with the snapshot (black) and 4hour (green) observations overlain. The smooth *u*,*v*-coverage profile is very good and predicts that there will not be problematic side-lobes in the PSF.

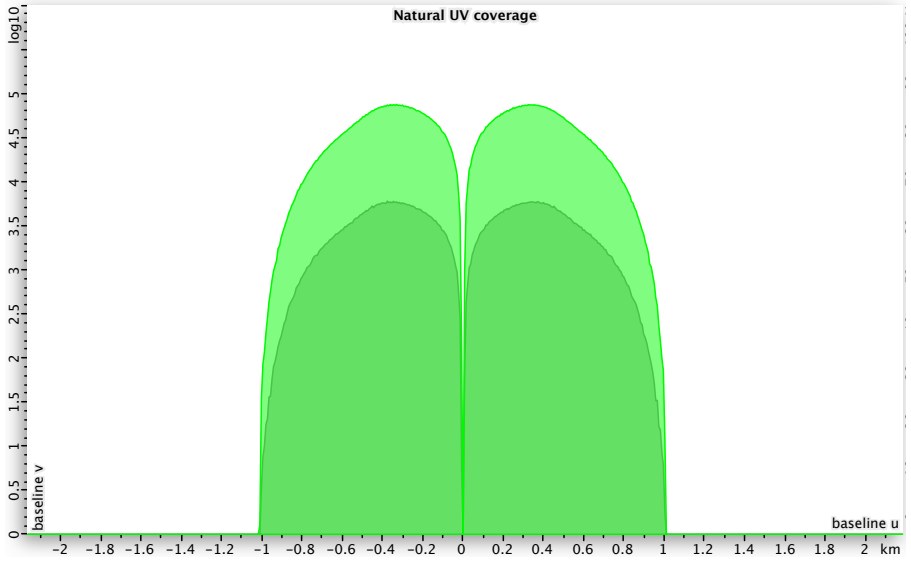

Figure 6.22: The *u*,*v*-coverage profile distribution for a 10 min (dark green) and 4 hour (green) observation with *Layout 1.1*.

The PSF for the snapshot observation are given by Fig.6.23. The PSF for the 4hour case is very similar and therefore not included here. Both PSFs are very smooth as expected from the good *u*,*v*-distributions.

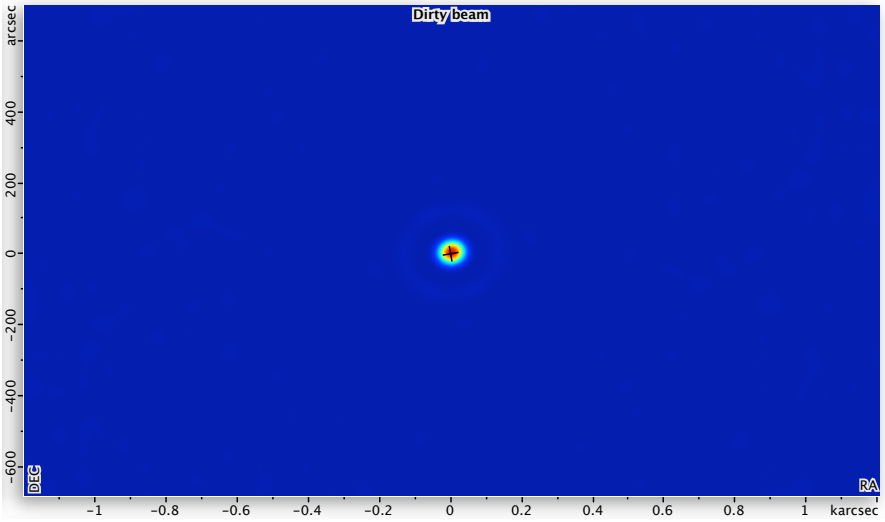

Figure 6.23: The PSF top view for a 10 min observation with *Layout 1.1*.

Fig.6.24 gives the horizontal profile of the PSF for the snapshot (black) and 4hour (green) observations, with a summary of the layout performance and system parameters given by Table 6.10.

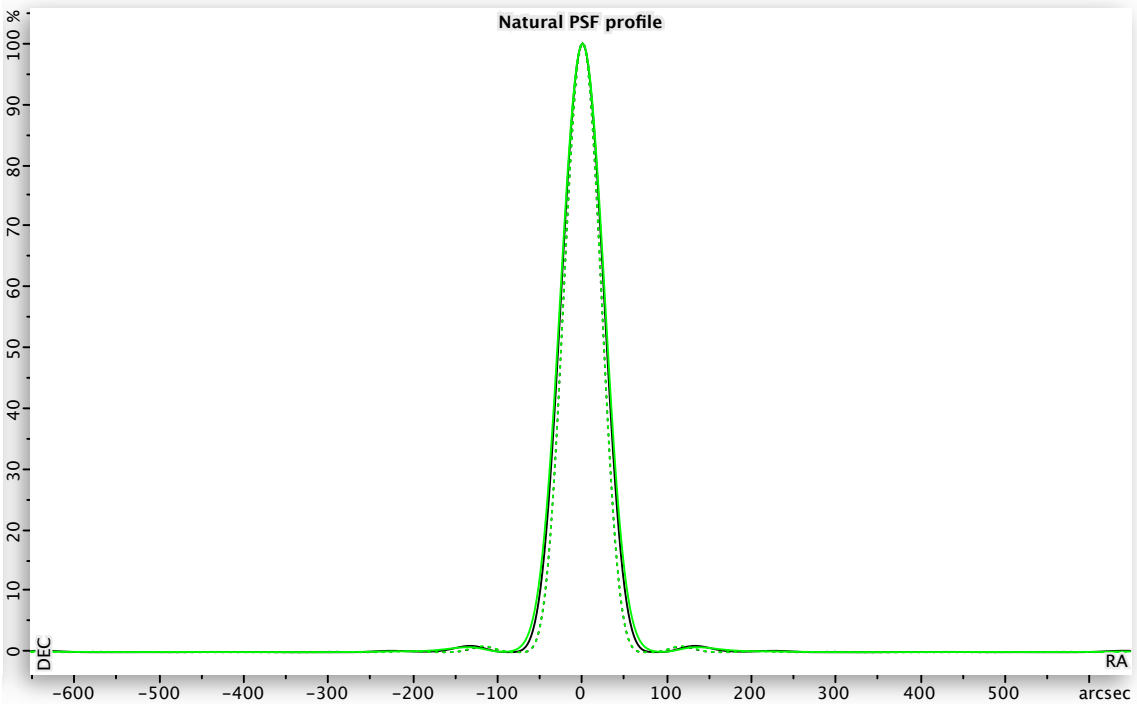

Figure 6.24: The horizontal profile of the PSF for snapshot (black) and 4hour (green) observations with *Layout 1.1*. The major and minor axis cross-sections are indicated by the solid and dotted lines respectively.

Table 6.10: Layout performance and parameters for for *Layout 1.1*.

	snapshot	**4 hour**
side-lobe level (major)	(0.9%, -0.1%)	(0.7%, -0.1%)
side-lobe level (minor)	(0.78%, -0.1%)	(0.85%, -0.1%)
FWHM resolution (at 1.4GHz)	41 arcsec	42.4 arcsec
Number of antennas	760	
Number of baselines	288420	
Configuration	random uniform	
Maximum baseline	1000.75 m	
Minimum baseline	12.42 m	
Frequency Range	9–15 GHz	
Instantaneous Bandwidth	400MHz	
Number of polarisations	2	
A_{eff}	$60167.78m^2$	
$sensitivity$	$2005.6m^2/K$	
FoV	1 $\deg^2$ (at 1.4GHz)	

The side-lobe levels are all very good - under 1% that of PSF main beam. The theoretical highest resolution with b_{max} = 1000.75 m at 1.4GHz gives ∼44.1 arcsec. The simulated PSF resolution compares very well with this theoretical value. The minimum baselines of 12.4 m apply to a few antennas at the centre of the array and

means the antennas are physically very close together. This was to make the design very compact without shadowing being a problem. For future design, the minimum baselines should be longer to about 20m, according to the SKA specifications. The layout can also be optimised that may result in even lower side-lobe levels.

To compare the MeerKAT core with *Layout 1.1*, the following performance metrics in Table 6.11 are calculated (refer to Appendix B.2).

Table 6.11: The MeerKAT core layout compared to *Layout 1.1* performance metrics.

	MeerKAT core	***Layout 1.1***
Effective collecting area (A_{eff})	4195.91 m^2	60167.78 m^2
Sensitivity (A_{eff}/T_{sys})	139.86 m^2/K	2005.6 m^2/K
FoV	1 $\deg^2$ at 1.4GHz	1 $\deg^2$ at 1.4GHz
Gain	1.5195 K/Jy	21.7897 K/Jy
Survey Speed	19560.82 $m^4 deg^2/K^2$	4022431.36 $m^4 deg^2/K^2$
System equivalent flux density (*SEFD*)	19.74 Jy	1.38 Jy
Rms noise	0.959 $nJy/beam$ (for t_{obs}=300s) 0.277 $nJy/beam$ (for t_{obs}=3600s)	1.514 $nJy/beam$ (for t_{obs}=3600s)

With both layouts having the same FoV, the survey speed difference is a direct result from the sensitivity. The sensitivity and gain of *Layout 1.1* is 14.3 times higher than for the MeerKAT core layout, giving an increase in the survey speed by a factor of 205. The rms noise is much lower for *Layout 1.1*, due to the large number of baselines and low SEFD.

Layout 1.2: Galactic and Extragalactic plane

This survey searches for pulsars at the Galactic and extragalactic planes of sight with the frequency range f_{low}= 0.5–5 GHz. The specifications for this survey as discussed in section 6.5 will now be used to extend the ASKAP core layout design to an optimal pulsar layout. The following changes in design should be considered.

- The frequency is over a wider range from 0.5–5GHz. Therefore, the same feed technology will be used (PAF) for the galactic plane survey, and dense AA for all sky surveys.
- The correlator needs to have a higher time-resolution of $\sim 50\mu s$. The number of channels is sufficient and the instantaneous bandwidth should be increased from 300MHz to 400MHz.
- The configuration should be a 1km diameter core, while the number of antennas must increase. A 34% increase in sensitivity from $58.81 m^2/K$ to $2000 m^2/K$ is required and therefore an increase in antennas from 26 to 886.

For the all sky survey, dense AA can be closely packed as they do not shadow each other [1]. Therefore, a higher sensitivity can be achieved for the same physical area. Although only $2000 m^2/K$ is required, we design the layout for at least $10000 m^2/K$. This is to add significantly to the collecting area within the core so that the SKA requirement of 50% within 5km diameter is met. This corresponds to a physical collecting area of

$437500m^2$ that will be distributed within a larger 1.5km diameter core as shown in Fig.6.25. This design will not be simulated here.

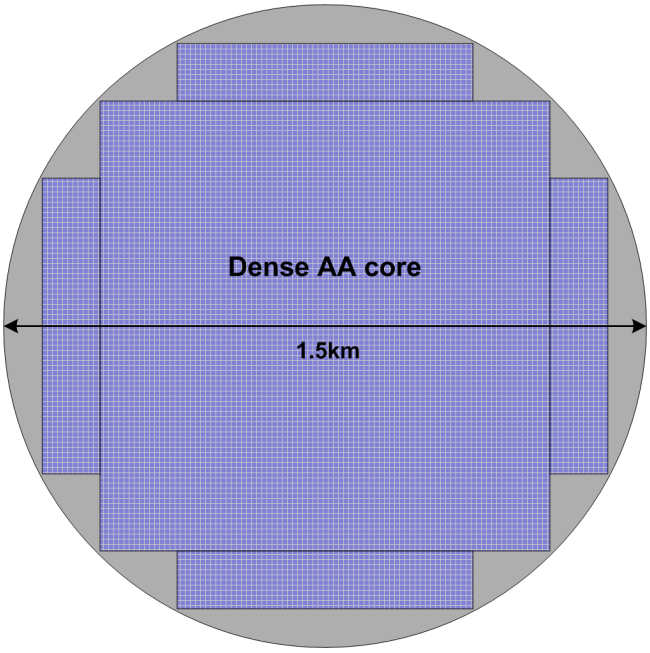

Figure 6.25: An illustration of the dense AA core design.

–> The resulting layout design consists of 886 PAF antennas distributed uniformly within a 1km diameter core, as given by Fig.6.26 and will be referred to as *Layout 1.2*.

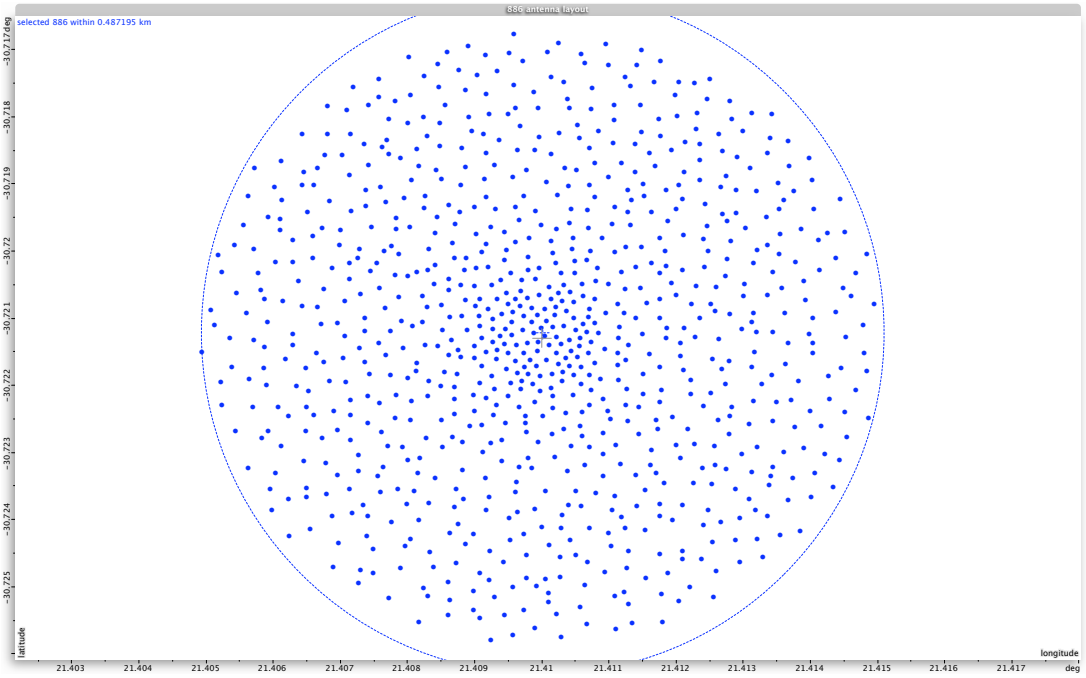

Figure 6.26: *Layout 1.2*: 886 antennas within 1km diameter.

In terms of the simulation results, the *u*,*v*-coverage and PSF top views are almost identical to that of *Layout 1.1* and will not be included here, refer to (Fig.6.20, Fig6.21 and Fig.6.23). Consider the *u*,*v*-distribution profile given by Fig.6.27 with the snapshot (black) and 4hour (green) observations overlain.

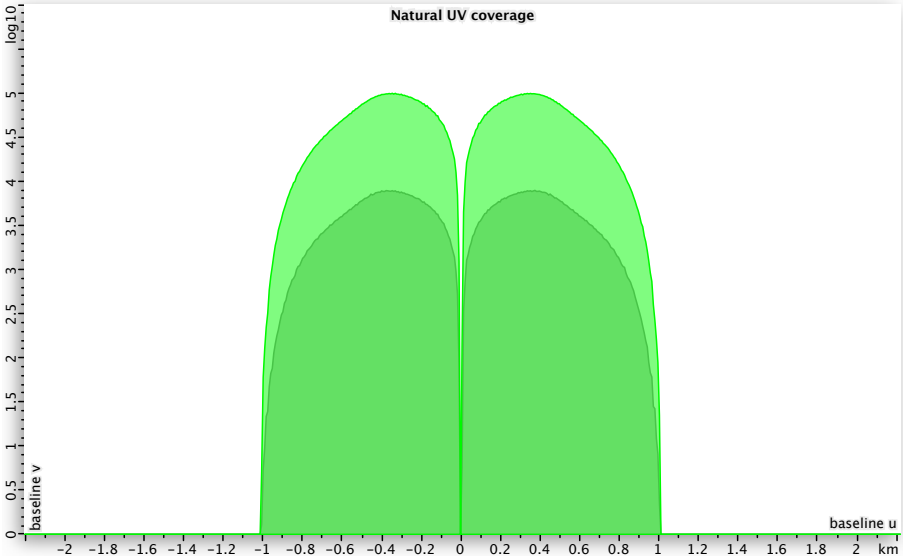

Figure 6.27: The *u*,*v*-coverage profile distribution for a 10 min (dark green) and 4 hour (green) observation with *Layout 1.2*.

As with *Layout 1.1*, the *u*,*v*-distribution profile is smooth and gives good coverage. Fig.6.28 gives the horizontal profile of the PSF for the snapshot (black) and 4hour (green) observations, followed by a summary of the layout performance and system parameters in Table 6.12.

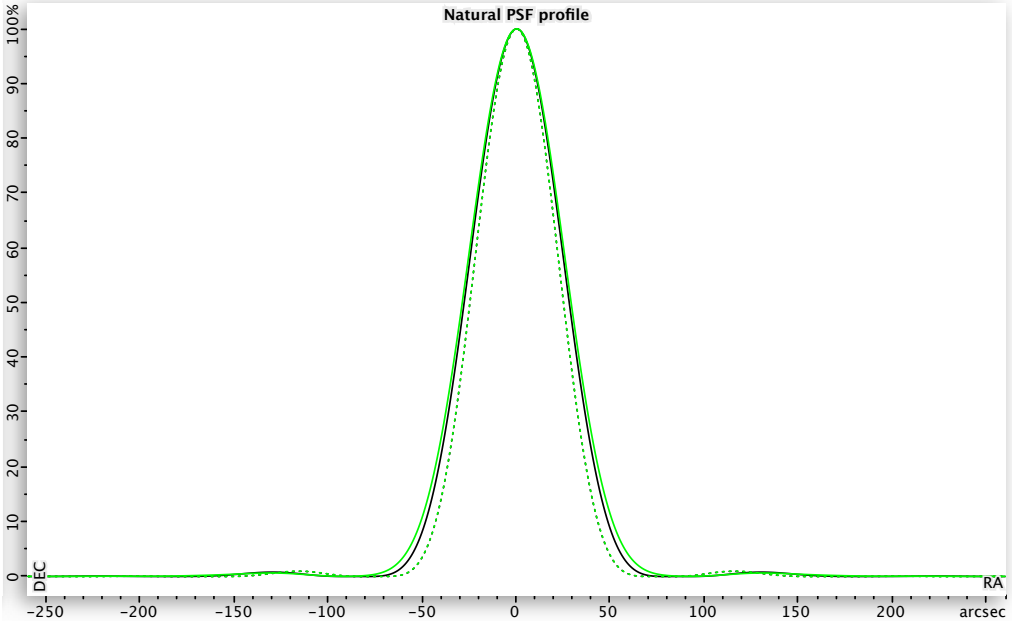

Figure 6.28: The horizontal profile of the PSF for snapshot (black) and 4hour (green) observations with *Layout 1.2*. The major and minor axis cross-sections are indicated by the solid and dotted lines respectively.

Table 6.12: Layout performance and parameters for for *Layout 1.2*.

	snapshot	**4 hour**
side-lobe level (major)	(0.7%, -0.1%)	(0.5%, -0.1%)
side-lobe level (minor)	(0.85%, -0.1%)	(0.87%, -0.1%)
FWHM resolution (at 1.4GHz)	39.84 arcsec	41.44 arcsec
Number of antennas	886	
Number of baselines	392055	
Configuration	random uniform	
Maximum baseline	1000.75 m	
Minimum baseline	12.42 m	
Frequency Range	0.5–5GHz	
Instantaneous Bandwidth	400MHz	
Number of polarisations	2	
A_{eff}	$70142.97m^2$	
$sensitivity$	$2004.08m^2/K$	
FoV	1 $\deg^2$ (at 1.4GHz)	

The side-lobe levels are all very good - under 1% of the PSF main beam. The theoretical highest resolution with b_{max} = 1000.75 m at 1.4GHz gives $\sim$44.1 arcsec. The simulated PSF resolution compares very well with this theoretical value.

To compare the ASKAP core with *Layout 1.2*, the following performance metrics in Table 6.13 are calculated (refer to Appendix B.2).

Table 6.13: The ASKAP core layout compared to *Layout 1.2* performance metrics.

	ASKAP core	***Layout 1.2***
Effective collecting area (A_{eff})	2058.37 m^2	70142.97 m^2
Sensitivity (A_{eff}/T_{sys})	58.81 m^2/K	2004.08 m^2/K
FoV	30 $\deg^2$ at 1.4GHz	1 $\deg^2$ at 1.4GHz
Gain	0.745 K/Jy	25.4 K/Jy
Survey Speed	103758.48 m^4deg^2/K^2	4016336.646 m^4deg^2/K^2
System equivalent flux density ($SEFD$)	46.95 Jy	1.38 Jy
Rms noise	6.1384 $\mu Jy/beam$ (for t_{obs}=300s) 1.772 $\mu Jy/beam$ (for t_{obs}=3600s)	1.2987 $nJy/beam$ (for t_{obs}=3600s)

The increase in antennas of *Layout 1.2*, results in a sensitivity and gain that is 34 times that of the ASKAP core. The ASKAP array has a very large FoV of 30 $\deg^2$. The FoV for layout 1.2 is smaller with 1 $\deg^2$, but the high sensitivity results in a survey speed of $\sim$38 times faster than the ASKAP layout. For future design, the use of multiple beams with the PAF technology can make the FoV of *Layout 1.2* larger and thus increase the survey speed even more.

If we were to evaluate the dense AA layout, we get the following results as given by Table 6.14.

Table 6.14: The dense AA design layout performance metrics.

Frequency range	0.5–5GHz	
Bandwidth	400MHz	
Number of polarisations	2	
	Full sensitivity	Fraction of full sensitivity
Physical collecting area	437500 m^2	87500 m^2
A_{eff}	350000 m^2	70000 m^2
Sensitivity	10000 m^2/K	2000 m^2/K
FoV	$\sim$200 deg^2	$\sim$200 deg^2
Gain	158.44 K/Jy	2.54 K/Jy
Survey Speed [$m^4 deg^2/K^2$]	2×10^{10}	8×10^8
System equivalent flux density (SEFD)	0.276 Jy	1.38 Jy

The assumption is that the dense AAs will have a FoV of at least 200 deg^2 at 700MHz. If we only use a fraction of the total collecting area design that corresponds to a sensitivity of 2000 m^2/K, the result is a very high survey speed that is 200 times faster than even for *Layout 1.2*. This feasibility of this will however depend on the computing power of the correlator.

Layout 1.2 is now compared with other single dish instruments that are often used for their pulsar survey capability. Table 6.15 summarises the performance parameters and metrics for the *Parkes 64m dish*, *Arecibo L-band Feed Array (ALFA)* and the *Green Bank Telescope (GBT)* [9].

Table 6.15: Performance parameters and results for various telescopes.

	Parkes 64m dish	***Arecibo (ALFA)***	***GBT***
Dish diameter (D_{dish})	64m	305m	100m
Aperture efficiency (A_{eff})	0.57	0.4	0.7
Frequency	1.23–1.53 GHz	1.225–1.525 GHz	1.15–1.73 GHz
Bandwidth	288MHz	300MHz	400MHz
Number of channels	96	1024	1024
Number of polarisations (n_{pol})	2	2	2
Number of beams (N_b)	13	7	1
Beamsize ($FWHM$)	14 arcmin	3.6 arcmin	9.2 arcmin
Sampling time	250 μs	64 μs	64 μs
Integration time (t_{obs})	2100s	268s	900s
System temperature (T_{sys})	23.5K	30K	20K
FoV	0.8 deg^2	0.027 deg^2	0.027 deg^2
Affective collecting area	1833.68 m^2	29224.67 m^2	5497.79 m^2
Sensitivity	78.03 m^2/K	974.16 m^2/K	274.89 m^2/K
SEFD	35.39 Jy	2.83 Jy	10.05 Jy
Gain	0.66 K/Jy	10.58 K/Jy	1.99 K/Jy
Survey Speed [$m^4 deg^2/K^2$]	4870.9447	25622.6681	3020.2418
Rms noise	0.03217 $mJy/beam$	7.0574 $\mu Jy/beam$	0.0118 $mJy/beam$

The Parkes dish is known for its excellent capability of pulsar surveys. The multiple beams used (as mentioned in section 5.3.1), results in a large FoV of ∼80% of the SKA requirement, giving it a high survey speed. *Layout 1.2* however has the largest FoV from using the smallest dish diameter. It also has a higher sensitivity of ∼25 times that of the Parkes, resulting in a survey speed that is faster with a factor of ∼820. Arecibo is the largest single dish telescope in the world and has the highest sensitivity of the three telescopes discussed here. *Layout 1.2* has a higher sensitivity with a factor of ∼2 compared to the Arecibo and a factor of ∼7 compared with the GBT. The rms noise for *Layout 1.2* is a factor of 184 or more lower than the other instruments, due to the large number of baselines and low SEFD.

As a final remark, from the simulations made in this section, it was shown that with ∼760 antennas, the *u*,*v*-plane is filled efficiently even in snapshot mode. The resulting natural PSF therefore has ideal low side-lobes. For future designs, the minimum baselines should be made larger (∼20m) according to the SKA specifications. These layouts do not take the terrain restrictions into account and therefore will need to be designed with this in mind. The layouts could also be optimised that may lead to a better PSF with lower side-lobes. Within the minimum and maximum baseline requirements, there are only a limited number of antennas that can be fitted into the 1km diameter area. This gives a maximum sensitivity which is about 2 times higher than any existing radio instrument. To increase the survey speed, a larger FoV is required that can be achieved by using the beamforming capability of the PAFs. The AAs can also provide very high survey speed, depending on the systems computational capability. Nevertheless, the current FoV specification together with the high sensitivity

for both *Layout 1.1* and *1.2* results in a very fast survey speed compared to existing instruments, with a factor of ∼150 times.

6.6.3 Pulsar timing layout simulations

For pulsar timing, there are factors that limit the time-of-arrival precision and therefore a high sensitivity is required [9]. This can be achieved by using a large fraction of the total SKA collecting area. About $10000m^2/K$ or even up to $20000m^2/K$ will be required; this means we will need to use more antennas than for the pulsar survey case to increase the collecting area. For the SKA design, the layout beyond the 5km diameter will most likely be in the form of antenna stations, distributed in spiral form. Seeing that the configuration is not critical for pulsar timing, we will therefore follow from this design and use a central core with the minimum added antenna stations to get a sensitivity of $10000m^2/K$. The station layout design was chosen to give optimal *u*,*v*-coverage and keep to the SKA collecting area requirements. As mentioned in section 6.5, beamforming will be required with 50–100 $beams/deg^2$ as well as multi-frequency observations. These requirements can be implemented by the PAF and AA technologies, by using different feed types simultaneously or forming sub-arrays. The sampling time should be faster than for pulsar searches, about $\leq 1\mu s$ to provide more accuracy.

First we need to define the main core layout. The design chosen here was to combine the PAF (*Layout 1.2*), WBSPF (*Layout 1.1*) and AA core layouts into a single main core. Further antennas were then added onto this main core to increase the collecting area while also providing a more complete *u*,*v*-coverage. It was placed in such a way that gave the lowest side-lobes. This results in a 2.7km diameter core that makes up ∼57% of the total SKA collecting area. Although the SKA specifies 50% of the collecting area within 5km diameter, it was found that the combination of these three layouts give better *u*,*v*-coverage when placed closer together. Fig.6.29 shows the layout structure[2].

[2]For the purposes of the simulation, the AA core was represented as dishes. This is to add physical aperture to fill the AA gap and must be kept in mind when evaluating the total layout performance.

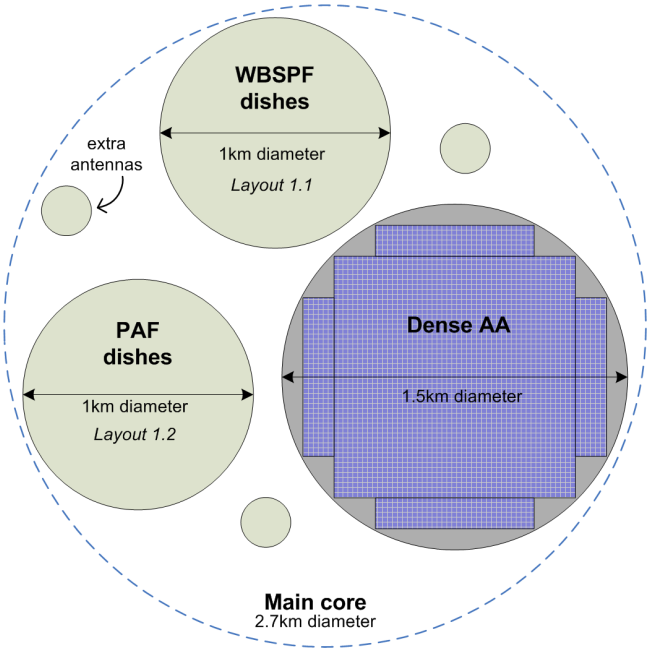

Figure 6.29: The main core design consisting of *Layout 1.1*, *Layout 1.2* and the AA layout with 3 disks of added antennas

The main core *u*,*v*-coverage top view and profile for snapshot mode is given by Fig.6.30. This gives a good *u*,*v*-coverage, although not perfectly circular. As can be seen by the *u*,*v*-distribution profile, the peaks are flattened that will cause side-lobes in the PSF.

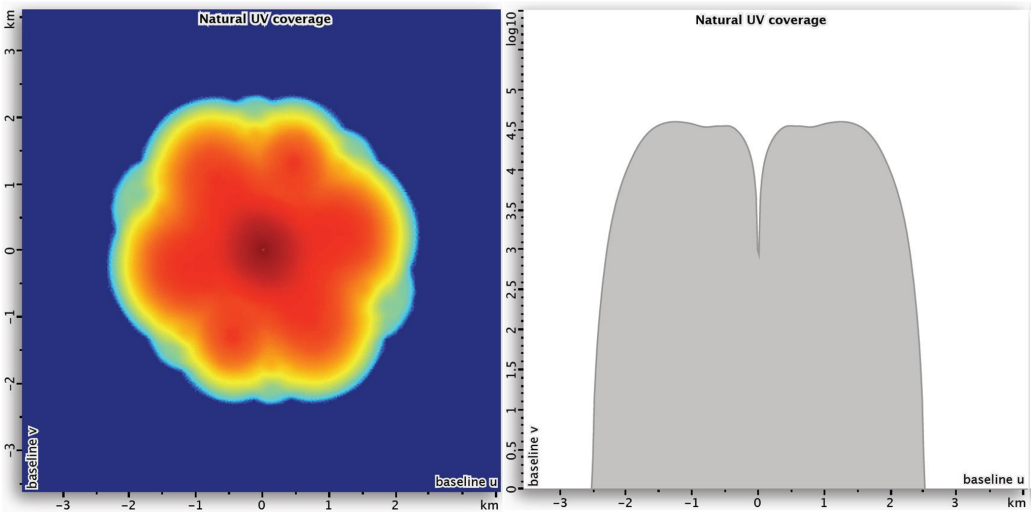

Figure 6.30: The *u*,*v*-coverage top view (left) and profile (right) for snapshot mode with the main core layout.

The PSF top view for the snapshot case is given by Fig.6.31. It is relatively smooth with noise near the centre. The PSF profile for the snapshot case is given by Fig.6.32. The side-lobe levels are not ideal - about 4.7% of the main beam, but will be less when the observing time is increased when used with the spiral layout.

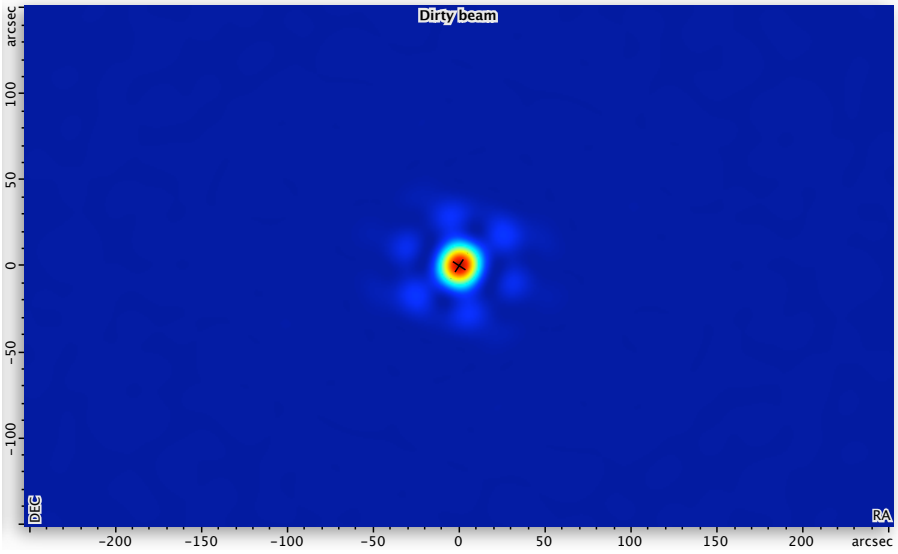

Figure 6.31: The PSF top view for snapshot mode with the main core layout.

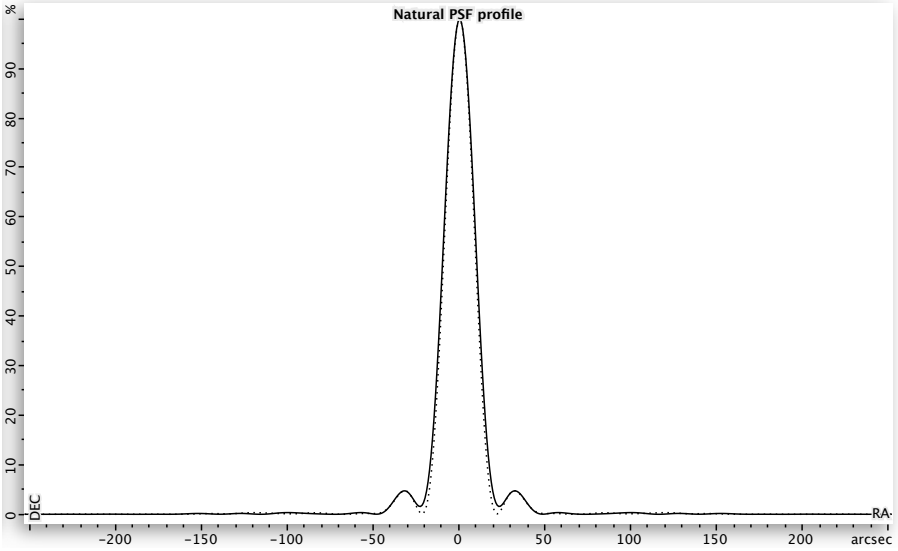

Figure 6.32: The PSF profile for snapshot mode with the main core layout.

Layout 2.1

This main core is now used as part of the spiral layout design given by Fig.6.33 and is described as follows. A total of 30 stations made up of 90 antennas each are distributed in the form of a 5-arm log spiral so that each arm consists of 6 stations. The antenna signals per station will most likely be phased together to simulate a single antenna.

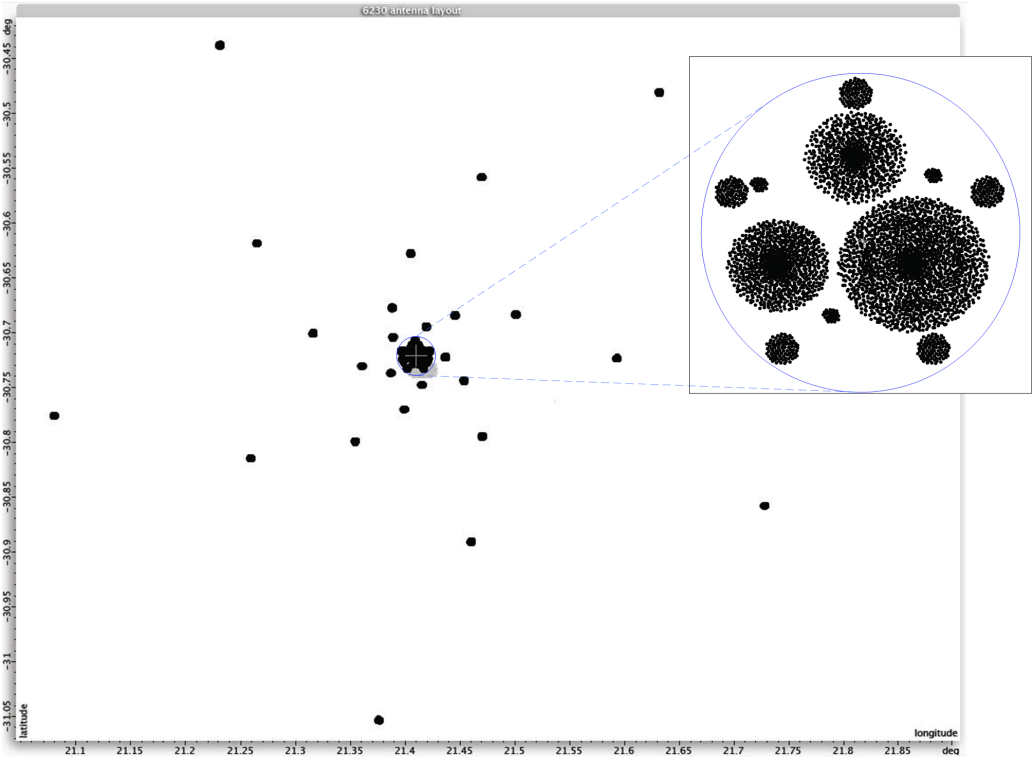

Figure 6.33: *Layout 2.1*: The main core with added stations in a 5-arm log spiral.

The baselines will therefore only be formed between stations and the main core [103]. The spiral shape concept is part of the SKA configuration design. The number of antennas was chosen that, together with the main core it can result in a sensitivity of $\sim 10000 m^2/K$. The result is that the spiral (without the main core) contributes $\sim$30% of the SKA collecting area within $\sim$70km diameter. The *u*,*v*-coverage and PSF for a 4hour observation with *Layout 2.1* is given by Fig.6.34.

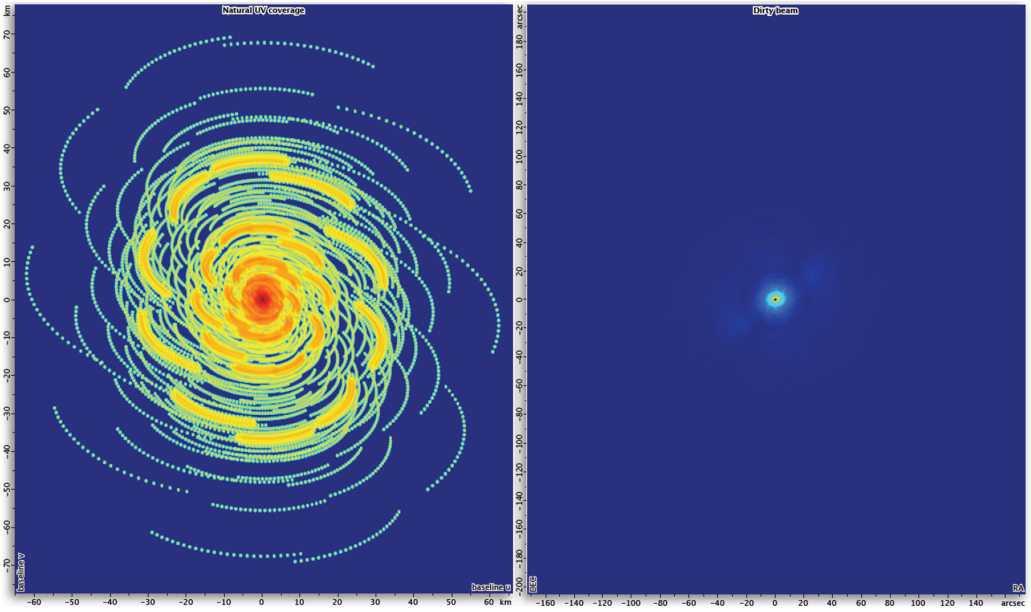

Figure 6.34: The *u*,*v*-coverage (left) and PSF (right) for a 4hour observation with *Layout 2.1*.

The spiral layout takes advantage of the fact that the Earth rotates and result in arcs that form on the *u*,*v*-plane to give increased *u*,*v*-coverage compared to a snapshot observation. The *u*,*v*-coverage profile is given by Fig.6.35 for a 4 hour observation. Various spikes can be seen that will cause side-lobes.

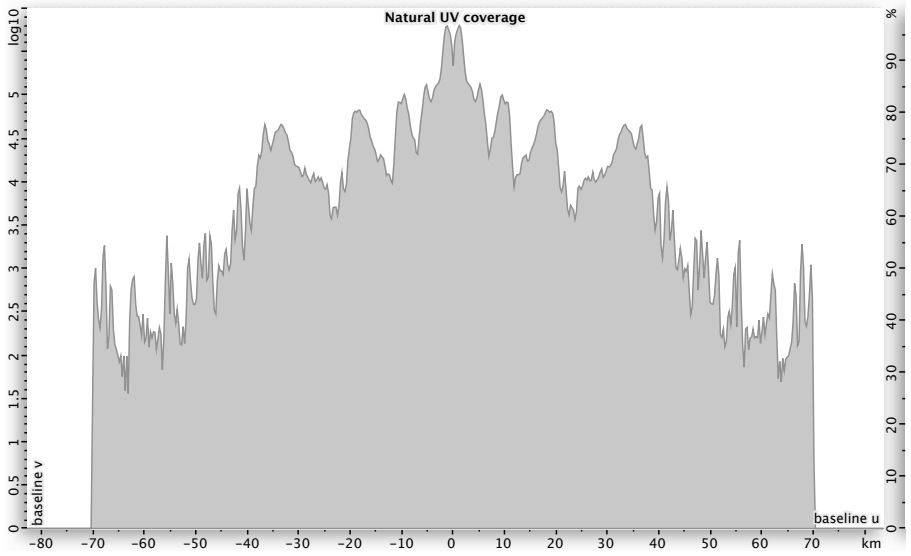

Figure 6.35: The *u*,*v*-coverage profile for a 4hour observation with *Layout 2.1*.

Fig.6.36 gives the PSF profile for both a snapshot (green) and 4hour (black) observation.

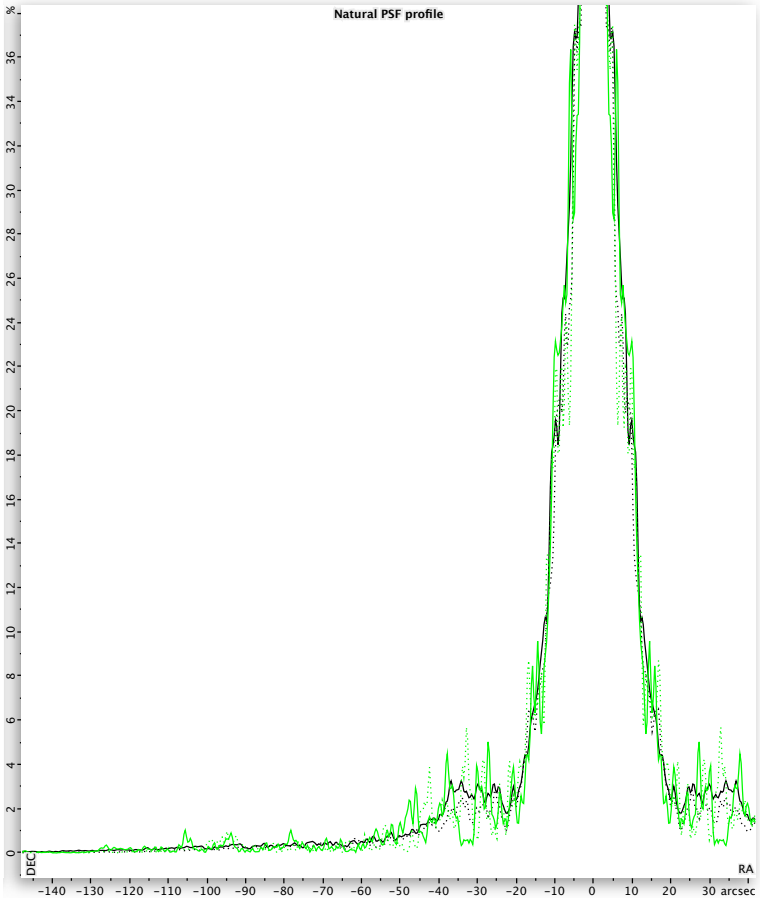

Figure 6.36: The PSF profile for both a snapshot (green) and 4hour (black) observation with *Layout 2.1*.

The side-lobe levels for the snapshot case are not ideal, while the 4hour case gives a better result with a maximum level of ∼3.5% that of the main PSF beam. The larger baselines used for this layout results in a very narrow PSF beam. The theoretical resolution given a maximum baseline, b_{max} of ∼70km is 0.6 arcsec. The simulated value is higher with ∼1.52 arcsec, as the PSF is not an ideal Gaussian beam. The added number of antennas for the spiral stations is 2700, so that the sensitivity is increased with $6107m^2/K$. When these PAF antenna stations are used together with the main core PAF antennas, it gives a total sensitivity of $\sim 8156m^2/K$. Any fraction of the main core AA layout can then also be added to increase the collecting area and thus the sensitivity.

As discussed in section 5.3.2, the ASKAP (36 antenna) layout will be able to include precision pulsar timing as one of its science goals. Compared to the ASKAP, *Layout 2.1* has a higher sensitivity with a factor of 100. When compared to existing telescopes, it has a factor of ∼8 times the sensitivity of Arecibo and ∼104 times that of the Parkes telescope. For future work, the layout of the main core may be optimised to reduce the side-lobe levels. As mentioned, the configuration for pulsar timing is not critical. Therefore the spiral layout design given here is flexible and can be adapted to include other science cases.

6.7 Conclusion

In this chapter, the basic pulsar receiver system was introduced with a general idea of the factors that influence this design. The SKA pulsar science case was discussed in detail, resulting in a set of goals and specifications. It continued to give the general SKA system designs for pulsar search, timing and astrometric observations that can be built on to developed more refined systems in the future. The last section explored possible antenna configurations for the SKA pulsar survey and timing observations. These simulation results were compared with the MeerKAT and ASKAP layouts as well as current working telescopes.

Chapter 7

Conclusion

A large part of this thesis focuses on presenting basic radio astronomy fundamentals. Concepts like interferometry and the u,v-plane proves to play an important role. The classification of radio sources by thermal or non-thermal radiation, together with the flux density spectra clarifies the methods used to observe these sources. This is complimented with a chapter on various examples of radio sources and their emission.

The attention then shifts to the Square Kilometre Array (SKA), with a background description given on the current pathfinders, technologies and Key Science Projects (KSPs). It then evaluates various SKA pathfinders systems. It finds that the Experimental Development Model (XDM), KAT-7 and MeerKAT projects proves to be good demonstrators of parabolic focus fed dishes with Wide-Band Single Pixel Feeds (WBSPFs), both as a single dish and array use [5]. The Australian Square Kilometre Array Pathfinder (ASKAP) project also demonstrates focus fed dishes, but with Phased Array Feed (PAF) technology [6]. The Parkes in turn shows how a horn cluster feed can be used [4], while Electronic Multi-Beam Radio Astronomy Concept (EMBRACE) contributes to the development of dense aperture arrays [7]. Simulations are made of the antenna layouts for the KAT-7, MeerKAT and ASKAP arrays. The results reflects the influence of the configuration on the particular u,v-coverage and Point Spread Function (PSF).

The pulsar observations science case was chosen as one of the KSPs to consider in more detail. This entailed a relevant background study of pulsars and their properties that leads to the implications on the telescope receiver system [93]. With a general idea of what is required for a pulsar observing system, the specific SKA pulsar science case goals and specifications are looked at [8] [9]. This leads to a discussion of optimal system designs for pulsar searches, timing and astrometric observations. It finds that these designs can only be specified to a certain level, after which more development and testing is needed from working systems. One such a specification - the configuration is then chosen to explore further with the aid of *iAntConfig* computer software [17]. Some layouts are designed following from the specifications for the pulsar search and timing observations. Simulations results are compared with parts of the MeerKAT and ASKAP layouts. The performances are also evaluated and measured against some of the current working radio telescopes used for pulsar studies. It finds that the layouts for pulsar surveys give good results in terms of their u,v-coverage and PSFs. They also have good performance regarding their sensitivity and survey speed compared to existing instruments. The layout for pulsar timing observations is very flexible and can work well with a main core to give high sensitivity.

The natural course from the work presented here, would be to continue with a detailed study of all the KSP goals and specifications. Optimal system designs and configuration simulations can then be evaluated and

improved on for each science case. This can eventually be integrated into a single SKA system design that takes into consideration all aspects of the science to be achieved. The focus on SKA pulsar systems can lead to more detailed designs with the focus on any part of the system and its specifications.

This work contributes to forming a basis for future work in developing radio telescope systems. It serves as a study of the background needed to start a project that requires knowledge of basic radio astronomy concepts, interferometry and antenna receiver systems. The SKA project itself is rich in opportunities for research and development in a number of fields. This thesis hopes to encourage and assist in such future work.

Whether this instrument will result in a major paradigm shift in our understanding of the universe and our place in it, or propel us even more into the vastness of space and time is debatable. What we do know is that our curious nature as human beings will persevere so that we will continue to find ways that will enable us to answer the most fundamental questions of the universe.

Appendix A

System Architecture

A.1 Stokes Parameters

The Stokes parameters are a set of 4 parameters that indicate the state of polarisation of an Electromagnetic (EM) signal, e.g., linear or circularly polarised [13]. It is included here as it is essential in analysing radio astronomy data and often included in polarisation studies. Theses parameters can be obtained using a correlator. The correlator performs two tasks; the Fourier Transform (FT) and multiplication (see section A.1.1). The FT is done by the filterbank component and thus converts the time signal into the frequency domain. The multiplication component of the correlator performs various computations including determining the Stokes parameters.
Let us assume we are receiving a linearly polarised EM wave. The electric field of the signal has two orthogonal complex components we will refer to as E_H and E_V (for horizontal and vertical polarisation respectively), and therefore two channels. The Stokes parameters are then calculated as follows, depending on if you are using a single dish or antenna array [104].

Single dish
The correlator takes both polarisation channels (E_H and E_V) as input and performs auto- and cross-correlations. The output is the power of the signal, given here by (A.1.1), with P_{XY} the power resulting from correlating the E_X and E_Y components.

$$P_{XY} = E_X E_Y^* \tag{A.1.1}$$

The result will typically be in the form: P_{HH}, P_{VV}, P_{HV} and P_{VH}. The Stokes parameters (I, Q, U and V) can then be calculated from this output. For broadband radiation, using a linear polarised co-ordinate system, the time-averaged Stokes parameters are calculated [1], see (A.1.2):

$$\begin{aligned} I &= \langle E_H E_H^* \rangle + \langle E_V E_V^* \rangle \\ Q &= \langle E_H E_H^* \rangle - \langle E_V E_V^* \rangle \\ U &= \langle E_H E_V^* \rangle + \langle E_V E_H^* \rangle \\ V &= \frac{1}{i} \langle E_H E_V^* \rangle - \langle E_V E_H^* \rangle \end{aligned} \tag{A.1.2}$$

[1] Note that the Stokes parameters are a function of time and frequency.

Antenna array
The correlator takes both polarisation channels (E_H and E_V) as input and does so for all the antennas forming part of the array. When using an interferometer, it is necessary to combine the signals of each antenna pair forming a baseline. The correlator therefore calculates the cross-correlation for each baseline in the array. It also computes the auto-correlation and cross-polarisation of each antenna. The calculations can be seen as a matrix multiplication of the whole antenna array with itself for all polarisation combinations. The output data used to calculate the Stokes parameters is then typically P_{HH}, P_{VV}, P_{HV} and P_{VH} for each baseline. The result is 4 visibilities (I, Q, U and V) and thus 4 images, for each baseline.

To demonstrate this with an example, lets consider 2 antennas with two linear polarisation channels (E_H and E_V) each, the Stokes are computed as follows. First, the cross-correlations are calculated and averaged as given by (A.1.3).

$$\left\langle \begin{pmatrix} E_{H1} \\ E_{V1} \end{pmatrix} \times \begin{pmatrix} E_{H2} \\ E_{V2} \end{pmatrix} \right\rangle = \begin{pmatrix} \langle E_{H1}E_{H2} \rangle \\ \langle E_{H1}E_{V2} \rangle \\ \langle E_{V1}E_{H2} \rangle \\ \langle E_{V1}E_{V2} \rangle \end{pmatrix} \tag{A.1.3}$$

With E_{H1} and E_{V1} the horizontal and vertical polarisation components respectively for antenna 1
E_{H2} and E_{V2} the horizontal and vertical polarisation components respectively for antenna 2

The Stokes parameters are then obtained by using the result from (A.1.3) to perform the matrix multiplication as given by (A.1.4).

$$\begin{pmatrix} I \\ Q \\ U \\ V \end{pmatrix} = \frac{1}{2} \begin{pmatrix} 1 & 0 & 0 & 1 \\ 1 & 0 & 0 & -1 \\ 0 & 1 & 1 & 0 \\ 0 & -i & i & 0 \end{pmatrix} \begin{pmatrix} \langle E_{H1}E_{H2} \rangle \\ \langle E_{H1}E_{V2} \rangle \\ \langle E_{V1}E_{H2} \rangle \\ \langle E_{V1}E_{V2} \rangle \end{pmatrix} \tag{A.1.4}$$

This result can now be used to determine the polarisation state of the received radiation and can be further processed to form images [105].

A.1.1 Correlators

When using multiple antennas for radio observations, the received signals need to be correlated for each baseline resulting in the cross power spectrum or visibility spectrum [106]. This is the task of the correlator. Two types architectures are mentioned, namely *FX* and *XF* correlators[2].
In the XF correlator, the cross correlation function is measured before it is Fourier Transformed. The result is the cross power spectrum. Fig.A.1(left) shows the architecture of a basic XF correlator with 2 antenna inputs, *D* the delay, *X* the multiplication and *A* the accumulation [108].

[2]The '*F*' indicates the Fourier Transform and '*X*' the multiplication.

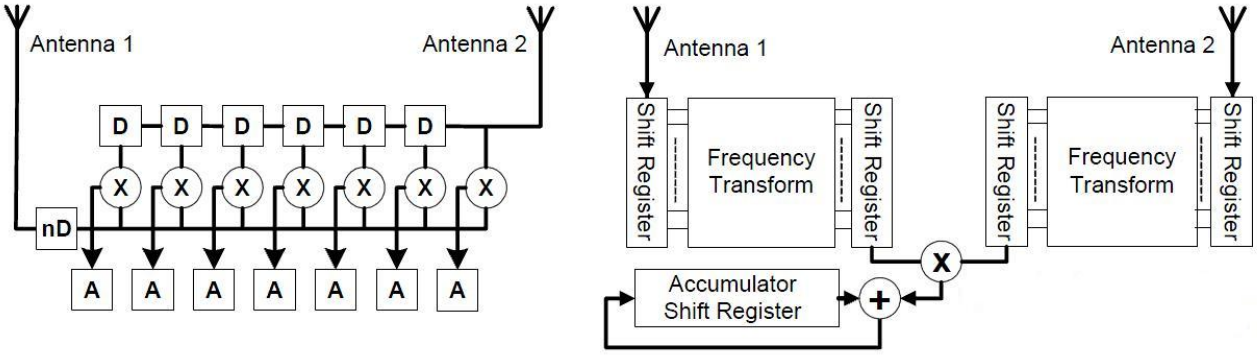

Figure A.1: Basic XF correlator (left) and FX correlator (right) with a two antenna input, from [107].

For the FX correlator, the Fourier Transformation of the data takes place before the cross multiplication operation is performed. The cross power spectrum can then be measured directly for each spectral channel. An advantage of this type of correlator is that the computational load is reduced, especially when dealing with a large number of baselines. Fig.A.1(right) shows the architecture of a basic FX correlator [107].

A.2 Beamformers

Beamformers are used to combine antennas like Aperture Arrays (AAs), or the feed elements of an antenna (PAFs) to produce separate beams as output. An amplitude (a_k) and phase weight (θ_k) is assigned to each component or element in the array, after which these weighted signals are added together to form beams. This is called the complex weight, w_k (for the k^{th} antenna or element) and is represented by (A.2.1) [109].

$$w_k = a_k e^{j\sin(\theta_k)} \tag{A.2.1}$$

Fig.A.2 shows a block diagram of a digital beamformer, where the complex weights are multiplied with the antenna signals.

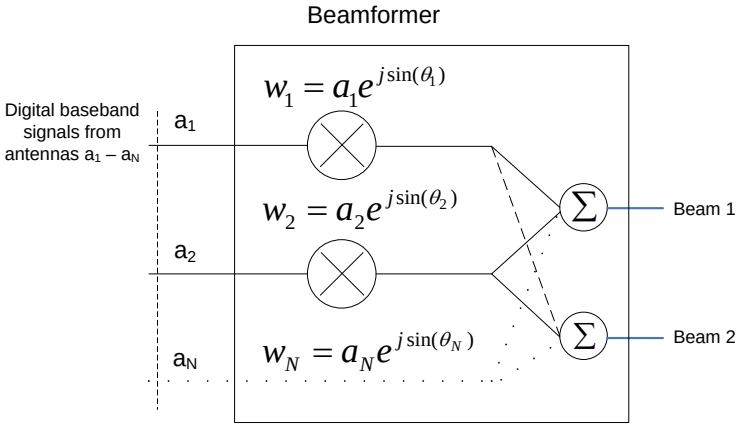

Figure A.2: Complex weights in a digital beamformer.

Multiple beams can be implemented by using a single Field of View (FoV) with multiple pencil beams like in Fig.A.3 (left). Another method is to from multiple FoV, each also containing several smaller beams like in

Fig.A.3 (right). Multiple FoV means that the different beams can be used by more than one user at the same time. Or when doing pulsar timing observations, the pulsars can be timed simultaneously. This will however increase the processing load [110].

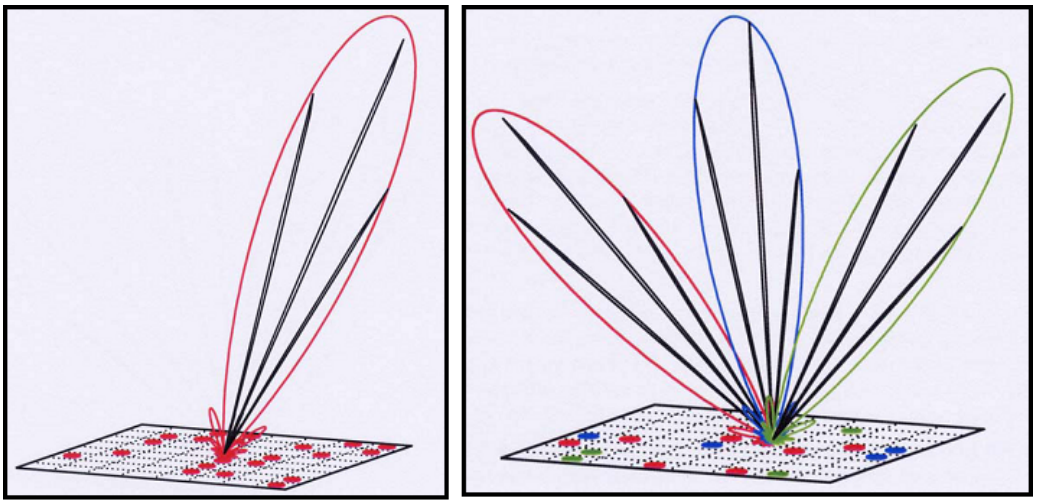

Figure A.3: Multiple beams within a FoV (left) and multiple FoV (right), from [110].

Appendix B

System Specifications and Metrics

B.1 Technical Specifications for the SKA

Fig.B.1 gives the SKA Pulsar science specifications as described in section 6.4.

Topic	Required Specification					
	δt (μs)	A/T (m^2/K)	ν_{max} (GHz)	Configuration	FOV Sampling	Polarization (output, isolation)
Searching						
Galactic Census	50	f_c 20,000	2.5	"core," with large f_c	full	Total
Galactic Center	50	f_c 20,000	15	"core," with large f_c	full	Total
Extragalactic	50	f_c 20,000	1.5	"core," with large f_c	full	Total
Globular Clusers	50	f_c 20,000	1.5	"core," with large f_c	full	Total
Targeted	50	f_c 20,000	1.5	"core," with large f_c	full	summed
Timing						
GR tests, NS-BH binaries, MSPs	< 1	20,000	15	non-critical if phasable	100 beams/deg^2	full Stokes, -40dB
GR tests, Galactic center NS-BH binaries	100	20,000	15	non-critical if phasable	10 beams/deg^2	full Stokes, -40dB
VLBI						
gated astrometry (proper motion, parallax)	200	> 2000	8	intercontinental baselines	~ 3 beams	Total

Figure B.1: Technical specification parameters for the SKA pulsar science case, from [9].

What follows is the top-level SKA technical requirements from [111] [112] [1]:

Frequency Range
A wide frequency range specified as 100MHz – 25GHz is required for the SKA to achieve various science goals and also to maximize the value of the instrument. The total frequency range may not be possible to realise with only one type of antenna technology and is therefore divided into sub-ranges. A factor that influences this specification is that there exists a trade-off between cost and the maximum frequency so that cost increases with ν^n with n$\sim$1 for dishes and n$\sim$2 for phased arrays.

Sensitivity

The sensitivity is a measure of the weakest detectable radio emission and is related to the collecting area of the telescope or array as given by:

$$Sensitivity = \frac{A_{eff}}{T_{sys}} \tag{B.1.1}$$

with A_{eff} the effective collecting area

T_{sys} the system temperature

The specification for the SKA at 1.4GHz as given by Table B.1 and is found by taking the total collecting area of 1 km^2, aperture efficiency (e_{ap}) of 50% and system temperature of 25K so that:

$$Sensitivity = \frac{0.5 \times 1000000m^2}{25K} = 20000m^2/K \tag{B.1.2}$$

Table B.1: SKA sensitivity specifications.

Sensitivity	Frequency
5000 m^2/K	200MHz
20000 m^2/K	0.5–5 GHz
15000 m^2/K	15GHz
10000 m^2/K	25GHz

Number of observing bands

This requirement is 2 pairs, which is the number of frequency bands that can be observed with simultaneously. The centre frequency separation is required to be a factor of 3.

Field-of-view

The FoV requirement is 1 deg^2 at 1.4GHz, 200 deg^2 at 700MHz and scaling with λ^2 between 0.5–1 GHz. The FoV is the solid angle of the sky that can be viewed at a given time. For the parabolic reflectors with WBSPFs the FoV (in steradians) can be determined by:

$$FoV = \left(\frac{\lambda}{D_{dish}}\right)^2 \tag{B.1.3}$$

For PAFs, the FoV does no longer depend on the frequency, and is extended by a certain factor. The Aperture Array gives a FoV of about half of the sky.

Number of FoVs

This is the number of separate FoV that can be used to observe separate parts of the sky and is specified as:
1 FoV with full sensitivity, 10 simultaneous sub-arrays.

Number of instantaneous pencil beams

This is the number of beams formed within one FoV simultaneously to observe different point sources and is

specified as 100 beams.

Angular Resolution
The ability to measure the angular separation of objects in the sky, required to be 0.1 arcsec at 1.4GHz. It depends on the maximum baseline of the array. The minimum resolution is set by the continuum confusion at 1.4GHz, while the highest resolution is set by Very Long Baseline Interferometry (VLBI) science.

Number of Spatial Pixels
This is the number of spatial resolution elements within the FoV imaged and is required to be 10^8.

Surface Brightness Sensitivity
The minimum continuum surface brightness detected for a given resolution, required to be $1K$ at 0.1 arcsec. It may be a function of frequency and is determined from the sensitivity, bandwidth and resolution.

Instantaneous bandwidth
This forms a fraction of the total frequency range that is observed simultaneously and is specified as 25% of the observing band centre frequency and a maximum of 4GHz for frequencies >16 GHz. It is set by the Intermediate Frequency (IF) filter bandwidth before the signal is digitised and depends on the correlator or processor capability.

Clean Beam Dynamic Range
This is set by the ratio of the strongest continuum source to the weakest detectable source within the FoV imaged at a given frequency. It is specified as 10^6 at 1.4GHz.

Polarisation Purity
The error in Stokes parameters Q, U, and V as a fraction of I for a strong radio source after all processing, required to be -40dB. It is a measure of how much power from one polarisation leaks into another polarisation after calibration.

B.2 Performance Metrics

The equations for the system performance metrics used in section 6.6 are given here with short descriptions.

System equivalent flux density (SEFD)
This is the equivalent point source flux density given the antenna system temperature [113].

$$SEFD = \frac{2kT_{sys}}{A_{eff}} \quad [Jy] \tag{B.2.1}$$

RMS noise
This is the expected rms noise for a point source also known as the *point source sensitivity*. For a single dish with the assumption that the source is smaller than the antenna beam, it is given by [114]:

$$\sigma_s = \frac{2kT_{sys}}{A_{eff}\sqrt{n_{pol} \times \Delta\nu \times t_{obs}}} \quad [Jy/beam] \tag{B.2.2}$$

with t_{obs} the integration time
$\Delta\nu$ the bandwidth

For an interferometer with N dishes the RMS noise is given by [115]:

$$\sigma_s = \frac{2kT_{sys}}{A_{eff}\sqrt{0.5 \times N(N-1) \times n_{pol} \times \Delta\nu \times t_{obs}}} \quad [Jy/beam] \tag{B.2.3}$$

Gain
The gain is a measure of the antenna or array performance, without taking the system temperature into consideration. It can be seen as the antenna temperature due to a point source with flux density of 1Jy and is given by [113]:

$$G = \frac{A_{eff}}{2k} \quad [K/Jy] \tag{B.2.4}$$

Survey speed
This is a measure of how fast a survey can be done and is determined by the FoV and sensitivity of the antenna array [1].

$$SS = FoV\left(\frac{{A_{eff}}^2}{T_{sys}}\right) \quad [m^4 deg^2/K^2] \tag{B.2.5}$$

List of References

[1] R. T. Schilizzi, P. Alexander, J. M. Cordes, P. E. Dewdney *et al.*, "Preliminary Specifications for the Square Kilometre Array," December 2007, SKA Memo 100. [Online]. Available: http://www.skatelescope.org/pages/page_memos.htm 1, 2, 3, 86, 132, 149, 168, 171

[2] C. Greenwood, "Status of Pathfinder Telescopes and Design Studies," December 2007, International SKA Project Office. [Online]. Available: http://www.skatelescope.org/ 1

[3] C. L. Carilli and S. Rawlings, "Motivation, Key Science Projects, Standards and Assumptions," *New Astronomy Reviews*, vol. 48, no. 11–12, pp. 979– 984, 2004, Science with the Square Kilometre Array. [Online]. Available: http://www.sciencedirect.com/science/article/B6VNJ-4DKD4N5-1/2/1410d95efe1fa2b0932395b93ca94235 1

[4] W. E. Wilson, M. W. Sinclair, M. R. Leach, E. R. Davis *et al.*, "The Parkes 21cm Multibeam Receiver," CSIRO. 2, 89, 97, 162

[5] J. Jonas, "MeerKAT: The South African Array With Composite Dishes and Wide-Band Single Pixel Feeds," *Proceedings of the IEEE*, vol. 97, no. 8, pp. 1522–1530, August 2009. 2, 107, 132, 162

[6] D. R. DeBoer, R. G. Gough, J. D. Bunton, T. J. Cornwell *et al.*, "Australian SKA Pathfinder: A High-Dynamic Range Wide-Field of View Survey Telescope," *Proceedings of the IEEE*, vol. 97, no. 8, pp. 1507–1521, August 2009. 2, 89, 114, 162

[7] G. W. Kant, P. D. Patel, J. A. van Houwelingen, and A. van Ardenne, "Electronic Multi-beam Radio Astronomy Concept: Embrace the European Demonstrator for SKA Program." [Online]. Available: http://www.skads-eu.org/PDF/embrace_final_02_8.pdf 2, 120, 162

[8] M. Kramer, D. C. Backer, J. M. Cordes, T. J. W. Lazio *et al.*, "Strong-Field Tests of Gravity Using Pulsars and Black Holes," *New Astronomy Reviews*, vol. 48, no. 11–12, pp. 993–1002, 2004, Science with the Square Kilometre Array. 3, 92, 129, 130, 134, 162

[9] J. M. Cordes, M. Kramer, T. J. W. Lazio, B. W. Stappers *et al.*, "Pulsars as Tools for Fundamental Physics & Astrophysics," *New Astronomy Reviews*, vol. 48, no. 11–12, pp. 1413 –1438, 2004, Science with the Square Kilometre Array. 3, 125, 129, 130, 133, 153, 155, 162, 168

[10] C. A. Balanis, *Antenna Theory: Analysis and Design*, 3rd ed. John Wiley, 2005. 5, 7

[11] J. D. Kraus, *Radio Astronomy*. Cygnus-Quasar Books, 1986. 5, 6, 7, 8, 10, 11, 33, 35, 36, 37, 38, 40, 43, 44, 49, 50, 52, 55, 56, 57, 58, 59, 61, 62, 65, 66, 67, 70, 76, 77, 80, 82, 123

[12] D. Fisher. (1998, April) Basics of Radio Astronomy. Jet Propulsion Laboratory. JPL, NASA. [Online]. Available: http://www2.jpl.nasa.gov/radioastronomy/ 9, 32, 33, 34, 39, 40, 41, 44, 45, 46, 49, 58, 59, 60, 63, 69, 73, 74, 80, 81

[13] B. F. Burke and F. Graham-Smith, *An Introduction to Radio Astronomy*. Cambridge University Press, 1997. 14, 15, 17, 18, 46, 47, 63, 72, 123, 164

[14] NRAO. [Online]. Available: http://images.nrao.edu/Telescopes 16

[15] B. Tubbs. Development of Radio Interferometry. [Online]. Available: http://www.geocities.com/capecanaveral/2309/page3.html 16

[16] T. L. Wilson and K. Rohlfs, *Tools of Radio Astronomy*, 5th ed. Springer, 2009. 18, 125

[17] M. de Villiers, "iAntConfig." 23, 28, 103, 107, 115, 135, 162

[18] D. E. Gary. Radio Astronomy. NJIT. Physics 728. [Online]. Available: http://web.njit.edu/~gary/728/ 24, 26, 27, 31, 32, 33, 36, 38, 39, 40, 41, 56, 57, 63, 69, 74

[19] Introduction to Interferometry. NRAO. [Online]. Available: http://www.astro.indiana.edu/catyp/radio/Indiana.interferometry.ppt 25

[20] A. Faltenbacher. (2010) Radio Astronomy for Engineers: Lecture 2: Radio Imaging. [Online]. Available: http://sites.google.com/site/faltenbacher/lectures 27, 28

[21] [Online]. Available: http://scipp.ucsc.edu/~haber/ph5B/ 31

[22] W. J. Kaufmann, *Universe*, 2nd ed. W. H. Freeman, 1988. 40, 75, 80, 81

[23] J. J. Condon and S. M. Ransom. Essential Radio Astronomy. NRAO. [Online]. Available: http://www.cv.nrao.edu/course/astr534/ERA.shtml 41

[24] R. P. Feynman, R. B. Leighton, and M. L. Sands, *The Feynman Lectures on Physics Vol. 1*. Addison-Wesley Publishing Co., 1989, vol. 1. 41, 42, 43

[25] V. L. Ginzburg and S. I. Syrovatskii, "Cosmic Magnetobremsstrahlung (Synchrotron Radiation)," *Annual Review of Astronomy and Astrophysics*, vol. 3, pp. 297–350, 1965. 43, 44

[26] G. R. Huguenin, "Pulsar Observing Techniques," in *Astrophysics: Radio Observations*, ser. Methods in Experimental Physics, M. L. Meeks, Ed. Academic Press, 1976, vol. 12, Part 3, pp. 78–91. 47, 123, 124

[27] R. Beck and B. M. Gaensler, "Observations of Magnetic Fields in the Milky Way and in Nearby Galaxies with a Square Kilometre Array," *New Astronomy Reviews*, vol. 48, no. 11–12, pp. 1289–1304, 2004, Science with the Square Kilometre Array. 47

[28] NRAO. [Online]. Available: http://images.nrao.edu/Solar_System/Planets/22 58

[29] NRAO. [Online]. Available: http://images.nrao.edu/Solar_System/Planets/27 60

[30] NRAO. [Online]. Available: http://images.nrao.edu/Galaxy/Peculiar/116 64

[31] NASA. [Online]. Available: http://hubblesite.org/newscenter/archive/releases/2006/01/image/a/format/large_web/ 64

[32] NRAO. [Online]. Available: http://images.nrao.edu/images/Orion_VR13A_med.jpg 64

[33] NRAO. [Online]. Available: http://images.nrao.edu/images/l483j_top.jpg 68

[34] NRAO. [Online]. Available: http://images.nrao.edu/images/l483_bottom.jpg 68

[35] NASA. [Online]. Available: http://hubblesite.org/gallery/album/nebula/pr1995044a/large_web/ 69

[36] Paris Observatory. [Online]. Available: http://www.obspm.fr/actual/nouvelle/nov01/n160_large.jpg 70

[37] NASA. [Online]. Available: http://ipac.jpl.nasa.gov/media_images/ssc2005-14c_medium.jpg 71

[38] NASA. [Online]. Available: http://hubblesite.org/gallery/album/nebula/pr2005037a/large_web/ 71

[39] Inter University Institute for High Energies. WIMPs Analysis. [Online]. Available: http://w3.iihe.ac.be/icecube/3_Activities/ 72

[40] [Online]. Available: http://farm3.static.flickr.com/2106/1767929218_3807ff9978_o.png 73

[41] NASA. [Online]. Available: http://www.nasa.gov/centers/marshall/images/content/100080main_cygx3_low_m.jpg 73

[42] NRAO. [Online]. Available: http://images.nrao.edu/images/HydrogenSky_VR87_med.jpg 75

[43] Indiana University. [Online]. Available: http://woodahl.physics.iupui.edu/Astro105/18_12Figurec.jpg 75

[44] C. Flynn. Astrophysics II. Tuorla Observatory, University of Turku. Lecture 4B: Radiation case studies. [Online]. Available: http://www.astro.utu.fi/~cflynn/astroII/ 76

[45] NASA. [Online]. Available: http://antwrp.gsfc.nasa.gov/apod/ap061126.html 76

[46] NASA. [Online]. Available: http://antwrp.gsfc.nasa.gov/apod/ap050617.html 77

[47] NASA. [Online]. Available: http://antwrp.gsfc.nasa.gov/apod/ap060510.html 77

[48] SEDS. [Online]. Available: http://seds.org/messier/Pics/Jpg/m87comp.jpg 77

[49] NASA. [Online]. Available: http://antwrp.gsfc.nasa.gov/apod/ap961117.html 78

[50] NASA. [Online]. Available: http://antwrp.gsfc.nasa.gov/apod/ap080822.html 78

[51] NASA. [Online]. Available: http://antwrp.gsfc.nasa.gov/apod/ap080110.html 79

[52] NRAO. [Online]. Available: http://images.nrao.edu/images/CygA-YellowOrange_med.jpg 79

[53] NRAO. [Online]. Available: http://images.nrao.edu/images/3c279_mosaic_med.jpg 81

[54] University of Wisconsin-Madison. [Online]. Available: http://www.astro.wisc.edu/~bank/img/inversecompton.jpg 82

[55] P. Dewdney. (2010, March) SKA System Overview. SKA2010 - International SKA Science and Engineering Meeting. 85, 88, 89

[56] R. Beresford, "ASKAP Photonic Requirements," in *International Topical Meeting on Microwave Photonics*, Gold Coast, Queensland, Australia, 30 September–3 October 2008, pp. 62–65. 86, 112

[57] T. Cornwell, "ASKAP Industry Technical Briefing," July 2009, CSIRO. 86

[58] A. van Ardenne, "The European Aperture Array SKA Demonstrator: Electronic MultiBeam Radio Astronomy ConcEpt (EMBRACE)," ASTRON, NL. [Online]. Available: http://www.skatelescope.org/ 86

[59] W. A. van Cappellen, S. J. Wijnholds, and J. D. Bregman, "Sparse Antenna Array Configurations in Large Aperture Synthesis Radio Telescopes," in *European Radar Conference*, Manchester, England, United Kingdom, 13–15 September 2006, pp. 76–79. 87, 88

[60] A. J. Faulkner, P. Alexander, M. E. Jones, R. Bolton *et al.*, "Design of an Aperture Phased Array System for the SKA." [Online]. Available: http://www.skads-eu.org/PDF/URSI_paper_AJF_final.pdf 87

[61] P. D. Patel, "Wideband Antennas for Radio Astronomy," in *European Conference on Antennas and Propagation*, Nice, France, 6–10 November 2006, pp. 1–6. 87

[62] J. Welch, D. Backer, L. Blitz, D.-J. Bock *et al.*, "The Allen Telescope Array: The First Widefield, Panchromatic, Snapshot Radio Camera for Radio Astronomy and SETI," *Proceedings of the IEEE*, vol. 97, no. 8, pp. 1438–1447, August 2009. 87

[63] S. Jackson, "RF Design of a Wideband CMOS Integrated Receiver for Phased Array Applications," in *The Square Kilometre Array: An Engineering Perspective*, P. Hall, Ed. Springer Netherlands, 2005, pp. 201–210. 89

[64] R. P. Armstrong, K. Z. Adami, and M. E. Jones, "A Wideband Four-Element All-Digital Beamforming System for Dense Aperture Arrays in Radio Astronomy," *ArXiv e-prints*, October 2009, Astrophysics: Instrumentation and Methods for Astrophysics. 89

[65] A.-J. Boonstra. (2007, September) SKA Signal Processing. Part of SKA2007 Inter-WG Meeting. [Online]. Available: http://www.skatelescope.org/pages/SKA2007/15_Boonstra_SKA2007_Day1.pdf 89, 90

[66] J. Bunton, "SKA Correlator Advances," *Experimental Astronomy*, vol. 17, pp. 251–259, 2004. 90

[67] T. Adams, J. Bunton, and M. Kesteven, "The Square Kilometre Array Molonglo Prototype (Skamp) Correlator," *Experimental Astronomy*, vol. 17, pp. 279–285, 2004. 90

[68] A. Parsons, D. Werthimer, D. Backer, T. Bastian *et al.*, "Digital Instrumentation for the Radio Astronomy Community," *ArXiv e-prints*, 2009. 90

[69] A. Langman. Road to MeerKAT KAT-7 DBE. [Online]. Available: http://casper.berkeley.edu/presentations/workshop_august08/slides/langman_meerKATDBE.pdf 90

[70] CASPER. [Online]. Available: http://casper.berkeley.edu/ 91

[71] T. Joseph, W. Lazio, J. C. Tarter, and D. J. Wilner, "The Cradle of Life," *New Astronomy Reviews*, vol. 48, no. 11–12, pp. 985–991, 2004, Science with the Square Kilometre Array. 92

[72] B. M. Gaensler, R. Beck, and L. Feretti, "The Origin and Evolution of Cosmic Magnetism," *New Astronomy Reviews*, vol. 48, no. 11–12, pp. 1003–1012, 2004, Science with the Square Kilometre Array. 92

[73] S. Rawlings, F. B. Abdalla, S. L. Bridle, C. A. Blake *et al.*, "Galaxy Evolution, Cosmology and Dark Energy with the Square Kilometer Array," *New Astronomy Reviews*, vol. 48, no. 11–12, pp. 1013–1027, 2004, Science with the Square Kilometre Array. 92

[74] C. L. Carilli, S. Furlanetto, F. Briggs, M. Jarvis *et al.*, "Probing the Dark Ages with the Square Kilometer Array," *New Astronomy Reviews*, vol. 48, no. 11–12, pp. 1029–1038, 2004, Science with the Square Kilometre Array. 92

[75] A. Peens-Hough, February 2010, private communication. 93, 95

[76] CSIRO. [Online]. Available: http://www.atnf.csiro.au/research/multibeam/instrument/description.html 97

[77] Filterbank Systems. CSIRO. [Online]. Available: http://www.atnf.csiro.au/research/pulsar/obtain/fbdata/fbsystems.html 98

[78] L. Ball, N. McClure-Griffiths, R. Braun, P. Edwards *et al.*, "ATNF Science in 2010–2015," August 2008. [Online]. Available: http://www.atnf.csiro.au/observers/planning/priorities/ATNF_Science_Priorities_v1.0.pdf 98, 118, 130

[79] B. Veidt, "Focal-Plane Array Architectures: Horn Clusters vs. Phased-Array Techniques," February 2006, SKA Memo 71. [Online]. Available: http://www.skatelescope.org/PDF/memos/71_Veidt.pdf 98

[80] "SKA Newsletter Volume 17," January 2010. [Online]. Available: www.skatelescope.org 99

[81] R. S. Booth, W. J. G. de Blok, J. L. Jonas, and B. Fanaroff, "An open invitation to the Astronomical Community to propose Key Project Science with the South African Square Kilometre Array Precursor MeerKAT." [Online]. Available: http://www.ska.ac.za/temp/rfp_meerkat.pdf 99, 107, 111, 112

[82] M. van der Merwe, "KAT-7 front end design," March 2010, private communication. 101

[83] E. de Blok, B. Frank, A. Bouchard, and M. de Villiers, "Outline of a MeerKAT configuration." [Online]. Available: aramis.obspm.fr/SKA/forum09/roy_conf.pdf 111

[84] "ASKAP Science Update," October 2009, CSIRO. [Online]. Available: http://www.atnf.csiro.au/projects/askap/science_update_newsletter.html 112

[85] "ASKAP Digital Signal Processing Systems: System Description & Overview of Industry Opportunities," March 2009, CSIRO. [Online]. Available: http://www.atnf.csiro.au/projects/askap/ASKAP_dst_v1.0_final.pdf 114

[86] ASKAP Technologies: Data Transport and Signal Transmission. CSIRO. [Online]. Available: http://www.atnf.csiro.au/projects/askap/data_transport.html 114

[87] N. Gupta, S. Johnston, I. Feain, and T. Cornwell, "The Initial Array Configuration for ASKAP," October 2008, Australia Telescope National Facility, CSIRO. [Online]. Available: http://www.atnf.csiro.au/SKA/newdocs/configs-3.pdf 115

[88] S. Johnston and R. Edwards, "Pulsar surveys with the xNTD," September 2006, CSIRO. [Online]. Available: http://www.atnf.csiro.au/SKA/newdocs/psr_survey.pdf 118

[89] A. V. Ardenne, P. N. Wilkinson, P. D. Patel, and J. G. B. D. Vaate, "Electronic Multi-beam Radio Astronomy Concept: Embrace a Demonstrator for the European SKA Program," *Experimental Astronomy*, vol. 17, pp. 65–77, 2004, 10.1007/s10686-005-2868-4. 119

[90] G. W. Kant, "The Building of EMBRACE," November 2009, SKADS. [Online]. Available: http://www.skads-eu.org/limelette2/presentations/SKADSconference20091105-Kant.pdf 119

[91] G. Bianchi, J. Morawietz, F. Perini, and M. Schiaffino, "EMBRACE LO distribution system," 2008, IRA Internal Report. [Online]. Available: http://www.ira.cnr.it/Library/rapp-int/426_08.pdf 120

[92] O. Maron, J. Kijak, M. Kramer, and R. Wielebinski, "Pulsar Spectra of Radio Emission," *Astronomy and Astrophysics Supplement Series*, vol. 147, no. 2, pp. 195–203, December 2000. 123

[93] D. R. Lorimer and M. Kramer, *Handbook of Pulsar Astronomy*. Cambridge University Press, 2005. 123, 125, 126, 162

[94] Y. Gupta. Low Frequency Radio Astronomy: Chapter 17: Pulsar Observations. GMRT. [Online]. Available: http://gmrt.ncra.tifr.res.in/gmrt_hpage/Users/doc/WEBLF/LFRA/pdf/ch17.pdf 123, 125, 127

[95] J. Cordes and M. Kramer, "SKA Key Science Project: Gravity: Pulsars and Black Holes," October 2005, Part of SKA Memo 89. [Online]. Available: http://www.skatelescope.org/ 124, 129, 132, 134

[96] M. Hobbs. An Introduction to Pulsars. CSIRO. [Online]. Available: http://outreach.atnf.csiro.au/education/everyone/pulsars/ 124

[97] E. Pfahl and A. Loeb, "Probing the Spacetime around Sagittarius A* with Radio Pulsars," *The Astrophysical Journal*, vol. 615, pp. 253–258, 2004. 130

[98] R. Smits, M. Kramer, B. Stappers, D. R. Lorimer *et al.*, "Pulsar Searches and Timing with the SKA," November 2008, SKA Memo 105. [Online]. Available: http://www.skatelescope.org/ 130, 132

[99] B. Gaensler and J. Lazio, "Trade-offs between Science and Engineering for the Square Kilometre Array," August 2006, SKA Memo 82. [Online]. Available: http://www.skatelescope.org/ 130, 132

[100] S. Johnston, M. Bailes, N. Bartel, C. Baugh *et al.*, "Science with the Australian Square Kilometre Array Pathfinder," *Publications of the Astronomical Society of Australia*, vol. 24, pp. 174–188, 2007. 132

[101] E. Fomalont and M. Reid, "Microarcsecond Astrometry using the SKA," *New Astronomy Reviews*, vol. 48, pp. 1473–1482, 2004. 134

[102] M. Wright, J. Bregman, R. Braun, J. Bunton *et al.*, "SKA Survey Optimization," June 2006, SKA Memo 81. [Online]. Available: http://www.skatelescope.org/ 136

[103] M. Wright, "SKA Imaging," February 2004, SKA Memo 46. [Online]. Available: http://www.skatelescope.org/ 158

[104] J. N. Chengalur. Low Frequency Radio Astronomy: Chapter 15: Polarimetry. GMRT. [Online]. Available: http://gmrt.ncra.tifr.res.in/gmrt_hpage/Users/doc/WEBLF/LFRA/pdf/ch15.pdf 164

[105] L. Schwardt, April 2010, private communication. 165

[106] D. A. Roshi. Low Frequency Radio Astronomy: Chapter 8: Correlator I: Basics. GMRT. [Online]. Available: http://gmrt.ncra.tifr.res.in/gmrt_hpage/Users/doc/WEBLF/LFRA/pdf/ch8.pdf 165

[107] J. D. Bunton, "New Generation Correlators." [Online]. Available: http://rp.iszf.irk.ru/hawk/URSI2005/pdf/J06.6(0311).pdf 166

[108] J. D. Bunton, "Implementing Correlators for the SKA," in *Workshop on the Applications of Radio Science*, Leura, NSW Australia, 20–22 February 2002, p. J1. [Online]. Available: http://www.ips.gov.au/IPSHosted/NCRS/wars/wars2002/proceedings/index.htm 165

[109] T. Haynes, "A Primer on Digital Beamforming," March 1998. [Online]. Available: www.spectrumsignal.com 166

[110] S. Montebugnoli, G. Bianchi, A. Cattani, F. Ghelfi *et al.*, "Some Notes on Beamforming," the Medicina IRA-SKA Engineering Group. [Online]. Available: http://www.med.ira.inaf.it/BEST/documents/IRA_353-04.pdf 167

[111] R. Ekers, "SKA Technical Specifications," December 2001, SKA Memorandum 4. [Online]. Available: http://www.skatelescope.org/ 168

[112] D. L. Jones, "SKA Science Requirements: Version 2," February 2004, SKA Memo 45. [Online]. Available: http://www.skatelescope.org/ 168

[113] C. Salter, "Notes Relevant to Spectral-Line Calibration," August 2000, National Astronomy and Ionosphere Center. [Online]. Available: http://www.naic.edu/~astro/aotms/ 171

[114] J. Condon, "Sensitive Continuum Surveys with the SKA: Goals and Challenges," July 2009, SKA Memo 114. [Online]. Available: http://www.skatelescope.org/ 171

[115] S. Johnston and A. Gray, "Surveys with the xNTD and CLAR." [Online]. Available: http://www.atnf.csiro.au/SKA/newdocs/xntd_clar.pdf 171